

Structural Studies of Bacterial Adhesion

Name: Nina Isabel Sulkowski

DPhil in Molecular Biology in Health and Disease

Student ID: 1106573

Supervisors: Dr Tanmay Bharat and Professor Christoph Tang

Submitted in partial fulfilment of the requirements for the DPhil in Molecular Biology in Health and Disease, University of Oxford

Certificate of Original Authorship

"I certify that this document has not already been submitted for any degree and is not being submitted as part of candidature for any other degree. I also certify that the document has been written by me and that any help that I have received in preparing this document, and all sources used, have been acknowledged in the document."

Final word count: 46,858

Signature of candidate:



Acknowledgements

I begin by thanking my supervisor Dr Tanmay Bharat for his guidance on the scientific method, critical thinking and problem solving. I sincerely thank my co-supervisor Professor Christoph Tang for his generous mentorship and support throughout my DPhil. To the entire Bharat Lab, including Dr Abul Tarafder, Dr Charlotte Melia, Andriko von Kügelgen, Jan Böhning and Matthew Herdman; for their experimental advice, friendship, humour and productive coffee breaks. To Angus Menzies, for being a pleasure to co-supervise and the opportunity to develop myself as a mentor. To my college supervisor, Dr Mohammad Mofatteh, for philosophical discussions and personal guidance. I thank the Sir William Dunn School of Pathology and Clarendon Fund for granting my scholarship and providing an environment to create and explore. To my fellow Australians at the COSMIC facility, Dr Errin Johnson and Adam Costin, for technical support on the microscopes and endless encouragement. I thank our collaborators including Professor Yves Brun, Dr Gail Hardy, Professor Alain Filloux, Eleni Manoli, Kira Glatzel and Dr Jani Reddy Bolla for generously lending their time and expertise. I sincerely thank Lincoln College, for hosting me during my studies and for the kind hearts of our porters; Simon, Christiano, Bob, Joe, Peter and Teagan. I thank my friends, both at Oxford and abroad, for walking alongside me throughout the DPhil experience including Alex, Alicia, Manmeet, Mark, Matt, Quyen, Sandra, Soraiya and Xanita. I thank my entire family for their unconditional love, time and patience. To my dearest grandparents, for installing honour, integrity and curiosity in our family. And finally, to my mother, for exemplifying the determination, grit and bravery required for the last leg of the journey. This is for you.

Abbreviations

AMP	Ampicillin
BSA	Bovine serum albumin
cAMP	cyclic adenosine monophosphate
c-di-GMP	cyclic di-guanosine monophosphate
CF	Cystic fibrosis
CUP	Chaperone usher protein
Cryo-EM	Electron cryomicroscopy
Cryo-ET	Electron cryotomography
DSC	Donor strand complementation
DSC	Donor strand exchange
EHEC	Enterohaemorrhagic *E. coli*
EPS	Exopolysaccharide
ETEC	Enteropathogenic *E. coli*
FSC	Fourier shell correlation
FT	Fourier transform
Hfa	Holdfast anchor protein
Hfs	Holdfast secretion protein
H-NS	Histone-like nucleoid-restructuring
Ig	Immunoglobulin
HRP	Horseradish peroxidase
KAN	Kanamycin
N.D	Not determined
NTE	N-terminal extension
OD	Optical density
OM	Outer membrane
OMP	Outer membrane protein
PCR	Polymerase chain reaction
PDB	Protein data bank
PDE	Phosphodiesterase
pI	Isoelectric point
POTRA	Polypeptide transport-associated
RT	Room temperature
SCV	Small colony variant
SD	Standard deviation
SDS	Sodium dodecyl sulphate
SEM	Scanning electron microscopy
SIRT	Simultaneous iterative reconstruction technique
SPA	Single particle analysis
TCS	Two component system
TEM	Transmission electron microscopy
Tris	Tris (hydroxymethyl) aminomethane
UPEC	Uropathogenic *E. coli*
WBP	Weighted back projection
WCL	Whole cell lysate
WT	Wild-type

Units

In addition to SI units, the following units are referenced:

bp	Base pair
cfu	Colony forming units
Da	Dalton
hrs	Hours
x g	g-force or relative centrifugal force (RCF)
kb	Kilobase
kDa	Kilodalton
mins	Minutes
pH	$-\log_{10} c$, where c is $[H^+]$ in mol/L
rpm	Revolutions per minute
s	Seconds
U	Enzyme unit

Table of Contents

Certificate of Original Authorship.....i

Acknowledgements.....ii

Abbreviations.....iv

Units.....v

Table of Contents.....i

List of Figures.....vii

List of Tables.....x

Abstract.....xi

CHAPTER 1. Introduction.....13

1.1. Adhesion during biofilm development.....13

1.2. Regulation of adhesin expression and biofilm formation.....14

1.2.1. c-di-GMP secondary messenger signalling.....14

1.2.2. Two component systems.....16

1.2.3. Quorum sensing.....18

1.3. Bacterial adhesins.....19

1.3.1. Proteinaceous adhesins.....19

1.3.1.1. Type IV pili.....19

1.3.1.2. Classification and subunit maturation.....19

1.3.1.3. Structure, assembly and disassembly of classical type IVa pili.....20

1.3.1.4. Curli and functional amyloids....22
1.3.1.5. Assembly of curli fibres at the cell surface....22
1.3.1.6. Functional amyloid fibres (Fap) of *P. aeruginosa*....23
1.3.1.7. Canonical Chaperone Usher Fimbriae....25
1.3.1.8. Molecular structure of CUPs....25
1.3.1.9. CUP Assembly....28
1.3.1.10. Subunit ordering of CUP fimbriae....30
1.3.1.11. Classification of CUPs....33
1.3.1.12. Regulation of fimbrial expression....34
1.3.1.13. Predicted CUP of *P. aeruginosa*....36
1.4. Clinical significance of *P. aeruginosa*....38
1.4.1.1. CupA....38
1.4.1.2. CupB and CupC....43
1.4.1.3. CupD....47
1.4.1.4. CupE....48
1.4.2. Polysaccharide adhesins....51
1.4.2.1. Polysaccharide biosynthesis....51
1.4.2.2. PIA and PNAG....54
1.4.2.3. Psl and Pel....56
1.4.2.4. Alginate....58
1.4.2.5. Capsular polysaccharide....59

1.4.2.6. Polysaccharide anchoring 60

1.4.2.7. Holdfast 60

1.4.2.8. Investigation of biological specimens using cryo-EM 64

PROJECT AIMS 70

CHAPTER 2. METHODS AND MATERIALS 71

2.1. Bacterial strains and growth conditions 71

2.2. DNA manipulations and sequencing 71

2.3. *C. crescentus* sample preparation 72

2.4. Cryo-EM grid preparation 72

2.5. Cryo-EM and cryo-ET data collection 72

2.6. Image processing of stalk tips 73

2.7. Image processing of rosettes 74

2.8. Image processing of CupE filaments 75

2.9. Solubilization of HfaB inclusion bodies 76

2.10. Purification and refold of monomeric HfaB 76

2.11. Tryptic digestion and tandem mass spectrometry (LC/MS-MS) (denaturing) 77

2.12. Electrospray mass spectrometry (ESI-MS) (denaturing) 78

2.13. Native mass spectrometry 79

2.14. Shearing and precipitation of CupE filaments 79

2.15. Purification of recombinant CupA1 80

2.16. Purification of polyclonal anti-CupA1 antibodies 81

2.17. Purification of recombinant CupE1 81

2.18. SDS-PAGE and Western Blotting 82

2.19. Immunofluorescence Microscopy (IFM) 82

2.20. Crystal Violet Biofilm Assay 83

2.21. Growth of PAO1 biofilms at the air-liquid interface 83

2.22. Bacterial Strains and Plasmids 85

CHAPTER 3 AIMS 89

CHAPTER 3. RESULTS 90

3.1. The holdfast anchor complex is associated with the outer membrane 90

3.2. Determinants of holdfast anchor complex assembly at the outer membrane 92

3.3. The holdfast anchor complex spans the cell envelope. 97

3.4. The major holdfast anchor protein, HfaB, does not form a visibly ordered array beneath the OM. 103

3.5. Purification and characterisation of recombinant HfaB 109

3.5.1. Protein sequence analysis 109

3.5.2. Construct design and expression tests 111

3.5.3. Purification of HfaB from inclusion bodies 112

3.6. The anchor complex is observed beneath the outer membrane of other bacteria .. 115

CHAPTER 3 DISCUSSION 117

Acknowledgements 120

CHAPTER 4 AIMS 121

CHAPTER 4. RESULTS 122

4.1. Deletion of the phosphodiesterase PA2133 upregulates filaments on the surface of *P. aeruginosa* PAO1 122

4.2. CupE filaments are upregulated on the surface of *P. aeruginosa* PAO1 Δ*PA2133* 124

4.3. *In vitro* purification of recombinant CupA1 and polymerization trials 127

4.3.1. Protein sequence analysis 127

4.3.2. Construct design and purification..... 128

4.3.3. *In vitro* polymerisation trials..... 131

4.4. *In vitro* purification of recombinant CupE1 133

4.4.1. Protein sequence analysis 133

4.4.2. Construct design and purification..... 135

4.5. Sub-tomogram averaging as a strategy for 3D reference generation and symmetry determination. 137

4.6. CupE filaments are helical, consistent with classical chaperone usher assemblies 141

CHAPTER 4 DISCUSSION 149

Acknowledgements 153

CHAPTER 5 AIMS 154

CHAPTER 5. RESULTS 155

5.1. Fluorescent labelling and imaging of the CupE5-usher 155

5.2. Immunofluorescent labelling of cell surface CupE filaments 157

5.3. CupE contributes to biofilm formation in a Δ*PA2133*‡ genetic background 159

5.4. Upregulation of CupE in a Δ*PA2133*‡ background influences cell clustering and biofilm architecture.....162

CHAPTER 5 DISCUSSION.....166

Acknowledgements.....168

CHAPTER 6. CONCLUDING REMARKS 169

REFERENCES.....173

List of Figures

Figure 1.1: The basic stages of biofilm formation and maturation. 14

Figure 1.2: The assembly and structure of type IV pili 21

Figure 1.3: The assembly of curli amyloid fibres across the cell envelope.....24

Figure 1.4: The assembly of prototypical chaperone usher (CUP) fimbriae. 26

Figure 1.5: The cryo-EM structures of Pap and Fim fimbriae from *E. coli* 29

Figure 1.6: Structure of the FimD usher and mechanism of Fim assembly at the outer membrane 32

Figure 1.7: Genetic organisation of chaperone usher proteins in *P. aeruginosa* 37

Figure 1.8: Regulation of *cupA* expression in *P. aeruginosa* 42

Figure 1.9: Overview of the two-component systems regulating *cup* gene expression in *P. aeruginosa*.....46

Figure 1.10: Structure of the archaic CsuE:CsuC adhesin-chaperone complex of *Acinetobacter baumanni*.....50

Figure 1.11: Polysaccharide synthesis and secretion across the bacterial cell envelope.....53

Figure 1.12: Molecular structures of bacterial polysaccharide adhesins.....55

Figure 1.13: Overview of the *C. crescentus* cell cycle.....61

Figure 1.14: Schematic model of the *C. crescentus* holdfast synthesis, secretion, and anchor machinery.....63

Figure 1.15: Basic concept of cryo-EM image reconstruction 65

Figure 1.16: Correction of the contrast transfer function (CTF).....68

Figure 3.1: Identification of the cryo-EM density corresponding to the holdfast anchor complex.....91

Figure 3.2: The anchor complex assembly is present beneath the outer membrane, independent of synthesis machinery, and depends on the holdfast secretion proteins (HfsDAB). 94

Figure 3.3: The anchor complex assembly is primarily comprised of HfaB. 96

Figure 3.4: Comparison of stalk tips with and without the holdfast anchor complex. 98

Figure 3.5: Subtomogram averaging of the holdfast secretion complex mutant (Δ*hfsDAB*). 100

Figure 3.6: The holdfast anchor complex spans the outer membrane of *C. crescentus*. 102

Figure 3.7: Purification of *C. crescentus* rosettes 104

Figure 3.8: HfaB-mCherry localises at the centre of *C. crescentus* rosettes. 106

Figure 3.9: Image processing of *C. crescentus* rosetted-stalk tips. 107

Figure 3.10: Determination of holdfast anchor complex architecture from rosetted stalks. . 108

Figure 3.11: Bioinformatic analysis of the major anchor complex protein, HfaB. 110

Figure 3.12: Purification of recombinant HfaB in detergents 114

Figure 3.13: The anchor density is situated beneath the OM of *Hirschia baltica* and *Asticcacaulis* cells 116

Figure 4.1: Deletion of *PA2133* results in cell surface filament expression in *P. aeruginosa* PAO1 124

Figure 4.2: Purification of native CupE filaments from the surface of *P. aeruginosa* PAO1 Δ*PA2133* 125

Figure 4.3: A mutant panel confirms the filaments upregulated in *P. aeruginosa* PAO1 Δ*PA2133* are CupE. 126

Figure 4.4: Multiple sequence alignment of the CupA1 fimbrial subunit against PapA and FimA 128

Figure 4.5: Purification and characterisation of recombinant CupA1 130

Figure 4.6: Multiple sequence alignment of the CupE1 fimbrial subunit against structural homologs 134

Figure 4.7: Purification and digestion trials of CupE1-MBP-His 136

Figure 4.8: Sub-tomogram averaging analysis of CupE filaments using RELION 139

Figure 4.9: Sub-tomogram averaging analysis of CupE filaments using a modified AV3 package. 140
Figure 4.10: 2D classification of CupE filaments confirms a helical assembly 142
Figure 4.11: Single particle-based helical reconstruction of CupE 143
Figure 4.12: Cryo-EM structure of CupE filaments at 4.54Å resolution 145
Figure 4.13: Removal of curved CupE filament classes from single particle datasets in RELION 147
Figure 4.14: 3D classification of CupE filaments in RELION 148
Figure 5.1: Fluorescence imaging of a PAO1 Δ*PA2133*‡ CupE5-sfGFP fusion strain 156
Figure 5.2: Comparison of fluorescent signal in single *C. crescentus* cells and rosettes, illustrates the limit of detection 156
Figure 5.3: Immunofluorescent labelling of native CupE filaments using generated anti-CupE1 antibodies 158
Figure 5.4: Assessment of CupE-mediated adhesion using the crystal violet biofilm assay. 161
Figure 5.5: Experimental setup for examination of biofilm formation at the air-liquid interface 162
Figure 5.6: Morphological features of PAO1 biofilms at the air-liquid interface 163
Figure 5.7: CupE upregulation results in increased cell clustering and organisation at the microscopic level 165
Figure 6.1: Schematic of investigations into the holdfast anchor at the cell surface of *C. crescentus*. 170
Figure 6.2: Schematic of investigations into the regulation and structure of CupE of *P. aeruginosa* 172

List of Tables

Table 1.1: Summary of sensor kinase and response regulators in *P. aeruginosa*. 17

Table 1.2: Summary of ligand/receptor interactions for classical and non-classical CU fimbriae. 27

Table 1.3: Regulation of chaperone usher pathways in *P. aeruginosa* 37

Table 2.1: Bacterial strains and plasmids used in this study. 85

Table 2.2: Oligonucleotides used in this study 87

Table 3.1: Occurrence of anchor and holdfast densities in tomograms. 92

Table 4.1: Summary of conditions trialled for reconstitution of CupA filaments. 132

Abstract

Adhesion to abiotic and biotic surfaces is essential for numerous bacterial developmental processes including biofilm formation (1). While the general role of adhesins in biofilm formation has been explored, the arrangement of these structures on the cell surface and how these structures interact with substrates at the molecular level remain unclear. In this project, the CupE chaperone usher fimbriae of *Pseudomonas aeruginosa* and the holdfast polysaccharide of *Caulobacter crescentus* were investigated as models of proteinaceous and polysaccharide-mediated adhesion respectively.

Using structural biology methods, including electron cryomicroscopy (cryo-EM) and electron cryotomography (cryo-ET), this thesis provides molecular details of a previously uncharacterized mechanism of polysaccharide adhesion. The holdfast is a polysaccharide adhesin which is anchored to the surface of *C. crescentus* by a defined molecular complex made up of the HfaABD proteins. The HfsDAB secretion proteins are required for assembly and localization of the HfaABD anchor, which spans the outer membrane of the stalk tip. The anchor protein HfaB is the major component of the anchor complex located on the periplasmic side of the outer membrane, while HfaA and HfaD are located on the cell surface. HfaB is the critical component of the complex, without which no HfaABD complex is observed in cells. Finally, anchor densities are present along the cell envelope of other alphaproteobacteria including *Asticcacaulis* and *Hirschia* spp., supporting a conserved mechanism in holdfast anchoring.

Additionally, this thesis provides insight into the regulation, structure and physiological role of archaic CupE fimbriae in *P. aeruginosa.* Deletion of the *PA2133* phosphodiesterase gene upregulates CupE filaments under static conditions, indicating that filament assembly is promoted upon c-di-GMP elevation and surface sensing. CupE fimbriae are a major contributor

to biofilm formation in Δ*PA2133* mutants, with increased biofilm formation at the air-liquid interface, as well as cell clustering and organisation at the microscopic level. The diameter of CupE filaments is ~4 nm, consistent with fimbriae of the archaic σ-clade. The cryo-EM structure of native CupE, at a resolution of 4.5 Å, reveals a single-start, helical morphology that does not resemble the tubular structure of classical chaperone usher assemblies. These findings provide the first structural insights into a fully assembled, archaic chaperone usher filament in bacteria and support CupE fimbriae function as an adhesin during biofilm formation.

CHAPTER 1. INTRODUCTION

1.1. Adhesion during biofilm development

The majority of the bacterial biomass in nature do not as exist as single, free-living (planktonic cells), but rather as multi-cellular bacterial communities called biofilms. The biofilm environment facilitates cooperative behaviour between bacteria, as well as protection against external stressors (2). Adhesion is critical for biofilm formation and occurs at several key stages. First, planktonic bacterial cells encounter surfaces and reversibly attach using type IV pili and flagella (3). Bacteria then irreversibly attach using type IV pili as well as large, multi-subunit fimbriae assembled by the chaperone usher pathway (CUP) (4). Biofilm maturation occurs as microcolonies expand and are encapsulated in a protective exopolysaccharide matrix (EPS) consisting of polysaccharide and proteinaceous adhesins (5). Over time, the biofilm may assume characteristic spatial architectures involving intricate interactions between the constituent cells. As the biofilm maturates, bacterial cells downregulate adhesins and are dispersed back into the environment, where they resume a planktonic lifestyle and colonise new surfaces (6) (Figure 1.1).

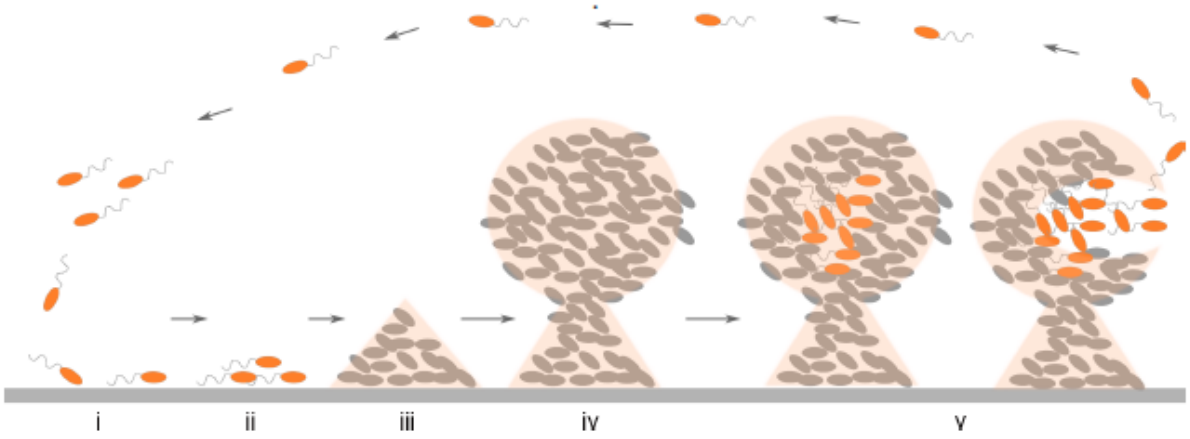


Figure 1.1: The basic stages of biofilm formation and maturation.

The process of biofilm formation can be divided into (i) reversible adhesion of planktonic cells which is mediated by flagella and type IV pili, (ii) irreversible attachment which is mediated by chaperone usher fimbriae (iii) microcolony formation, (iv) maturation and (v) dispersal. Figure adapted from Muhl, D., 2014 (7).

1.2. Regulation of adhesin expression and biofilm formation

The expression of adhesins during the transition from a planktonic to biofilm lifestyle is dictated by a complex set of regulatory networks, in conjunction with signalling from the external environment. These networks include secondary messenger cyclic di-guanosine (c-di-GMP) signalling, two component systems (TCS) and quorum sensing (QS) (8).

1.2.1. c-di-GMP secondary messenger signalling

Bacterial secondary messengers are linear or cyclic, nucleotide-based molecules linked to intracellular signal transduction networks that sense changes in the internal and external environment. Secondary messengers include c-di-GMP, cyclic adenosine monophosphate (cAMP), cyclic GMP-AMP (3′3′-cGAMP) and cyclic adenylate (c-di-AMP), which transduce signals relevant to nutrient response (9, 10), cell-cycle progression, motility (11), host attachment (12) and biofilm formation (11).

c-di-GMP is ubiquitous across Gram positive and Gram negative bacteria, including *P. aeruginosa*. Intracellular c-di-GMP concentration coordinates a switch in lifestyle, with

elevated c-di-GMP associated with biofilm formation, whilst low c-di-GMP levels with motility and dispersion (13). In *P. aeruginosa*, c-di-GMP influences flagellar and type IV pili retraction, exopolysaccharide secretion and surface adhesion expression (14). Intracellular c-di-GMP concentration is regulated by the activity of two enzymes; GGDEF domain-containing diguanylate cyclases (DGC) and EAL-domain containing phosphodiesterases (PDE). Many proteins contain both GGDEF and EAL domains, whose activity is allosterically modulated by intracellular c-di-GMP concentration. For example, homodimerization of GGDEF domains, a prerequisite for c-di-GMP production, is inhibited upon binding of product to their inhibitory or I-site (15, 16). c-di-GMP is synthesized from two GTP molecules by DGC's and hydrolysed by PDE's to linear pGpG, followed by GMP (17).

Analysis of the *P. aeruginosa* PAO1 genome has identified the presence of over 41 genes encoding proteins implicated in c-di-GMP metabolism (18). The most studied DGC protein in *P. aeruginosa* is WspR of the Wsp chemosensory TCS (19). In the Wsp system, the transmembrane chemoreceptor WspA is believed to be methylated by WspC upon surface sensing. WspA then activates the histidine kinase, WspE, resulting in the phosphorylation of WspR and c-di-GMP production (20-22). The elevated c-di-GMP induces a dramatic biofilm phenotype characterised by cell aggregation, small colony variant (SCV) formation and secretion of EPS (19, 23). Conversely, the BifA PDE of *P. aeruginosa* PA14 degrades cellular c-di-GMP and induces swarming motility. This phenotype is inversely regulated by the DGC, SadC (24). Although BifA encodes both GGDEF and EAL domains, only PDE activity has been demonstrated experimentally (25).

c-di-GMP can bind and have effect at the transcriptional, post-transcriptional and post-translational level (26). The Lap system of *P. fluroescens* produces a large repetitive repeat-in-toxins (RTX) adhesin called LapA. Cell-surface association of LapA is dependent on the activity of a periplasmic protease called LapG, which cleaves and releases LapA into the

extracellular space (27). This reduces capacity for cell-cell and cell-surface attachment and consequently, biofilm formation. The enzymatic activity of LapG is regulated by an inner membrane protein called LapD, which undergoes a conformational change upon c-di-GMP binding. This causes LapD to bind to LapG, inhibiting LapG-induced cleavage of LapA. Similarly, the large CdrA adhesin of *P. aeruginosa* is anchored to the cell surface by the CdrB outer membrane protein at high c-di-GMP levels and released into the extracellular milieu by LapG upon reduced c-di-GMP (28, 29). Thus under conditions favourable for biofilm formation and high c-di-GMP, LapA and CdrA remain associated at the cell surface (30, 31).

1.2.2. Two component systems

Bacterial two component systems (TCS) are designed to quickly sense and respond to a range of internal and external stimuli. These systems generally consist of a transmembrane sensor kinase, phosphorylation cascade and activation of a downstream cytoplasmic response regulator (32). The *P. aeruginosa* genome encodes over 60 TCS, with over half of which have been mapped to virulence, antibiotic resistance and/or biofilm formation (Table 1.1).

The Gac (global activator of antibiotic and cyanide synthesis) system is a highly characterised TCS of *P. aeruginosa*. The central kinase, GacS, phosphorylates its target DNA-binding response regulator, GacA, orchestrating the switch from acute to chronic infection. This is achieved by upregulation of two non-coding RNA's, RsmY and RsmZ, through binding of phosphorylated GacA to the *rsmY* and *rsmZ* promoter regions (33, 34). Activated RsmY and RsmZ then sequester RsmA and RsmN, two transcriptional regulators which downregulate genes associated with acute infection and upregulate those involved in chronic infection. This includes upregulation of EPS secretion and type-VI adhesin secretion and downregulation of motility and type III adhesin secretion (35-40). Gac-dependent signalling is additionally controlled by a multi-sensor kinase network which include RetS, LadS and PA1611 (41). LadS upregulates *rsmY/rsmZ* expression through phosphorylation of GacS, promoting a biofilm

lifestyle in response to calcium levels (42, 43). In contrast, RetS antagonises signalling by heterodimerisation with GacS, thus preventing phosphorylation of GacS, the ligand for which remains unknown (44). PA1160 sequesters RetS, thus freeing GacS to be phosphorylated by GacA (45).

Table 1.1: Summary of sensor kinase and response regulators in *P. aeruginosa*.

Table adapted from Francis et al., 2017 (46) and Gooderham et al., 2007 (32) .

Sensor Kinase	**Response regulator**	**Function**	**Reference**
GacS	GacA	Quorum sensing, biofilm formation, swarming motility, iron homeostasis, T3 and T6 secretion, antibiotic resistance	(35, 36, 44, 47-49)
RocS1 (SadS)	RocA1 (SadA) RocR (SadR)	Regulation of CupB and CupC fimbrial adhesins, T3 section, antibiotic resistance	(50-52)
RocS2	RocA2	Regulation of CupB and CupC fimbrial adhesins, antibiotic resistance	(50, 52)
PvrS, RcsC	PvrR, RcsB	Regulation of CupD fimbrial adhesin, phenotypic variation, antibiotic resistance, biofilm formation	(53, 54)
PprA	PprB	Regulation of CupE fimbrial adhesin and type IVb pili, membrane permeability, antibiotic resistance	(55-57)
FimS	AlgR	Alginate synthesis, twitching and swarming motility, cyanide production, T3 secretion	(58, 59)
PilS	PilR	Type IV pili expression, twitching and swarming motility	(60-63)
PhoR	PhoB	Quorum sensing and motility	(64-66)

1.2.3. Quorum sensing

Quorum sensing (QS) enables bacteria to coordinate gene expression in a cell-density dependent manner (8). As the bacterial population increases, cell-to-cell communication is achieved through the release and accumulation of extracellular signalling molecules known as autoinducers. These signals allow bacteria to sense cell number and composition, and gene expression to be altered accordingly. Quorum sensing is important for biofilm formation, which demands a high energy cost to the single bacterial cell, but becomes increasingly efficient and beneficial when undertaken as a collective (67).

The most common class of autoinducers in Gram negative bacteria are acyl-homoserine lactones (AHLs). AHL's vary in the length of their acyl chain and substitution. The LuxI family of synthase enzymes are responsible for synthesis of AHLs, deriving the lactone moiety from S-adenosylmethionine (SAM) and the acyl chain from fatty acid metabolism. Synthesized AHLs are then sensed by LuxR-type transcriptional regulators as intracellular levels accumulate (67, 68). *P. aeruginosa* encodes a hierarchical QS circuit which includes LasI/LasR and Rh1I/Rh1R which share significant homology with LuxI/LuxR system (69). The LasI/LasR system responds to N-3-oxo-dodecanoyl homserine lactone (3-oxo-C_{12}-HSL) which is produced by LasI synthase and sensed by LasR (70). The second system, RhI, responds to N-butanoyl homoserine lactone (C_4-HSL), which is produced by Rh1I synthase and sensed by Rh1R (71). A third system known as PQS involves the synthesis and sensing of 2-heptyl-3-hydroxy-4-quinolone or *Pseudomonas* quinolone signal (PQS) which is synthesized from esters and chemically distinct from AHLs (72). The activation of these QS systems generally leads to the upregulation of downstream virulence factors such as elastases (LasA, LasB), rhamnolipids (RhiAB), exotoxin (ToxA) and pyocanin (23, 69).

1.3. Bacterial adhesins

Biofilm formation requires the recruitment of cell-surface and secreted adhesins, which affect surface sensing, attachment and biofilm architecture. These adhesins include proteinaceous structures such as type IV pili, functional amyloid fibres and chaperone usher fimbriae (CUPs), as well polysaccharide adhesins such as Pel, Psl, alginate, capsular polysaccharides and holdfast (73). In line with the focus of this project, the chaperone usher fimbriae of *P. aeruginosa* and holdfast of *C. crescentus* will be emphasized.

1.3.1. Proteinaceous adhesins

1.3.1.1. Type IV pili

Type IV pili are polymeric, cell-surface appendages which contribute significantly to the virulence of Gram-negative bacteria. The physiological functions of type IV range from motility (74), DNA uptake (75), host-cell adhesion (76), microcolony and biofilm formation, cell signalling (77) and phage attachment (78). These filaments are typically 5-7 nm in diameter and several μm in length, and are resistant to motor forces >100 pN (79). Further, type IV pili extend and retract in a grapple-like fashion at rates of 1,000 subunits per second (78).

1.3.1.2. Classification and subunit maturation

Two major classes of type IV pili are distinguished based on characteristics of the major pilin subunits and organisation in pilus genes. Further, each pilus is assembled by distinct assembly complexes (80-83). Three key subtypes of type IV pili have been classified, including type IVa, type IVb and type IVc or tight-adherence (tad) pili (84, 85). A defining characteristic of pre-pilin subunits is the presence of a type III signal peptide, which targets cytoplasmic subunits for cleavage at the inner membrane. In contrast, classical type I and II signal peptides target precursors to the periplasm. The inner membrane embedded PilD peptidase cleaves the signal peptide of type IVa and type IVb, whilst tad pili are cleaved by the FppA peptidase (83,

86). Type IVa subunits encode a short signal peptide (5-10 amino acids) and are 150-160 residues in length, type IVb subunits encode a long signal peptide (15-30 amino acids) and are 180-200 residues in length, whilst tad pili are shortest at 50-80 residues in length with a short signal peptide (10-26 amino acids).

1.3.1.3. Structure, assembly and disassembly of classical type IVa pili

Type IVa pili are synthesized from a cytoplasmic pool of the major pilin subunit, PilA, as well as minor pilins. Precursor pilin subunits are inserted in the inner membrane by the SecYEG machinery. Subunits are then cleaved and methylated by the prepilin peptidase, PilD (83, 87). The mature pilin subunit is comprised of a conserved, hydrophobic N-terminal α-helical domain, as well as a C-terminal globular domain (Figure 1.2C), orientated toward the periplasm during polymerisation.

The type IV assembly machinery is comprised of four sub-complexes; the outer membrane secretin, the inner membrane motor, the alignment complex and the helical pilus (88) (Figure 1.2A).The outer membrane secretin complex consists of the PilQ secretin channel and the PilF lipoprotein which assembles PilQ at the outer membrane (89, 90). The motor complex consists of the PilB, PilT and PilU ATPases, which are docked upon the platform protein, PilC. PilB is responsible for pilus assembly, whilst PilT and PilU coordinate pilus retraction (91, 92). The alignment complex consists of PilM, PilN, PilO, PilP and FimV, which directs the growing pilus across the inner membrane and periplasmic space for secretion (93). During assembly, minor pilin subunits form an initiation complex which forms the base of the growing pilus (94). PilA subunits are then incorporated by action of PilB. Individual subunits are believed to interact via their methylated N-termini, as well as salt bridge formation via a conserved glutamate residue (95-97). The assembled helical pilus consists of major pilin subunits (PilA), minor pilin subunits (FimU, PilV, PilW, PilX and PilE) and adhesins (PilY1) (Figure 1.2B). The hydrophobic N-termini of subunits are believed to face inward toward the

pilus core, whilst globular domains face out into the environment (97, 98). Retraction of the pilus is driven by the proteins PilT and PilU (99). The subunits are then recycled into the cytoplasmic membrane for future pilus assembly.

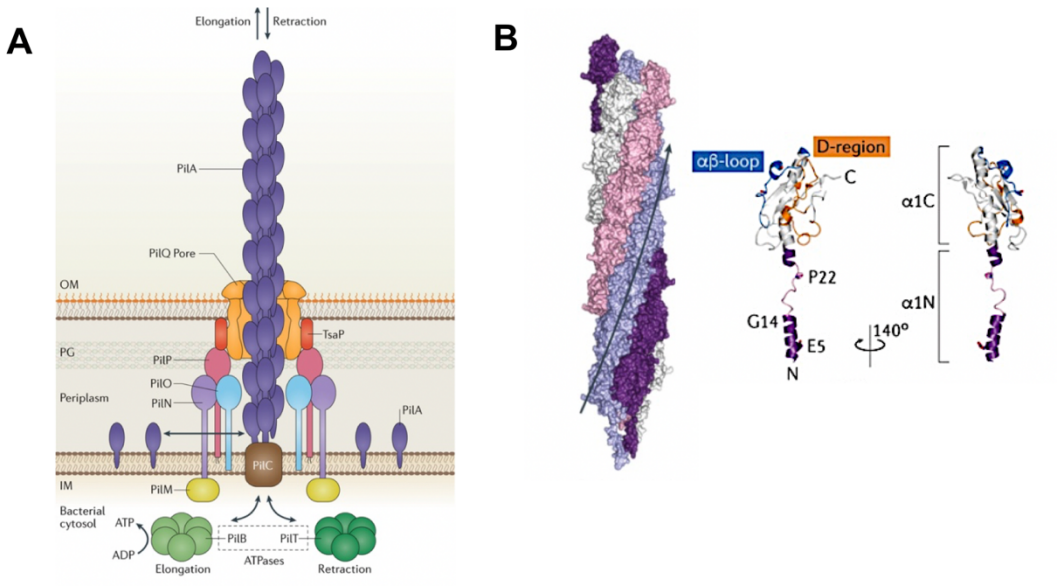


Figure 1.2: The assembly and structure of type IV pili

(A) Diagram illustrating the localisation of the type IV assembly machinery across the bacterial cell envelope. Layers corresponding to the outer membrane (OM), inner membrane (IM), peptidoglycan (PG), periplasm and cytosol are labelled respectively. The growing type IV pilus, consisting of PilA subunits, is aligned through the PilM/N/O/P complex and translocated to the cell surface by the PilQ pore. Pilus assembly is driven by the ATPase PilB and retraction through PilT. (B) (Left) Cryo-EM structure of the assembled type IV pilus of *Neisseria meningitidis* at 6Å resolution (PDB: 5KUA). (Right) Crystal structure of the PilE subunit of *N.meningitidis* at 1.44Å resolution (PDB: 5JW8). The α1-N helical and α1-C globular domains are labelled accordingly. The D-loop region which participates in disulphide bridge formation during polymerization and the disordered αβ-loop are also labelled (98). Figure adapted from Hospenthal et al., 2017 (100).

1.3.1.4. Curli and functional amyloids

Functional amyloid fibres play a significant role in bacterial adhesion and structural integrity of the biofilm matrix (101, 102). A diverse range of functional amyloids have been identified including curli (*E.coli*) (102), Fap (*Pseudomonas*) (103), TasA (*Bacillus*) (104), Bap (*Staphyloccocus*) (105) and MTP (*M. tuberculosis*) (106). Curli are thin, highly aggregative fibres (2-5 nm) which vary in length, forming mesh-like structures on the cell surface and extracellular space (102). These fibres are characterised by the ability to bind Congo red and thioflavin T (ThT) dyes, extreme heat and chemical stability and β-sheet structure (107). Amyloids are resistant to boiling in the presence of sodium dodecyl sulphate (SDS), proteinase K digestion and sodium hydroxide, and require >70% formic acid to induce disassociation of subunits (108). The robust nature of these structures provides the biofilm environment with resistance to external stressors.

1.3.1.5. Assembly of curli fibres at the cell surface

Given the propensity of amyloids to aggregate, assembly is tightly coordinated by a dedicated set of regulatory genes and machinery. Curli fibres are assembled by genes encoded on two divergent operons: *csgBAC* and *csgDEFG* (109). CsgA is the major curli subunit, which is transported to the cell surface in an unfolded state (Figure 1.3). CsgB is a minor curli subunit, which nucleates the folding and polymerisation of CsgA upon interaction at the cell surface (110). Interestingly, curli subunits may also self-assemble through 'seeding' with pre-existing curli fibres *in vitro* (111). CsgE and CsgF play a chaperone-like function, facilitating transport of both CsgB and unfolded CsgA to the cell surface (112, 113). CsgC is believed to bind CsgA, maintaining it in a stable, secretion-competent conformation in the periplasm. In support of this, CsgC possesses an immunoglobulin-like fold and CxC motif similar to DsbD, responsible for disulphide bridge formation (114). CsgD is a transcriptional regulator, controlling amyloid

fibre expression and biofilm formation (115). Finally, the CsgG protein forms a nonameric pore through which CsgA and CsgB translocate the outer membrane (116, 117) (Figure 1.3).

1.3.1.6. Functional amyloid fibres (Fap) of *P. aeruginosa*

Functional amyloid fibres (Fap) are present on the surface of several *Pseudomonas* strains, including *P. aeruginosa* PAO1, *P. fluorescens* and *P. putida* (118). These fibres are encoded by the *fapA-F* operon whose over-expression promotes cell aggregation and biofilm formation (103). Consistent with amyloids, Fap fibres bind ThT dye, are predominantly β-sheet in structure and dissociate upon formic acid treatment (103). Fap fibres appear to be comprised majorly of FapB, as well as minor amounts of FapC. FapA is believed to affect the distribution of FapC in the final filament, given its deletion results in fibrils primarily consisting of FapB (118). Bioinformatic analyses predict FapF is an outer membrane porin, whilst FapD is a protease believed to process FapB and FapC subunits. The function of FapE remains unknown but is co-purified with Fap filaments (118). The precise structure of Fap, as well as many other human and bacterial amyloids, remains unknown given inherent chemical resistance and high degree of structural polymorphism under various study conditions *in vivo* and *in vitro* (119).

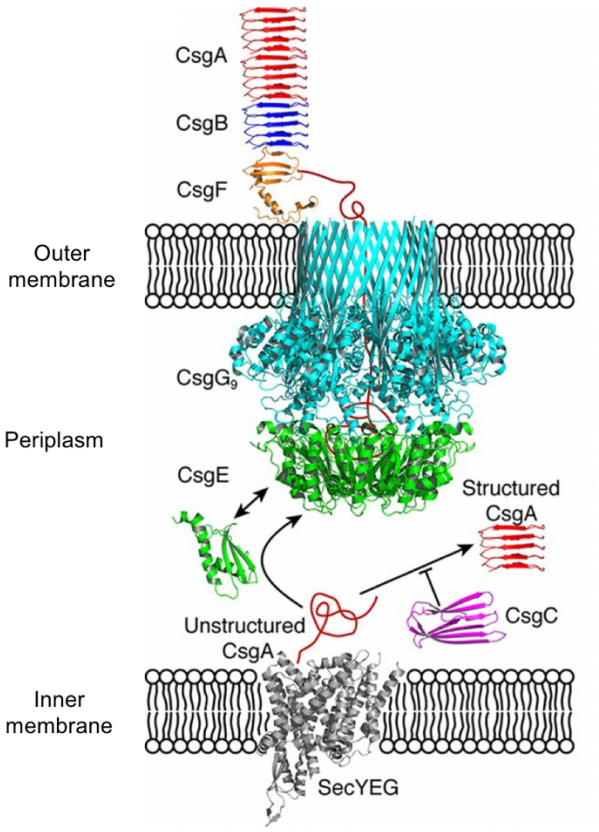


Figure 1.3: The assembly of curli amyloid fibres across the cell envelope

Diagram depicting the molecular machinery involved in assembly of curli amyloid at the bacterial cell surface. Layers of the bacterial cell envelope are labelled accordingly. Unstructured CsgA is transported across the inner membrane by the SecYEG pathway. Periplasmic CsgC binds CsgA and is believed to prevent assembly of structured CsgA in the periplasm. CsgE chaperones CsgA, delivering it the outer membrane porin, CsgG. Once translocated, CsgA is chaperoned by CsgF at the cell surface, where it interacts with the CsgB nucleator, initiating the assembly of amyloid fibrils. Figure adapted from Klein et al., 2018 (120).

1.3.1.7. Canonical Chaperone Usher Fimbriae

Chaperone usher pili/fimbriae (CUP) are the most abundant adhesive appendage found on the surface of *Enterobactericeae* as well as *Pseudomonas, Haemophilus* and *Bordetella* spp. (73). CUP operons are characterised by genes which encode at least one usher, chaperone and fimbrial subunit. Prototypical CUP fimbriae are those assembled by the *fim* (Type 1) and *pap* (Type P) operons of uropathogenic *Escherichia coli,* which facilitate binding to host bladder and upper urinary tract cells respectively (121).

1.3.1.8. Molecular structure of CUPs

Prototypical pap fimbriae can be structurally divided into two parts; a distal flexible tip and proximal fimbrial rod (Figure 1.4A). The flexible tip consists of a single PapG adhesin at its distal end, followed by the adapter protein PapF, the minor pilin subunit PapE and the adaptor protein PapK. This assembly connects to a rigid, 1-2 μm long, helically wound fimbrial rod consisting of up to 1000 PapA subunits (122). Fim fimbriae possess a similar structure, with a comparatively shorter flexible tip (Figure 1.4A) (100). Substrate specificity is determined by the tip adhesin, which consists of an N-terminal lectin domain and C-terminal pilin domain which participate in substrate binding and co-polymerization respectively (123, 124). Several adhesin-substrate interactions have been investigated for classical and non-classical CUP fimbriae, primarily in the context of pathogenic *E. coli* (Table 1.2) (125).

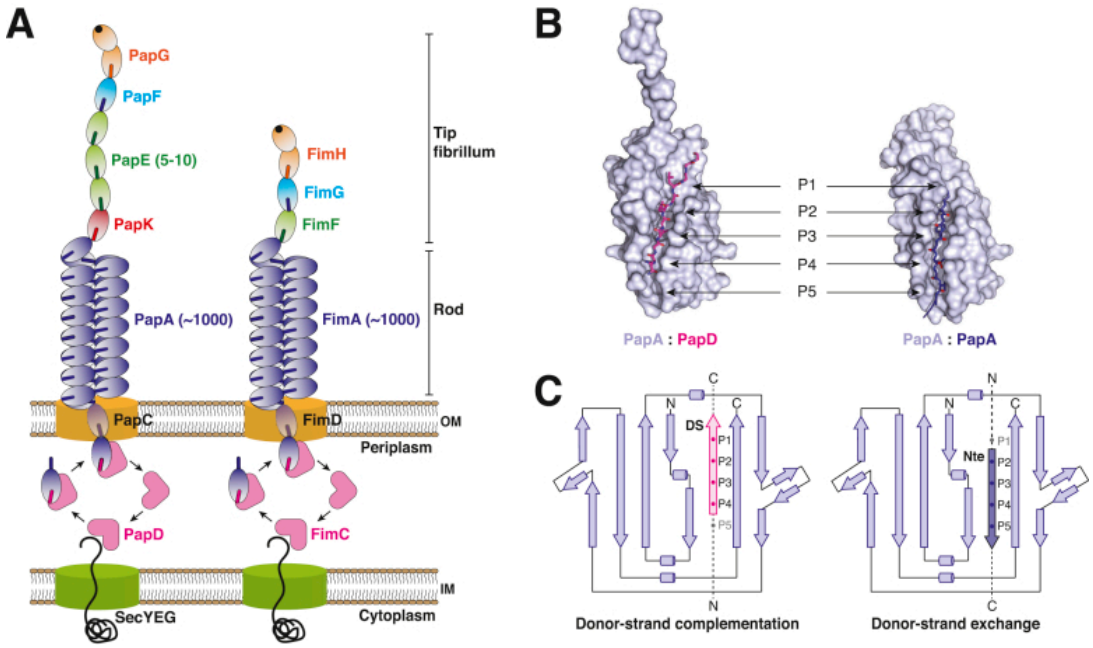


Figure 1.4: The assembly of prototypical chaperone usher (CUP) fimbriae.

(A) Diagram illustrating the structure and assembly of Fim and Pap fimbriae of *Escherichia. coli*. (B) Left - The G_1 strand (pink) of the PapD periplasmic chaperone complements the Ig incomplete fold (P1-P5 groove) of PapA pilin subunit during DSC. Right - The Nte (dark blue) of one PapA subunit binds and stabilises the P1-P5 groove of another PapA subunit during DSE. (C) Topology diagrams demonstrating the Ig fold of canonical pilin subunits, and the insertion of the G_1 strand (pink) during DSC and Nte (dark blue) during DSE. Figure adapted from Hospenthal et al. 2016 (126).

Table 1.2: Summary of ligand/receptor interactions for classical and non-classical CU fimbriae.

Table adapted from Kline et al., 2009 (127) and Werneberg et al., 2018 (125). UPEC = Uropathogenic *E.coli,* ETEC = Enteropathogenic *E.coli*. N.D = not determined.

Fimbriae	**Organism**	**Gene cluster**	**Adhesin**	**Ligand /Receptor**	**Disease**	**Ref.**
Pap	UPEC	*papAHCDJKEFG*	PapG	Digalactoside (Gal∝1,4-Galβ, GbO3, GbO4, GbO5)	Pyelonephritis and cystitis	(128-133)
Fim	UPEC	*fimAICDFGH*	FimH	Mannosylated glycoproteins (uroplakin UP1a, laminin, CD48, collagen)	Cystitis	(134-136)
F17	ETEC	*F17aADCG*	F17	N-acetyl D-glucosamine (GlcNAc)	Diarrhoeal disease	(137, 138)
CFA/I CS1	ETEC	*cfaABCE cooBACD*	CfaE CooD	Intestinal epithelial cells, erythrocytes	Diarrhoeal disease	(139-142)
S	*E.coli* K1	*sfaADEFGSAH*	SfaH	Sialic acid (NeuAc-α-2,3-Galβ)	Urinary tract infections, neonatal meningitis	(143, 144)
F1C	UPEC	*focAICDFGH*	FocH	Digalactoside (Gal∝1,4-Galβ)	Pyelonephritis and cystitis	(145)
F1	*Yersinia pestis*	*caf1M1A1*	Caf1A	Human IL-1β, respiratory tract epithelial cells	Bubonic plague	(146, 147)
Csu	*Acinetobacter baumannii*	*csuA/BABCDE*	CsuE	Plastic, abiotic surfaces	Biofilm formation	(148)
Cup	*Pseudomonas aeruginosa*	Several (*cupA-E* operons)	N.D	N.D	Biofilm formation	(3, 4, 53, 56, 149)

1.3.1.9. CUP Assembly

The biogenesis of CUP fimbriae begins with transport of fimbrial subunits across the inner membrane to the periplasm via the Sec pathway (100). Subunits associate with periplasmic chaperones which target them to the usher protein embedded in the outer membrane. During this process, the chaperone and usher protein participate in donor strand complementation (DSC) and donor strange exchange (DSE) to facilitate fimbrial assembly (150). Canonical fimbrial subunits, such as those of the Fim and Pap system, possess an incomplete immunoglobulin-like (Ig) fold, whereby they lack the C terminal β-strand (G_1). The absence of the G_1 strand produces a deep groove (referred to as the P1-P5 pocket) along the surface of the fimbrial subunit (Figure 1.4B). This fold places the fimbrial subunit in a high energy state, requiring stabilisation. To facilitate this, periplasmic chaperones participate in DSC, whereby their G_1 strand is donated upon binding, complementing the incomplete Ig fold of the fimbrial subunit *in trans* (Figure 1.4C) (122). The chaperone-fimbrial subunit complex arrive at the usher protein where subunit polymerisation proceeds via DSE. During DSE, the G_1 strand of the chaperone is released from the fimbrial subunit and replaced by the N terminal subunit (Nte) of the usher, in a zip-in zip-out like mechanism (Figure 1.4C) (151). This process docks the fimbrial subunit to the usher. The pilus then extends as the Nte of the docked fimbrial subunit is donated to incoming chaperone-fimbrial subunit complexes, and the process repeats. The termination subunit stops pilus assembly due to the lack of an Nte, which inhibits DSE from proceeding further (150). The cryo-EM structures for both Fim and Pap fimbriae have been described at a resolution of 4.2Å and 3.8Å respectively. Fim fimbriae possess 3.13 subunits per turn with a helical rise of 8.0Å, whilst Pap fimbriae possess 3.28 subunits per turn and a helical rise of 7.7Å (Figure 1.5) (126, 152).

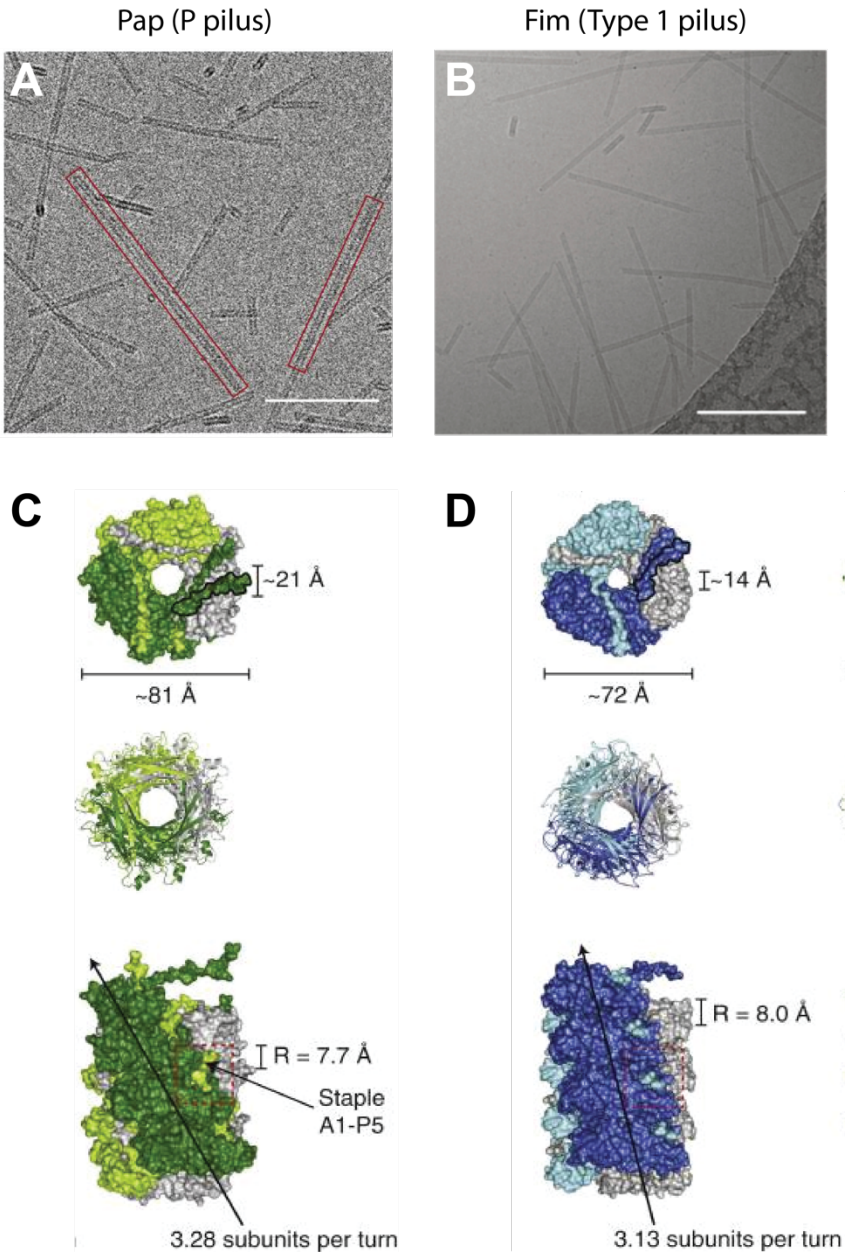


Figure 1.5: The cryo-EM structures of Pap and Fim fimbriae from *E. coli*

(A) Cryo-electron micrograph of purified Pap (Type P) fimbrial rods. Red boxes highlight rods. Scale bar –100 nm. (B) Cryo-electron micrograph of purified Fim (Type 1) fimbrial rods. Scale bar –100 nm. (C) Top and side views of the cryo-EM Pap structure at 3.8Å resolution (PDB: 5FLU). (D) Top and side views of the cryo-EM Fim structure at 4.2Å resolution (PDB: 5OH0). For both (C, D), the dimensions of the outer and inner lumen diameters are annotated in the top view, and the helical parameters of rise (R) and subunits per turn are annotated in the side view. Image adapted from Hospenthal et al., 2016 (126) and Hospenthal et al., 2017 (152).

1.3.1.10. Subunit ordering of CUP fimbriae

The coordination of fimbrial biogenesis and subunit ordering is dictated largely by Nte-P5 groove complementarity and affinity of the usher for chaperone-subunit complexes (153-156). This specificity is believed to be a consequence of co-evolution of fmbrial subunits within pilin operons over time. The Nte is generally 10-20 residues in length, contains a conserved cysteine and glycine and alternating hydrophobic residues. Groove-Nte specificity has been extensively demonstrated during Pap fimbrial assembly (153, 157, 158). Deletion of the Nte of PapK or replacement of the PapF Nte with the PapE Nte (Nte_EPapF) both result in loss of PapG at the pilus tip (158). In a Δ*papF* background, replacement of the PapE Nte with PapF (Nte_FPapE) does not interrupt in pilus formation, with successful complementation of PapG by Nte_FPapE. Similarly, replacement of the Nte of PapK with PapE (Nte_EPapK) results in complementation of PapF by PapK and pilus assembly in a Δ*papE* background (157, 158). The DSE rate of all six Pap subunit-chaperone complexes against with all five Nte sequences has been assessed *in vitro*. Out of the 30 combinations, DSE rate was highest between cognate partners (located adjacent in the filament) and slowest between non cognate partners, strengthening the Nte and groove complementarity influences subunit ordering (153). The slower DSE rate between non cognate partners has been illustrated in Δ*papK* deficient *E. coli*, which generate pilus rods double the length of the wild type, a consequence of DSC between PapE and PapA (132). In line with occurring as multimers in the Pap filament and self-complementation, PapE and PapA exhibit self-assembly *in vitro* (159).

The OM usher consists of four functional domains; a periplasmic N-terminal domain (NTD), periplasmic C-terminal domains (CTD_1, CTD_2), a central β-barrel translocation pore and plug domain which occludes the pore in its resting state (160) (Figure 1.6A). The structures for both PapC and FimD have been solved, providing insight into DSC, DSE and subunit translocation (161-163). Binding of the adhesin-chaperone complex to the NTD induces a

conformational change whereby the plug domain of the usher swings out into the periplasm, opening the central pore (163, 164) (Figure 1.6B). The central pore also changes from kidney-shaped to circular to accommodate the movement of subunits (165). Though the usher binds all incoming subunit-chaperone complexes, it possesses the highest affinity for the adhesin-chaperone complex (166). In addition, the adhesin-chaperone complex is the only complex which can induce activation and conformational change of the usher, as demonstrated between FimC-FimH/FimD and PapC/PapG-PapD (155, 167). This preferential affinity provides an explanation for the placement of FimH at the distal end of the fimbrial rod (156, 168). Given the affinity between the usher and other subunit-chaperone complexes (FimC-FimA, FimC-FimG, FimC-FimF) are relatively similar, Nte-groove complementarity is believed to have a greater influence on subunit ordering as the pilus grows. The transfer of adhesin complexes to the CTDs and NTD binding of incoming subunit complexes acts as a catalyst for DSE, by placing fimbrial subunits in close proximity (167). Indeed, DSE occurs within minutes *in vivo* as compared to several hours to days *in vitro*, supporting the usher plays a key role in promoting pilus biogenesis (153, 169).

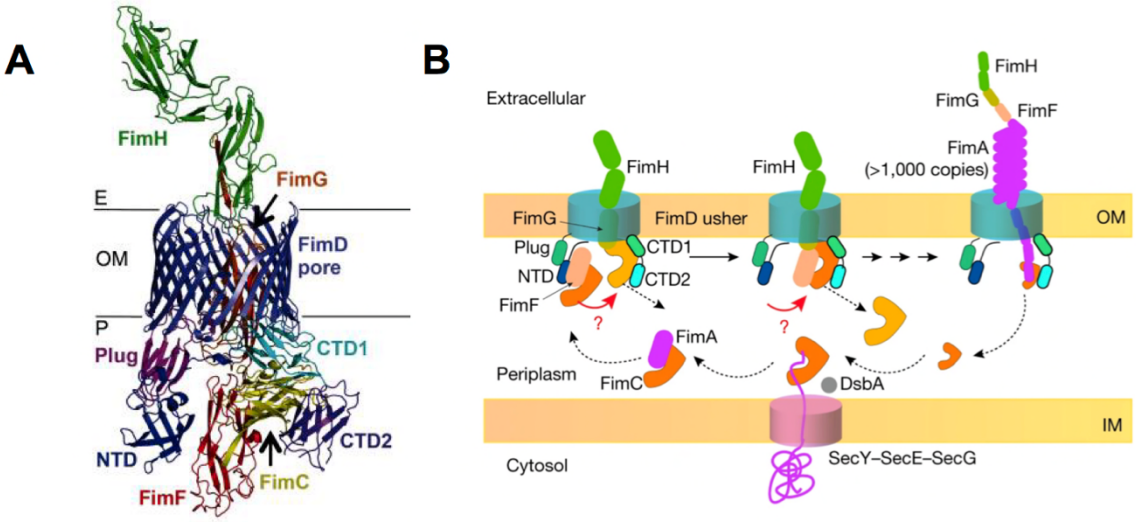


Figure 1.6: Structure of the FimD usher and mechanism of Fim assembly at the outer membrane

(A) Crystal structure of the FimD:FimC:FimG:FimH complex (PDB: 3BWU). Proteins are in ribbon representation; the FimD β-barrel, N-terminal domain (NTD) and CTD_2 (dark blue), CTD_1 (cyan), plug domain (purple), FimF (orange), FimC (yellow) and FimH (green) are shown. Figure adapted from Geibel et al., 2013 (170). (B) Diagram of fimbrial biogenesis at the outer membrane (OM). Fimbrial subunits (pink) are translocated through the inner membrane (IM) by the Sec pathway, bound to periplasmic FimC (orange) and shuttled to the FimD usher (blue embedded in OM). The FimH (green) adhesin translocates the usher first, followed by minor pilin subunits and the FimF adaptor (beige). The FimC:FimA complex binds the usher at the NTD, where a handover of FimA occurs between the NTD and CTD_2 and release of the chaperone (171).

1.3.1.11. Classification of CUPs

As genetic and structural information with respect to CUPs emerged over time, two classification systems were established (172, 173). Nuccio and Bäumler categorized six phylogenetic clades based on the genetic sequence of the usher; α, β, γ, κ, π and σ. Clade names were designated to recall a prominent member or quality of each; the alternate chaperone usher family (α), K88/F4 pili (κ), pyelonephritis-associated pili/P pili (π) and spore coat protein U from *Myxococcus xanthus* (σ). The γ clade is further divided into subclades; γ1, γ2, γ3 and γ4. The γκπ cluster share a common fimbrial subunit homology domain (PFAM00419). Of this cluster, the κ and π clades share gene arrangement, encoding first a major fimbrial subunit, usher and chaperone, whilst gene arrangement in the γ clade varies for each subclade. The α, β and σ clades possess their own unique gene arrangements and fimbrial homology domains; PFAM04449 (α), PFAM06551 (β) and COG5430 (σ) (172). The alternate/non-classical (α) CUPs share low sequence homology to classical systems such as Fim and Pap, but encoded pili assembled by similar mechanisms and often share structural homology (172, 174, 175). Both fimbrial and non-fimbrial structures are assembled by members of the σ (also referred to as archaic) clade. Examples include the Csu fimbriae of *Acinetobacter baumanni* implicated in biofilm formation and non-fimbrial spore coat U protein of *M. xanthus* which encapsulates the bacterium at its latter stages of development (176, 177).

An additional classification system was developed based on the chaperone structure, which distinguishes two subfamilies based on the length of a loop with connects the F1 and G1 strand of the chaperone (173). The long F1-G1 loop chaperones (FGL) assemble thin, flexible, non-fimbrial structures such as the Saf fimbriae of *Salmonella enterica, E. coli* Afa/Dr adhesins and F1 capsular antigen of *Yersinia pestis* (178-180). In contrast, short loop chaperones (FGS) assemble rigid, multi-subunit, rod-shaped fimbrial structures, exemplified by Fim and Pap

(154). The length of the F1-G1 loop influences DSE and DSC, with the F1-G1 loop of FGL chaperones occupying the entirety of the P1-P5 groove, whereas the F1-G1 loop of FGS chaperones interacts at the P1-P4 residue, leaving the P5 residue accessible (123, 154, 181, 182). The accessibility of the P5 residue influences chaperone-subunit and incoming subunit interaction. and subsequently the rate of fibre formation (183). FGL chaperones are found in the γ3 clade, whereas FGS chaperones can be divided into several clades; β, γ1, γ4, κ and π (172).

1.3.1.12. Regulation of fimbrial expression

Fimbrial gene expression is intricately controlled by invertible DNA elements, DNA methylation, c-di-GMP and transcriptional regulators, and is often coordinated with the expression other appendages (184).

Many fimbrial operons are controlled by phase variation in which gene expression is switched between an 'on' or 'off' phase. The expression state is inheritable but reversible, resulting in mixed populations of 'on' and 'off' cells arising from a single parent cell. The rate of switching events is characteristic for operons and dependent on environmental cues (184). In *E. coli*, *fim* expression is controlled in a phase variable manner by the orientation of an invertible DNA segment (*fimS*), consisting of the *fimA* promoter flanked by two 9-bp invertable repeats (185). This feature is referred to as the '*fim* switch' given transcription of *fimA* is driven in one orientation and inhibited in the other. The orientation of *fimS* is controlled by two site specific recombinases, FimB and FimE, which bind the inverted repeats (186, 187). FimE drives transcription from an 'on' to 'off' state, whilst FimB drives transcription in both directions. Other regulatory elements influence inversion of *fimS* including leucine-responsive regulatory protein (Lrp), integration host factor (IHF) and histone-like nucleoid-structuring proteins (H-NS) (188). In addition, phase variation is driven by environmental cues, including amino acids (leucine and alanine), amino sugars (N-acetyl-D-glucosamine [GalNac] and N-

acetylneuraminic acid [Neu_5A_c]), iron status, osmolarity, pH, temperature, and cross-talk with regulatory elements controlling Pap fimbrial expression (189-193).

In contrast to *fim*, phase variation in *pap* is controlled by the DNA methylation status of intergenic regions. The *papBA* promotor controls *pap* expression and lies in an intergenic region encoding genes for the PapI and PapB regulators (194). The intergenic region contains two GATC sequences ($GATC_{prox}$ and $GATC_{dist}$) which are methylated by the constituently-expressed deoxy-adenosine methyltransferase (DAM) (195). The intergenic regions also contain six binding sites for Lrp, as well as H-NS and cyclic AMP-catabolite activator protein (CAP) (196, 197). Lrp is found in complex with the DNA-binding protein, PapI, at the intergenic region. Binding of Lrp is cooperative, with simultaneous binding to either sites 1-3 or 4-6, which encompass the $GATC_{prox}$ and $GATC_{dist}$ sequences at site 2 and 5 respectively (198). The Lrp-PapI complex competes with DAM for GATC-binding, controlling methylation state and subsequent *pap* transcription (199). Gene transcription is repressed when Lrp-PapI is bound to sites 1-3 and activated when Lrp-PapI is bound to sites 4-6. Thus, when $GATC_{prox}$ is methylated, *pap* expression is kept in the 'on' state, whilst $GATC_{dist}$ methylation induces the 'off' state (200, 201). H-NS represses the *papBA* promoter in a temperature-dependent manner (202), whilst CAP controls phase variation in response to carbon source (198).

Elevated c-di-GMP levels promote biofilm formation by downregulating flagella and type IV pili and upregulating chaperone usher fimbriae (203, 204). The *mrk* operon of *Klebsiella pneumoniae* encodes thin fimbrie (2-4 nm), part of the type 3 fimbrial family of adhesins (γ4 clade). These structures bind the basement membrane of respiratory and urinary tract epithelia (100, 205) and are detected by agglutination of tannic-acid treated erythrocytes *in vitro* (206). The *mrkA* gene encodes a major fimbrial subunit, whilst *mrkD* encodes a putative adhesin (207). The *mrkHIJ* gene cluster, encoded downstream of the *mrk* operon, controls fimbrial expression through secondary messenger modulation and sensing. MrkI is a LuxR-

type transcriptional factor whilst MrkH is a PilZ-domain containing protein capable of binding c-di-GMP (208). Both MrkI and MrkH positively regulate the *mrkHIJ* operon and expression of type 3 fimbriae. Conversely, MrkJ is an EAL-domain phosphodiesterase which inhibits fimbrial assembly through c-di-GMP degradation (209).

1.3.1.13. Predicted CUP of *P. aeruginosa*

P. aeruginosa encodes five chaperone usher pathways; *cupA* (chaperone usher pathway A), *cupB*, *cupC*, *cupD* and *cupE*. Although little is known about the physiological function and structure of these appendages, evidence supports a role at various stages of biofilm formation (3, 53, 56, 149). The *cupA*, *cupB*, *cupC* and *cupE* operons are present in the genome of many sequenced *P. aeruginosa* strains including PAO1, PAK, PA14 and M18, whilst *cupD* is encoded within a pathogenicity island in PA14. Gene organisation varies within each cluster; however, all encode at least one pilin subunit, a chaperone and an usher (Figure 1.7). The *cupA*, *cupB*, *cupC* and *cupD* are classified into the γ4 clade, whereas the *cupE* cluster is classified in the σ clade. Further, all clusters are grouped in the FGS class based on chaperone structure (172, 210). Evidence supports *cup* expression is controlled by a complex regulatory network involving environmental stimuli, c-di-GMP signalling, two components systems and transcriptional regulators (summarised in Table 1.3); however, their coordination and relative contribution during biofilm formation remain unclear. Further, no *cup* fimbriae have been imaged on the *P. aeruginosa* cell surface at high resolution and no atomic structures of assembled *cup* fimbriae have been reported to date.

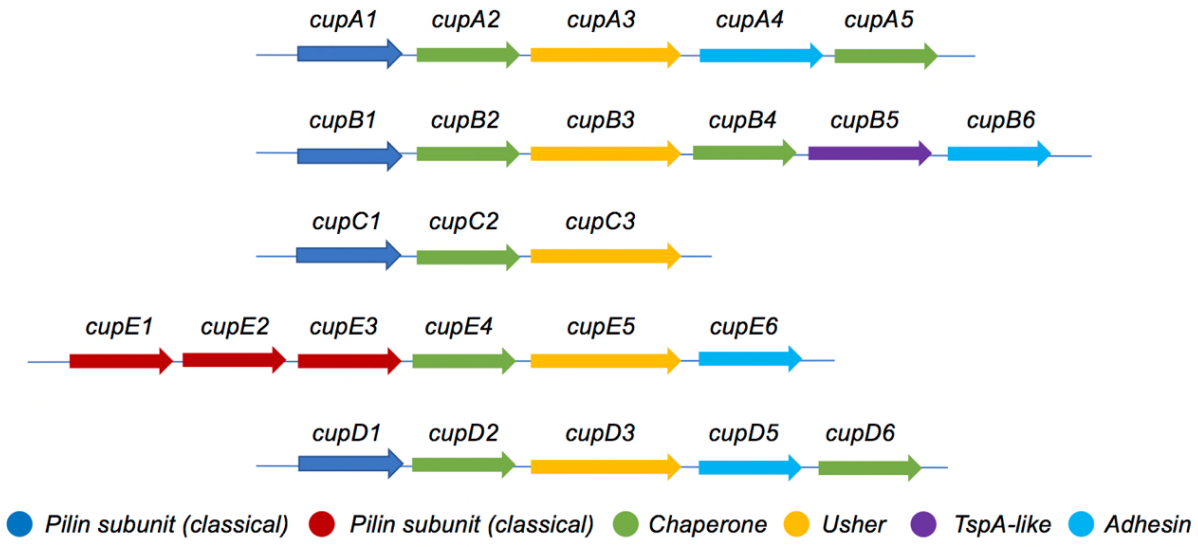


Figure 1.7: Genetic organisation of chaperone usher proteins in *P. aeruginosa*

Schematic illustrating the arrangement of cup genes in *P. aeruginosa*. Gene components have been colour coded as per legend. Each cluster encodes at least one pilin subunit (classical or aclassical), chaperone, usher and adhesin. The *cupB* cluster additionally encodes a TspA-like protein.

Table 1.3: Regulation of chaperone usher pathways in *P. aeruginosa*

Summary of the proteins and pathways identified in regulating the expression of *cup* clusters in *P. aeruginosa*. Table adapted from Giraud and Bentzmann (210). N.D = not determined. TCS = two component systems. H-NS = histone-like nucleoid structuring proteins.

Cluster	c-di-GMP	TCS	H-NS	Other	Reference
cupA	SiaD, MorA, WspR, PA1120, PvrR, PA2133	N.D	MvaT, MvaU	CgrABC	(4, 211-214)
cupB	N.D	RocS1/ RocS2	MvaT	N.D	(18, 50, 52, 149)
cupC	RocR	RocS1/ RocS2	MvaT	N.D	(18, 50, 52, 149)
cupD	PvrR	RscBC/PvrSR	N.D	N.D	(53, 215, 216)
cupE	N.D	PprA/PprB	MvaT	N.D	(4, 56)

1.4. Clinical significance of *P. aeruginosa*

P. aeruginosa is a Gram-negative opportunistic pathogen, widely distributed in soil, water and plants (217). In hospital environments, *P. aeruginosa* is found on biotic and abiotic surfaces including urinary catheters, respiratory machines, surgical sites and water supplies. Nosocomial infections associated with these biofilms include ventilator-associated pneumonia, cystic-fibrosis (CF) pneumonia, and chronic wound infections (218, 219). In 2017, the World Health Organisation published a list of organisms in the 'critical' category for antibiotic research and development, highlighting those multi-drug resistant bacteria for which either a single therapy or no therapy is available. These include carbapenamase *P. aeruginosa*, *A. baumanni* and Enterobacteriacae (220). As such, *P. aeruginosa* has been flagged as the organism of highest burden on European intensive care units, as well as increasing clinical and economic burden in the United States (221-223). The ability of *P. aeruginosa* to form biofilms in diverse environments is attributable to an arsenal of virulence factors controlled by a conserved network of regulatory genes (224-227).

1.4.1.1. CupA

The *cupA* operon of *P. aeruginosa* encodes the components of classical CUP assemblies; including a major fimbrial subunit (CupA1), chaperones (CupA2 and CupA5), usher (CupA3) and adhesin (CupA4). The role of *cupA* in attachment was discovered through a transposon insertion library screen of a non-piliated *P. aeruginosa* PAK strain; where disruption in *cupA2* and *cupA3* genes resulted in loss of biofilm formation (3). Regulation of *cupA* expression has been most characterised relative to other *cup* clusters in *P. aeruginosa* (summarised in Figure 1.8). The *cupA* operon is negatively regulated by the global transcriptional regulator MvaT, a H-NS protein thought to silence gene expression by directly binding to AT rich chromosomal regions (4, 228). MvaT influences the expression of more than 150 genes, including *cupB*, *cupC* and *cupE*, and is linked to quorum sensing responses, pyocyanin and PA-IL lectin

production, drug-resistance, biofilm formation and motility (4, 229, 230). MvaT represses *cupA* genes in a phase-variable (on/off) manner, resulting in mixed population of *cupA*-expressing and non-expressing cells (231). An additional H-NS protein with structural homology to MvaT, MvaU, has been identified in *P. aeruginosa* which is capable of both homodimerization and heterodimerisation with MvaT (Figure 1.8). In an Δ*mvaT* mutant, *mvaU* over-expression rescues phase-variable repression of *cupA*, suggesting that MvaU is similarly capable of *cupA* repression (231). Consistent with this, H-NS proteins are implicated in phase-variable repression of Pap and Fim fimbriae in *E.coli* (202, 232, 233).

Phase variable expression of CupA is positively regulated under conditions of anaerobiosis through the global regulator of anaerobic gene expression, Anr (214) (Figure 1.8). Anr is an FNR-like protein, known to activate the transcription of genes in response to anoxia in *E.coli* (234). Anr is thought to bind the promoter region of *cgrABC*, located directly upstream of the *cupA* operon, based on a putative Anr-binding site. This activates expression of *cgrABC* gene products which positively regulate *cupA* gene expression. *cgrABC* over-expression upregulates 12 genes, of which the *cupA* is most affected, suggesting local regulation (214). Whilst their precise role remains unknown, CrgA is a putative member of the adenine nucleotide α-hydrolase superfamily, CgrB a putative member of the GNAT family of acetyltransferases and CrgC is a ParB-like, DNA-binding protein which binds the *cupA* promoter region directly. CrgA-CrgC interaction has been demonstrated and is required for phase-variable expression of *cupA* (235). The *cgrABC* genes are negatively regulated by MvaT in aerobic conditions, though whether this is through direct interaction with CrgABC remains unclear (214). The influence of anoxia on *cupA* expression is thought to reflect adaptation to the anaerobic environment of the cystic fibrosis lung (236, 237).

In addition to environmental cues, the expression of *cupA* and formation of *cupA*-dependent auto-aggregative small colony variants (SCVs) in the cystic fibrosis lung are

influenced by intracellular c-di-GMP levels (211). A transposon insertion library of clinically-isolated SCVs revealed disruption in *cupA*, the motility regulator protein MorA or hypothetical protein PA2110 leads to loss of auto-aggregation. Structural predictions indicate both MorA and PA2110 contain GGDEF and EAL domains, implicating these proteins in c-di-GMP signalling. In line with this, *morA* and *PA2110* transposon mutants demonstrate decreased c-di-GMP levels in bacterial extracts. Further, complementation of *morA* or *PA2110* restores *cupA* expression in their respective SCV mutant backgrounds, reaffirming c-di-GMP influences fimbrial expression (Figure 1.8). Indeed, c-di-GMP levels are twice elevated in SCVs relative to wild type strains (211). *cupA*-dependent auto-aggregation is antagonized by PvrR, an EAL-domain containing phosphodiesterase (211). CupA3 deletion induces loss of a wrinkled colony phenotype in PAO1, additionally supporting CupA influences auto-aggregation in laboratory adapted strains (212).

The *saiABCD* operon regulates auto-aggregation in PAO1 under conditions of detergent stress (238). SiaA is a transmembrane protein, SiaB and SiaC are proteins of unknown function and SiaD a putative GGDEF-domain containing diguanylate cyclase. *cupA* expression is elevated under conditions of detergent stress, presumably by SaiD-elevated c-di-GMP levels (Figure 1.8). Deletion of *cupA1* or *cupA3* in the presence sodium dodecyl sulphate (SDS) returns a smooth colony phenotype, supporting CupA-mediated auto-aggregation in this context (238).

The *cupA* operon encodes a EAL domain-containing phosphodiesterase immediately after the *cupA5* gene, annotated as PA2133. Previous studies support PA2133 hydrolyses c-di-GMP, regulating several physiological process such as type III secretion (239, 240), extracellular DNA release, biofilm formation (19, 238, 241, 242), polysaccharide expression (19) and chemotaxis (240). Interestingly, surface attachment of PAO1 is completely abolished by over-expression of PA2133, indicating that it has an important influence on adhesin

expression (19). Given its proximity to the *cupA* cluster in the genome, PA2133 is hypothesized to influence CupA-mediated attachment (Figure 1.8). However, a direct effect on *cupA* expression has not been demonstrated to date.

Based on HHPred analysis (243), CupA1 shares highest structural similarity with FimA, CupA2 and CupA5 with CupB2 and FimC chaperones, CupA3 with the FimD usher and CupA4 with the CupB6 and FimH adhesin (243). Although no atomic structures are reported, CupA filaments have been observed on the surface of clinically-isolated SCVs using negative-stain TEM and immuno-gold labelling SEM (211). CupA appear to be flexible, thick filaments (~10 nm in diameter) and are localised along the entirety of the cell surface (211).

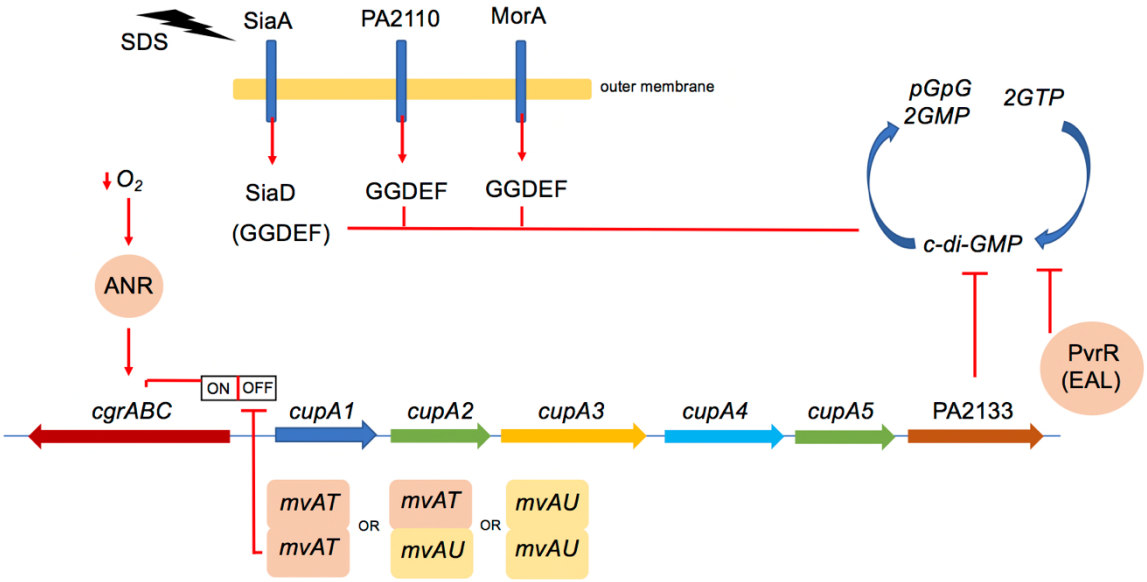


Figure 1.8: Regulation of *cupA* expression in *P. aeruginosa*

Schematic illustrating the proteins and pathways regulating CupA fimbrial expression in *P. aeruginosa*. The H-NS like proteins MvaT and MvaU form either homo- or hetero-dimers which repress *cupA* expression. Anaerobiosis stimulates activation of the *crgABC* genes by the ANR, whose gene products positively regulate *cupA* expression. The EAL-domain containing phosphodiesterases, PA2133 and PvrR, reduce c-di-GMP levels which subsequently represses *cupA* expression. The GGDEF-domain containing protein, SiaD, is activated by detergent stress sensed by SiaA at the outer membrane. SiaD, PA2110 and MorA synthesize c-di-GMP through their diguanylate cyclase activity which upregulates *cupA* expression. Figure adapted from Giraud and Bentzmann, 2011 (210).

1.4.1.2. CupB and CupC

The *cupB* operon encodes a hybrid chaperone usher system; which includes a major fimbrial subunit (CupB1), chaperones (CupB2 and CupB4), usher (CupB3), adhesin (CupB6), as well as a TspA-like protein, CupB5. TspA-like genes are commonly found in clusters of the γ4 clade, though their roles remain unexplored in this context (172, 244). Two-partner secretion (TPS) systems are widespread in Gram-negative bacteria and typically involve a TpsA secreted protein and TpsB outer membrane transporter. TpsB proteins contain a C-terminal β-barrel membrane domain, as well as a POTRA (polypeptide-transport associated) domain which chaperones interaction with TpsA (245). Classic functions of TpsA proteins range from adhesion, cytotoxicity, and proteolysis to contact-dependent growth inhibition (246, 247). CupB5 is predicted to share similarity with other TpsA-like proteins such as FHA of *Bordetella pertussis* and HxuA of *Haemophilus influenzae*. Although, no TpsB-like transporter has been identified in the *cupB* cluster, a dual role in translocation may by be carried by the CupB3 usher. Structural analysis indicates that CupB3 encodes the canonical POTRA domain of TpsB proteins (248). Further, deletion of Δ*cupB3* results in loss of CupB1 and CupB5 in the supernatant fraction. Truncation of the CupB3 POTRA domain disrupts both CupB5 and CupB1 secretion, however does not disrupt CupB1 secretion in a Δ*cupB5* mutant background. This suggests that CupB5 may be stalled at the outer membrane of POTRA-domain mutants disrupting CupB1 translocation; and that CupB5 is translocated prior to CupB1 (248). Absence of the CupA4 chaperone results in loss of CupB1 and CupB5 secretion, supporting CupA4 is the corresponding chaperone for both proteins (248).

Based on HHPred analysis (243), CupB1 shares structural homology with a fimbrial subunit encoded by *Burkholderia pseudomallei* (Q63UH6), CupB2 and CupB4 to the FimC chaperone, CupB3 to the FimD usher and CupB6 to *E. coli* Lpf fimbriae (243). The *cupC* operon encodes the simplest CU pathway in *P. aeruginosa*, consisting of a single fimbrial

subunit (CupC1), chaperone (CupC2) and usher (CupC3). Based on HHPred analysis, CupC1 shares structural homology to the Q63UH6 fimbrial subunit encoded by *Burkholderia pseudomallei*, CupC2 to CupB2 and FimC chaperones and CupC3 to the FimD usher (243).

Crystal structures for both the CupB2 chaperone and CupB6 adhesin are published (249, 250). The CupB2 structure reveals the boomerang-shaped fold of classical CU chaperones, consisting of two immunoglobulin (Ig) domains (249). Functional experiments demonstrate purified CupB2 is binds CupB1 but does not bind CupB6 (249). This is consistent with experimental evidence which supports CupA4 as the corresponding chaperone to CupB6 and CupB5 (248). The crystal structure of CupB6, bound to CupB1, reveals both pilin domains to possess a classical Ig fold (250). The CupB6 pilin domain shares structural homology the LpfD pilin subunit from the long fimbriae protein of *E. coli*, known to bind intestinal epithelium (251). The adhesin domain shares most structural similarity to the F17 fimbriae of *enteropathogenic E. coli*. F17 fimbriae interact with GlcNAc residues by a conserved tryptophan residue within the binding site (138) (Table 1.2). The CupB6 adhesin does not appear to share similarity in binding residues, including lack of aromatic residues, suggesting CupB filaments bind an alternate substrate (250).

Although *cupB* and *cupC* expression are increased in an Δ*mvaT* background, CupB1 and CupC1 assembly is not witnessed, supporting additional regulators (4, 210). The RocS1/A1 two-component system modulates *cupB* and *cupC* expression in *P. aeruginosa* PAK (50) and is comprised of three proteins RocS1, RocA1 and RocR (Figure 1.9). These proteins share homology to components of the BvgAS two-component system of *Bortedella* spp. which regulate a range of virulence factors (252). RocS1 is a sensor kinase with homology to BvgA, RocA1 a response regulator with homology to BvgS and RocR an EAL-domain protein with homology to BvgR and PvrR. Studies confirm the EAL-domain of RocR possesses phosphodiesterase activity, supporting c-di-GMP signalling influences *cupB* and *cupC*

expression (253). Upregulation of RocS1 and RocA1 activates *e*xpression of *cupB* and *cupC*, presumably through phospho-relay transduction. Although the influence of RocR on *cupB* expression has not been directly examined, RocR activity represses RocA1, which subsequently reduces *cupC* expression (50, 52). In a RocS1 overexpression background, biofilm formation is lost upon deletion of Δ*cupB3* or Δ*cupC3* and restored upon complementation. Further, CupB and CupC filaments are sheared from the surface of this strain, supporting a role in adhesion (149). CupB and CupC filaments have been visualised on the PAO1 cell surface in a *rocS1*-overexpression background using transmission electron microscopy, however the resolution of these images limits structural conclusions (149, 248).

The RocS1/A1 system cross talks an additional two-component system, RocS2/A2, in a complex manner (52) (Figure 1.9). RocS2 is a paralog of the RocS1 sensor kinase (45% identity) and RocA2 a paralog of the RocA1 response regulator (59% identity). Interestingly, RocS2 positively regulates *cupC* expression through the response regulator RocA1, but not RocA2. Further, whilst RocS2 positively regulates *cupB*, expression persists in Δ*rocA1*, Δ*rocA2* and Δ*rocA1-A2* double mutants, suggesting additional signalling components (52). Whilst a link to *cupB* or *cupC* expression has not been shown, RocA2 represses the *mexAB-oprM* and *mexR* genes encoding the machinery and regulatory components of a multi-drug efflux pump. In support of this, Δ*rocA2* mutants are increasingly resistant to aztreonam and carbenicillin antibiotics (52). RocR negatively regulates *cupC* expression through repression of RocS2, highlighting cross-talk between pathways (52). The complexity of *cupB* and *cupC* regulation suggests intimate coordination in the assembly of CupB and CupC fimbriae during surface attachment or biofilm formation. This network may extend to other *cup* clusters, given RocA2 downregulates *cupA3* and upregulates *cupE4* (52).

Finally, the *pvcABCD* operon encodes components for the biosynthesis of pyoverdine and pseudopyoverdine metabolites which function as a primary siderophores in *P. aeruginosa*

(254). The *pvcABCD* operon also synthesizes a secondary metabolite called paerucumarin, an isonitrile-functionized cumarin whose function remains largely unexplored (255). The *pvc* cluster is negatively regulated by iron and positively regulated by the transcriptional regulator, PtxR (254). The over-expression of *pvcABCD* upregulates *rocS1* and *rocS2*, resulting in expression of *cupB and cupC* and biofilm formation (256). This effect is believed to be through action of paerucumarin, given over-expression or exogenous application of paerucumarin upregulates *rocS1*, *rocs2*, *cupB2* and *cupC2* gene expression (256).

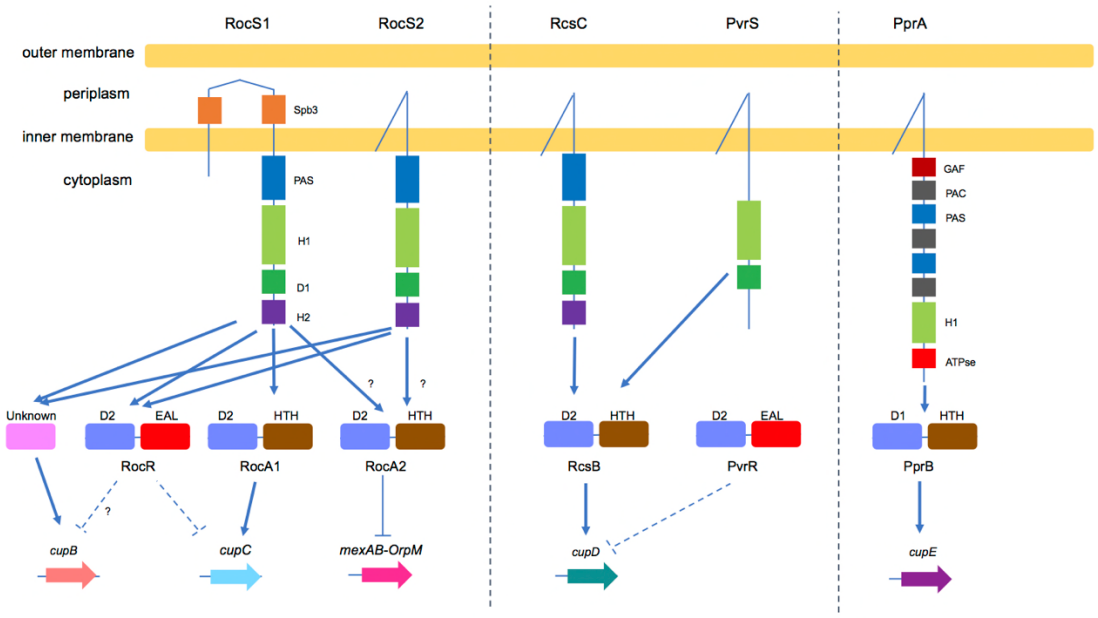


Figure 1.9: Overview of the two-component systems regulating *cup* gene expression in *P. aeruginosa*

Layers of the bacterial cell envelope are labelled accordingly. Protein domains are labelled as follows; sensory domains include sbp3, PAS, PAC and GAF, transmitter domains = H1, receiver domains = D1, Hpt domain= H2, output domains include a helix-turn-helix motif for DNA binding (HTH) or phosphodiesterase activity (EAL). The expression of *cupB*, *cupC* and *mexAB-OprM* are under the influence of the RocS1/A1 and Rocs2/A2 system. The expression of *cupD* is under the influence of the RscC/B and PvrS/R system. The expression of *cupE* is under the influence of the PprA/B system. Figure adapted from Giraud and Bentzmann 2011 (210) and Muhl, D., 2014 (7).

1.4.1.3. CupD

The *cupD* operon is encoded on the PAP-1 pathogenicity island of the *P. aeruginosa* PA14 strain and encodes a fimbrial subunit (CupD1), chaperones (CupD2 and CupD5), usher (CupD3) and adhesin (CupD4) (215). PA14 shares a similar host range to PAO1 but is significantly more virulent. Based on HHPred analysis, CupD1 fimbrial subunit shares highest structural homology to the Q63UH6 fimbrial subunit of *Burkholderia pseudomallei*, CupD2 and CupD4 to the CupB2 chaperone, CupD3 to the FimD usher and CupD5 to the CupB6 adhesin (243).

The *cupD* operon is found clustered with genes corresponding to the RscAB and PvrRS two-component systems; the RcsC sensor kinase, RscB response regulator, the putative PvsR sensor kinase and PvrR response regulator RocR (Figure 1.9). RcsB positively regulators *cupD* expression and cell-surface assembly of CupD, whilst RscC inhibits *cupD* expression (215, 216, 257). Over-expression of RscB in PA14 results in increased SCV formation, decreased motility and biofilm formation, consistent with a sessile lifestyle (215). This phenotype is abolished upon Δ*cupD* deletion, supporting CupD filaments play a role in these processes. Over-expression of the PvrR antagonises RscB activity, resulting in decreased *cupD* expression and loss of sessile phenotype, presumably through its phosphodiesterase activity (53, 257). Finally, PvrS downregulates *cupD* expression by effect on the RscB response regulator, as oppose to PvrR (216).

1.4.1.4. CupE

The *cupE* operon encodes the genes for assembly of archaic CupE fimbriae; including three fimbrial subunits (CupE1-E3), a chaperone (CupE4), usher (CupE5) and adhesin (CupE6). The *cupE* cluster is encoded in the genome of all sequenced *P. aeruginosa* strains. Although archaic pili have a wider phylogenetic distribution, comparatively less is known about these structures. HHPred analysis reveals CupE1-E3 and CupE6 share greatest structural homology with CsuE adhesin of *A. baumannii* (258), CupE4 to the CupB2 chaperone and CupE5 to the FimD usher (243). Each of the CupE1-E3 fimbrial subunits and CupE6 adhesin possess the characteristic COG5430 and spore-coat protein U (SPCU) domains of the archaic σ clade (172).

The *csu* cluster of *A. baumannii* shares highest homology to *cupE* and encodes three fimbrial subunits; CsuA/B, CsuA, CsuB and the tip adhesin, CsuE. The crystal structures of CsuA/B and CsuE in complex with the CsuC chaperone provided the first insights into the structure of archaic pili (174, 258). CsuE and CsuA/B are maintained in a relatively disordered state when complexed with CsuC as compared with classical chaperones, supporting an alternative DSC mechanism (174, 258). In support of this, the N-terminal extensions of Csu subunits lack the conserved glycine and alternating hydrophobic residues. The crystal structure of CsuE reveals two β-barrel domains whose fold adopts an overall C-shape (258) (Figure 1.10A). The CsuE pilin domain possesses an incomplete immunoglobulin fold whose C-terminal, G_1 strand is complemented by the CsuC chaperone (Figure 1.10B). The CsuE adhesin domain contains a flexible, three-fingered structure at the tip, which are highly hydrophobic (Figure 1.10C). This structure differs to the hydrophobic binding grooves of lectin-binding domains of classical pili (Figure 1.10D). Two of the loops are highly conserved amongst archaic pili, whilst the third is unique to Csu pili. Mutation of the loop regions abolish biofilm

formation, supporting a role in attachment. Amino acid sequence alignment confirms finger-like loops at the tip of the CupE6 adhesin (258).

Literature supports CupE filaments play a role in attachment and biofilm formation (56). In wild-type PAO1, filaments are detected on the surface of cells grown on static surfaces relative to shaking conditions suggesting a solid substrate is required for expression. Mature *P. aeruginosa* biofilms are characterised by elevated, multi-cellular, mushroom-shaped structures (259). A transcriptional *cupE*-GFP fusion library revealed these structures are lost upon Δ*cupE1*, Δ*cupE5* or Δ*cupE6* deletion, suggesting CupE is recruited in the latter stages of biofilm formation (56). Whilst CupE filaments were imaged on the cell surface using negative-stain TEM, the resolution of these images limits structural conclusions (56). Cell surface filaments are lost upon Δ*cupE5* deletion, supporting CupE translocates the CupE5 usher during assembly. CupE filaments appear to be comprised majorly of CupE1, given Δ*cupE2* and Δ*cupE3* deletion does not result in loss of CupE1 in the cell-surface sheared fraction (56). Further, Δ*cupE6* deletion results in loss of CupE1 in the sheared fraction, supporting the hypothesis that CupE6 is the first to translocate the usher and nucleate filament assembly (56).

The PprAB two-component system controls *cupE* expression through the PprA sensor kinase and PprB response regulator (Figure 1.9). The PprAB TCS additionally regulates expression of Bap adhesin and type-IVb pili (57, 82). PprB encodes a DNA-binding helix-turn-helix (HTH) motif and positively regulates *cupE* expression by direct binding to the promoter region (56). In support of this, *pprB* and *cupE* expression are upregulated in cells grown under static conditions. Further, whilst expression of *cupE* is not detected in cells grown under shaking conditions, it is induced through over-expression of *pprB*-plasmid (56). These results support *cupE* expression is negatively regulated under static conditions, potentially through *pprAB* repression.

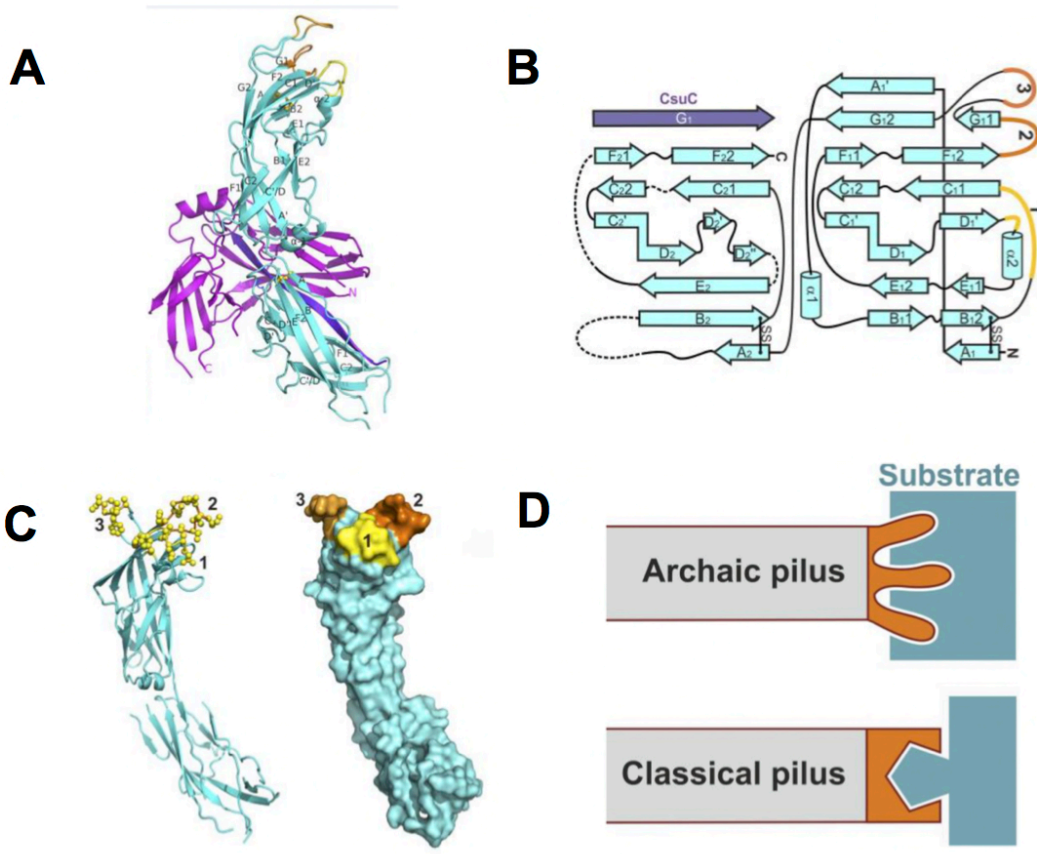


Figure 1.10: Structure of the archaic CsuE:CsuC adhesin-chaperone complex of *Acinetobacter baumanni*

(A) Ribbon diagram of the crystallized CsuE-CsuC complex (PDB: 6FJY) reveals an overall C-shaped conformation. CsuE is coloured cyan, with the finger-like loop residues at the adhesin tip coloured yellow and orange. The CsuC chaperone is coloured purple. (B) Topology diagram of CsuE complemented by the G_1 strand of CsuC (purple). (C) Ribbon (left) and molecular surface (right) diagrams of the CsuE adhesin (cyan) highlighting hydrophobic loop structures at the distal end of the tip (yellow and orange residues). (D) Cartoon diagram illustrating proposed difference in binding mechanism of the finger-loop domain of archaic vs. lectin-binding domain of classical pili. Figure adapted from Pakharukova et al., 2018 (148).

1.4.2. Polysaccharide adhesins

Both Gram-positive and Gram-negative bacteria produce polysaccharide adhesins such as Psl, Pel (260), polysaccharide intercellular adhesin (PIA/PNAG) (261, 262), alginate (263), capsular polysaccharides (264) and holdfast (265). These secreted polysaccharide are diverse in their composition, chemical and physical properties and have a significant impact on biofilm formation (266). Whilst much is known with respect to the biosynthesis, structure and function of polysaccharide adhesins, how these molecules are anchored at the bacterial cell surface remains relatively unexplored.

1.4.2.1. Polysaccharide biosynthesis

Because Gram-negative bacteria have an outer membrane, the biosynthesis, secretion and anchoring of exopolysaccharides requires specialized molecular machinery. Numerous studies have been conducted to elucidate the pathways and enzymes associated with exopolysaccharide biosynthesis in Gram-negative bacteria. Three major pathways have been identified in bacteria; the Wzx/Wzy-dependent, the ATP-binding cassette (ABC) transporter-dependent and the synthase-dependent pathway (267). In the Wzx/Wzy dependent pathway, activated sugar precursor is assembled on the undecaprenyl-diphosphate lipid carrier by inner membrane embedded glycosyltransferases (268), followed by secretion by the Wzx flippase (269). Polymerization is coordinated in the periplasm by the Wzy protein before export to the cell surface (270). Export across the outer membrane is mediated by the polysaccharide co-polymerase (PCP) and outer membrane polysaccharide export (OPX) family of transporters, also known as Wzz/Wzc and Wza respectively (Figure 1.11) (271). In contrast, polysaccharides assembled by the ABC transporter-dependent pathway are fully polymerised by inner membrane-embedded glycosyltransferases. The assembled polysaccharides are then linked to undecaprenyl-diphosphate, as in the case of O-polysaccharides or diacylglycerol phosphate, as in the case for capsular polysaccharides which also uniquely carry a conserved

phosphatidylglycerol and poly-2-keto-3-deoxyoctulosonic acid (KDO) lipid moiety (272). Finally, transport across the inner membrane is coordinated by a tripartite efflux pump-like complex consisting of an ABC-transporter, as well as PCP and OPX proteins which share close homology to that of the Wzx/Wzy pathway (Figure 1.11) (273). In the synthase-dependent pathway, secretion occurs in the presence of absence of a lipid acceptor molecule (274, 275). Polymerisation and inner membrane transport is simultaneously mediated by an membrane-embedded glycosyltransferase (276). In Gram-negative synthase secretion systems such as that of *P. aeruginosa,* polymerisation is also co-regulated by an inner membrane receptor or co-polymerase which binds c-di-GMP to activate polysaccharide production (277, 278). Polymerised polysaccharide is believed to be protected from degradation by a periplasmic tetratricopeptide repeat (TPR)-containing scaffold protein before export through the outer membrane by a β-barrel porin (Figure 1.11) (279).

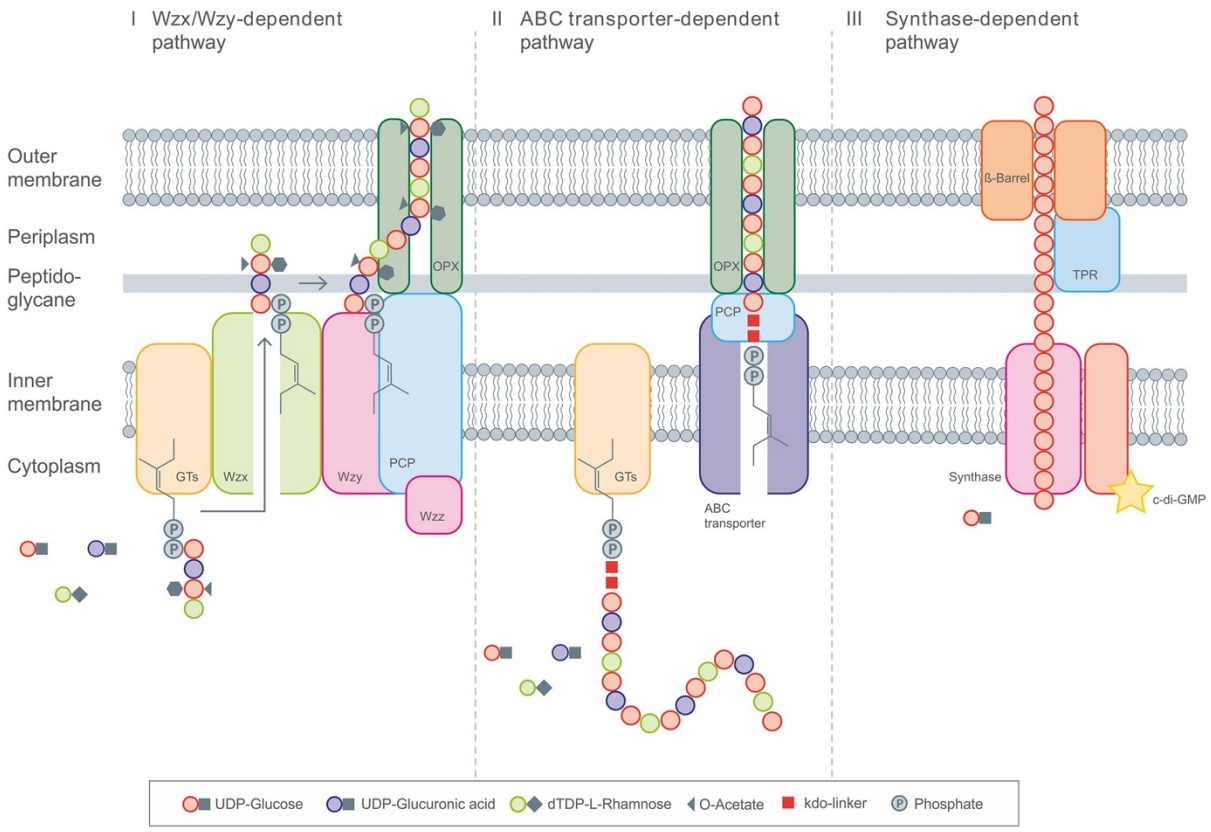


Figure 1.11: Polysaccharide synthesis and secretion across the bacterial cell envelope

(A) In the Wzy/Wzx dependent pathway heteropolymers are assembled by inner-membrane embedded glycosyltransferases (GTs) and transported across the inner membrane to the periplasm by Wzx. Polymerization is mediated by Wzy, followed by export to the cell surface by PCP/Wzc/Wzz and OPX/Wza proteins. (B) In the ABC transporter-dependent pathway, heteropolymers are fully assembled in the cytoplasm by inner membrane GTs. These polysaccharides often contain a conserved KDO lipid moiety at the C-terminus (represented by red blocks at the end of polymer). Polymerised polysaccharide is then exported via the ABC-transporter:PCP:OPX tripeptide complex to the cell surface. (C) The synthase pathway generally assembles simpler polysaccharides via an inner membrane embedded synthase and co-polymerase (orange protein) that additionally relies on c-di-GMP activation. Tetratricopeptide repeat (TPR)-containing scaffold proteins prevent degradation in the periplasm and export is facilitated by a β-barrel protein across the outer membrane. Figure adapted from Schmid et al., 2015 (267).

1.4.2.2. PIA and PNAG

Polysaccharide intracellular adhesin (PIA), also referred to as poly ß-1,6-N-acetylglucosamine adhesin (PNAG), is implicated in cell to cell adhesion in Gram-positive staphylococci including *Staphylococcus aureus* and *Staphylococcus epidermidis* (261). Biofilm infections associated with these bacteria include endocarditis, osteomyeleitis and sepsis, primarily as a consequence of in-built medical devices such as prostheses (280, 281). PIA is structurally composed of linear ß-1,6-N-acetylglucosamine, synthesized from UDP-N-acetylglucosamine precursor (Figure 1.12A). In both *S. aureus* and *S. epidermidis*, PIA synthesis and export machinery are encoded by the *icaADBC* locus (261, 282). IcaA and IcaD are involved in PIA synthesis, IcaC for translocation to the cell surface and IcaB in the deacetylation of PIA (283, 284). Deacetylation is crucial in introducing positive charge to PIA, facilitating its fixation at the negatively charged cell surface (285). An additional gene, *icaR*, is encoded for upstream of the *icaADBC* locus which transcriptionally represses *icaA* and PIA secretion (286). Several quorum sensing networks and sigma factors have been implicated in the regulation of PIA production, either through direct binding to the *icaABDC* promotor or regulation of *icaR* expression, including SarA (287), LuxS (288), σ^B (289) and TcaR (290). Although PIA contributes to adhesion, several clinical isolates (including methicillin-resistant *Staphylococci*) demonstrate *ica*-independent biofilm formation, supporting the importance of additional adhesion factors (291-293). Orthologs of the *icaADBC* locus have been identified in Gram-negative pathogens including *E. coli* (262), *Yersinia pestis* (294) and *A. baumanni* (295), suggesting a conserved role for PIA synthesis in biofilm formation.

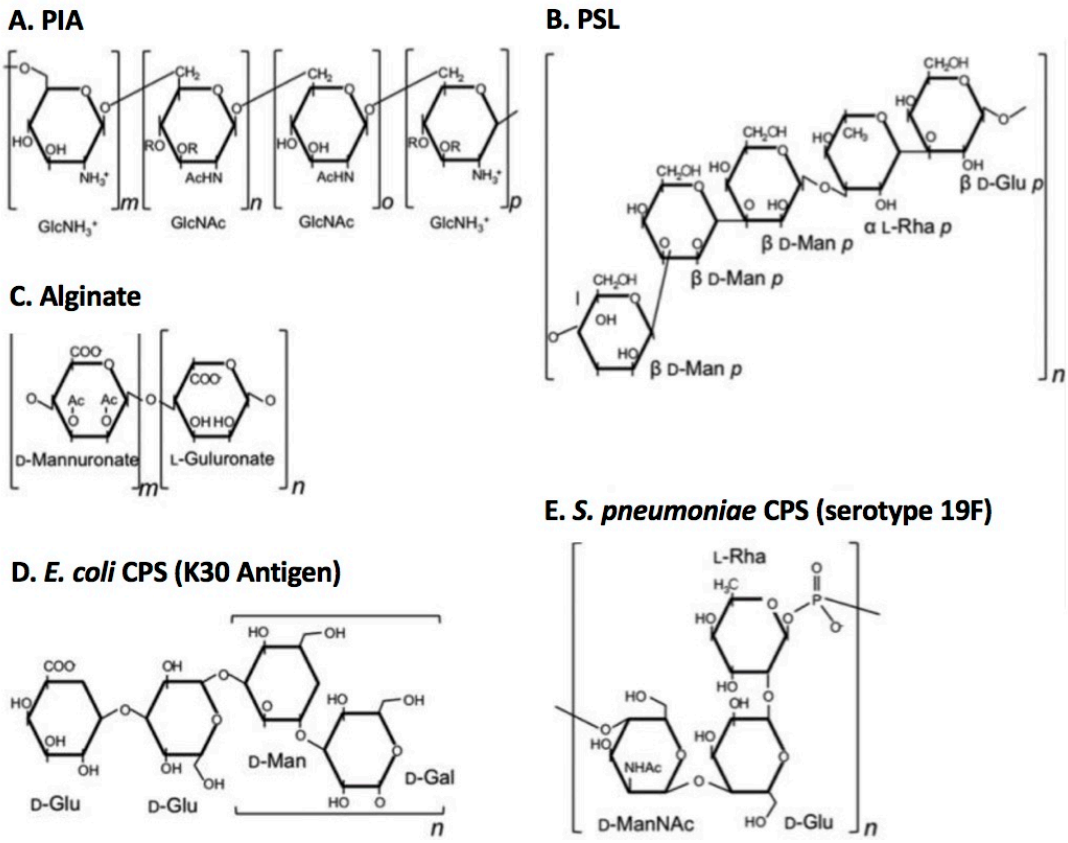


Figure 1.12: Molecular structures of bacterial polysaccharide adhesins

(A) Polysaccharide intracellular adhesin (PIA) is structurally comprised of a linear chain of ß-1,6-N-acetylglucosamine residues. (B) Psl is a penta-saccharide comprised of D-mannose, D-glucose and L-rhamnose sugars. (C) Alginate consists of non-linear 1,4-linked L-guluronic and O-acetylated D-mannuronic acids. (D) Capsular polysaccharides such as the K30 antigen of *E. coli* and (E) capsule of *Streptoccoccus pneomoniae* are diverse in composition. Figure adapted from Limoli et al., 2015 (296).

1.4.2.3. Psl and Pel

Psl (polysaccharide synthesis locus) and Pel (pellicle operon) are exopolysaccharides secreted by environmental and clinical isolates of *P. aeruginosa* (260, 263). These carbohydrates are major constituents of the biofilm matrix, promoting cell to cell adhesion and biofilm formation (297-300). Structurally, Psl is a neutral penta-saccharide, consisting of D-mannose, D-glucose and L-rhamnose sugars (301) (Figure 1.12B). Lectin staining demonstrates Psl decorates the *P. aeruginosa* cell surface in a helical pattern (259). Although the mechanism for Psl anchoring remains unclear, studies reveal purified LecB, a lectin associated with the outer membrane, bind the mannose residues of Psl (302, 303). In addition, the large CdrA adhesin is suggested to tether Psl to the cell surface, thereby promoting cell aggregation and matrix stability. This interaction is similarly disrupted by addition of mannose (28). The *psl* operon encodes 15 co-transcribed genes (*pslA-O*), 11 of which are essential for Psl production and cell surface association (304). The precise function of each *psl* gene component remain incompletely characterised. PslB is an enzyme responsible for production of sugar-nucleotide precursor (GDP-mannose). The enzymes AlC, RmlC and GalU are encoded by other biosynthetic pathways and are additionally required for precursor activation (304). PslF, PslH, PslI and PslC are predicted as glycosyltransferases which incorporate sugar nucleotides into the repeating Psl structure. Inner membrane domains are predicted in PlsA, PslE, PslJ, PslK and Psl, and are predicted to orchestrate Psl polymerization and secretion (305). PslA and PslE share homology with the WbaP and Wzc components of the *E.coli* Wzy-dependent export system, and may be similarly responsible for initial targeting of cytoplasmic polysaccharide to the inner membrane and secretion respectively (306). PslD shares similarity to the Wza transporter of *E. coli* and is hypothesized to export assembled Psl across the outer membrane to the cell surface (305, 307). PslG is a glycosyl hydrolase reported to degrade periplasmic Psl, as well as disrupt biofilm development and architecture when applied

exogenously (308, 309). Two forms of Psl have been identified; a high molecular weight, cell-associated form and a low molecular weight, secreted form, believed to be produced as a result through the hydrolytic activity of PslG (304).

The Pel exopolysaccharide derives its name from the observation that *pel* mutants are deficient in pellicle formation, a biofilm formed at the air-liquid interface (310). Similar to Psl, Pel exists as a high molecular weight cell-associated form and in a low molecular weight, secreted form. Secreted Pel is rich in partially acetylated GlcNac and N-acetyl-galactosamine (GalNac) (311). The synthesis, secretion and export of Pel require the protein products of the *pelABCDEFG* operon, however the molecular details remain largely unknown. PelF is a cytoplasmic glycosyltransferase which is believed to synthesize Pel from UDP-glucose precursor (312). The periplasmic deacetylase, PelA, catalyses the removal of N-acetyl groups from polymerized Pel rendering it positively charged/cationic. This modification appears essential for the function of mature Pel with deletion of PelA resulting in aberrant biofilm formation (311, 313). Positively charged Pel cross-links extracellular DNA and interacts with anionic host-derived polymers such as mucin and hyaluronan (311). The PelB/PelC complex is reported to export Pel across the outer membrane, whilst PelD/PelE/PelG complex secretes Pel across the inner membrane (314-317).

The expression of Psl and Pel is intimately associated with intracellular c-di-GMP levels. Hyper-aggregative *P. aeruginosa* strains, such as rugose small colony variants (RSCVs) are commonly isolated from the cystic fibrosis lung (318). The aggregative phenotype is a result of mutation in the *wspF* gene, which results in elevated c-di-GMP and constitutive Pel and Psl hyper-production (319). The transcriptional flagella gene regulator FleQ, represses the Psl and Pel operons and is inhibited by elevated c-di-GMP (38). PelD, which activates Pel synthesis and secretion, binds and is allosterically regulated by c-di-GMP (320). The Gac TCS negatively regulates *psl* expression through binding and post transcriptional modification of *psl*-encoding

mRNA by RmsA (321). Additionally, quorum sensing networks govern Pel expression with decreased Pel secretion in Lasl and Rh1I mutants (322). Although many *P. aeruginosa* strains have the capacity to express both Psl and Pel, studies have demonstrated redundancy in their function (323). For example, in PAO1, Psl is the primary polysaccharide of the biofilm matrix, whilst deletion of *pel* does not affect biofilm formation. In contrast, PA14 does not produce Psl, with Pel being the major constituent of the biofilm matrix (311, 324).

1.4.2.4. Alginate

P. aeruginosa strains are commonly divided into mucoid or non-mucoid depending on their predominant extracellular polysaccharide. Non-mucoid strains primarily produce Pel and Psl, whilst mucoid strains primarily express alginate (297, 325). Mucoid isolates are frequently isolated from the cystic fibrosis lung as opposed to the external environment (326) where alginate promotes the formation of thick, highly structured biofilms in the lung and enhances immune and antibiotic evasion (327-331). Alginate is a negatively charged polymer consisting of non-repeating units of 1,4-linked L-guluronic and D-mannuronic acids, with O-acetylation normally at the 2, 3 position of the D-mannuronic residues (332, 333) (Figure 1.12C). Alginate is localised at both the cell surface and extracellular space where it displays high affinity for various divalent cations (e.g.: Ca^{2+}, Mg^{2+}) (296, 334).

The biosynthetic and secretion pathways of alginate are encoded by the *algD* operon and bear similarity to the synthase-dependent pathway (335, 336). AlgA, AlgC and AlgD contribute to precursor synthesis through phosphomannose isomerase, phosphomannomutase and GDP-mannose dehydrogenase activity respectively (337-339). Polymerization of poly-D-mannuronic acid is carried out by the inner membrane embedded proteins Alg8 and Alg44 (340, 341). The Alg8 protein is proposed as a synthase/glycosyltranferase given the presence of both transmembrane and cytoplasmic domains, whilst Alg44, a co-polymerase with a c-di-GMP-binding PilZ domain. Mutation of the PilZ domain results in abrogated alginate

production, supporting a role in c-di-GMP signalling in exopolysaccharide regulation (277). Periplasmic epimerization of poly-D-mannuronic acid is carried out by AlgG, resulting in the addition of L-guluronic acid to the C5 position (342). AlgI, AlgJ and AlgF are implicated in O-acetylation of mannuronic residues, with AlgI and AlgJ localised along the inner membrane and AlgF localised in the periplasm (343). AlgL is a lyase believed to degrade alginate in the periplasm and may regulate polysaccharide length (344). Once synthesized, the TPR-containing outer membrane protein AlgK directs the alginate polymer through the outer membrane protein, AlgE (279, 345). Alginate biosynthesis is controlled by a complex regulatory network which includes sigma factors AlgU (AlgT/σ^{22}) and RpoN (σ^{54}) (346), the FimS/AlgR (347), KinB/AlgB (348) and GacA/GacS (349) two component systems and c-di-GMP signalling (277, 350).

1.4.2.5. Capsular polysaccharide

Bacterial capsules are repetitive polysaccharide structures found on the outer surface of many bacterial species including *E. coli* (351), *Haemophilus influenzae (352)*, *Neisseria meningitidis* (353), *Salmonella typhi* (354) and *Klebsiella pneumoniae* (355). Capsules frequently serve as the interface between the host cell and environment and play a role in adherence (356, 357), desiccation resistance (358) and defence against host cell immunity (359-361). Bacterial capsules consist of repeating monosaccharide units bound by glycosidic linkages (Figure 1.12D,E). The constituent monosaccharides, branching, glycosidic linkages and substitutions vary greatly between capsular polysaccharides, resulting in a diverse range of structures and biochemical properties. For example, 80 capsular polysaccharides (K antigens) have been identified in *E. coli* (272). Capsular polysaccharides are divided into four classes dependent on gene organisation and assembly mechanism. Group 2 and 3 capsules are secreted via the ABC-transporter mechanism and group 1 and 4 capsules secreted by the Wzx/Wzy translocation complex (272, 362). ABC-translocated capsules associate with the

outer membrane in one of two ways. The *Escherichia coli* K1 capsule, composed of polysialic acid (PSA), is anchored to the outer membrane via a conserved phosphotidylglycerol-poly KDO lipid moiety associated with the reducing end of the polysaccharide (363). A second group of bacteria with ABC-translocated capsules, including the *Salmonella typhi* Vi antigen, utilize a modification of the lipid A pathway to anchor the polysaccharide (364). The *E. coli* group I K30 capsule is one of the best-studied examples of an exopolysaccharide secreted via the Wzy-dependent pathway. Wzi is believed to function as a lectin and bind K30 capsule on the cell surface (365).

1.4.2.6. Polysaccharide anchoring

Whilst the importance of exopolysaccharides in bacteria is well recognized (366), the mechanism by which exopolysaccharide adhesins (including holdfast) are anchored to cells remains incompletely characterized. The best studied and described anchoring systems are related to capsular polysaccharides. However, there is a growing list of bacterial species that have polarly expressed polysaccharide adhesins (367-370). Further, whilst many bacteria have Wzi-like proteins associated with their *wzy*-dependent polysaccharide loci, some bacteria do not, suggesting other uncharacterized mechanisms of polysaccharide anchoring remain.

1.4.2.7. Holdfast

C. crescentus is an aquatic alphaproteobacterium which exhibits a dimorphic cell cycle, characterised by change in cell shape and adhesin expression (371). During the *C. crescentus* lifecycle, free-living swarmer cells attach using flagella and type IV pili localised at a single pole (367) (Figure 1.13). Upon surface sensing, the flagellar pole of the swarmer cell undergoes differentiation, resulting in the assembly a polar cytoplasmic extension of the cell envelope known as the stalk. The stalked cell is reproductively mature, producing daughter swarmer cells which are dispersed into the environment through asymmetric division (Figure 1.13).

Stable attachment of *C. crescentus* to surfaces requires an adhesive polysaccharide known as the holdfast, localized at the tip of the stalk (265) (Figure 1.13). The holdfast possesses the highest tensile strength of any known biological or synthetic adhesive and demonstrates remarkable versatility in substrate binding (372). The holdfast is a complex, multi-layered structure comprised of a mixture of molecules including GlcNac polysaccharides and proteins and DNA whose identity remains unknown (372). Studies using atomic force microscopy nano-indentation have shown that the holdfast possesses a stiff core surrounded by a flexible polymeric brush layer (372). The outer brush layer is sensitive to proteinase K and DNase I treatment, however this treatment is insufficient to abolish adhesion or achieve complete removal of the brush layer (372). Therefore, the precise composition and structure of the holdfast remain unknown.

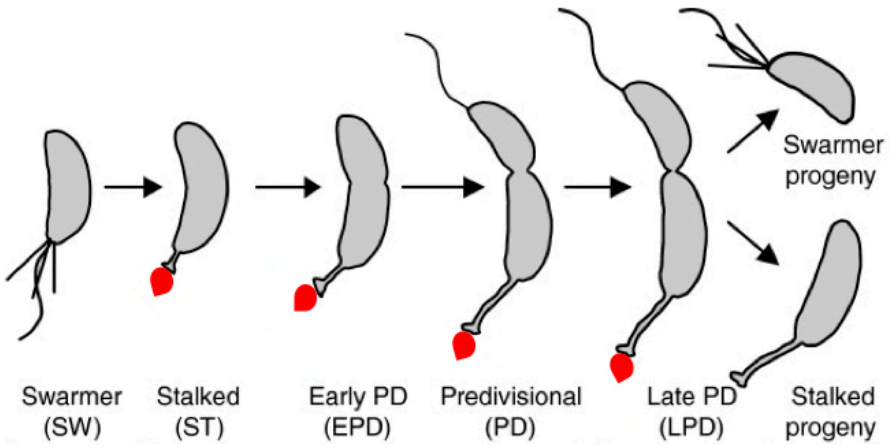


Figure 1.13: Overview of the *C. crescentus* cell cycle

The aquatic alphaproteobacterium, *C crescentus*, possesses a dimorphic lifecycle involving swarmer and stalked cells – each with distinct morphologies and adhesin expression. Free-living swarmer cells express flagella and type IV pili at a single cell pole and are devoted to dispersal. Flagella and type IV pili are downregulated upon surface sensing and replaced by the cylindrical stalk at the cell pole. The holdfast polysaccharide (red) is localised at the stalk tip and promotes irreversible adhesion. As stalked cells mature, asymmetric division occurs, resulting in swarmer and stalked progeny. Figure modified from Fang et al., 2013 (373).

The holdfast biosynthesis and secretion machinery are encoded by two major loci: *hfsEFGH* and *hfsDABC* and several unlinked genes (374-376). The *hfsEFGH* locus (Figure 1.14), as well as the unlinked genes *pssY*, *pssZ*, *hfsJ* and *hfsK*, encode a set of cytoplasmic proteins responsible for the synthesis and modification of the exopolysaccharide (376). The Wzy polysaccharide polymerase is encoded by *hfsC* and a paralog *hfsI*. The *hfsDAB* genes encode a secretion complex believed to span the inner and outer membrane of the *C. crescentus* cell envelope (Figure 1.14) which facilitates the translocation of holdfast from the cytoplasm to the bacterial cell surface (374). The HfsD, HfsA and HfsB proteins share homology to Wze, Wza and Wzc, suggesting holdfast may be modified and secreted in a Wzx/Wzy-dependent fashion.

Holdfast is anchored at the *C. crescentus* stalk tip via the holdfast anchor complex, encoded by the genes *hfaA*, *hfaB* and *hfaD* (375, 377-379) (Figure 1.14). In line with an anchor function, HfaA, HfaB and HfaD are enriched in the outer membrane of the cell and localized to the tip of stalks (377, 379). Further, deletion of any of the anchor proteins results in holdfast-shedding and decreased adherence and biofilm formation (377-379). HfaA shares similarity to the curli monomer, CsgA, and forms SDS and heat resistant multimers – consistent with the notion that they are amyloid-like proteins (377). HfaA multimer formation is dependent on the presence of HfaD, which shares limited sequence similarity to surface-layer proteins and other adhesins (380). HfaB shares similarity with the CsgG translocon, responsible for the secretion of CsgA across the outer membrane (116). The precise function of each anchor component is not known, although targeting of HfaA and HfaD to the outer membrane is reliant on HfaB suggesting that HfaB may form an outer membrane pore for their secretion (377). To date, the mechanistic details of how holdfast is anchored to the cell surface remain undescribed.

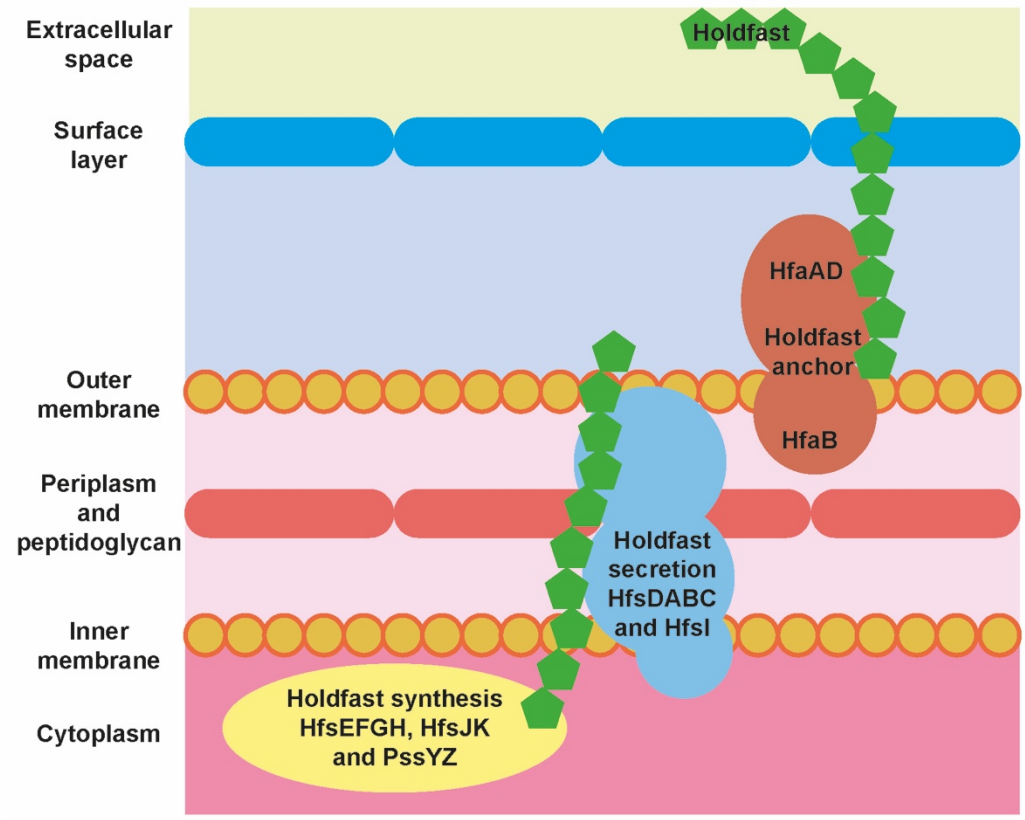


Figure 1.14: Schematic model of the *C. crescentus* holdfast synthesis, secretion, and anchor machinery.

The holdfast synthesis and polymerization machinery are comprised of proteins (PssY, PssZ, HfsEFGH, HfsJ, and HfsK) from several unlinked loci, all located in the cytoplasm or at the inner membrane of the cell. These proteins are responsible for manufacturing holdfast polysaccharide (green). The holdfast polymerases (HfsC and HfsI) and the holdfast secretion complex (HfsDAB) shuttle holdfast from the inner membrane and across to the outer membrane of the cell envelope. Holdfast polysaccharide is anchored on the cell surface by the holdfast anchor proteins (HfaABD). HfaB is located on the periplasmic side of the outer membrane, while HfaAD proteins are present on the outside.

1.4.2.8. Investigation of biological specimens using cryo-EM

Electron cryomicroscopy (EM) and electron cryotomography (cryo-ET) are imaging techniques which support high-resolution structural and cell biology investigations within bacterial cells (381). In these techniques, samples are frozen in a thin layer of vitreous ice and imaged at liquid nitrogen temperature, allowing preservation of cell ultrastructure. Electron microscopes generate high energy electrons at accelerating voltages of 200-300 kV and wavelengths of 2-4 picometers (pm, 10^{-12} m); generally through use of tungsten filaments or field emission guns. The electron beam is focused along the optical axis, to the sample of interest, through a condenser and objective electromagnetic lense series (382). As the atoms of proteins, macromolecules, organelles and cells encounter the electron beam, elastic and inelastic scattering events occur. These scattering events ultimately produce amplitude and phase contrast at the image plane (383). Elastically scattered electrons interact with the Coloumb potentials of the specimen, emerging phase-shifted at their original velocity. Inelastically scattered or 'noisy' electrons transfer energy to the sample resulting in radiation damage, and emerge at a reduced velocity (383). Phase contrast is produced by differences in the phase of elastically scattered electrons, interfered with each other and the unscattered electron beam. Amplitude contrast is produced as not all incident electrons reach the detector following scattering events. Unscattered and low-angle scattered electrons pass through the objective aperture of the microscope to the detector, whilst high-angle scattered electrons do not pass through the objective aperture or are removed by energy filters (382). Images are formed following detection using film, CCD cameras or direct electron detectors (384)

The three dimensional (3D) structure of targets of interest are studied using various EM methods including single particle analysis (SPA), helical reconstruction and cryo-ET. Based on the central slice theorem, the Fourier transform of a 2D projection image corresponds to a slice through a central region of the Fourier transform of a 3D object (385). In SPA, a large set

of 2D projection images are collected of the 3D object of interest. In cryo-ET, a set of 2D projection images are obtained at regular angular increments (tilt series) by tilting the specimen holder during image acquisition (386). In both methods, 2D projection images are inserted into 3D Fourier space based on the central slice theorem, from which a real-space 3D reconstruction is resolved by an inverse Fourier transform (Figure 1.15).

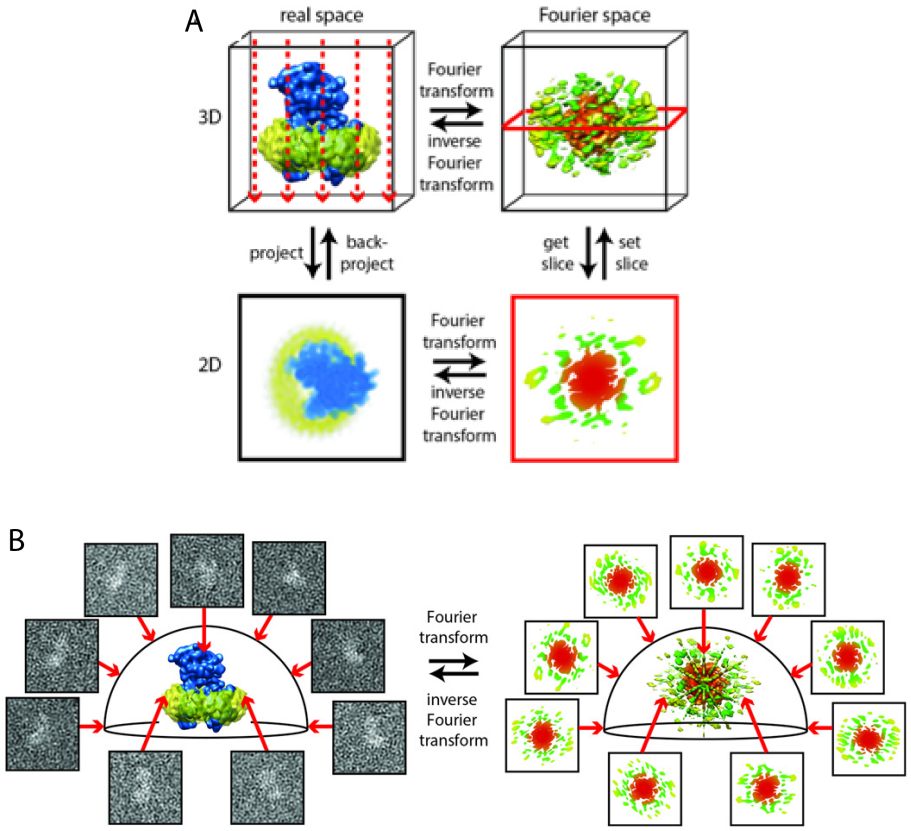


Figure 1.15: Basic concept of cryo-EM image reconstruction

(A) The central slice theorem states that a real space 2D projection image (left column) corresponds to a central slice (red box) in the Fourier transform of a 3D object (right column). (B) (Left) 3D reconstruction involves the collection of 2D projection images using cryo-EM, capturing various views of the target of interest. (Right) Based on the projection-slice theorem, 2D projection images correspond to a central slice of the Fourier transform of the object, defined by a unique set of amplitudes and phases. These images are then combined in Fourier space to obtain a 3D reconstruction of the original object by inverse Fourier transform. Figure adapted from Nogales and Scheres, 2015 (384).

Image processing workflows have been developed for the analysis of various cryo-EM datasets. These workflows generally include motion correction, alignment and classification, contrast transfer function (CTF) correction, 3D refinement and reconstruction (387). Motion correction accounts for the beam-induced motion experienced by samples during image collection; attributable to the radiation sensitivity of vitreous ice (388). Alignment and classification combats the low signal to noise ratio (SNR) exhibited by cryo-EM datasets by aligning and averaging the pixel intensities over several images. As particles are present in various orientations and conformations, algorithms have been developed to group similar particles prior to averaging (e.g.: regularized likelihood method in RELION) (389). Sub-tomogram averaging may also be applied to tomographic datasets in which 3D volumes containing particles of interest are extracted, aligned and averaged (390). The subsequent averages, with improved SNR, are then applied as references image for alignment during 3D reconstruction.

During image formation, elastic electron scattering produces phase shifts which are constructive, destructive or inverting. The effect on image formation can be described by a point spread function in real space or mathematically modelled by the CTF in reciprocal space (391) (Figure 1.16A, for mathematical formula). The CTF of a microscope is a sinusoidal function of spatial frequency, dependent on defocus and aberrations experienced by the objective lens. During data collection, the objective lens is often under-focused to improve image contrast (Figure 1.16A,B). Further, the objective lens is subject to spherical aberrations, chromatic aberrations and astigmatism (Figure 1.16A,B). CTF correction allows for information stored at weaker and phase flipped spatial frequencies to be retrieved, facilitating higher resolution reconstructions. Central to this process, is the fitting of theoretical CTFs to the power spectrum of an image based on known defocus values. Less reliable CTF fitting is experienced in cryo-ET datasets as compared to 2D cryo-EM datasets, given comparatively

lower dose per image, defocus gradients within individual images and specimen thickness. Cryo-ET datasets are hence corrected using a weighted 3D-CTF model. Here the 2D CTFs of tilt series images are placed into 3D Fourier space, with orientations determined by tilt angle. A weighted 3D CTF model is then generated in Fourier space by determining the per-particle defocus (using Z-coordinates of each particle and defocus values at each tilt) and dose-filtering (Figure 1.16C). Consideration of tilt angle between images, also allows for modelling of the missing wedge function (Figure 1.16C). As tomographic data collection is limited by tilt angle, images are generally collected between +60 and -60°. A missing wedge of information, stored at higher tilt angles, subsequently results in Fourier-space, which must be corrected to avoid artefacts during tomographic reconstruction.

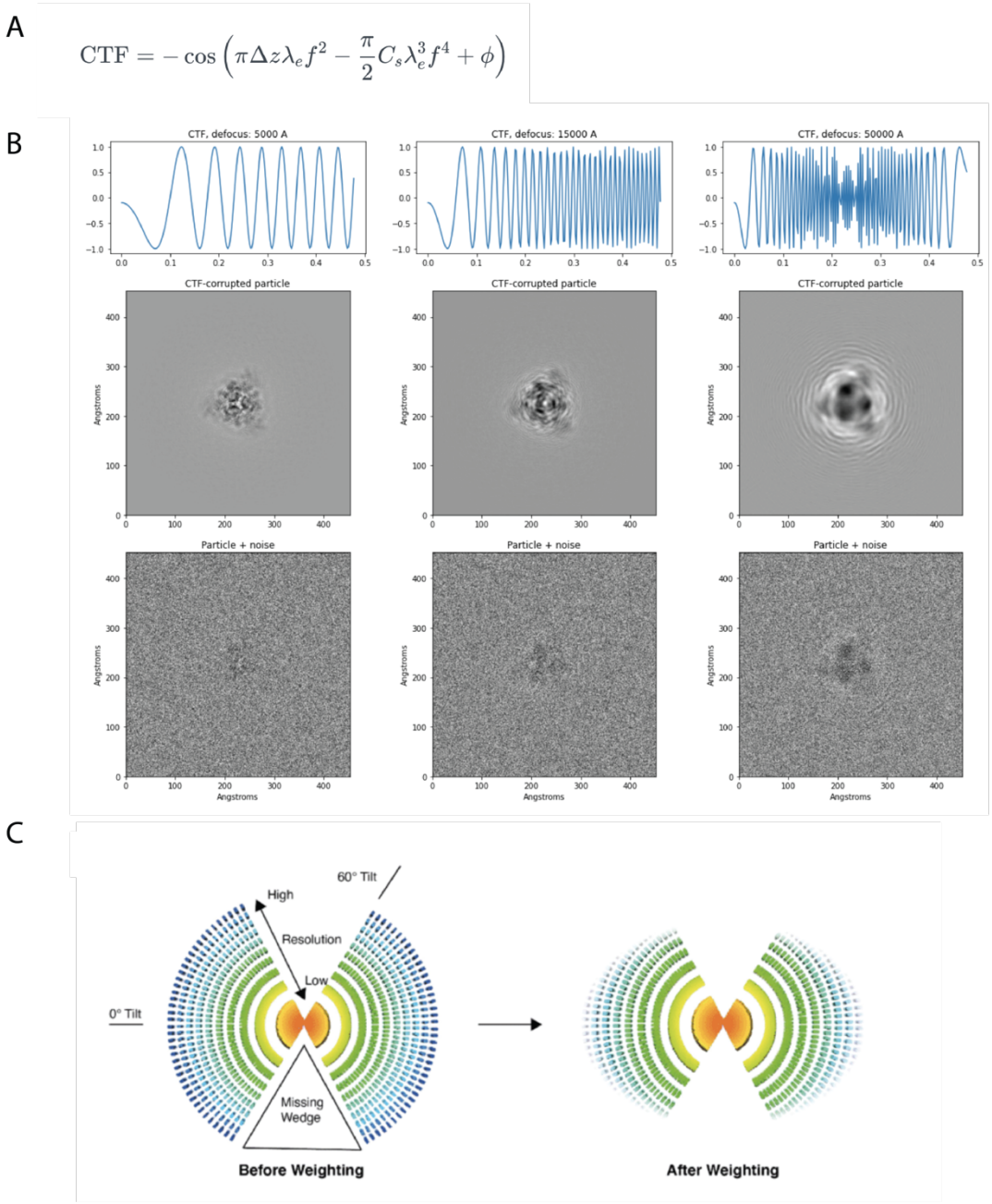


Figure 1.16: Correction of the contrast transfer function (CTF)

(A) Mathematical formula modelling the CTF where Δz is defocus, λ_e represents wavelength of incident electrons, C_s represents spherical aberration, ϕ represents phase shift factor and f represents spatial frequency. (B) (Top panel) Examples of CTF profiles at various defocus values. (Middle panel) The consequence of CTF on cryo-EM imaged particles at various defoci. Micrographs are shown without and (bottom panel) with noise, illustrating visible blurring of particles and variations in image contrast. (C) Central slice of a sub-tomogram 3D CTF model before (left) and after (right) CTF weighting, illustrating loss of high resolution information at higher tilt values. Images adapted from the CryoSPARC CTF estimation tutorial [Online] and Bharat and Scheres, 2015 (390).

Finally, the corrected and grouped images proceed onto 3D reconstruction and refinement. As noted previously, the central slice theorem allows the structure of 3D objects to be obtained by alignment of 2D projections images in Fourier space. The relative angle between projection images is generally determined using angular reconstitution (common line method) or template matching (reference based). Both methods are applied to 2D class averages given their higher signal and contrast. The common line method relies on the fact that 2D projections of a 3D object possess a common 1D line of amplitudes and phases (392). Whereas, template matching utilises a reference model for initial projection image generation, to which class averages are matched (393). For helical reconstructions, the imposition and refinement of helical symmetry parameters (rise and twist) is additionally applied (394). Reconstruction is an iterative process, involving cycles of re-projection, alignment and model generation until the final resolution is reached.

PROJECT AIMS

Adhesion to abiotic and biotic surfaces is essential for numerous bacterial developmental processes including biofilm formation (1). Stable attachment of bacteria to surfaces is facilitated by proteinaceous appendages such as pili, flagella and fimbriae, as well as extracellular polysaccharide adhesins such as holdfast (151). In this project, the CupE chaperone usher fimbriae of *P. aeruginosa* and the holdfast polysaccharide of *C. crescentus* were investigated as models of proteinaceous and polysaccharide-mediated adhesion respectively. How these appendages are assembled on the cell surface and contribute to adhesion were explored at the molecular and atomic level using structural biology methods, including electron cryomicroscopy (cryo-EM) and electron cryotomography (cryo-ET). In turn, this project aimed to resolve the structures of CupE fimbriae and the holdfast anchor using single particle-based helical reconstruction and direct cryo-ET imaging respectively. By doing so, this study provides insight into the fundamental processes and structures governing protein and polysaccharide-mediated adhesion in bacteria.

CHAPTER 2. METHODS AND MATERIALS

2.1. Bacterial strains and growth conditions

Bacterial strains and plasmids used in this study are listed in Table 2.1. *C. crescentus* and *Asticcacaulis* strains were grown in peptone-yeast-extract (PYE) medium (367) at 30°C, with antibiotic and carbon supplements at the following concentrations when appropriate: kanamycin (20 μg/ml [plate], 5 μg/ml [broth]). *H. balitca* was grown at 30°C in Marine Broth 2216 (BD Biosciences). *E. coli* strains were cultured at 37°C in Luria-Bertani (LB) medium. LB medium was supplemented with kanamycin (34 μg/mL) or ampicillin (100 μg/mL) where appropriate. All *P. aeruginosa* PAO1 strains were cultured at 37°C in liquid or agar LB medium without antibiotic.

2.2. DNA manipulations and sequencing

All primers used in this study (Table 2.2) were designed using the New England Biolabs (NEB) Builder Assembly tool [online] and purchased from Sigma-Aldrich (UK). PCR products were purified using Qiaquick spin columns (Qiagen). Chromosomal DNA was isolated using Promega Magic MiniPrep DNA purification system (Promega). Plasmids were assembled using the Gibson Assembly protocol using the commercial Gibson Assembly Kit (E5510, NEB) (395). Plasmids were purified using the Qiaprep Spin Miniprep Kit (Qiagen). The Q5 Site-Directed Mutagenesis Kit (EO554, NEB) was utilised for any site directed mutagenesis of plasmids. DNA sequencing was performed by Source Bioscience Sequencing (Oxford, UK). Sequencing data was analysed using ApE gene editing software (Utah, USA) (396). Chemically competent *E. coli* BL21 (DE3) or DH5α (C2987) cells (Table 2.1) were transformed using the heat shock method for plasmid overproduction and protein expression respectively. All commercial kits were utilised as per manufacturer's instructions.

2.3. *C. crescentus* sample preparation

For stalk preparations, *C. crescentus* strains were grown in peptone yeast extract (PYE) medium supplemented with 5 μg/mL kanamycin (except for CB15) at 30°C in a shaking incubator to an optical density (600 nm) of 0.5, before being plunge frozen onto cryo-EM grids. For rosette preparations, *C. crescentus* Abs2 (Table 2.1) was grown at 30°C in PYE medium for 3 days and rosette formation visually assessed using brightfield microscopy. A protocol was adapted to separate rosettes from cell bodies and free stalks using differential centrifugation (397). Briefly, upon observation of rosettes, cells were harvested at 17,000 rcf for 30 mins at 4°C. The pellet containing cell bodies was discarded and supernatant containing free stalks and rosettes centrifuged at 41,000 rcf for 1 hour at 4°C. The pellet, containing compacted rosettes, was incubated overnight at 4°C to encourage further stalk association. Rosettes were resuspended in 20 μL of PBS and screened using negative stain EM in 2% (w/v) uranyl acetate, before being plunge frozen onto cryo-EM grids. For mCherry-fused *C. crescentus* strains, cells were grown for 3 days to facilitate rosette formation, placed onto agar pads and imaged via light microscopy (Zeiss Axioimager).

2.4. Cryo-EM grid preparation

15 μL of liquid culture was mixed with 1μL of 10 nm protein-A gold fiducial beads (CMC Utrecht) and 2.5 μL applied to freshly glow-discharged 200 mesh Cu/Rh Quantifoil (3.5/1) grids. Grids were plunge-frozen into liquid ethane using a FEI Vitrobot (Mark IV) and stored in liquid nitrogen until cryo-EM or ET imaging.

2.5. Cryo-EM and cryo-ET data collection

Initial cryo-EM assessment of all samples was conducted on a FEI Talos Arctica 200 kV cryo-TEM fitted with Falcon 3 direct electron detector. For stalks, cryo-ET data collection was performed on Titan Krios microscopes operating at 300 kV (FEI/Thermofisher), each fitted

with a Quantum energy filter (slit width 20 eV) and a K2 direct electron detector (Gatan) running in counting mode with a dose rate of ~8 electrons/pixel/second at the camera level. Tilt series were collected between ±60º in two directions at a 1º increment using SerialEM (398). A total dose of ~121 $e^-/Å^2$ was applied, and data was sampled at pixel sizes of either 4.4Å or 4.2Å (scale bars are shown in each figure panel).

For rosettes, cryo-ET data collection was performed on the same Titan Krios microscope, now fitted with a K3 direct electron detector (Gatan), running in counting mode with a dose rate of ~7 electrons/pixel/second at the camera level. Tilt series were collected using a dose symmetric scheme between ±60º at 3º increments using SerialEM (398). A total dose of ~120 $e^-/Å^2$ was applied over the series, and data was sampled at a pixel size of 2.26 Å.

For CupE filaments, cryo-ET data collection was performed using the same K3-fitted Titan Krios microscope running in counting mode with a dose rate of ~11 electrons/pixel/second at the camera level. Tilt series were collected using a dose symmetric scheme between ±60º at 2º increments using SerialEM (398). A total dose of ~100 $e^-/Å^2$ was applied over the series, and data was sampled at a pixel size of 2.62Å. Cryo-EM datasets were collected at high throughput using the EPU software package on a Titan Krios microscope operating in counting mode at an unbinned, calibrated pixel size of 1.08Å. A combined total dose of approximately 43 $e^-/Å^2$ was applied with each exposure lasting 8s and 20 frames were recorded per movie. In total 2,367 movies were acquired between -1 to -3 μm defocus, across two independent sessions.

2.6. Image processing of stalk tips

Following data collection, contrast transfer function (CTF) parameters for each micrograph in the tilt series were estimated using CTFFIND4 (399). Tilt series alignment was performed using gold fiducial markers using IMOD (400). Gold fiducial densities were erased before CTF compensation within IMOD, followed by tomographic reconstruction using the Simultaneous Iterative Reconstruction Technique (SIRT) algorithm (400). Periodic sites along

the outer membrane of the *C. crescentus* stalk (containing visible anchor complex densities) were manually selected. A spline was fitted through each set of sites (MATLAB R2017b) and the in-plane rotation from the spline fit calculated for subsequent analysis as described previously (401). Briefly, sub-tomograms were extracted, collapsed onto a 2D image (402) along the fitted spline and subjected to two-dimensional averaging using regularized likelihood optimization in RELION2.1(403). Two-dimensional collapsed sub-tomograms from multiple *C. crescentus* stalk tips were averaged together. Averages were then mirrored across the horizontal and added with the mirror image in order to boost the signal to noise ratio, to produce the final averages shown. Final averages from different biological samples were then placed on the same spectral profile based on their individual power spectra (389) and the intensities in the average image were normalized to the intensity of the outer membrane. Due to the inherent variability between samples and different stalk tips, only the presence or absence of peaks in the line profiles were interpreted, rather than the absolute intensities.

2.7. Image processing of rosettes

Pre-processing of tilt series data was performed in the same manner as described in Section 2.6. To extract sub-tomograms, MATLAB R2017b scripts originally designed for extraction along the periphery of a sphere (adapted by Andriko von Kügelgen [DPhil student, Bharat Lab]) were customized in this work. In summary, two spheres were manually positioned in each tomogram using IMOD (400); with one sphere lining the outer membrane and the other sphere encompassing the HfaB density beneath the outer membrane. The coordinates corresponding to the region in which the two spheres intersected was then used as a cut-off to extract sub-tomograms. Sub-tomogram averaging was performed using the modified AV3 package (originally written and applied by Fredrich Förster) (404). Data was twice binned to generate the three dimensional average of the stalk envelope illustrated in Figure 3.9A. Sub-tomogram averaging was focused at the outer membrane for un-binned data to generate the

three-dimensional average illustrated in Figure 3.9B; with a particle box size of 60^3 pixels and a pixel size of 2.26 Å (reflected in scale bars).

2.8. Image processing of CupE filaments

For tilt-series data, pre-processing was performed in the same manner as described in Section 2.6. CupE filaments were selected manually within each tomogram using IMOD and their coordinates stored (400). Sub-tomogram averaging in RELION3.1 was performed using previously described workflows (402). Sub-tomograms were extracted (particle box size of 400^3 pixels), collapsed onto a 2D image and subjected to two-dimensional averaging using regularized likelihood optimization (403). The resulting 2D class averages were assessed and good classes (containing linear CupE filaments) selected. The resulting 2D classes were used to extract the corresponding subset of sub-tomograms using the python scripts (`relion_2Dto3D_star.py`) (402). A featureless cylinder was generated using the `relion_helix_toolbox` program (`--cylinder` function) to provide an initial reference for 3D refinement. Refinements were optimised as detailed in the results section. Helical symmetry was estimated from the final reconstruction using the `relion_helix_toolbox` program (`--search` function). The same filament coordinates were inputted for extraction and sub-tomogram averaging using the modified AV3 package (404).

For single particle data, movies were dose weighted and motion corrected using MotionCor2 (405). The CTFs of the resulting motion corrected micrographs were estimated using CTFFIND4.1 (406) and micrographs showing clear Thon rings retained. CupE filaments were auto-picked from micrographs and segments extracted along the filament (particle box size of 400^3 pixels). Segments were classified using reference-free 2D classification in RELION and classes demonstrating CupE filaments retained (246,558 particles). The cryo-ET determined helical symmetry parameters and corresponding 3D reconstruction were inputted

during 3D refinement in RELION3.1. CTF refinement, Bayesian polishing and B-factor sharpening were applied during post-processing. The resolution of the final reconstruction was estimated using the gold standard Fourier shell correlation (FSC) criterion of 0.143 (407). Densities were visualised using USCF chimera (408). Curved CupE filament classes were removed from the dataset using 2D classification and conformational heterogeneity explored using 3D classification as detailed in Section 4.6 and Figure 4.13.

2.9. Solubilization of HfaB inclusion bodies

E. coli BL21 (DE3) cells, transformed with pHIS17 *hfaB* plasmid (Table 2.1), were inoculated into LB+AMP liquid media (12L) and incubated at 37°C/180 rpm. Cells were induced with 1 mM IPTG at mid-log phase (OD_{600nm} 0.6) and incubated overnight at 18°C/180 rpm. Following overnight expression, cells were harvested and lysed at 4°C/15,000 psi. The pellet was harvested at 25,000 rcf for 20 mins at 4°C, then resuspended in 50 mM Tris-HCl pH 8.0, 2% (v/v) Triton X-100 to remove contaminating membranes. The inclusion bodies were harvested at 25,000 rcf for 20 mins at 4°C and washed twice in 50 mM Tris-HCl pH 8.0. The resulting pellet was placed in 25 mL of buffer containing 10 mM Tris-HCl pH 8.0, 250 mM NaCl, 6M guanidine hydrochloride and incubated at 4°C with gentle rolling overnight. Insoluble material was removed at 25,000 rcf for 20 mins at 4°C and the supernatant containing solubilised HfaB filtered using a 0.22 μm filter (Millipore). The solubilised material proceeded immediately onto purification and refold.

2.10. Purification and refold of monomeric HfaB

A protocol for purification and refold of monomeric HfaB was adapted from that developed for refold of OmpT from inclusion bodies of *E. coli* (167). In detail, filtered, solubilised HfaB was loaded onto a HisTrap nickel-nitrilotriacetic acid (Ni-NTA) column (GE Biosciences) and subjected to a linear gradient for purification. The wash buffer contained 20

mM Tris-HCl pH 8.0, 150 mM NaCl, 8M urea, 20 mM imidazole. The elution buffer contained the same base, supplemented with 500 mM imidazole. Protein concentration was determined using the Nanodrop spectrophotometer (Thermo Scientific), taking into consideration both the molecular weight and estimated extinction co-efficient (23505 M^{-1} cm^{-1} [Protparam]) of HfaB. 2-3 mg of affinity-purified HfaB was drop-wise added to a stirring beaker containing 50 mL of 20 mM Tris-HCl pH 8.0, 150 mM NaCl, 0.5% (w/v) lauryldimethylamine-N-oxide (LDAO) (Anatrace). The solution was incubated overnight at 4°C with gentle stirring to facilitate refolding. The solution was loaded onto a Ni-NTA column equilibrated with 20 mM Tris-HCl pH 8.0, 150 mM NaCl, 0.02% (w/v) *n*-dodecyl-β-D-maltopyranoside (DDM) (Anatrace). The protein was exchanged into DDM buffer and eluted using a linear gradient. The wash buffer contained 20 mM Tris-HCl pH 8.0, 150 mM NaCl, 0.02% (w/v) DDM. The elution buffer contained the same base, supplemented with 500 mM imidazole. Refolded HfaB was concentrated using a Vivaspin 20 (100,000 MWCO) membrane, snap frozen in liquid nitrogen and stored at -80°C until use. DDM-solubilised HfaB was submitted for protein identification (tandem and ESI mass spectrometry [MS]) at the Structural Genomics Consortium (University of Oxford). LDAO and C_8E_4-refolded HfaB were analysed using native MS by the Carol Robinson Lab (University of Oxford).

2.11. Tryptic digestion and tandem mass spectrometry (LC/MS-MS) (denaturing)

Sample processing and analysis were conducted by the Structural Genomics Consortium (University of Oxford). Gel bands were excised following SDS-PAGE, added to 200 µL of 50mM TCEP, 10% methanol (reducing buffer) and stored at 4°C for an hour. The reducing solution was removed and replaced with 200µ L of 100% acetonitrile for 5 minutes. The solution was replaced with 50 µL of 250 mM iodoacetamide, 100 mM ammonium bicarbonate pH 8.0 (alkylating buffer) and incubated in the dark at room temperature for 5 minutes. Alkylating buffer was substituted by 100% acetonitrile for 5 minutes. Buffer was then removed

and to each gel band 36μL of the endopeptidase working solution containing 1 μg trypsin in 25 mM ammonium bicarbonate added. Digestion proceeded at 50°C for 4 hours using a PCR Thermal Cycler (Biometra). Supernatants were transferred to a 96 well microplate and the reaction terminated by evaporation using a miVac DUO concentrator (Barnstead, GeneVac) at 56°C for 60 minutes. The solid digests were resuspended in 5μL of 0.1% formic acid and 2% acetonitrile.

Data were collected on a Dionex U3000 nano HPLC coupled to a Bruker AmaZon X ion trap mass spectrometer. The instrument parameters were set as follows: flow rate 2.5μL/min, positive ion enhanced resolution mode, 200 to 2000 m/z scan range, scan rate 8,1000 m/z/s, trap accumulation time 200msec and accumulation target of 350,000 counts. Data dependent peptide fragmentation was performed in auto MSMS mode. Compound extraction and peptide deconvolution was performed using the DA software package (Bruker Daltonik). Database searching was performed using the Mascot 2.5.1 search algorithm (MatrixScience).

2.12. Electrospray mass spectrometry (ESI-MS) (denaturing)

Sample processing and analysis were conducted by the Structural Genomics Consortium (University of Oxford). Prior to MS analysis, concentrated protein samples were diluted to 0.02 mg/mL in 0.1% formic acid. Data were collected on a 5μm Zorbax 300SB-C3 HPLC guard column (housed in an oven set at 40°C), coupled to 6530 ESI-QTOF mass spectrometer (Agilent Technologies Inc. USA). The ion source parameters were set as follows: capillary voltage at 4000V, nebulizer pressure at 60psig, drying gas at 350°C and drying gas flow rate at 12 L/min. The instrument ion optic voltages were as follows: fragmentor 250V, skimmer 60V, and octopole RF 250V. Data was analysed using the Masshunter Qualitative Analysis B.07.00 software package.

2.13. Native mass spectrometry

Sample processing and analysis were conducted by the Carol Robinson Lab (University of Oxford). Prior to native MS analysis, sample was buffer exchanged into 200 mM ammonium acetate pH 8.0 and twice the critical micelle concentration of detergent of interest (C8E4/LDAO) using Biospin-6 (BioRad) column. The sample was then introduced directly into the mass spectrometer using gold-coated capillary needles (prepared in-house, Carol Robinson Lab). Data were collected on a Q-Exactive UHMR mass spectrometer (ThermoFisher). The instrument parameters were set as follows: capillary voltage 1.2 kV, quadrupole selection from 1,000 to 20,000 m/z range, S-lens RF 100%, collisional activation in the HCD cell 200V, trapping gas pressure setting 7.5, temperature 200 °C, and resolution of the instrument 12,500. The noise level was set at 3 rather than the default value of 4.64. No in-source dissociation was applied. Data were analyzed using Xcalibur 4.2 (Thermo Scientific) software package.

2.14. Shearing and precipitation of CupE filaments

Lawn cultures of *P. aeruginosa* PAO1 strains were prepared on LB agar plates and incubated at 37°C overnight. Sterile PBS (2 mL) was pipetted onto agar plates and the adhered cells gently scraped from the surface using a cell spreader. The resuspended cells were collected into a 50 mL falcon tube and vortexed at maximum power for 1.5 min to shear surface organelles. Cells were separated from the supernatant fraction using two rounds of centrifugation at 16000 rcf for 5 mins at room temperature. The supernatant, containing sheared filaments, was precipitated by addition of 0.5M NaCl and 3% (w/v) polyethylene glycol (PEG) 6000 followed by incubation for 1 hr on ice. The precipitated proteins were harvested from the supernatant by centrifugation at 16000 rcf for 60 mins. The pellet, containing precipitated CupE filaments, was resuspended in 100 μL PBS or SDS-PAGE depending on the downstream application. Protein concentration was determined using the Nanodrop spectrophotometer

(Thermo Scientific). Sheared fractions were submitted for protein identification (tandem MS) at the Advanced Proteomics Facility (Biochemistry Department, University of Oxford).

2.15. Purification of recombinant CupA1

E. coli BL21 (DE3) cells, transformed with pETM11-*cupA1* plasmid (Table 2.1), were inoculated into LB+AMP liquid media (6L) and incubated at 37°C/180 rpm. Cells were induced with 1 mM IPTG at mid-log phase (OD_{600nm} 0.6) and incubated overnight at 18°C/180 rpm. Following overnight expression, cells were harvested and lysed at 4°C/15,000 psi. The suspension was centrifuged at 4°C/25,000 rcf/30 mins and supernatant filtered through a 0.45 μM filter (Millipore). The supernatant, containing crude solubilised CupA1, was loaded onto a HisTrap Ni-NTA column (GE Biosciences) and subjected to a linear gradient for purification. The wash buffer contained 50mM Tris-HCl pH 7.5, 150mM NaCl, 20mM imidazole. The elution buffer contained the same base, supplemented with 500mM imidazole. The N-terminal poly-histidine tag was removed by TEV protease digestion (4°C/overnight) and reverse nickel-affinity chromatography using the same buffers as previously. Contaminants were removed using gel filtration (wash buffer: 50mM Tris-HCl pH 7.5, 150mM NaCl) and ion exchange chromatography (wash buffer: 50 mM Tris-HCl pH 7.5, 150mM NaCl, elution buffer: same base, supplemented with 500mM NaCl). The CupA1 preparation was concentrated using a Vivaspin 20 (3000 MWCO) membrane and stored at -80°C until use. Protein concentration was determined using the Nanodrop spectrophotometer (Thermo Scientific), taking into consideration both the molecular weight and estimated extinction co-efficient (7575 M^{-1} cm^{-1} [Protparam]) of CupA1. Protein identification (tandem MS and ESI-MS) analyses were performed at the Advanced Proteomics Facility and Molecular Biophysics Facility (Biochemistry Department, University of Oxford).

2.16. Purification of polyclonal anti-CupA1 antibodies

The purified recombinant CupA1 protein (1.7 mg/mL) was submitted for antibody production (Davids Biotechnologie GmbH). Rabbit polyclonal anti-CupA1 antibodies were purified from the resulting crude anti-sera in-house using a HiTrap Activated NHS HP immuno-affinity chromatography column coupled with 1.3 mg of CupA1 protein as per manufacturer's instructions (GE Healthcare Lifesciences). A total of 316 μg polyclonal anti-CupA1 antibody was eluted from the column (final buffer: 150 mM Tris HCl pH 7.5, 50 mM NaCl, 30% (v/v) glycerol) and stored at -80°C until use. Protein concentration was determined using the Nanodrop spectrophotometer (Thermo Scientific).

2.17. Purification of recombinant CupE1

E. coli BL21 (DE3) cells, transformed with pETM44-*cupE1* plasmid (Table 2.1), were inoculated into LB+AMP liquid media (18L) and incubated at 37°C/180 rpm. Cells were induced with 1 mM IPTG at mid-log phase (OD_{600nm} 0.6) and incubated overnight at 18°C/180 rpm. Following overnight expression, cells were harvested and lysed at 4°C/15,000 psi. The suspension was centrifuged at 4°C/25,000 rcf/30 mins and supernatant filtered through a 0.45 μM filter (Millipore). The supernatant, containing crude solubilised CupE1-MBP-His, was loaded onto a HisTrap Ni-NTA column (GE Biosciences) and subjected to a linear gradient for purification. The wash buffer contained 50mM Tris-HCl pH 7.5, 150mM NaCl, 20mM imidazole, 20% (v/v) glycerol. The elution buffer contained the same base, supplemented with 500mM imidazole. Cleavage of the MBP-poly-histidine tag was trialled using either commercial HRV 3C protease (Pierce™ Thermo Scientific) or 3C protease purified previously in-house. Protein concentration was determined using the Nanodrop spectrophotometer (Thermo Scientific), taking into consideration both the molecular weight and estimated extinction co-efficient (18575 M^{-1} cm^{-1} [Protparam]) of CupE1.

2.18. SDS-PAGE and Western Blotting

Protein samples were loaded onto 4-12% denaturing sodium dodecyl sulphate-polyacrylamide (SDS-PAGE) gel and separated by electrophoresis. Gels were either stained with Coomassie Blue to visualise the resolved proteins or proceeded onto western blotting. For blots, gels were transferred onto an activated PVDF membrane (Immobilion®, Millipore) using the XCell II™ Western Blot transfer module (Invitrogen) as per manufacturer's instructions. Membranes were blocked overnight in Tris-buffered saline + 2% Tween20 (TBST) + 2% (w/v) skim milk powder at 4°C with slow rolling. Two polyclonal antibodies were raised against synthetic CupE1 peptides (NQWGTLDFGSHSDLTN and HASGGQRYMQNTTTTSE) and used for immunodetection at dilution of 1:5000 (Eurogentec). Polyclonal anti-CupA1 antibodies, raised and purified against recombinant CupA1 in this work, were utilised at a dilution of 1:50,000. A peroxidase-conjugated secondary antibody (goat anti-rabbit immunoglobulin HRP [Dako]) was used at a 1:20,000 dilution. HRP activity was activated using Amersham™ ECL Western Blotting Substrate (GE Healthcare Lifesciences) as per manufacturer's instructions, and chemiluminescence visualised on X-ray film using Amersham Imager 600 (Xograph).

2.19. Immunofluorescence Microscopy (IFM)

PAO1 strains were grown to mid-log phase as described (Section 2.1). Cells were harvested by centrifugation at 2000 rcf for 5 mins and resuspended in 1x PBS. A multi-test slide (Premium Grade, MP Biomedicals) was prepared by dispensing 0.1% (v/v) poly-D-lysine (10 µL) into each well and incubating for 2 mins. The wells were washed twice with pure water and allowed to dry. Cells were applied to the multi-test slide (10 µL) and incubated for 3 mins. The liquid was aspirated and wells washed 5 times with PBS. Anti CupE1 polyclonal antibodies (raised against NQWGTLDFGSHSDLTN and HASGGQRYMQNTTTTSE) were applied at varying concentrations (0, 1, 5, 10, 50 µg/mL, diluted in PBS + 0.1% [v/v] Tween 20) and

incubated for 2.5 hr in a humidified chamber. The wells were washed 5 times with PBS + 0.1% (v/v) Tween 20. Secondary antibody (Alexa-Fluor 488 Goat Anti-Rabbit IgG, Invitrogen) was diluted in PBS + 0.1% (v/v) Tween and added to each well. Slides were incubated for 1 hr in a humidified chamber (in the dark). Cells were washed 5 times in PBS + 0.1% (v/v) Tween 20, followed by 5 times in PBS only. The FM4-64 membrane stain (Invitrogen) was diluted in a 1:1 ratio of glycerol + PBS to a final concentration of 4 μg/mL. The membrane stain was added to each well and a clean coverslip sealed on top of the slide using nail polish. Microscopy was carried out using a Zeiss Axioimager microscope fitted with GFP and CY3 filter sets (green and red channels) for visualisation of the secondary antibody and FM4-64 fluorescence, respectively.

2.20. Crystal Violet Biofilm Assay

Biofilm formation upon 5mL polystyrene tubes and microtitre plates was assessed using the crystal violet assay, as described previously (409). A starter culture was grown overnight at 37°C in LB medium. Strains were then inoculated into 5 mL polystyrene tubes or microtitre plates at a 1:100 dilution and grown at 37°C under static conditions overnight. Following incubation, cells were removed by inversion and shaking, and washed twice in water. Tubes or plates were stained with 0.1% (w/v) crystal violet at room temperature for 10 mins, washed four times in water and inverted to dry overnight. Polystyrene tubes were photographed the following day. For microtitre plates, 30% (v/v) acetic acid was added to each well and incubated for 15 mins to solubilize the crystal violet stain. The absorbance was then quantified using a plate reader set at 550nm.

2.21. Growth of PAO1 biofilms at the air-liquid interface

Methods were adapted from those previously described by Xavier et al., 2009 (410). Square, glass coverslips (22x22mm) were mounted upon custom plastic slides (provided by Dr

Charlotte Melia [Bharat Lab]). Slides were submerged in 50 mL tryptone broth in Schott DURAN® bottles and angled so as to establish an air-liquid interface for study (Figure 5.5A,B). Strains were incubated for two days at room temperature under static conditions to allow biofilm formation. Following growth, coverslips were dismounted, washed gently in PBS to remove unadhered cells and imaged using a Zeiss Axioimager microscope.

2.22. Bacterial Strains and Plasmids

Table 2.1: Bacterial strains and plasmids used in this study.

Description of bacterial strains and plasmids used in this study is provided in this table.

Strain or plasmid	Description or construction	Source or reference
Strains		
E. coli		
BL21 (DE3) (200131)	Chemically competent BL21 (DE3) strain for protein over-expression (T7 expression)	Agilent
5-alpha *E. coli* (C2987)	Chemically competent *E. coli* strain for plasmid over-production (DH5α derivative)	NEB
C. crescentus		
CB15	Wild-type	Gail Hardy (367)
YB1109	CB15 NY111d1 is a clone that has the Abs phenotype (stalk abscission Abs2)	Gail Hardy (411)
YB2811	CB15 Abs2 *pstS*::miniTn5	Gail Hardy (412)
YB767	CB15N *pstS*::miniTn5	Gail Hardy (413)
YB7793	CB15 Abs2 *pstS*::miniTn5, Δ*hfsG*	Gail Hardy
YB7795	CB15 Abs2 *pstS*::miniTn5, Δ*hfsDAB*	Gail Hardy
YB7797	CB15 Abs2 *pstS*::miniTn5, Δ*hfaB*	Gail Hardy
YB8679	CB15 Abs2 *pstS*::miniTn5, Δ*hfaA*	Gail Hardy
YB8680	CB15 Abs2 *pstS*::miniTn5, Δ*hfaD*	Gail Hardy
YB8681	CB15 Abs2 *pstS*::miniTn5, Δ*hfaA*, Δ*hfaD*	Gail Hardy
YB4284	CB15 hfaB::pCHYC-1::hfaBmCherry	Gail Hardy
GH633	CB15 hfaE::pCHYC-1::hfaEmCherry	Gail Hardy
A. excentricus (YB258)	Wild-type	Gail Hardy
A. bisprothecum (YB5408)	Wild-type	Gail Hardy
H. baltica ATCC® 49814™ (YB5842)	Wild-type	Gail Hardy (414)
P. aeruginosa		
TBS037	PAO1 Δ*fliC*	Kevin Foster Lab
TBS140	PAO1 Δ*pilA*	Benoit-Joseph Levantie (Urs Jenal Lab)
TBS039	PAO1 Δ*pilA* Δ*fliC*	Eleni Manoli
TBS041	PAO1 Δ*mvaT* Δ*pilA* Δ*fliC*	Eleni Manoli
TBS054	PAO1 Δ*pilA* Δ*fliC* pBAD-*cupA (cupA1-A6)*	Eleni Manoli
TBS060	PAO1 Δ*mvaT* Δ*pilA* Δ*fliC* ΔPA2133	Eleni Manoli
TBS208	PAO1 Δ*mvaT* Δ*pilA* Δ*fliC* ΔPA2133::*p*PA2133 (plasmid complemented)	Kira Glatzel

TBS155	PAO1 Δ*mvaT* Δ*pilA* Δ*fliC* ΔPA2133 Δ*cupE1-E2*	Kira Glatzel
TBS179	PAO1 Δ*mvaT* Δ*pilA* Δ*fliC* ΔPA2133 Δ*cupA3*	Kira Glatzel
TBS206	PAO1 Δ*mvaT* Δ*pilA* Δ*fliC* ΔPA2133 Δ*cupE1-E2*::*cupE1-E2* (chromosomal complement)	Kira Glatzel
TBS209	PAO1 Δ*mvaT* Δ*pilA* Δ*fliC* ΔPA2133 *cupE5*-sfGFP (chromosomal tag)	Kira Glatzel
TBS159	PAO1 Δ*wspF*	Kevin Foster Lab
Plasmids		
pHIS-17 *hfaB* (TB053)	pHIS-17 parent vector containing codon optimised *hfaB* gene fragment without an N-terminal signal sequence	This study
pHIS-17 *hfaB* FL (TB054)	pHIS-17 parent vector containing the codon optimised, full length *hfaB* gene fragment	This study
pET22b(+) *hfaB* ser20 (TB059)	pET22b(+) parent vector containing the codon optimised *hfaB* gene fragment with site-directed mutagenesis of cysteine to serine at aa 20	This study (Angus Menzies)
pET22b(+) *hfaB* (Δ273-315) (TB060)	pET22b(+) parent vector containing the codon optimised *hfaB* gene fragment with deletion in C-terminal region between aa 273-315	This study (Angus Menzies)
pET22b(+) *hfaB* (Δ273-end) (TB075)	pET22b(+) parent vector containing the codon optimised *hfaB* gene fragment with deletion in C-terminal region from aa 273 onward	This study (Angus Menzies)
pET22b(+) *hfaB* OmpA (TB074)	pET22b(+) parent vector containing the codon optimised *hfaB* gene fragment and replacement of PelB signal sequence with OmpA signal sequence	This study (Angus Menzies)
pETM11 *cupA1* (TB007)	pETM11 parent vector containing the codon optimised *cupA1* gene fragment without the N-terminal signal sequence	This study (Abul Tarafdar)
pETM33 *cupA1* (TB008)	pETM33 parent vector containing the codon optimised *cupA1* gene fragment without the N-terminal signal sequence and GST tag	This study (Abul Tarafdar)
pETM44 *cupA1* (TB009)	pETM44 parent vector containing the codon optimised *cupA1* gene fragment without the N-terminal signal sequence and MBP tag	This study (Abul Tarafdar)
pETM11SUMO *cupA1* (TB038)	pETM11 parent vector containing the codon optimised *cupA1* gene fragments without the N-terminal signal sequence and SUMO tag	This study
pETDueT-1 *cupA1:cupA2* (TB031)	pETDuet parent vector containing codon optimised *cupA1* and *cupA2* gene fragments without the N-terminal signal sequences	This study

pMA-RQ *cupE1* (TB031)	PMA-RQ parent vector containing the codon optimised *cupE1* gene fragment without the N-terminal signal sequence	This study
pETM11SUMO *cupE1* (TB039)	pETM11SUMO parent vector containing the codon optimised *cupE1* gene fragment without the N-terminal signal sequence and SUMO tag	This study (Cara Press)
pETM44 *cupE1* (TB043)	pETM11SUMO parent vector containing the codon optimised *cupE1* gene fragment without the N-terminal signal sequence and MBP tag	This study (Cara Press)

Table 2.2: Oligonucleotides used in this study

Oligonucleotide sequences used in this study are listed in this table

Oligo Name	**Sequence (5' - 3')**	**Application**
FhfaupA	GCGATCACGAAGCTTACGAGGTAG	*hfaA* in-frame deletion
RmhfadownA	GGCGTCAATGAATTCCGAGCGGAT	*hfaA* in-frame deletion
FhfaupD	GGCATCACCAAGCTTAACTACAAC	*hfaD* in-frame deletion
RmHfadownD	GCGGCCTGGGAATTCTAGTCCTGA	*hfaD* in-frame deletion
FupSphhfsG	CTGCCCGCATGCGTCGGCCTC	*hfsG* in-frame deletion
RdwnBamHihfsG	GTTGAGATCGGATCCGTAGGTGAT	*hfsG* in-frame deletion
hfsDHindend	GATCAGCTTAAGCTTCTCCTCAGG	*hfsDAB* in-frame deletion
hfsBHindend	TCCATAGCCAAGCTTAGGCGCCGG	*hfsDAB* in-frame deletion
FhfaBup	GCCTTCACGCCGGGATCCAACAATCTGGGA	*hfaB* in-frame deletion
RmHfadownB	CACGTTGGCGAATTCCGACTGGCT	*hfaB* in-frame deletion
HfaBpHISFor	TTTAAGAAGGAGATATACATATGATGGTTAAACGTACCGGTG	*hfaB* insertion with signal sequence
HfaBpHISRev	TAATGATGATGATGATGATGGGATCCGTAACGACCACGTTTAGC	*hfaB* insertion with signal sequence
HfaBpHIS22For	TTTAAGAAGGAGATATACATATGTCTACCCCGGTTGCTTCTAC	*hfaB* insertion
HfaBpHIS22Rev	TAATGATGATGATGATGATGGGATCCGTAACGACCACGTTTAGCG	*hfaB* insertion
HfaBpet22For	CTGCCCAGCCGGCGATGGCCTGCGGTTCTACCCCGGTTG	*hfaB* insertion
HfaBpet22Rev	CAGTGGTGGTGGTGGTGGTGGTAACGACCACGTTTAGCGTC	*hfaB* insertion
HfaBserQ5For	GGCGATGGCCTCTGGTTCTACCCCG	cys to ser aa substitution
HfaBserQ5Rev	GGCTGGGCAGCGAGGAGC	cys to ser aa substitution
HfaB273295For	GACGACCCGTCTCGTTGG	273-295 aa deletion
HfaB273295Rev	GTTAGCAGCCATTTCAACGG	273-295 aa deletion
HfaB273endFor	CACCACCACCACCACCAC	273-end aa deletion
HfaB273endRev	GTTAGCAGCCATTTCAACGG	273-end aa deletion
HfaBOmpAFor	CTGGCTGGTTTCGCTACCGTTGCTCAGGCTTGCGGTTCTACCCCGGTT	OmpA signal sequence insertion

HfaBOmpARev	AGCAACAGCGATAGCGATAGCGGTTTTTT TCATATGTATATCTCCTTCTTAAAGTTAAA CAAAATTATTTCTAG	OmpA signal sequence insertion
CupA1pETM11For	CCCACTACTGAGAATCTTTATTTTCAGGGC GCAAACACTATCACATTCAGCG	*cupA1* insertion
CupA1pETM11Rev	CCGAACCGCCGCCGCCATGGCTCACTCGT AACGCAGCGT	*cupA1* insertion
CupA1pETM33For	GGAAGTTCTGTTCCAGGGGCCCGCAAACA CTATCACATTCAGCG	*cupA1* insertion
CupA1pETM33Rev	CGGATCCGGTACCTCATTAGTCCATTCACT CGTAACGCAGCGT	*cupA1* insertion
CupA1pETM44For	GGAAGTTCTGTTCCAGGGGCCCGCAAACA CTATCACATTCAGCG	*cupA1* insertion
CupA1pETM44Rev	CGGATCCGGTACCTCATTAGTCCATTCACT CGTAACGCAGCGT	*cupA1* insertion
CupA1pSUMO For	TCCTCGCCCTTGCTCACGGATTATTCGTAA CGCAGGGTG	*cupA1* insertion
CupA1SUMO Rev	TCCAGCAACAGACCGGTGGAGCTAACACC ATCACCTTC	*cupA1* insertion
CupA1pETDuet-1For	TATAAGAAGGAGATATACATATGGCAAACA CTATCACATTCAGCG	*cupA1* insertion
CupA1pETDuet-1Rev	GATATCCAATTGAGATCTGCTCACTCGTAA CGCAGCGTG	*cupA1* insertion
CupA2pETDuet-1For	TAAGAAGGAGATATACCATGAGCGTGGTG GTGACCGGG	*cupA2* insertion
CupA2pETDuet-1Rev	TGTGGTGATGATGGTGATGTGGCGATAGGT CATGACGGATATC	*cupA2* insertion
CupE1SUMOFor	CAACAGACCGGTGGAGCTGGTACCCTGAT CGGTC	*cupE1* insertion
CupE1SUMORev	GCCCTTGCTCACGGATTACCAAGCGATGGT AACC	*cupE1* insertion
CupE1pET44For	AAGTTCTGTTCCAGGGGCCCGCTGGTACC CTGATCGGT	*cupE1* insertion
CupE1pET44QRev	CCGGTACCTCATTAGTCCATTTACCAAGC GATGGTAACCAG	*cupE1* insertion

CHAPTER 3 AIMS

This project aimed to study the arrangement and organization of the holdfast anchor complex utilising electron cryotomography (cryo-ET) and sub-tomogram averaging, which support high-resolution structural and cell biology investigations within bacterial cells (91, 415). By examining a series of holdfast synthesis, secretion, and anchor complex mutants, this study provides insights into the molecular machinery involved in holdfast anchoring in *C. crescentus* cells, establishing the basis for future structural and cell biology studies on bacterial polysaccharide-mediated adhesion. Specifically, the project aims were as follows:

(i) Direct *in situ* imaging of *C. crescentus* cells to determine the composition and architecture of the holdfast anchor complex using cryo-ET and sub-tomogram averaging.

(ii) *In vitro* reconstitution of identified holdfast anchor components to provide insight into the atomic structure of the holdfast anchor complex and to support *in situ* findings

(iii) Comparison of polysaccharide mediated adhesion across other bacterial species encoding putative holdfast anchors using cryo-EM including *Asticcacaulis* and *Hirscha* spp.

A portion of results relevant to this chapter are published in Sulkowski and Hardy *et al*., *Journal of Bacteriology*, 2019.

CHAPTER 3. RESULTS

3.1. The holdfast anchor complex is associated with the outer membrane

To understand the architecture and arrangement of the holdfast on the surface of cells and to study how it is anchored at the cell envelope, a series of *C. crescentus* CB15 mutants were imaged using cryo-ET. First, wild-type CB15 *C. crescentus* cells were grown to mid-log phase in PYE medium and imaged (Materials and Methods). It is established that holdfast polysaccharide localises at the tip of *C. crescentus* stalks (265). In line with this, inspection of cryo-tomograms revealed a diffuse holdfast density at the stalk tip (Figure 3.1A, red arrowhead), which protrudes through the S-layer into the extracellular milieu.

To increase the abundance of stalk tips on cryo-EM grids, a stalk shedding mutant was utilized (CB15 NY111d1 or Abs2, Table 2.1). This strain lacks a periplasmic phosphate-binding protein required for phosphate uptake, promoting the formation of long stalks in rich medium (411, 412). Stalks were then purified away from the larger, thicker cell bodies, increasing the number of stalk tips available for imaging (Materials and Methods). In many tomograms, multiple stalks were attached to each other via the holdfast density, forming rosette structures (Figure 3.1B,C) characteristic of the *Caulobacter* species (416). The holdfast appears to be a complex, multi-layered structure with visible granularity (Figure 3.1A, blue arrows), in agreement with previous data (372).

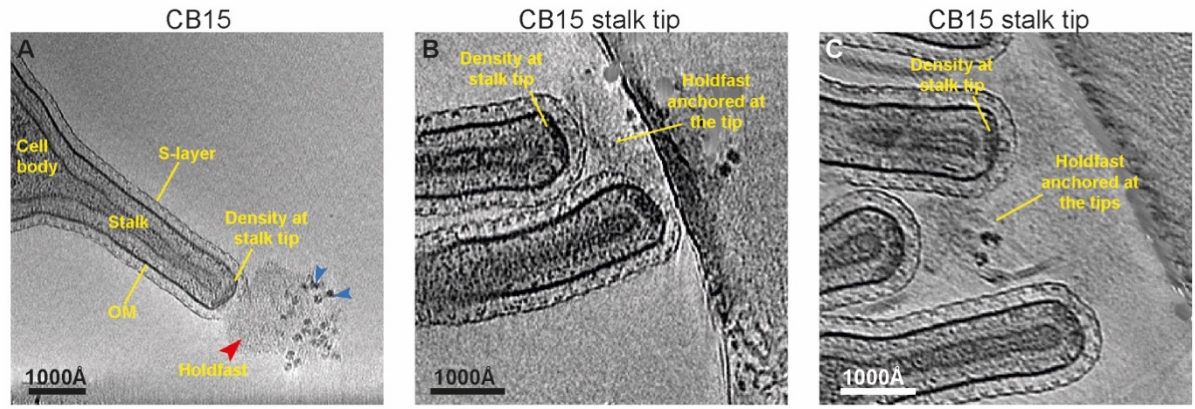


Figure 3.1: Identification of the cryo-EM density corresponding to the holdfast anchor complex.

(A) A virtual slice through a tomogram of a *C. crescentus* CB15 cell. The holdfast (red arrowhead) is visible near the stalk tip, where it appears to be anchored to a density directly beneath the outer membrane (marked). The holdfast displays visible granularity (blue arrows). (B-C) Magnified view of CB15 stalk tips illustrating the presence of the holdfast anchor complex together with the holdfast.

The holdfast density appeared to emanate from a thick, dense region situated on the periplasmic side of the outer membrane of the stalk tip (Figure 3.1A-C). In single cryo-ET slices, this cryo-EM density spanned the majority of the width of the hemispherical stalk tip, coating it uniformly. The holdfast was attached to the stalk tip of all cells possessing the cryo-EM density beneath the outer membrane (Table 3.1). Therefore, the dense region is likely the site of a complex that anchors the holdfast to the cell surface (377).

Table 3.1: Occurrence of anchor and holdfast densities in tomograms.

The stalk tips of *C. crescentus* strains in electron cryotomograms were assessed for the presence of the anchor complex density and the holdfast polysaccharide. The percentage of stalk tips with the densities present is reported in the table.

Strain	Anchor density at stalk tip (%)	Holdfast polysaccharide density (%)
CB15 (YB2811)	94 (n=18)	94 (n=18)
Δ*hfsG* (YB7793)	96 (n=27)	0 (n=27)
Δ*hfsDAB* (YB7795)	0 (n=19)	0 (n=19)
Δ*hfaB* (YB7797)	6 (n=51)	0 (n=51)
Δ*hfaA* (YB8679)	100 (n=6)	17 (n=6)
Δ*hfaD* (YB8680)	84 (n=6)	0 (n=6)
Δ*hfaAD* (YB8681)	93 (n=15)	20 (n=15)

3.2. Determinants of holdfast anchor complex assembly at the outer membrane

Holdfast biosynthesis and secretion are encoded by two major loci - *hfsEFGH* and *hfsDAB* (380), while the *hfaABD* genes are required for anchoring holdfast to the cell envelope (377). To determine if the cryo-EM density beneath the outer membrane was attributable to the anchor complex rather than the secretion complex or the base of the holdfast (i.e. to assign density to molecules), deletions in genes contributing to holdfast production were re-generated in the *C. crescentus* CB15 Abs2 background strain (Table 2.1). The effect of the mutations on cellular ultrastructure was then observed using cryo-ET. This included strains with deletions of holdfast synthesis and secretion genes (*hfsG, hfsDAB*), as well as the holdfast anchor genes (*hfaA, hfaB, hfaD*).

First, to determine if the cryo-EM density at the stalk tip is present in the absence of the holdfast, a *hfsG* deletion strain was imaged. Cells lacking HfsG, a putative cytoplasmic glycosyltransferase, are unable to synthesize the holdfast polysaccharide (376). Previous studies have shown that the holdfast anchor is retained at the stalk tip of a Δ*hfsG* deletion strain (417). In line with this, deletion of *hfsG* led to a loss of holdfast at the stalk tip, while the cryo-EM density beneath the outer membrane was retained (Figure 3.2A-C, Table 3.1). This

confirmed the periplasmic cryo-EM density is distinct from the holdfast itself and is most likely part of the holdfast anchor complex. Next, a mutant lacking the entire *hfsDAB* operon was imaged. The HfsDAB protein complex is predicted to span the inner and outer membrane of *C. crescentus* and is responsible for the translocation of holdfast polysaccharide to the cell surface (374). Both the holdfast and the cryo-EM density underneath the outer membrane were lost in the Δ*hfsDAB* mutant (Figure 3.2D-F, Table 3.1). These results confirm the previous observation that the HfsDAB proteins are important for correct localization of the holdfast anchor complex (377, 417) and suggest HfsDAB may contribute to the cryo-EM density beneath the outer membrane.

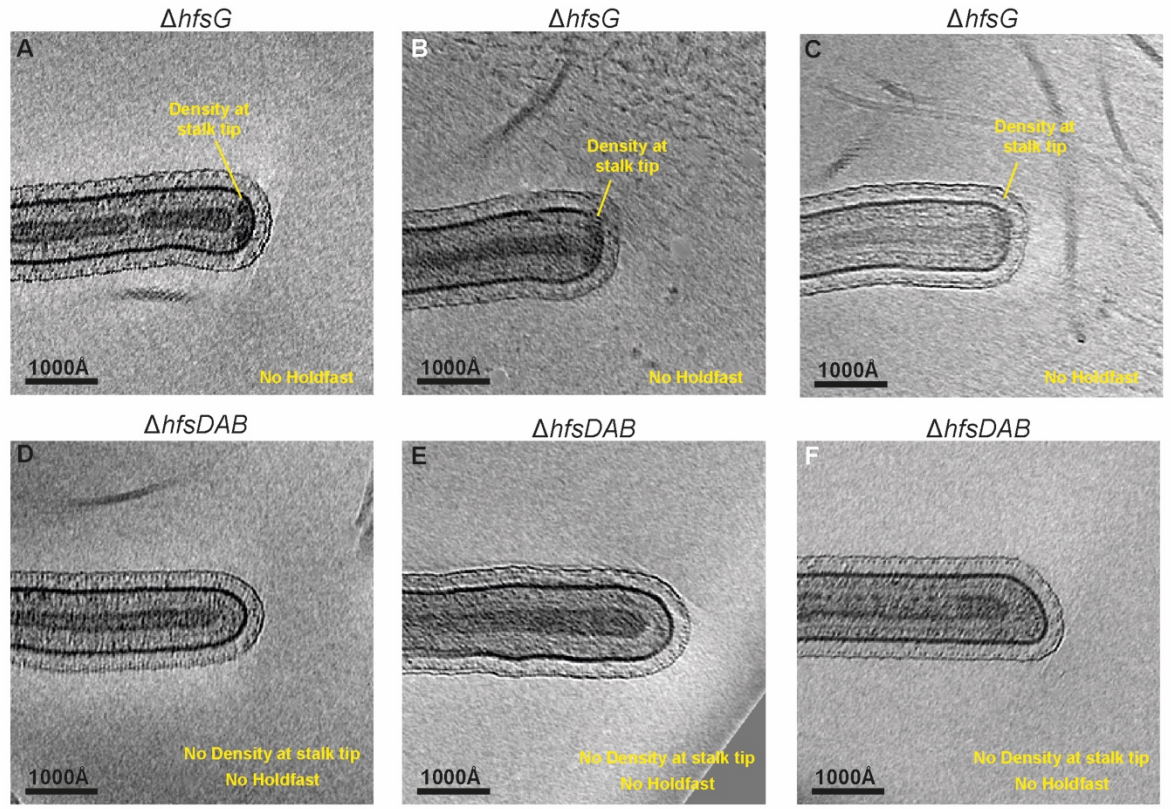


Figure 3.2: The anchor complex assembly is present beneath the outer membrane, independent of synthesis machinery, and depends on the holdfast secretion proteins (HfsDAB).

(A-C) The cryo-EM density beneath the outer membrane is observed in cells deficient in holdfast synthesis (Δ*hfsG*), indicating it does not consist of polysaccharide, but rather a molecular complex associated with the holdfast. (D-F) Deletion of the holdfast secretion genes, *hfsDAB,* leads to a complete loss of both the density underneath the outer membrane, as well as the holdfast polysaccharide.

To explore which of the holdfast anchor proteins (HfaA or HfaB or HfaD) contribute to the cryo-EM density beneath the outer membrane, a panel of *hfaABD* deletion mutants were imaged. These *hfa* mutants are able to synthesize holdfast normally, however have reduced ability to retain holdfast at the cell surface, causing shedding into the medium (377). As expected, the holdfast was poorly retained at the stalk tips of all *hfa* deletion strains, confirming these anchor proteins are required for holdfast retention (Figure 3.3A-L, Table 3.1). Furthermore, cryo-ET revealed the anchor density is retained beneath the outer membrane of single anchor mutants, Δ*hfaA,* Δ*hfaD*, and the double anchor mutant, Δ*hfaAD* (Figure 3.3A-I,

Table 3.1). The cryo-EM density beneath the outer membrane of these strains possessed the same microscopic appearance as that seen in wild-type CB15 stalk tips (Figure 3.1A-C). To investigate whether deletion of Δ*hfaA,* Δ*hfaD* or Δ*hfaAD* results in subtle changes in localization, the average coverage of cryo-EM density along the width of the stalk of wild-type CB15 and Δ*hfaA,* Δ*hfaD,* Δ*hfaAD* strains was measured. No significant difference between strains was observed (average coverage: 57.6%, p-value 0.99), reaffirming these proteins are not the major component of the cryo-EM density on the periplasmic side of the outer membrane. In contrast, the density beneath the outer membrane was completely lost in the Δ*hfaB* mutant (Figure 3.3J-L, Table 3.1). Collectively, these findings suggest the density on the periplasmic side of the outer membrane is comprised primarily of the holdfast anchor protein HfaB, or HfaB in complex with the holdfast secretion machinery, HfsDAB.

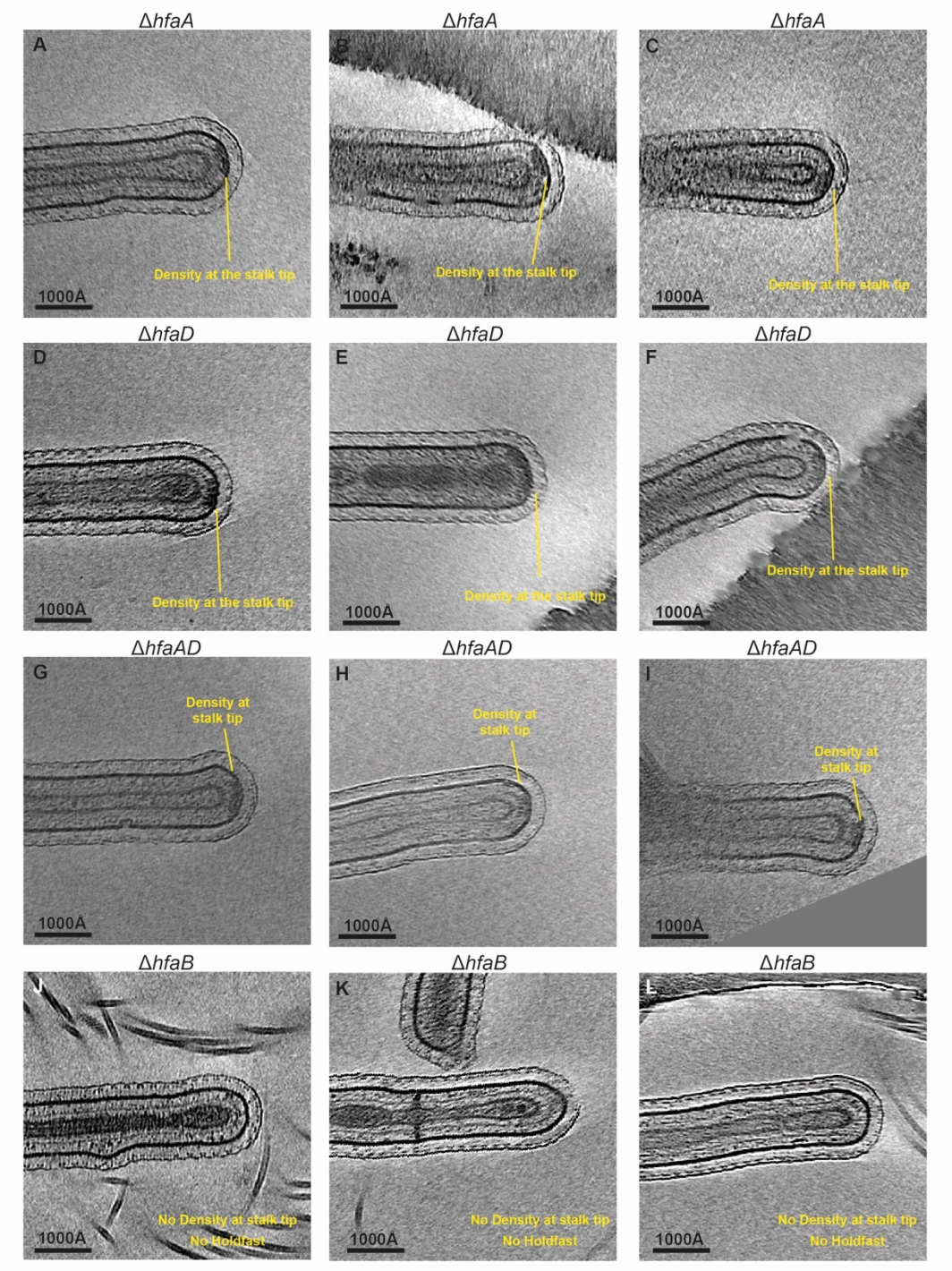


Figure 3.3: The anchor complex assembly is primarily comprised of HfaB.

(A-I) The anchor complex density is observed in stalk tips of the deletion mutants Δ*hfaA,* Δ*hfaD* and Δ*hfaAD*. (J-L) A strain with deletion of the holdfast anchor gene, *hfaB,* shows loss of the density underneath the outer membrane at the stalk tip.

3.3. The holdfast anchor complex spans the cell envelope.

To understand the architecture of the holdfast anchor complex, cryo-electron tomograms of anchor-complex-lacking (Δ*hfaB*) and anchor-complex-containing (Δ*hfsG*) strains (Figure 3.4A,B) were analysed using sub-tomogram averaging (Materials and Methods). Regions of tomograms containing the anchor complex density were selected manually. Periodic and overlapping sub-tomograms along the outer membrane of the cell stalk were extracted (401, 415). The extracted sub-tomograms were rotated to vertical orientation using the angle between successive overlapping sub-tomograms, in order to improve the accuracy of alignments in the analysis. Extracted sub-tomograms were collapsed onto a 2D image, and then aligned and averaged using a regularized likelihood algorithm implemented in the RELION software (402, 403). The accuracy of alignment was judged by carefully inspecting the class averages as well as by inspecting the Euler angles assigned to individual sub-tomograms.

Class average images showed distinct peaks in the density corresponding to the outer S-layer lattice, inner S-layer domains, the outer membrane, and the peptidoglycan layer in both the Δ*hfaB* and the Δ*hfsG* mutants (Figure 3.4C-D). The distance between the outer S-layer lattice and outer membrane was 230 Å, in agreement with previous tomographic studies of the *C. crescentus* cell envelope (418). Thus, the distance between the S-layer and outer membrane of the cell envelope was unaffected by the presence or absence of the holdfast anchor complex. Further inspection of sub-tomogram class averages revealed a strong density lining the periplasmic side of the outer membrane in the Δ*hfsG* mutant (Figure 3.4E, blue curve), corresponding to the periplasmic portion of the holdfast anchor complex. As expected from visual inspection of the raw data, these densities were absent underneath the outer membrane of Δ*hfaB* mutant (Figure 3.4E, red curve).

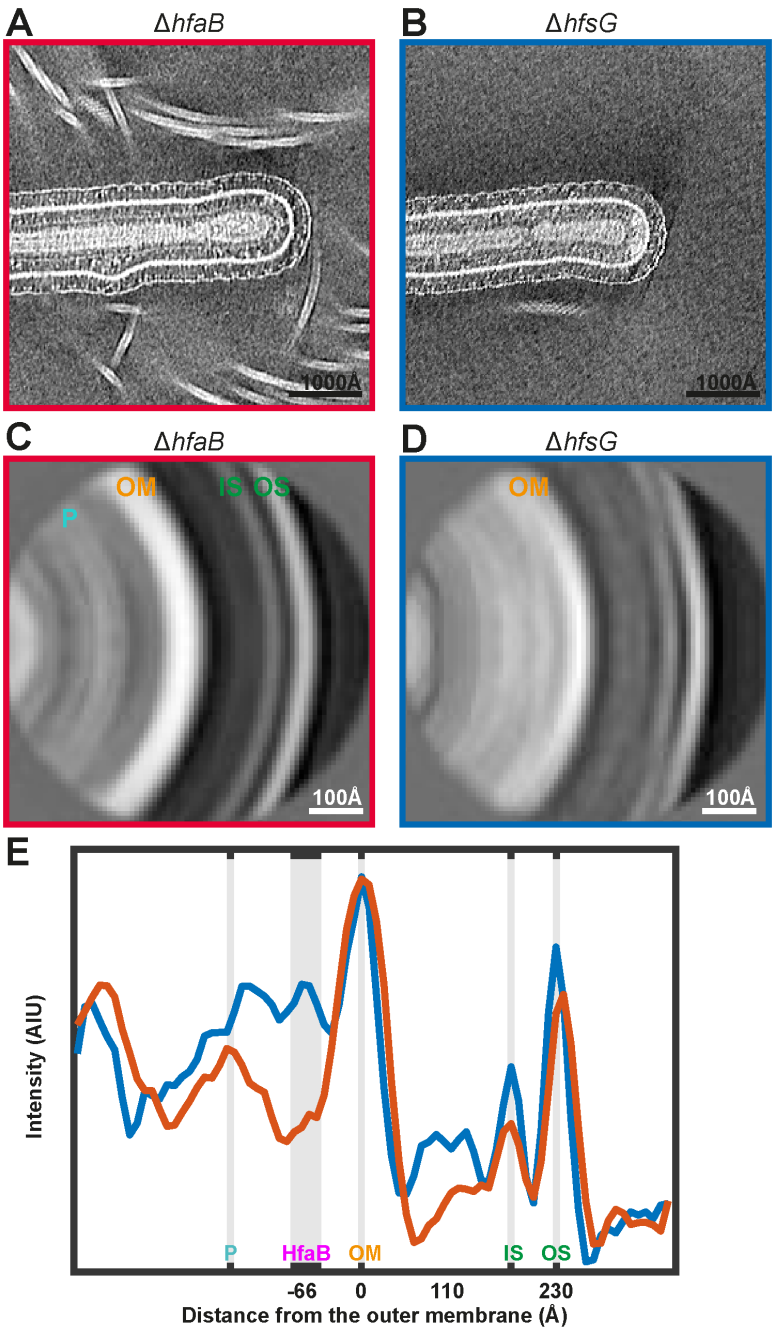


Figure 3.4: Comparison of stalk tips with and without the holdfast anchor complex.

(A) Inverted cryo-EM imaging of the stalk tip of the Δ*hfaB* strain that lacks the anchor complex. (B) Inverted cryo-EM imaging of the stalk tip of the Δ*hfsG* strain that possesses a visible anchor complex. (C-D) Sub-tomogram averaging analysis of tips without and with the anchor complex. The density layers corresponding to the outer S-layer (OS), inner S-layer (IS), outer membrane (OM) and peptidoglycan (P) have been marked. (E) Plots of the pixel intensity across the sub-tomogram averages, for the Δ*hfaB* (red curve) and the Δ*hfsG* (blue curve) strains. The outer S-layer, inner S-layer, outer membrane and peptidoglycan have been marked as in panel C. The density underneath the outer membrane corresponding to HfaB has also been marked.

As a further control, sub-tomogram averaging was performed on Δ*hfsDAB* stalks that also lack the cryo-EM density underneath the outer membrane to test whether this strain phenocopies the Δ*hfaB* mutant. Inspections of tomograms revealed that Δ*hfsDAB* stalks, in contrast with Δ*hfaB* (Figure 3.5A), displayed slightly deformed stalk tip morphologies, forming narrower, tapered, and cone-shaped stalk tips in many instances (Figure 3.5B-D). The consequence of aberrant stalk morphology is evident in the final class average where the outer membrane curvature in the Δ*hfsDAB* mutant is greater (Figure 3.5F) than that of the Δ*hfaB* mutant (Figure 3.4E). The variation in membrane curvature limits application and comparison of the Δ*hfsDAB* mutant with Δ*hfaB* using sub-tomogram averaging. Change in stalk morphology upon Δ*hfsDAB* deletion suggests the secretion complex plays a role in stabilising structures at the outer membrane of the stalk tip.

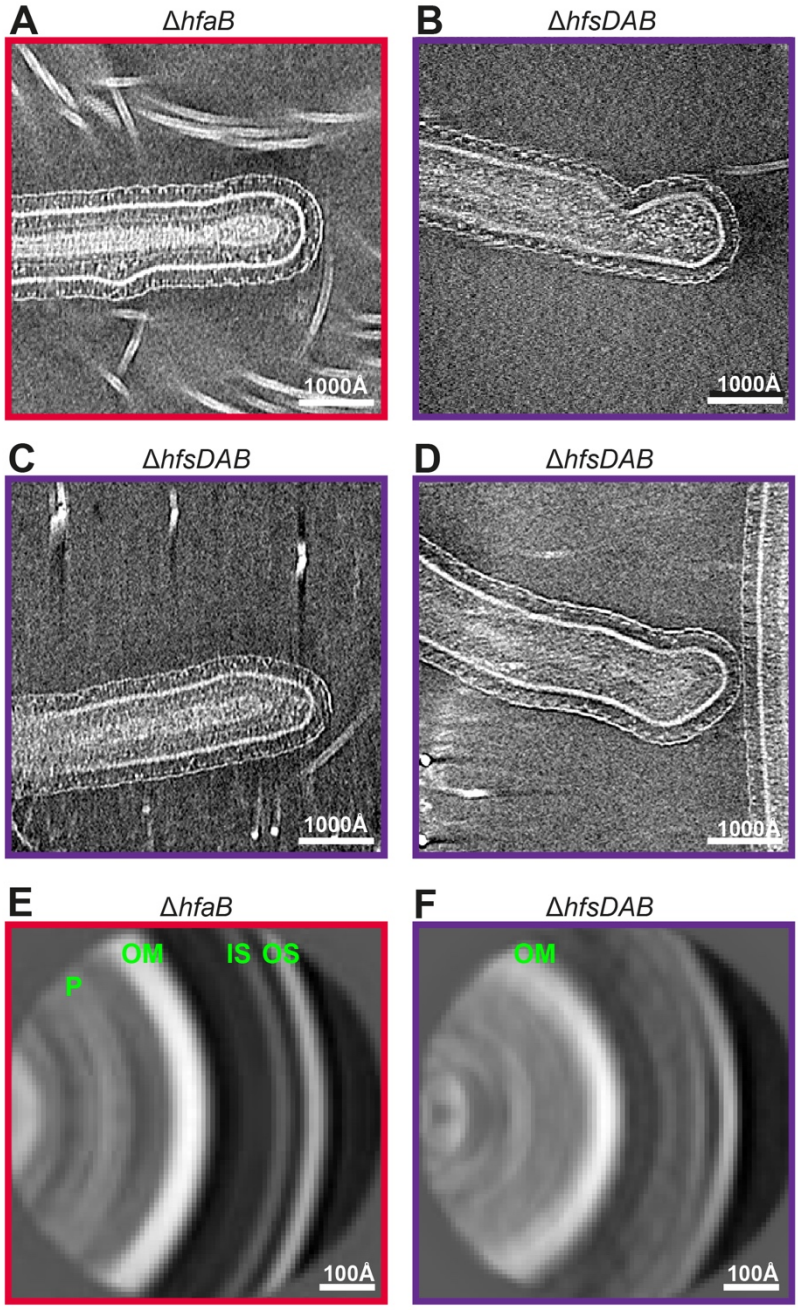


Figure 3.5: Subtomogram averaging of the holdfast secretion complex mutant (Δ*hfsDAB*).

(A) Inverted cryo-EM images of the Δ*hfaB* strain displays uniform curvature along the stalk tip. Panel A is the same as Figure 3.4A, shown here for comparison with B-D panels. (B-D) Inverted cryo-EM images of the Δ*hfsDAB* mutant displays aberration in stalk morphology, with visible narrowing at various regions near the tip. (E) Sub-tomogram averaging of Δ*hfaB* stalk tips. Panel E is the same as Figure 3.4C. The densities corresponding to the outer S-layer (OS), inner S-layer (S), outer membrane (OM), peptidoglycan (P) have been marked. (F) Subtomogram averaging analysis of Δ*hfsDAB* stalks reveals increased OM curvature in the final class average.

On comparing the linear density profiles of the two class averages presented in Figure 3.4E, an additional cryo-EM density peak was observed on the extracellular side of the outer membrane in the Δ*hfsG* mutant, which was absent in the Δ*hfaB* mutant. To test whether this density could be attributable to HfaAD, the same sub-tomogram analysis was repeated for the Δ*hfaAD* double mutant (Figure 3.6C). The peak on the extracellular side of the outer membrane was not observed in this mutant (Figure 3.6D, orange curve), while the HfaB peak on the periplasmic side was retained. This suggests that the broad peak of density on the extracellular side of the outer membrane is made up of HfaAD proteins either alone, or in conjunction with the base of the holdfast.

The centre of the HfaB density is situated ~66 Å away from the centre of the outer membrane (Figure 3.6D), which is comparable to the published size of CsgG, the outer membrane protein of the *E. coli* curli system which shares high structural similarity with HfaB (419). HfaB appears as a sharp peak (Figure 3.6D, blue curve), and it is clearly discernible by visual inspection of tomograms. The centre of the extracellular density corresponding to HfaAD proteins is ~110 Å away from the outer membrane and forms a broad peak (Figure 3.6D, compare blue and orange curves). This indicates that the anchor proteins likely form extended oligomers at the coating on the outer leaflet of the outer membrane, however further structural analysis is required to confirm this. Taken together, the data show that the holdfast anchor complex spans the outer membrane with different components of the complex situated on both sides of the outer membrane.

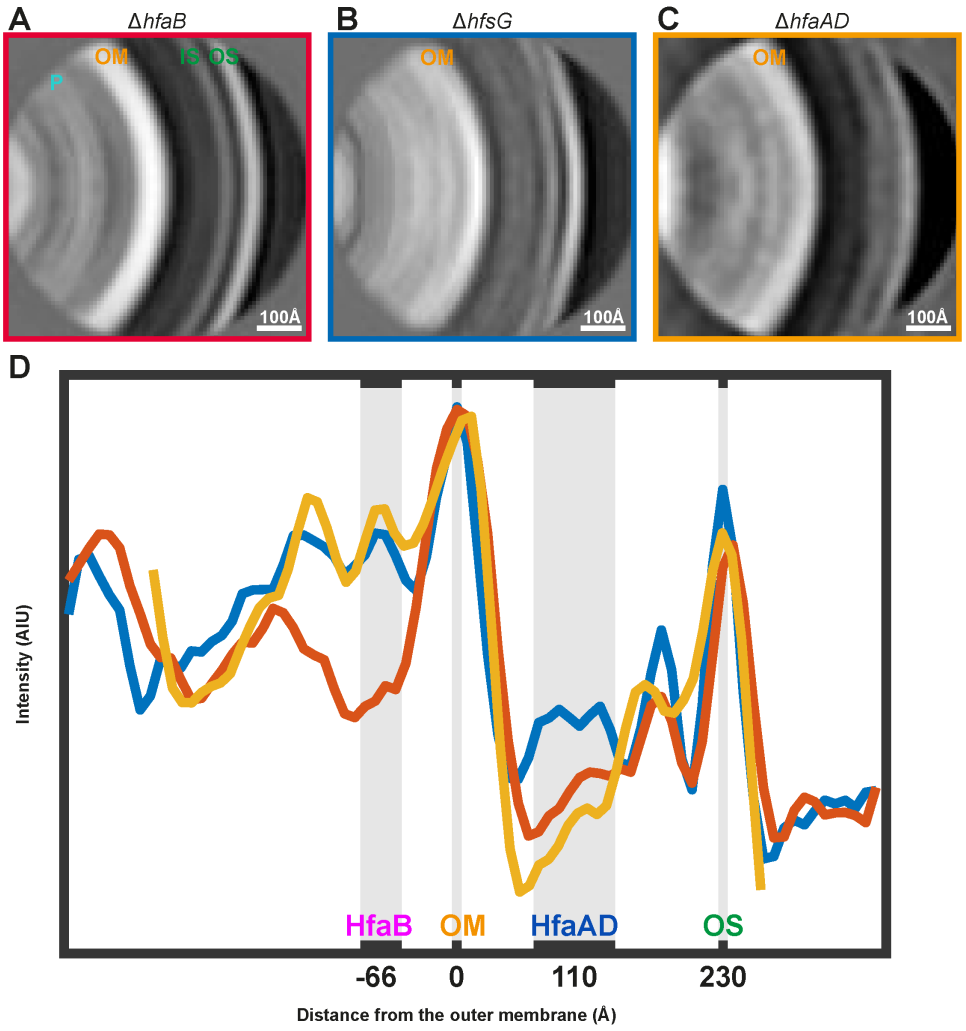


Figure 3.6: The holdfast anchor complex spans the outer membrane of *C. crescentus*.

(A-D) Sub-tomogram averaging of stalk tips from the Δ*hfaB,* Δ*hfsG* and Δ*hfaAD* strains. Panels A-B are same as Figure 3.4, shown here for comparison with panels C and D. Density layers corresponding to the outer S-layer (OS), inner S-layer (IS), outer membrane (OM) and the peptidoglycan (P) have been marked in panel A. (E) Plots of the pixel intensity across the sub-tomogram averages, for the Δ*hfaB* (red curve), the Δ*hfsG* (blue curve) and the Δ*hfaAD* (orange curve) strains. The outer S-layer, the outer membrane and the locations of the HfaABD proteins have been marked.

3.4. The major holdfast anchor protein, HfaB, does not form a visibly ordered array beneath the OM.

To gain insights into the architecture of the holdfast anchor complex at higher resolution, the number of complexes for subtomogram averaging was increased by imaging CB15 *C. crescentus* rosettes. These rosettes are well-characterised in *C. crescentus* and consist of numerous stalked cells bound by a central holdfast (416). First, *C. crescentus* Abs2 cells (Table 2.1) were grown in PYE media for an extended period to facilitate stalk elongation and rosette formation. Following three days of growth, cell clustering was observed using brightfield microscopy, indicative of rosette formation (Figure 3.7A). Staining using the membrane dye, FM464, revealed elongated stalks extending from the cell bodies, confirming the effect of phosphate starvation in this strain (Figure 3.7B) (413). Rosettes were separated from cell bodies by centrifugation and the pellet incubated overnight to further encourage stalk association and the formation of larger rosettes. Screening of the pellet using negative stain TEM revealed successful isolation of large, multi-stalk rosettes, with their stalk tips orientated toward a central position (Figure 3.7C). Rosettes were transferred onto cryo-EM grids and imaged using cryo-ET (Materials and Methods). HfaB densities were noted at the stalk tips in tomograms (Figure 3.7D), as well as the holdfast in the centre of rosettes (Figure 3.7D, red arrow).

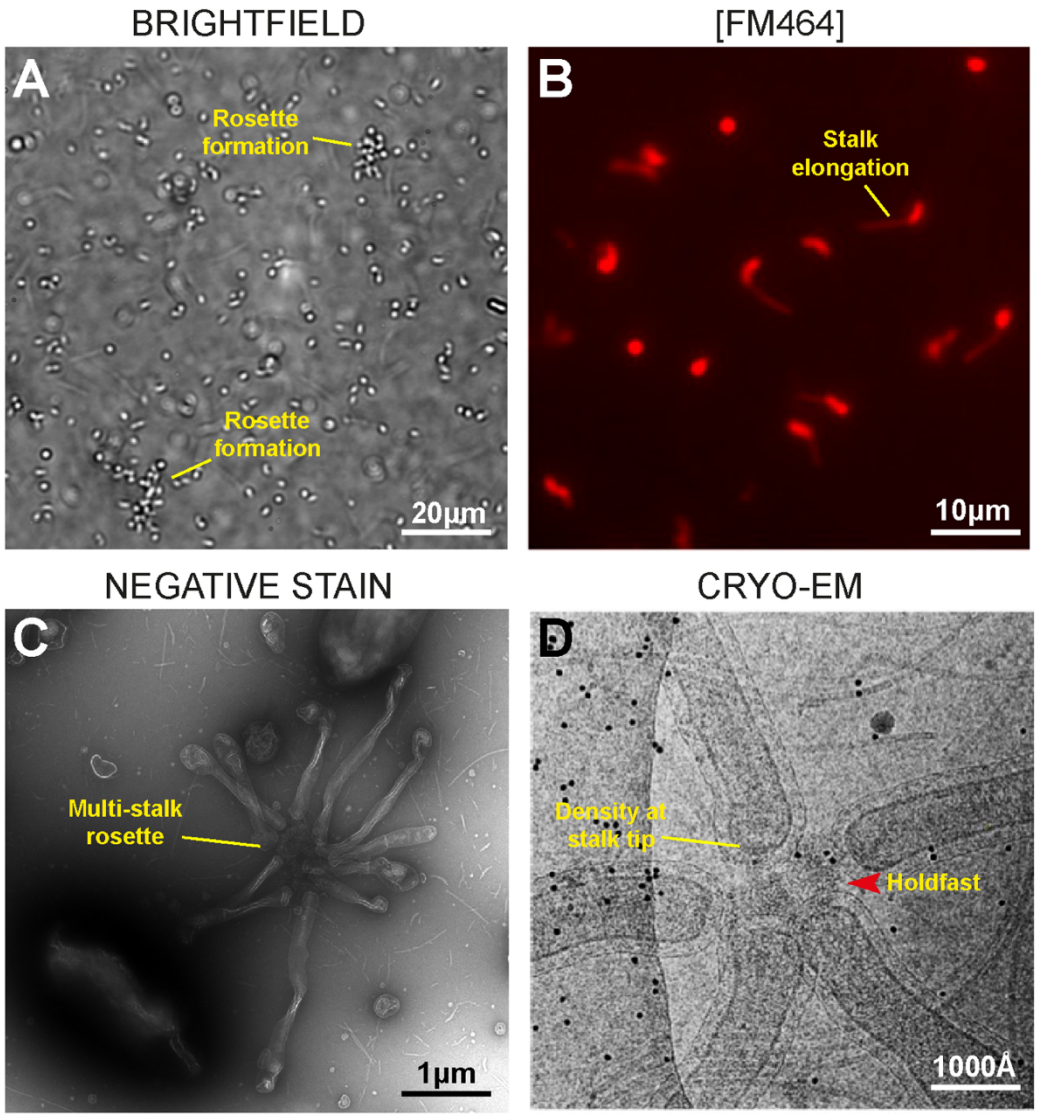


Figure 3.7: Purification of *C. crescentus* rosettes.

(A) Brightfield microscopy of *C. crescentus* Abs2 reveals clustering of cells in culture and rosette formation. (B) Membrane (FM464) staining of *C. crescentus* Abs2 cells highlights stalk elongation as a result of phosphate starvation (*pstS* mutation). (C) Screening of purified rosettes using negative staining in 2% (w/v) uranyl acetate confirms multiple stalks per rosette. (D) A virtual slice through a tomogram of *C. crescentus* Abs2 rosettes. The HfaB density is visible at the stalk tip, with multiple stalks bound to a central holdfast (red arrow).

To confirm once again that HfaB localises at the stalk tip of rosettes, a *C. crescentus* strain with the mCherry fluorescent protein fused to the C-terminus of HfaB was imaged (Table 2.1). Multiple rose-shaped cell clusters were visualised using light microscopy, consistent with *C. crescentus* rosettes (Figure 3.8A). HfaB-mCherry signal localises exclusively at the rosette centre, confirming HfaB co-localises with the holdfast (Figure 3.8B,C). As a control, a strain with mCherry fused to the C-terminus of HfaE was imaged (Table 2.1). HfaE is a recently identified attachment protein whose deletion results in holdfast shedding as observed under brightfield microscopy (420). Rosettes were similarly formed by this strain, with HfaE signal localised at the rosette centre. Single cells do not exhibit HfaE-mCherry signal at the stalk tip, suggesting lack of holdfast anchoring at the tip of these cells, or that the signal intensity falls below the limit of detection (Figure 3.8D-F).

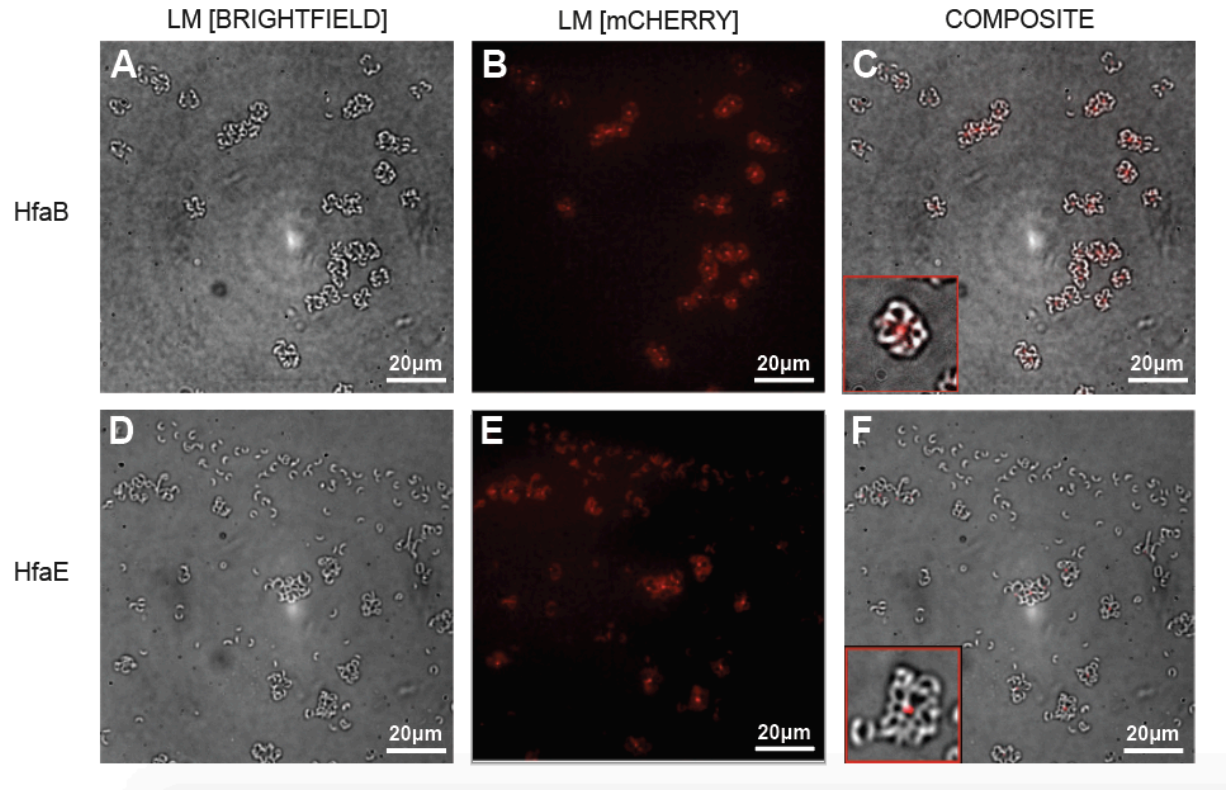


Figure 3.8: HfaB-mCherry localises at the centre of *C. crescentus* rosettes.

(A) Light microscopy imaging of *C. crescentus* HfaB-mCherry fusion strain, which forms multiple rosettes in liquid culture. (B) HfaB-mCherry localises at the centre of rosettes as evident under the red fluorescence channel and (C) mCherry:brightfield composite. Inset in the left hand corner of panel C contains a zoomed image of a rosette. (D) Light microscopy imaging of *C. crescentus* HfaE-mCherry fusion strain, illustrating rosettes and single cells in liquid culture. (E) HfaE-mCherry localises at the centre of rosettes as evident under the red fluorescence channel and (F) mCherry:brightfield composite. HfaE-mCherry signal is not visualised at the stalk tip of single cells. Inset in the left hand corner of panel F contains a zoomed image of a rosette. All images were contrasted manually using Fiji/ImageJ image analysis software (421).

Cryo-ET data collection of rosettes from *C. crescentus* Abs2 cells (Materials and Methods) resulted in the acquisition of 144 stalks across 25 tomograms. To extract sub-tomograms, two spheres were positioned at the stalk tip; one with its periphery lining the outer membrane of the stalk and another overlaid to encompass the HfaB density beneath the outer membrane (Figure 3.9A). The coordinates corresponding to the region of overlap between the two spheres was then used as a cut-off to map stalk positions containing the HfaB density. Coordinates were overlaid with the original tomograms and visually assessed using USCF Chimera (Figure 3.9B) (408). Finally, sub-tomograms were extracted and subjected to sub-tomogram averaging in three dimensions (Materials and Methods).

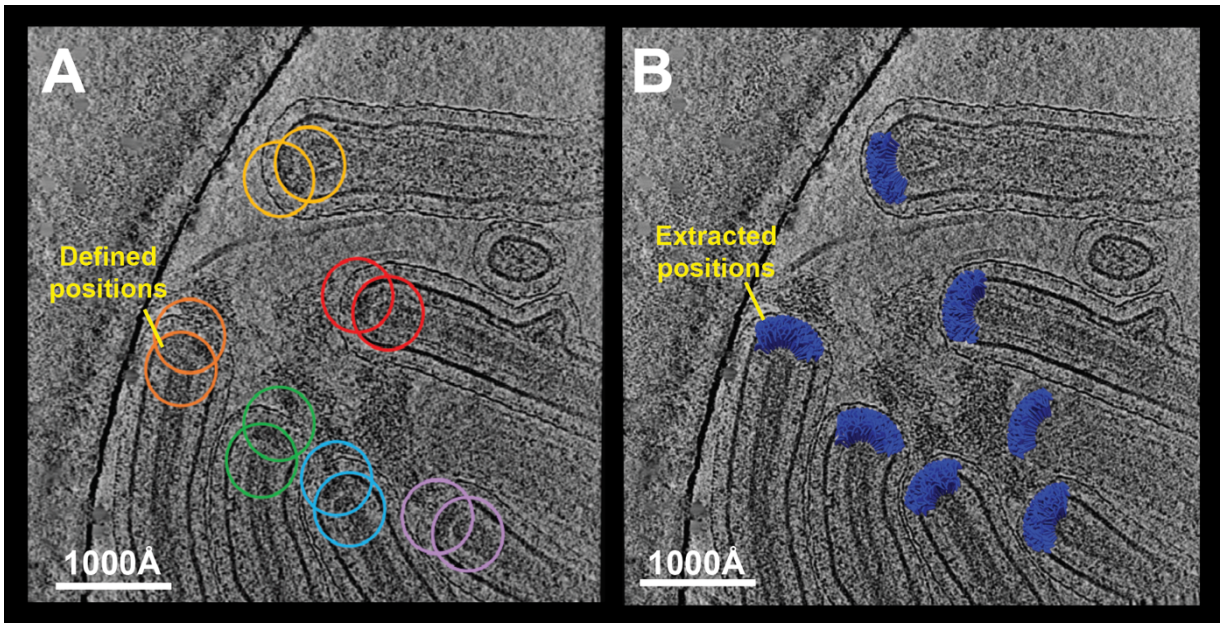


Figure 3.9: Image processing of *C. crescentus* rosetted-stalk tips.

(A) A virtual slice through a tomogram of *C. crescentus* Abs2 rosettes. The area beneath the OM containing the visible HfaB density was defined by manually positioning two spheres along the stalk tip (coloured spheres), such that the HfaB density is encompassed in the area of overlap between the two spheres. (B) Overlay of virtual tomogram slice illustrating extracted positions at the cell stalk for downstream sub-tomogram averaging (blue, clustered arrows).

Distinct layers corresponding to the cell envelope including the S-layer, outer membrane, periplasm and inner membrane were resolved in the resulting averaged, three-dimensional volume (Figure 3.10A). Focused sub-tomogram averaging at the outer membrane similarly revealed a thick density corresponding to the OM and periplasm (Figure 3.10B). The region beneath the outer membrane was inspected to discern whether a notable density corresponding to the HfaB anchor complex protein was present. The volume did not illustrate evidence for an ordered feature or repetitive array beneath the OM, with visible disorder throughout the periplasmic/peptidoglycan layer (Figure 3.10B). The resolution achieved by sub-tomogram averaging is limited by particle number and thus optimal for targets which exist as repeating units. These results hence suggest HfaB does not appear as an ordered lattice beneath the OM, stalk to stalk variation in the arrangement of HfaB or that additional disordered components contribute to the HfaB density.

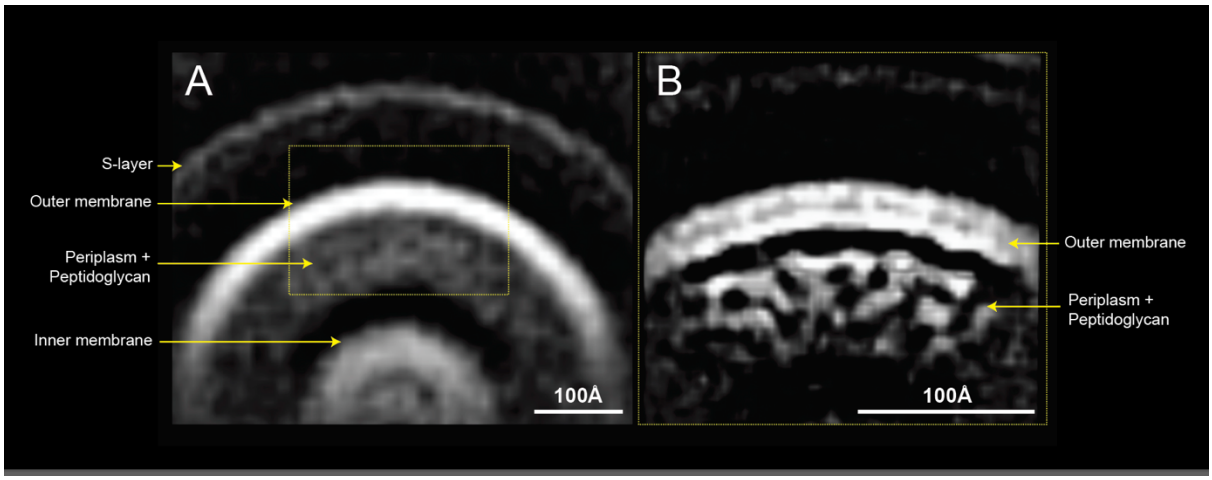


Figure 3.10: Determination of holdfast anchor complex architecture from rosetted stalks.

(A) A virtual Z-slice through sub-tomogram averaged stalk tips of *C. crescentus* Abs2 rosettes. Density layers corresponding to the S-layer, outer membrane, periplasm/peptidoglycan and inner membrane are marked along the visible cell envelope. (B) Sub-tomogram averaging at the outer membrane of the stalk tip. Density layers corresponding to the outer membrane and periplasm/peptidoglycan have been marked. Evidence of a distinct density beneath the OM, corresponding to HfaB, is not resolved from the average. Panels A and B both represent slices through the three dimensional volume.

3.5. Purification and characterisation of recombinant HfaB

3.5.1. Protein sequence analysis

In parallel with *in situ* structure determination in this project, the purification and reconstitution of recombinant HfaB was pursued *in vitro*. Sequence analysis of the major anchor protein, HfaB, was performed to inform the design of recombinant constructs using programs packaged in the MPI Bioinformatics Toolkit (243). HHPred revealed the outer membrane porin of the *E.coli* curli system, CsgG, shares 23% structural similarity with HfaB (probability 99.76, E value 3.6 $x10^{-16}$). ClustalΩ alignment of HfaB and CsgG amino acid sequences revealed a conserved N-terminal cysteine residue, the site at which the CsgG protein is cleaved and lipidated prior to membrane insertion (Figure 3.11A, red coloured 'C') (419, 422). The cysteine residue is not annotated as the site of signal peptide cleavage for HfaB in the Uniprot database (rather a serine residue at position 22) and is suspected as a mis-annotation (personal correspondence, Brun Lab [Indiana]). The greatest difference between HfaB and CsgG is at the C-terminus of HfaB (residues 273-315) where there are an additional 42 amino acids (Figure 3.11A), green coloured residues). Secondary structure analysis showed the 42 amino acid region does not possess secondary structure and may form a disordered loop (Figure 3.11B). The predicted structure of the HfaB monomer, modelled against CsgG monomer, further illustrated structural similarities in three dimensional space (Figure 3.11C).

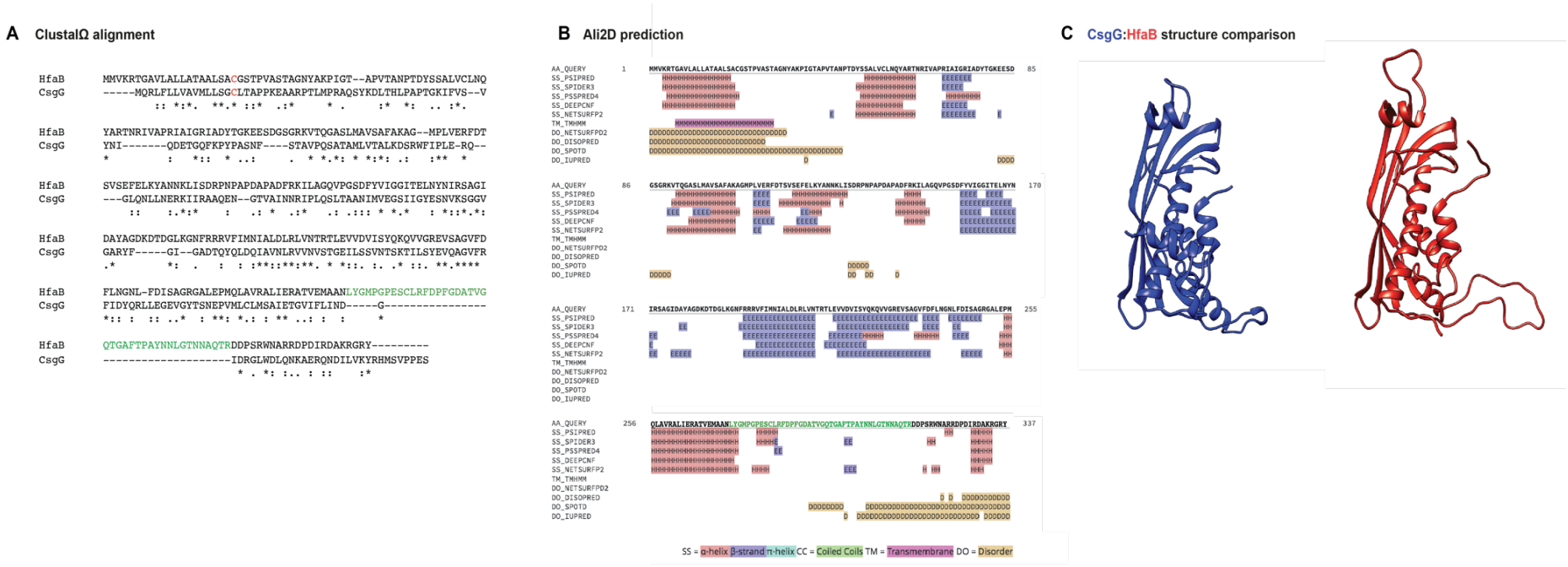


Figure 3.11: Bioinformatic analysis of the major anchor complex protein, HfaB.

(A) ClustalΩ alignment of the HfaB amino acid sequence against the CsgG amino acid sequence reveals conservation of a cysteine residue (coloured red), as well as additional amino acid residues at the C-terminus of HfaB that are not present in CsgG (coloured green). The symbol '*' denotes perfect alignment, ':' in groups exhibiting strong similarity and '.' in cases of groups exhibiting weak similarity. (B) Ali2D secondary structure prediction of HfaB illustrates ß-sheet rich regions and reveals the extended C-terminal region (amino acids 273-315, coloured green) is predicted to be disordered (C) Comparison of the predicted three dimensional structure of HfaB monomer (red ribbon, generated by Modeller), modelled against the crystal structure of CsgG monomer (blue ribbon, PDB reference: 4UV2) (419). The disordered loop (amino acid residues (273-315) is incompletely modelled in the hypothetical HfaB structure presented given lack of structural homology to CsgG in this region. The predicted HfaB structure is therefore restricted to amino acid residues 46-286. All bioinformatic analyses were performed using the MPI Bioinformatic Toolkit (243)

3.5.2. Construct design and expression tests

Given the structural homology of HfaB with CsgG, CsgG purification workflows were adapted for expression of HfaB in this project. The atomic structure of CsgG has been determined by crystallization of the nonameric, lipid-assembled pore in previous studies. This was achieved through over-expression of the native CsgG gene in *E.coli* with either a C-terminal inserted Strep-tag II or N-terminal His-tag. Detergent extraction using LDAO or DDM was then used to isolate the natively assembled membrane complex (117, 419, 422). More recently, the atomic structure of nonameric CsgG in complex with the accessory protein CsgF was solved using cryo-EM, similarly by overexpression and detergent extraction (423). A soluble, periplasmic CsgG construct was also crystallized by replacement of the N-terminal cysteine with a serine residue (422). In cells, proteins destined for the outer membrane are lipidated at the inner membrane through modification of the N-terminal cysteine with diacylglycerol thioether or aminoacylation. The lipid anchor binds to periplasmic LolA protein which shuttles the lipoprotein to the outer membrane for insertion (424, 425). Therefore, removal of the N-terminal cysteine residue results in retention of monomeric CsgG in the periplasm (422).

A library of constructs was designed to test the expression of either cytoplasmic, periplasmic or membrane-inserted HfaB for downstream purification and structural biology (Table 2.1). All constructs possessed a C-terminal poly-histidine tag. Early trials using the native *C. crescentus hfaB* gene (amplified from *C. crescentus* genomic DNA) did not achieve protein expression in *E. coli*. This may be attributable to differences in codon usage between the two bacteria as *C. crescentus* is an alphaproteobacterium whereas *E. coli* is a gamma-proteobacterium. The *C. crescentus hfaB* gene sequence was hence codon optimised for protein expression in *E. coli* henceforth.

First, a construct lacking the N-terminal signal peptide was cloned for expression of HfaB in the cytoplasm (Table 2.1). This construct was successfully expressed in *E. coli*, producing a band at the expected size of HfaB without a signal peptide (~35 kDa) in cell lysates via SDS-PAGE (Figure 3.12A). Solubilisation in urea and guanidine denaturants confirmed the protein was present as inclusion bodies in the insoluble fraction. The protein was insoluble in DDM suggesting that it is not membrane associated (Materials and Methods). Next, a periplasmic construct was trialled in which the N-terminal cysteine residue (position 20) was converted to a serine residue to prevent lipidation and membrane insertion of HfaB (Table 2.1). Despite this strategy being successful in expressing soluble, periplasmic CsgG, the HfaB construct was found in inclusion bodies, suggesting the protein accumulates either in the cytoplasm or periplasm. Replacement of the N-terminal signal sequence with either the *E. coli* PelB or OmpA signal sequence (Table 2.1) did not improve HfaB solubility or achieve membrane insertion. Finally, mutation of the C-terminal region of HfaB, which differs significantly to that of CsgG, was explored to see if the biochemical behaviour of HfaB could be promoted towards that of CsgG (Table 2.1). However, both deletion of the 42 amino acid disordered region or entire C-terminus of HfaB did not alter solubility. Optimisation of expression conditions was screened for all constructs, including the use of LB media supplemented with 1% glucose, reduced IPTG concentration and auto-induction media.

3.5.3. Purification of HfaB from inclusion bodies

As a soluble or membrane-inserted construct of HfaB could not be purified, a protocol to purify HfaB from inclusion bodies was optimised in this study. This protocol was derived in part from that reported for the inclusion body purification and refold of the *E.coli* outer membrane protein, OmpT (Materials and Methods) (426). The pHIS-17 *hfaB* plasmid (Table 2.1) was selected, given it expresses HfaB at high levels in cytoplasmic inclusion bodies, possesses a C-terminal His-tag and lacks the N-terminal signal peptide.

The HfaB inclusion bodies were soluble in guanidium hydrochloride or urea at large scale, with urea selected as the denaturant of preference (Figure 3.12B) (Materials and Methods). The first round of affinity purification was performed under denaturing conditions to separate urea-solubilised HfaB from the supernatant. An absorbance peak at 280 nm was observed immediately after application of wash buffer, suggesting weak binding of the HfaB His-tag to the Ni-NTA column. HfaB refolding was performed by drop-wise addition of the protein into a solution of DDM, followed by overnight incubation (Materials and Methods). Affinity purification of refolded HfaB resulted in similar binding behaviour, with HfaB eluting immediately after wash buffer application. This binding behaviour was likewise observed by collaborators during independent purification trials (personal correspondence, Robinson Lab [Oxford]). The eluted protein was concentrated and appeared pure, with a single ~35 kDa band visualised using SDS-PAGE (Figure 3.12C). The final yield of the HfaB preparation was ~12 mg, expressed from 12L of BL21 cell culture.

Circular structures of varying size were visualized in the concentrated preparation using negative stain TEM (Figure 3.12D). The irregularity in the size of the structures indicated they were most likely free DDM micelles rather than the HfaB pore, which is predicted to have a diameter comparable to that of the 120Å β-barrel of CsgG. In addition, high resolution cryo-EM imaging did not reveal evidence for oligomerisation or higher order assembly (Figure 3.12E) (427). The HfaB preparation was subjected to tandem and ESI-MS (Materials and Methods) which returned positive for HfaB peptide identification, with a mass of 35,172 Da (Figure 3.12F). Native MS analysis (Materials and Methods) of HfaB reconstituted in LDAO and C_8E_4 detergents illustrated the protein is present in its monomeric state in solution (Figure 3.12G,H). The presence of monomeric HfaB suggests that higher protein concentration, accessory proteins (e.g.: HfaA or HfaD) or other factors are necessary for pore reconstitution *in vitro*.

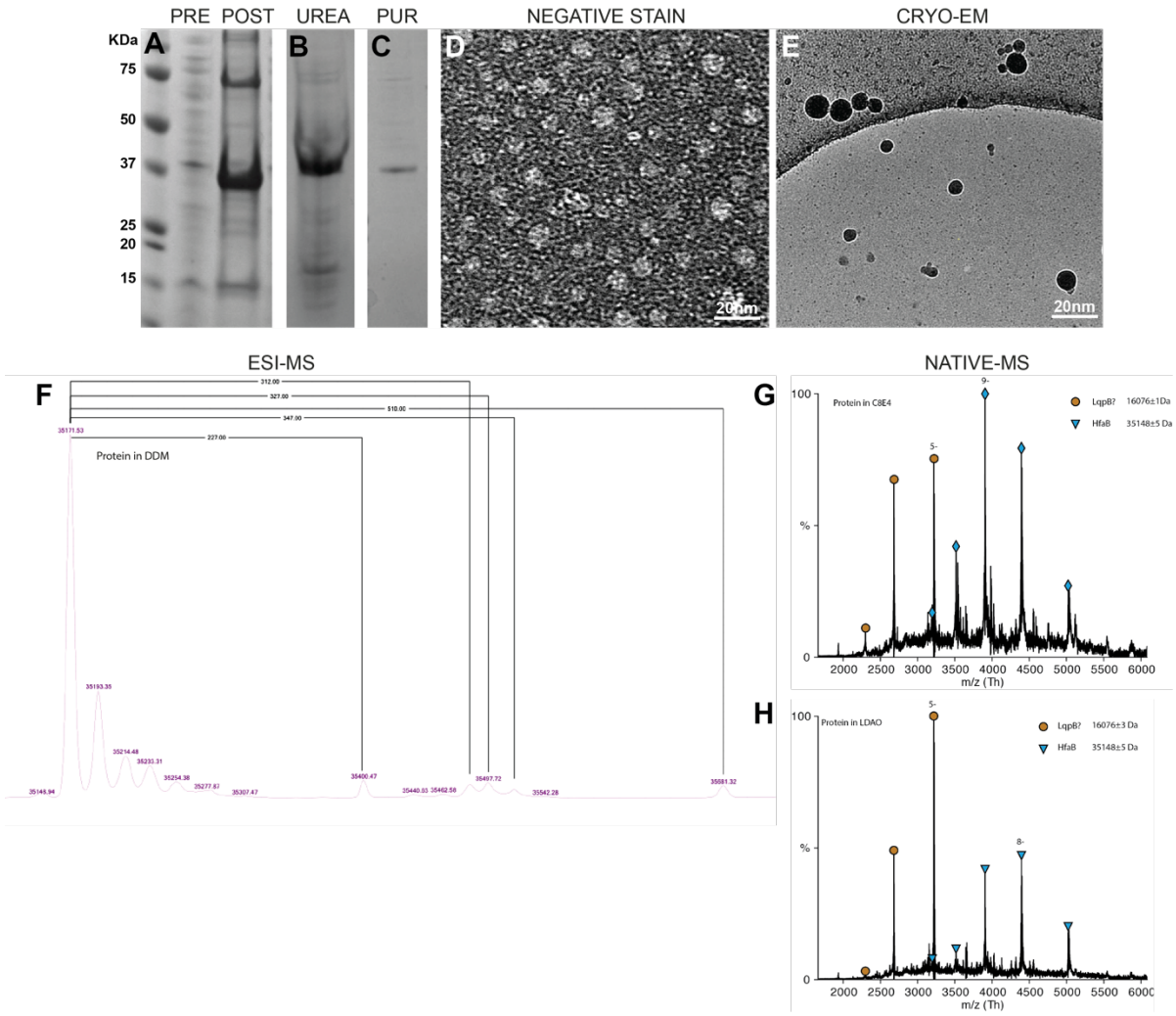


Figure 3.12: Purification of recombinant HfaB in detergents

(A) SDS-PAGE gel loaded with cell lysate of pHIS17 *hfaB*-transformed BL21 pre and post induction with 1mM IPTG (labelled pre and post respectively). Overexpression of HfaB is evident in the post induction sample, with a prominent band at ~35 kDa. (B) SDS-PAGE gel loaded with the supernatant fraction following overnight solubilisation of HfaB inclusion bodies in 8M urea. (C) SDS-PAGE gel loaded with final, concentrated HfaB preparation following purification and refold. (D) Negative stain TEM of the HfaB preparation reveals spherical structures of varying size, suspected to be detergent micelles. (E) Cryo-EM image of the HfaB preparation illustrating small, dispersed proteins (dark spots) and no evidence for HfaB oligomerisation. (F) Deconvolution of ESI-MS spectra reveals a molecular mass of ~35,000 Da for HfaB reconstituted in DDM. (G, H) Native mass spectrometry reveals HfaB is in its monomeric form when reconstituted in (G) C_8E_4 and (H) LDAO, with a molecular mass of ~35,000 Da.

3.6. The anchor complex is observed beneath the outer membrane of other bacteria

The alphaproteobacteria, *Hirschia baltica, Asticcacaulis excentricus* and *Asticcacaulis bisprosthecum*, are phylogenetically related to *C. crescentus* and encode putative holdfast synthesis, secretion and anchor genes (367, 428-430). To explore whether the anchor density is present beneath the outer membrane of these organisms, *Asticcacaulis* and *Hirschia* cells were grown to mid-log phase in PYE and Marine Broth respectively, plunge frozen onto cryo-EM grids and imaged using cryo-EM (Materials and Methods). Thick densities, resembling that of HfaB in *C. crescentus*, were visualised beneath the outer membrane these bacteria which was exclusively localised at the cell pole (Figure 3.13A-D). In many cells, the holdfast was found closely associated with the cryo-EM density (Figure 3.13B, red arrow), suggesting a conserved holdfast anchoring mechanism across alphaproteobacteria.

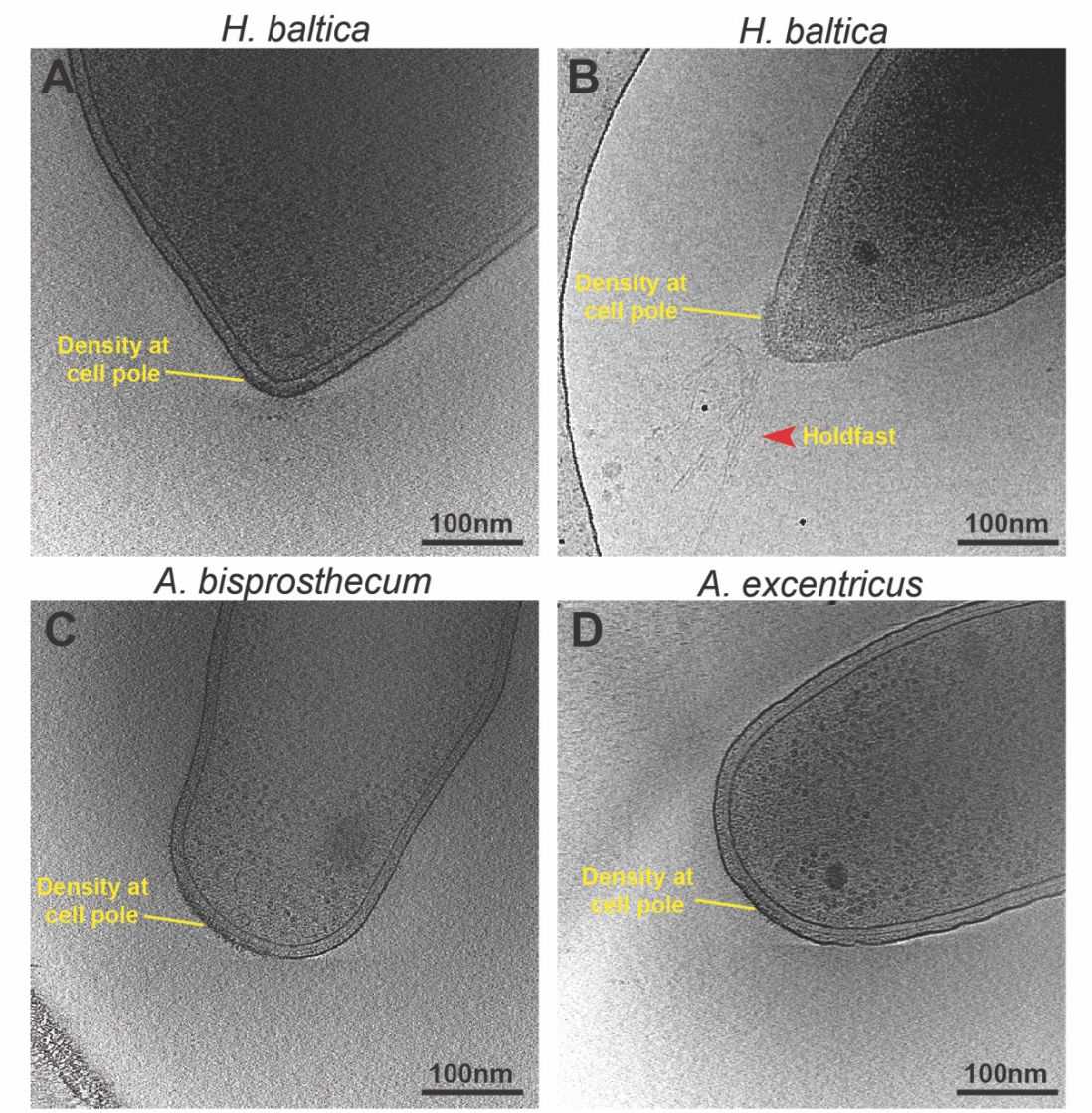


Figure 3.13: The anchor density is situated beneath the OM of *Hirschia baltica* and *Asticcacaulis* cells

(A) Cryo-EM imaging of *H. baltica* cells reveals a thick cryo-EM density beneath the OM of the cell pole. (B) The holdfast (red arrow) emanates from the cryo-EM density into the extracellular milieu. (C) Cryo-EM imaging of *A. bisprosthecum* demonstrating a cryo-EM density lining the OM of the cell pole. (D) Cryo-EM imaging similarly reveals the presence of cryo-EM density beneath the OM of *A. excentricus*.

CHAPTER 3 DISCUSSION

Attachment of bacteria to surfaces via proteinaceous adhesins such as pili and fimbriae has been extensively studied, however comparatively less is known about polysaccharide-mediated adhesion. For the Gram-negative bacterium *C. crescentus*, initial adhesion of swarmer cells is mediated by pili and flagella (85, 431, 432). Stable, irreversible attachment is then achieved by the holdfast (374, 375, 379).

In this study, the location, composition and arrangement of the holdfast anchor complex at the *C. crescentus* stalk tip were identified. The components of the holdfast anchor complex are localized on both sides of the outer membrane of the stalk. The sharp, regular cryo-EM density of the anchor complex on the inner side of the outer membrane is comprised primarily of the holdfast anchor protein HfaB, consistent with previous genetics and cell biology studies (377). The cryo-EM density corresponding to the anchor complex is lost upon Δ*hfsDAB* deletion. Previous work has suggested that HfaB and HfsD of the holdfast secretion complex interact directly, since proper localization of HfaB requires HfsD (417). The aberrant stalk morphology of HfsDAB mutants suggests the complex may be integrally associated with the cell envelope. Indeed, HfsD and HfsA share homology with proteins known to export exopolysaccharide across membranes (374). In line with this, localization of HfaB at the stalk tip was disrupted by the Δ*hfsDAB* deletion (377, 417). It remains unclear if other components of the HfsDAB complex associate with HfaB and systematic deletion of individual secretion genes may help to elucidate details of this interaction in the future.

Both HfaA and HfaD are known to localize at the outer membrane of *C. crescentus* cells (377), and were found to contribute to the broad cryo-EM density associated with extracellular side of the outer membrane in this study. Immunofluorescence microscopy has shown that both proteins are localized on the cell surface (377), therefore they are not expected to contribute to

the cryo-EM density on the periplasmic side of the outer membrane. Further structural and cell biology investigations will be needed to understand which components of the HfaABD complex directly tether sugar moieties of holdfast to cells.

It is important to note that systematic deletion of holdfast anchor proteins and subsequent examination of densities along the cell envelope using cryo-EM does not account the possibility of an upstream function of these proteins which may influence density profiles. The composition and localisation of the holdfast anchor complex should therefore be supported by additional experiments in the future (e.g.: immuno-labelling of deletion mutants), to ensure density changes are in fact attributable to a direct effect on these proteins.

HfaB has a predicted structural similarity with CsgG, an outer membrane porin responsible for the translocation of the curli amyloid subunits to the cell surface (116). As HfaB is closely associated with the outer membrane of the *C. crescentus* stalk (with the centre of the HfaB peak only ~66 Å away), and is thought to interact with the holdfast secretion complex, HfsDAB, it is highly likely that a part of HfaB is buried in the outer membrane and plays a similar role in secretion to CsgG. Indeed, the localization of HfaA and HfaD at the cell surface depends on the presence of HfaB supporting its function as a putative translocon (377).

The atomic structure of HfaB will help provide insights into its potential role in holdfast transport and anchoring. Although the HfaB density is macroscopically visible in cryo-EM images, HfaB is not arranged as a regular, ordered array beneath the outer membrane of the stalk tip which may limit the application of *in situ* subtomogram averaging. Recombinant, monomeric HfaB was successfully stabilised in a number of detergents in this study, opening additional avenues for structural investigations both *in vitro* and *in situ*. Strategies such as template matching, in which a cross correlational search is performed between tomograms and a three-dimensional molecular volume (e.g.: predicted or *in vitro* determined HfaB structure), may be applied to better elucidate the position and orientation of HfaB particles in cells in the

future (433, 434). The number of imaged stalks could also be increased in the case of particle number/data limitation (435).

The mechanism by which polysaccharide adhesins are anchored to the cell body in *C. crescentus* and many other bacterial species remains largely uncharacterized. Holdfast anchor proteins (HfaABD) are encoded within the genomes of *H. baltica* and *Asticaccaulis* species and deletion of these genes results in holdfast shedding from the cell surface (367, 428-430). In this study, cryo-EM densities were identified along the cell pole of *H. baltica*, *A. excentrius* and *A. bisprosthecum*, often in association with holdfast polysaccharide. The macroscopic appearance of these densities resembles that of HfaB in *C. crescentus* and may similarly represent HfaB in these organisms. Indeed, the amino acid sequences of HfaB in *H. baltica*, *A. excentricus* and *A. bisprosthecum* share 60%, 65% and 67% identity with that in *C. crescentus* respectively. These findings support the potential for a conserved structure and mechanism involved in polysaccharide anchoring at the cell envelope of alphaproteobacteria.

Since polysaccharides play a crucial role in adhesion and biofilm formation of many bacteria, there is an urgent need to delineate the fundamental principles of polysaccharide anchoring, adhesion and their regulatory effect in bacteria. This study thus sets the framework for future structural and cell biology studies of the holdfast anchor complex and reveals insights into a fundamental but under-explored area, crucial in improving understanding of polysaccharide-mediated adhesion in bacteria.

Acknowledgements

I gratefully acknowledge Dr Tanmay Bharat for his assistance across cryo-EM and cryo-ET data collections at the Sir William Dunn School of Pathology. Cryo-EM images in Figure 3.1 and Figure 3.2 were collected by Dr Tanmay Bharat at the MRC Laboratory of Molecular Biology (Cambridge). Image processing and sub-tomogram averaging of rosettes, including modification of scripts, were supported by Andriko von Kügelgen (DPhil student, Bharat Lab). A proportion of recombinant HfaB cloning and purification was assisted by Angus Menzies (undergraduate student, Bharat Lab) under the supervision of myself and Dr Tanmay Bharat. I thank Dr Jani Reddy Bolla (Robinson Lab, Oxford) for his advice regarding membrane protein purification, independent HfaB refold trials and in-tact mass spectrometry of HfaB (in LDAO and C_8E_4). Finally, I sincerely thank Gail Hardy (Indiana State University, USA) and Professor Yves Brun (Université de Montréal, Canada) for genetic manipulation and provision of *C. crescentus, Asticacaulis* and *Hirschia* strains.

CHAPTER 4 AIMS

The pathogen *P. aeruginosa* PAO1 encodes four putative chaperone usher proteins (CupA, CupB, CupC and CupE) which contribute to biofilm formation (4, 56, 149). To date, these filaments have not been visualised on the surface of PAO1 at high resolution. Additionally, no high resolution structures have been reported. This project hence aimed to study PAO1 cell surface CUPs and resolve the structure of identified CupE filaments using single particle based helical reconstruction. By providing insight into the regulation and structure of CupE filaments, this work sheds light on CupE-mediated biofilm formation in *P. aeruginosa*. More specifically, the project aims were:

(i) Identification of genetic components which result in up-regulation of CUP filaments on the PAO1 cell surface.

(ii) Purification and imaging of natively assembled (*in situ*) CupE filaments from the cell surface of PAO1 cells to determine their composition and structure using electron cryo-microscopy and single particle-based helical reconstruction.

(iii) *In vitro* reconstitution of identified CUP filaments to provide insight into the structure of filaments and to further support *in situ* findings.

CHAPTER 4. RESULTS

4.1. Deletion of the phosphodiesterase PA2133 upregulates filaments on the surface of *P. aeruginosa* PAO1

To maximise the number of cell surface filaments for downstream structural investigations, a series of *P. aeruginosa* PAO1 mutants were engineered and examined (Table 2.1). All strains harboured deletion of the major type IV pilin subunit, PilA, as well as the major flagella subunit, FliC, to ensure that any filamentous structures observed were independent of these appendages (77). The expression of the *cupA, cupB, cupC* and *cupE* gene products are repressed by the global transcriptional regulator, MvaT (4). MvaT is a member of the H-NS family of proteins in *P. aeruginosa,* thought to silence gene expression by direct binding to AT rich chromosomal regions (228). As MvaT deletion results in a 15-fold increase in gene expression of the major fimbrial subunit, *cupA1,* CupA filaments were suspected to be upregulated on the PAO1 cell surface (4). Despite this, an Δ*mvaT* deletion strain (Table 2.1) did not exhibit cell surface filaments when imaged using negative-stain EM or cryo-EM. A strain with pBAD promoter upstream of the *cupA* operon (arabinose inducible) was therefore engineered to drive the over-expression of CupA filaments (Table 2.1, plasmid encompassed the *cupA1-A6* genes). However, no filaments were observed on the surface of pBAD mutants following arabinose induction suggesting repression of the *cupA* operon.

The *cupA* operon encodes a putative phosphodiesterase directly adjacent to the *cupA5* gene, annotated as *PA2133* (*cupA6*), in addition to the fimbrial subunits and machinery necessary for filament assembly (*cupA1-A5*). As the entire *cupA* operon (*cupA1-A6*) was encompassed in the pBAD overexpression strain examined in this study (Table 2.1), *PA2133* overexpression was hypothesized to suppress CupA filament assembly. Previous studies demonstrate *cupA* expression is influenced by GGDEF and EAL-domain containing proteins, presumably through modulation of intracellular c-di-GMP levels (211, 213). Further, over-

expression of *PA2133* reduces detectable c-di-GMP levels, disrupts biofilm formation and increases antibiotic susceptibility (19, 240, 436). To test whether PA2133 represses filament assembly in PAO1, a strain harbouring deletion in the *PA2133* gene was engineered in an Δ*mvaT* Δ*fliC* Δ*pilA* background* and imaged using negative-stain EM (Table 2.1). Cells displaying surface filaments were then quantified by visual assessment across two independent trials. Thin filaments (~4 nm in diameter) were observed upon the surface of Δ*PA2133*‡ mutants grown in broth culture/shaking conditions (7%, n=18), compared to the control strain (0%, n=18, p-value 0.18) (Δ*mvaT* Δ*fliC* Δ*pilA*) (Figure 4.1A, yellow asterisk). Similarly, a marked increase in cell surface filaments was observed in Δ*PA2133*‡ mutants grown on agar plates/static-conditions (77%, n=18), compared to the control strain (8%, n=18, p-value 0.02) (Figure 4.1B, yellow asterisks). Cryo-EM imaging confirmed filaments are successfully preserved on paraformaldehyde-fixed planktonic cells following plunge freezing, with multiple filaments visibly radiating out from the cell surface (Figure 4.1C, yellow asterisks). These results support the hypothesis that PA2133 represses filament expression in PAO1 and that filament expression is upregulated to a greater extent on static surfaces.

* For simplicity, the Δ*PA2133* Δ*mvaT* Δ*fliC* Δ*pilA* mutant will be referred to as the Δ*PA2133*‡ mutant here-forth.

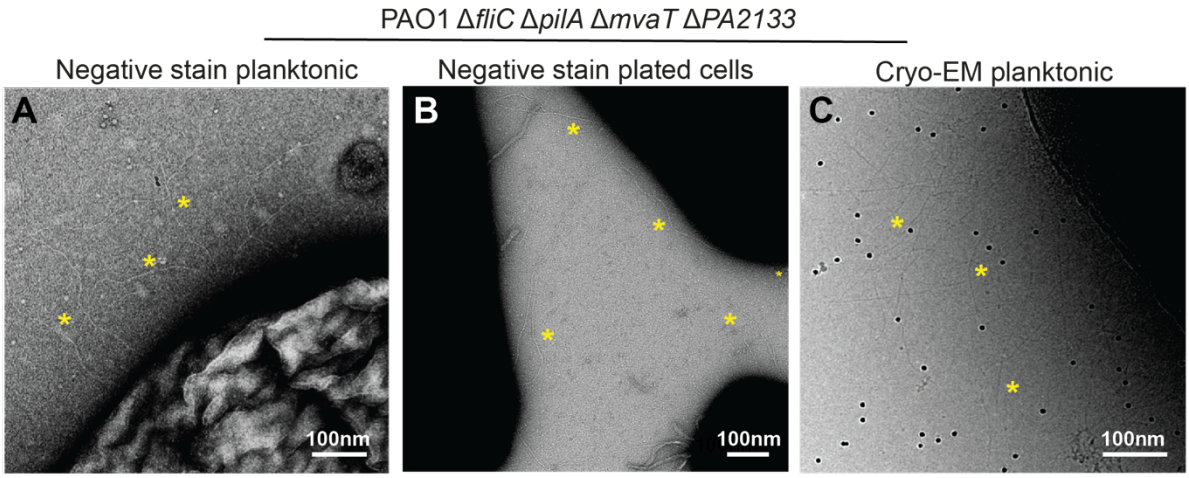


Figure 4.1: Deletion of *PA2133*‡ results in cell surface filament expression in *P. aeruginosa* PAO1

(A) Negative stain EM demonstrates multiple filaments upon the surface of PAO1 Δ*PA2133*‡ cells grown in liquid culture. (B) Negative stain TEM demonstrates cell surface filaments which extend within regions between Δ*PA2133*‡ cells lifted from the surface of agar plates. (C) Cryo-EM reveals preservation of filaments on the surface of Δ*PA2133*‡ cells following plunge freezing. Areas containing filaments are highlighted by yellow asterisks in images A-C.

4.2. CupE filaments are upregulated on the surface of *P. aeruginosa* PAO1 Δ*PA2133*‡

To determine the identity of the upregulated filaments in PAO1 Δ*PA2133*‡ mutants, a protocol was adapted to isolate and enrich filaments from the cell surface. A combination of mechanical shearing and ammonium sulphate precipitation has been reported for separation of native CupB, CupC and CupE; as detected by immunoblotting (56, 149). Further, the atomic structure of native Fim fimbriae was resolved following shearing and precipitation of filaments using high salt and macromolecular crowding agents (PEG 6000) (152). Given the greatest upregulation in filaments was observed under static conditions, lawn cultures of PAO1 Δ*PA2133*‡ cells were cultivated. Adhered cells were scraped from the surface of agar plates and vortexed to mechanically shear cell surface appendages (Materials and Methods). The supernatant fraction, containing sheared filaments, was then subjected to precipitation with either ammonium sulphate or high salt combined with macromolecular crowding agent (PEG 6000) to screen for optimal precipitants. A prominent band at ~16 kDa was observed by SDS-

PAGE in fractions precipitated in 0.5M NaCl and 3% (w/v) PEG6000 (Figure 4.2A). Tandem MS analysis of the 16 kDa species (Materials and Methods) returned positive identification for the major fimbrial subunit, CupE1, with 37% sequence coverage (Figure 4.2E). Antibodies raised against two synthetic CupE1 peptides (amino acid sequences NQWGTLDFGSHSDLTN and HASGGQRYMQNTTTTS) were tested against the sheared fraction (Materials and Methods) (56). Both anti-CupE1 antibodies detected CupE successfully via western blot, with a prominent band visible at ~16 kDa (Figure 4.2B). Negative stain-EM imaging of the sheared fraction illustrated isolation of multiple thin, straight filaments (Figure 4.2C). The concentrated filaments were successfully transferred onto cryo-EM grids where they maintained a straight morphology and were evenly dispersed (Figure 4.2D).

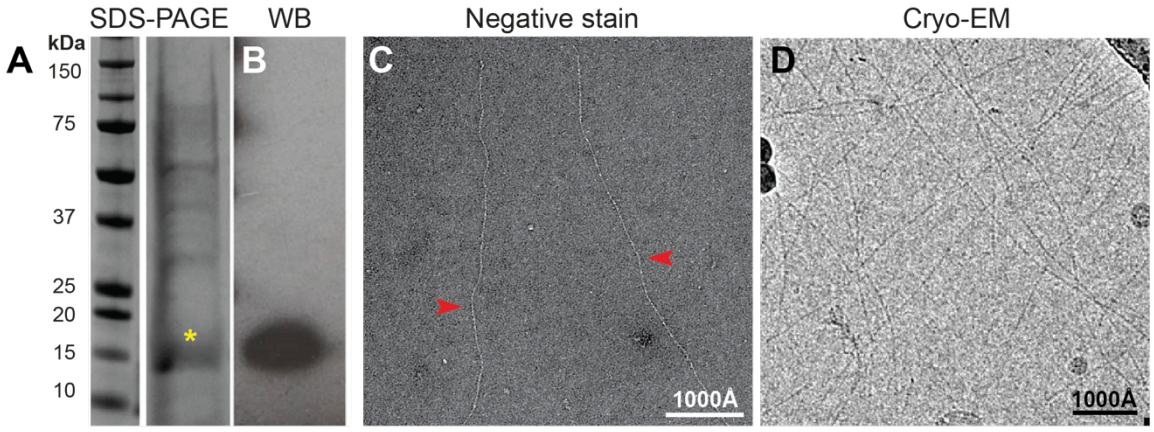


Figure 4.2: Purification of native CupE filaments from the surface of *P. aeruginosa* PAO1 Δ*PA2133*‡

(A) SDS-PAGE of the precipitated, sheared fraction of PAO1 Δ*PA2133*‡ reveals multiple bands including a prominent species at ~16 kDa (yellow asterisk). (B) Polyclonal anti-CupE1 antibody successfully binds the ~16 kDa species by western blot (WB). (C) Negative-stain EM illustrates the presence of straight, thin filaments in the Δ*PA2133*‡ sheared fraction (red arrows). (D) Cryo-EM of the Δ*PA2133*‡ sheared fraction confirms successful transfer of filaments onto grids following plunge freezing. (E) Amino acid residues of the major fimbrial subunit, CupE1, with red letters illustrating residues covered by tandem MS analysis (37% of the unprocessed CupE1 sequence).

To further confirm the identity of the sheared filaments as CupE, as opposed to other CUP fimbriae or filamentous appendages, a series of PAO1 mutants were generated in a Δ*PA2133*‡ background (Table 2.1). Filaments were sheared from the cell surface of each mutant as described previously and the resulting fractions examined by cryo-EM. A strain with genetic deletion in the major fimbrial subunits, Δ*cupE1-E2*, demonstrated complete loss of filaments in the sheared fraction (Figure 4.3A). This loss was visibly rescued upon chromosomal complementation of *cupE1-E2* in the original Δ*cupE1-E2* mutant background (Figure 4.3B, yellow asterisks). Finally, given *PA2133* is encoded in the *cupA* gene cluster, a strain with deletion in the Δ*cupA3* usher was examined. Cryo-EM images illustrated filaments in the sheared fraction of the Δ*cupA3* mutant strain, confirming the filaments do not correspond to CupA and/or that the filaments do not translocate via the CupA3 usher (Figure 4.3C, yellow asterisks). Collectively, these results establish and reinforce the filaments upregulated on the surface of PAO1 Δ*PA2133*‡ cells are indeed CupE.

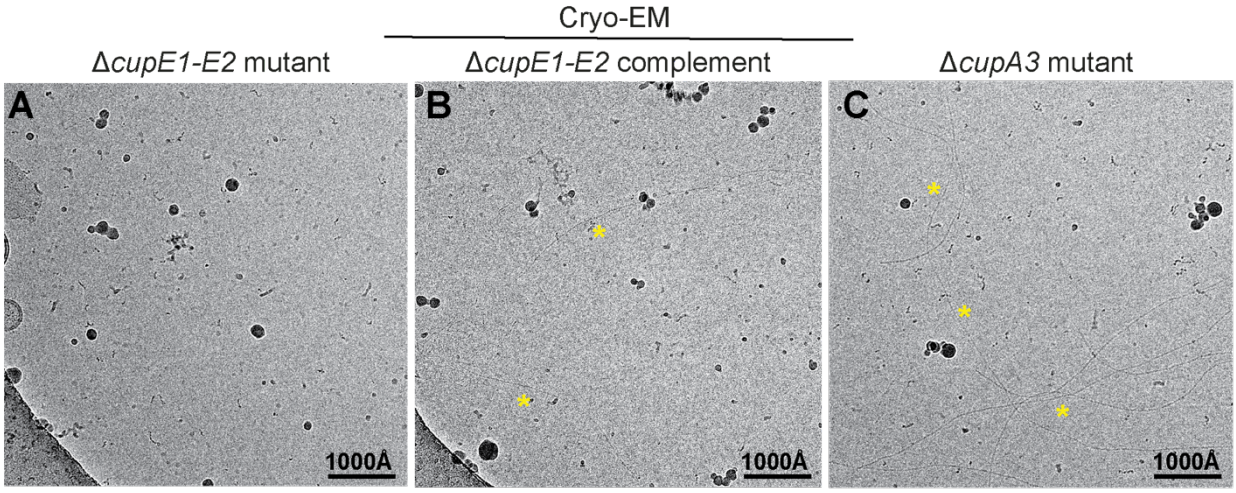


Figure 4.3: A mutant panel confirms the filaments upregulated in *P. aeruginosa* PAO1 Δ*PA2133*‡ are CupE. (A) Cryo-EM of the sheared fraction of PAO1 Δ*PA2133*‡ Δ*cupE1-E2* mutants, demonstrating loss of CupE filaments. (B) Cryo-EM of the sheared fraction of following chromosomal complementation of *cupE1-E2* genes in a PAO1 Δ*PA2133*‡ Δ*cupE1-E2* mutant background. (C) Cryo-EM of the sheared fraction of PAO1 Δ*PA2133*‡ Δ*cupA3* mutants. Areas containing filaments are highlighted by yellow asterisks in images B and C.

4.3. *In vitro* purification of recombinant CupA1 and polymerization trials

4.3.1. Protein sequence analysis

The filaments sheared from the surface of Δ*PA2133*‡ mutants were originally suspected as CupA given *PA2133* is encoded in the *cupA* operon and that gene expression of *cupA1* is most highly upregulated in the absence of Δ*mvaT* (4). Further, the size of processed CupE1 and CupA1 are similar (15 kDa and 16 kDa respectively), making differentiation difficult in early SDS-PAGE gels of the Δ*PA2133*‡ sheared fraction. In light of these factors, *in vitro* reconstitution of CupA filaments from recombinant CupA1 was trialled in parallel to obtain the CupA filament structure and/or compliment *in situ* findings. Sequence analysis of the major fimbrial subunit, CupA1, was performed to inform the design of recombinant constructs using programs packaged in the MPI Bioinformatics Toolkit (243). HHPred analysis (243) revealed CupA1 shares ~19% structural similarity with FimA and PapA of *E. coli* (probability 99.83, E value 3.2 x 10^{-18} and probability 99.8, E value 1.1 x 10^{-17} respectively). The N-terminal extension of fimbrial subunits consist of strictly conserved glycine and cysteine residues, as well as hydrophobic residues within the P2-P5 pocket (437). ClustalΩ alignment of CupA1 against FimA and PapA confirmed the N-terminus of CupA1 encodes glycine and cysteine residues, as well as hydrophobic isoleucine, valine and phenylalanine residues in the P2-P5 pocket (Figure 4.4). These findings suggest that CupA1 monomers are capable of participating in donor strand complementation (DSC) during fimbrial assembly.

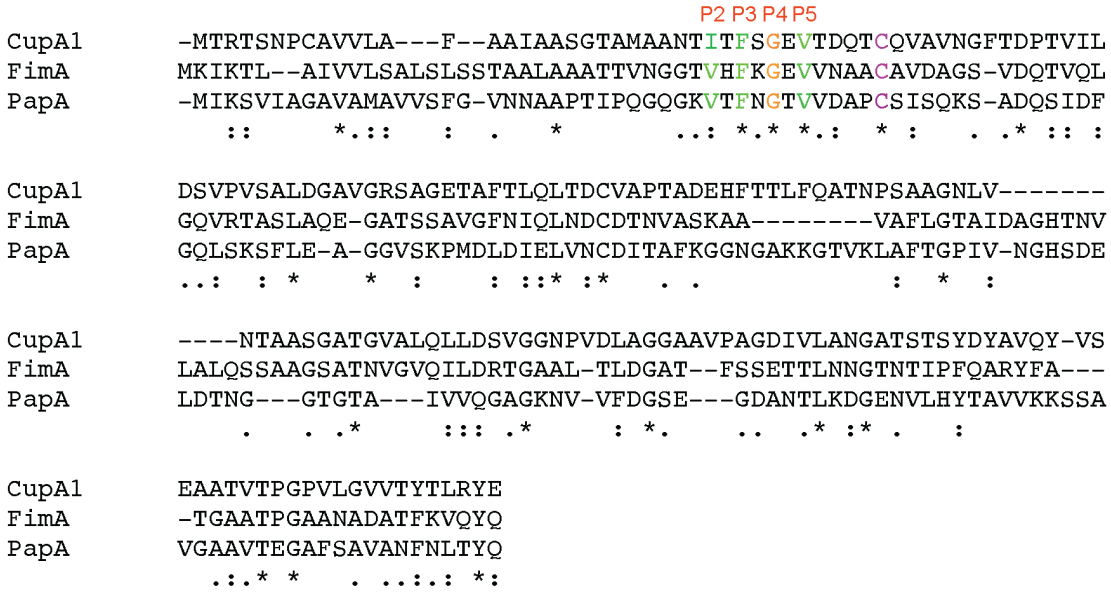


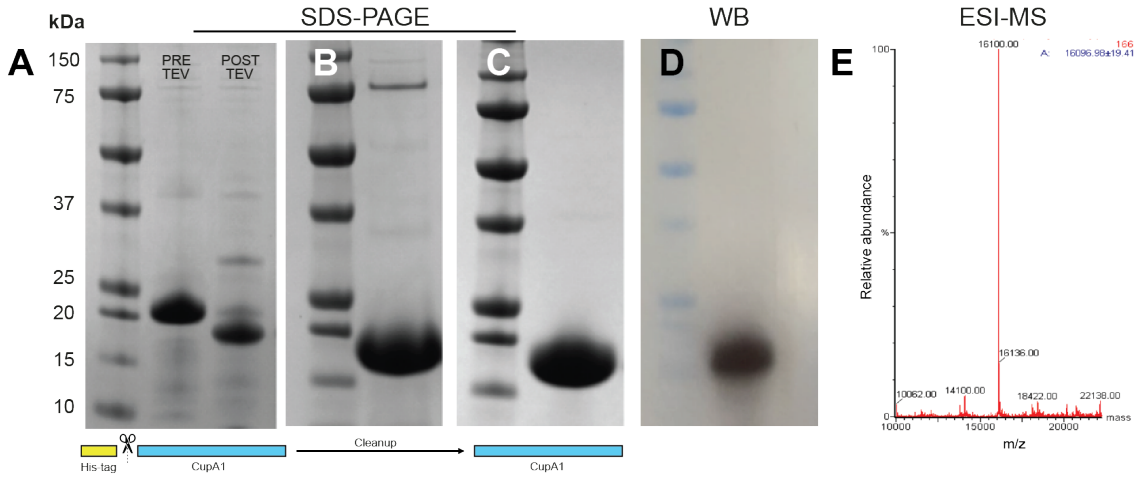
Figure 4.4: Multiple sequence alignment of the CupA1 fimbrial subunit against PapA and FimA

ClustalΩ alignment of the CupA1 amino acid sequence against FimA and PapA reveals conservation of a cysteine residue (coloured purple), a glycine residue (coloured orange) and hydrophobic residues (coloured green), within the P2-P5 pocket of the N-terminal extension. The symbol '*' denotes perfect alignment, ':' in groups exhibiting strong similarity and '.' in cases of groups exhibiting weak similarity.

4.3.2. Construct design and purification

Given the success in reconstitution of Fim and Pap filaments *in vitro*, similar strategies were adopted for polymerisation of CupA filaments (126, 152, 438). Fim filaments were reconstituted by over-expression of FimA monomer and incubation under acidic conditions, demonstrating the monomer is capable of self-assembly *in vitro* (152). In contrast, Pap reconstitution requires co-expression of PapA and the PapD chaperone, suggesting chaperone stabilisation promotes *in vitro* assembly (126, 438). During this work, CupA1 and the CupA2 chaperone were cloned into pETDuet vectors for co-expression (Table 2.1), however poor protein yields limited the scope of experiments. The reconstitution of CupA filaments from purified recombinant CupA1 was hence prioritised. The native *P. aeruginosa* PAO1 *cupA1* gene was codon optimised for expression in *E. coli* in all constructs (Table 2.1). In other work,

recombinant FimA has been demonstrated as insoluble when expressed in the cytoplasm, localising within inclusion bodies (152). Although MBP, GST and SUMO solubility tags were trialled, removal of the N-terminal signal sequence (residues 1-25) and incorporation of an N-terminal poly-histidine tag were sufficient to achieve soluble, cytoplasmic CupA1 (Table 2.1). As the N-terminal extension is essential for DSC, separation of CupA1 and poly-histidine tag was achieved by TEV protease digestion and reverse nickel chromatography (Materials and Methods) (Figure 4.5A). Gel filtration and ion exchange chromatography were effective in purifying CupA1 away from contaminants, with SDS-PAGE of the final preparation revealing a single, major band at 16 kDa (Figure 4.5B,C). Polyclonal anti-CupA1 antibodies, generated against recombinant CupA1 in this work, successfully bound recombinant CupA1 via western blot (Figure 4.5D). The identity of the major product was confirmed as CupA1 by tandem and ESI-MS analysis (79.8% sequence coverage) (Figure 4.5F), with a mass of 16.1 kDa (Figure 4.5E). The concentration of the final CupA1 preparation was 4.8 mg/mL (buffer composition: 50mM Tris/HCl pH 7.5, 150mM NaCl), obtained from an original 6L culture.



F COVERAGE BY TANDEM-MS

MTRTSNPCAVVLAFAAIAASGTAMAANTITFSGEVTDQTCQVAVNGFTDPTVILDSVPVSALDGAVGRSAGETAFTLQLTD
CVAPTADEHFTTLFQATNPSAAGNLVNTAASGATGVALQLLDSVGGNPVDLAGGAAVPAGDIVLANGATSTSYDYAVQYVS
EAATVTPGPVLGVVTYTLRYE

Figure 4.5: Purification and characterisation of recombinant CupA1

(A) SDS-PAGE of recombinant CupA1 before (pre) and after (post) TEV cleavage, illustrating shift to a ~16 kDa species following digestion. (B) SDS-PAGE following gel filtration chromatography of CupA1, illustrating the major ~16 kDa band and a minor contaminant at ~75 kDa. (C) SDS-PAGE following ion-exchange chromatography illustrates removal of the 75 kDa contaminant, resulting in purified CupA1. (D) Anti-CupA1 antibodies bind to purified, recombinant CupA1, with strong signal at 16 kDa via western blot. (E) ESI-MS spectra illustrates a major peak at 16.1 kDa. (F) Amino acid residues of the major fimbrial subunit, CupA1, with red letters illustrating residues covered by tandem MS analysis (79.8% of the unprocessed CupA1 sequence).

4.3.3. *In vitro* polymerisation trials

Negative-stain EM was used to screen the CupA1 preparation for evidence of polymerization and/or filament formation. Grids revealed aggregates of varying size; indicative of protein instability and that higher order assembly had not occurred. The recombinant CupA1 preparation was therefore subjected to a range of conditions in an effort to promote polymerization (the details and rationale for each summarised in Table 4.1). Upon completion of each trial, solutions were centrifuged and the corresponding supernatants and pellets screened using SDS-PAGE and negative-stain EM. Despite these efforts, CupA1 polymerization was not observed, suggesting additional factors such as increased CupA1 protein concentration, monomer stabilisation by chaperones (CupA2 or CupA5) or filament nucleation by the usher (CupA3) are required for filament assembly *in vitro*.

Table 4.1: Summary of conditions trialled for reconstitution of CupA filaments.

Adjusted parameters	Buffer/s	CupA1 concentration	Rationale
Incubation time and temperature Incubated for 24, 48, 72 hrs or 1 week at either 4°C or room temperature	50 mM Tris, 150 mM NaCl, pH 7.5	50-100μM	Donor strand complementation is a slow process *in vitro*; on the time scale of hours to days (150). Fim filaments were reconstituted from 50 μM of FimA monomer after 7 days incubation at room temperature (152). Similarly PapA filaments were reconstituted from 50 μM PapD:PapA preparations after 72 hours incubation at room temperature (126).
pH	20 mM acetic acid NaOH pH 4, 150 mM NaCl 50 mM Tris/HCl pH 6.5 or 8.5, 150 mM NaCl	50-100μM	*In vitro* assembly of fimbrial rods from FimA monomers (50 μM) was achieved at a pH near the isoelectric point of FimA (pI:5) (152). As the theoretical pI of CupA1 is 3.78, a pH of 4 was initially screened, as well as pH 6.5 and 8.5.
Addition of crowding agents	50mM Tris/HCl, 150 mM NaCl pH 7.5, 2% (w/v) PEG 6000	50-100μM	The use of crowding agents such as PEG may promote protein:protein interactions. Native Fim filaments were precipitated using PEG6000 previously (152).
Buffer Exchange	25 mM HEPES /NaOH pH 7.5, 150 mM NaCl	50-100μM	Protein stability may be improved in HEPES buffer given its pH stability across a range of temperatures.
Salt concentration	50mM Tris/HCl pH 7.5 with either 50mM, 500 mM or 1M NaCl 50% (w/v) ammonium sulphate precipitation	50-100μM	The solubility of proteins is affected as ionic strength is varied. As CupA1 monomers are salted in or out, protein:protein interactions may occur. Native CupB, CupC and CupE sheared filaments were precipitated using 50% (w/v) ammonium sulphate previously (149).

4.4. *In vitro* purification of recombinant CupE1

4.4.1. Protein sequence analysis

Following identification of CupE1 in filaments sheared from the surface of the Δ*PA2133*‡ mutant, efforts were made to purify recombinant CupE1 to complement structural investigations of natively-assembled CupE filaments. CupE1 shares highest structural similarity to the fimbrial subunit of Csu pili of *A. baumanni*, CsuE (16.5%, probability 99.46, E-value: $8.2x10^{12}$), as well as a putative fimbrial subunit expressed by the pathogen *Burkholdheria pseudomallei* (16.8%, probability 99.59, E-value: $3.33x10^{14}$) (Uniprot ID: Q63UH6). ClustalΩ alignment of CupE1 against CsuE, Q63UH6, FimA and PapA confirmed the N-terminal extensions of CupE1, CsuE and Q63UH6 encode a conserved cysteine residue, whilst only Q63UH6 encodes a conserved glycine reside in the P4 position of the P2-P5 pocket (Figure 4.6). In addition, hydrophobic P2 and P5 residues are present in CupE1, CsuE and Q63UH6, but are lacking in the P3 position of CupE1 and CsuE (Figure 4.6). These results illustrate potential differences in the mechanism of donor strand complementation of these fimbrial subunits compared to that of canonical FimA and PapA.

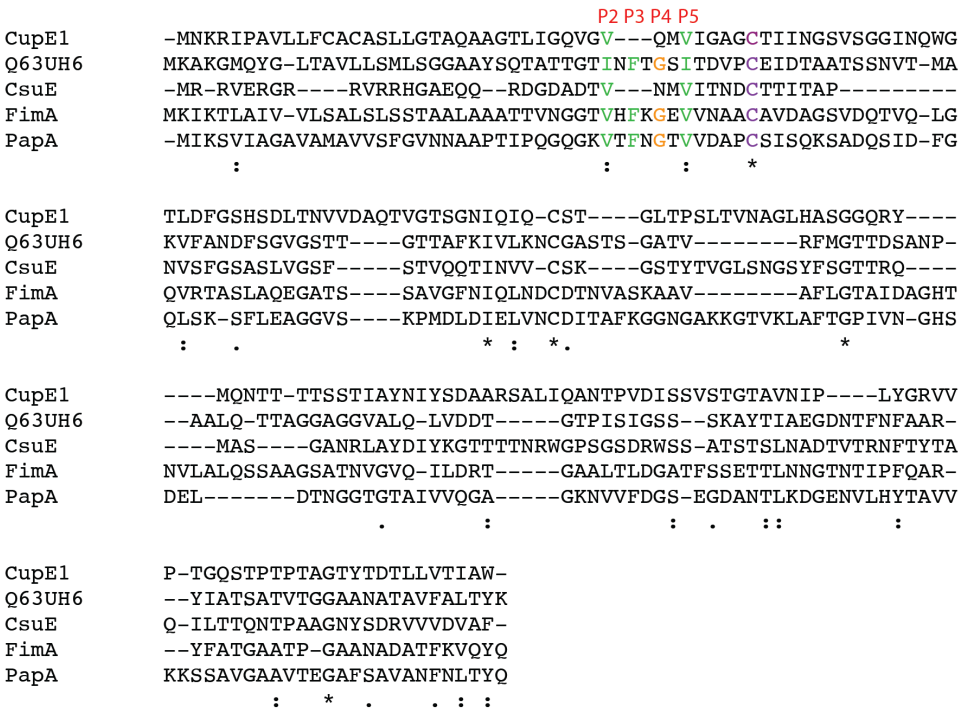


Figure 4.6: Multiple sequence alignment of the CupE1 fimbrial subunit against structural homologs

ClustalΩ alignment of the CupE1 amino acid sequence against CsuE, Q63UH6, FimA and PapA reveals CupE1 encodes a conserved cysteine residue (coloured purple) but lacks a conserved glycine residue in the P4 position (coloured orange). Hydrophobic residues (coloured green) are encoded in the P2 P5 pocket of CupE1, but lacking in the P3 position. The symbol '*' denotes perfect alignment, ':' in groups exhibiting strong similarity and '.' in cases of groups exhibiting weak similarity.

4.4.2. Construct design and purification

Given the structural similarity of CupE1 to CsuE and Q63UH6, purification workflows applied for structural biology of these proteins were adapted for CupE1 in this work. The CsuC-CsuE complex was crystallized from *E. coli* periplasm by co-expression of the chaperone (CsuC) with the fimbrial subunit (258). In contrast, the Q63UH6 dimer was crystallized by over-expression of processed Q63UH6 monomers in the cytoplasm (439). As such a library of constructs were designed for the purification of soluble, cytoplasmic CupE1. The native *P. aeruginosa* PAO1 *cupE1* gene was codon optimised for expression in *E. coli* in all constructs (Table 2.1). Initial cloning revealed expression of the processed *cupE1* gene fragment results in accumulation of insoluble CupE1 in inclusion bodies. SUMO and MBP tags were therefore cloned upstream of the *cupE1* gene to improve solubility. An N-terminal MBP-poly-histidine tag was found to be successful in achieving over-expression of soluble, cytoplasmic CupE1 (Figure 4.7A). CupE1-MBP-His was successfully purified using nickel-affinity chromatography (Figure 4.7B), where addition of 20% (v/v) glycerol was essential to prevent precipitation following elution (Materials and Methods). The protein was subjected to 3C protease digestion to separate CupE1 from the MBP-poly-histidine tag; freeing the N-terminus for donor strand complementation. SDS-PAGE gels revealed the protein was resistant to digestion with commercially purchased and in-house purified 3C proteases, with visibly low yields of the 16 kDa CupE1 product relative to undigested protein (Figure 4.7B,C). A commercial GST-Syk control yielded cleavage products at the expected size, confirming the enzymatic activity of 3C protease (Figure 4.7D). These yields were not improved by varying the protease concentration (2U-8U trialled), incubation temperature (room temperature or 4°C) or time (12, 24 and 48 hrs), suggesting protein fold or aggregation may be affecting accessibility of the 3C protease cleavage site. As efforts were prioritised to structural investigations of natively-assembled CupE filaments, this construct was not explored further.

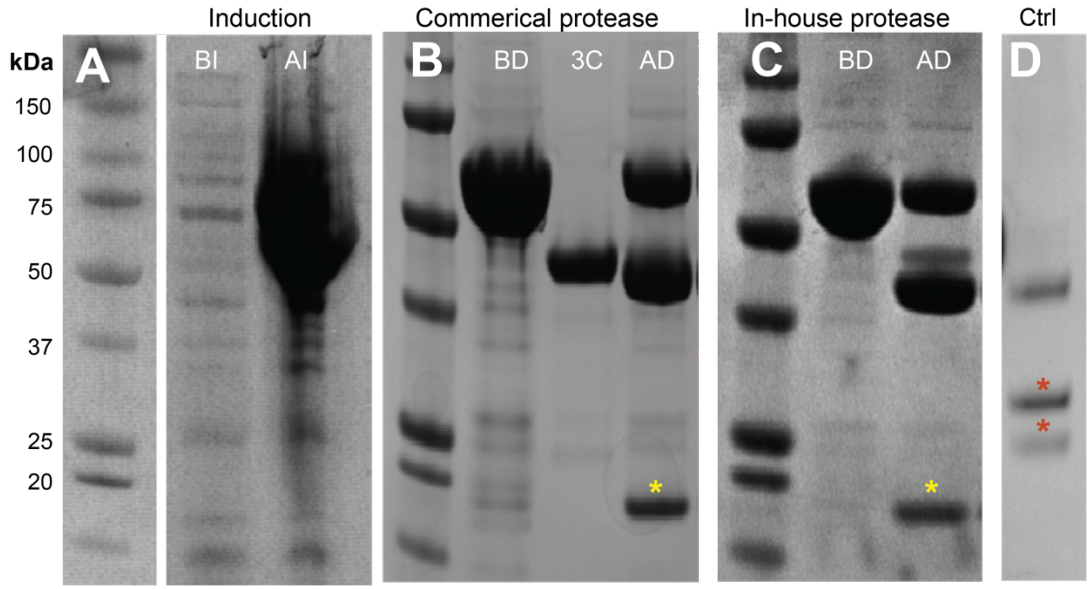


Figure 4.7: Purification and digestion trials of CupE1-MBP-His

(A) SDS-PAGE of cell lysates of *E.coli* BL21 transformed with pETM44-*cupE1*, before induction (BI) and after induction (AI) with 1mM IPTG. CupE1-MBP-His is visibly over-expressed with a band at ~58 kDa. (B) SDS-PAGE of CupE1-MBP-His before digestion (BD) with commercial HRV 3C protease (labelled 3C, ~47 kDa) and after digestion (AD); yielding the CupE1 cleavage product (~16 kDa, yellow asterisk). (C) SDS-PAGE of CupE1-MBP-His before digestion (BD) and after digestion (AD) with in-house purified 3C protease (~47 kDa); yielding the CupE1 cleavage product (~16 kDa, yellow asterisk). (D) SDS-PAGE of GST-Syk control digested by commercial HRV 3C protease, demonstrating bands at the expected size for the 3C protease (higher band ~47 kDa) and GST-Syk digestion products (orange asterisks, based on manufacturer's description).

4.5. Sub-tomogram averaging as a strategy for 3D reference generation and symmetry determination.

Classical chaperone usher filaments are helical assemblies as illustrated by the atomic structures of Fim and Pap fimbriae (126, 152). HHPred sequence analysis of CupE1 reveals ~14% structural similarity with the major fimbrial subunits, FimA (probability 99.25, E value 5.8 $x10^{-10}$) and PapA (probability 99.19, E value 3.2 $x10^{-9}$) (MPI Bioinformatics Toolkit) (243). This study hence aimed to resolve the structure of natively-assembled CupE filaments using single particle-based helical reconstruction, given the structural similarity in subunits and presence of accessory genes in the *cupE* operon encoding classical assembly machinery.

When resolving high-resolution structures of filamentous samples, knowledge of their symmetry allows the appropriate structural constraints to be applied during reconstruction (394, 440). Helical symmetry parameters are defined by the helical rise (translation) and twist (rotation) along the helical axis and are classically determined by Fourier-Bessel ordering, in which the layer lines in diffraction patterns are indexed (441). In this project, cryo-ET was used to determine the helical symmetry parameters of CupE filaments (442). As cryo-ET generates 2D images at multiple tilt angles from which a 3D volume of the specimen is reconstructed, symmetry can be measured by inspection of the volume (443). To trial this approach, an independent tomography dataset was acquired and reconstructed to generate a reference for symmetry determination of CupE filaments.

Ten tomograms of the Δ*PA2133*‡ sheared fraction were generated and subjected to sub-tomogram averaging using pipelines previously described in RELION (Materials and Methods) (390). CupE filaments were manually selected within each tomogram using IMOD and coordinates used for picking in RELION (400), with a total of 2,696 particles extracted. Sub-tomograms were extracted, collapsed onto a 2D image and subjected to two-dimensional averaging using regularized likelihood optimization (403). Inspection of 2D class averages

confirmed the presence of filaments, which were visibly helical in morphology (Figure 4.8A). A featureless cylindrical volume was generated using the `relion_helix_toolbox` program and used as the initial reference map for 3D refinement, with no helical symmetry imposed. The resulting reconstruction reached a resolution of 23Å following 3D refinement and post-processing in RELION. Visual inspection of the 3D volume revealed severe flattening of the helix (Figure 4.8B). Image processing strategies were hence applied to improve helix morphology; drawing from troubleshooting advice described in the RELION wiki (http://www2.mrc-lmb.cam.ac.uk/relion [Online, accessed 2020-21]). These strategies included variation in box size (increased to improve alignments by including more helical subunits into the reconstructed map), variation of initial angular sampling during 3D refinement and removal of 30Å duplicates prior to refinement (to prevent any overlapping of helical subunits during alignment). Despite these approaches, no improvement in the final 3D reconstruction was observed.

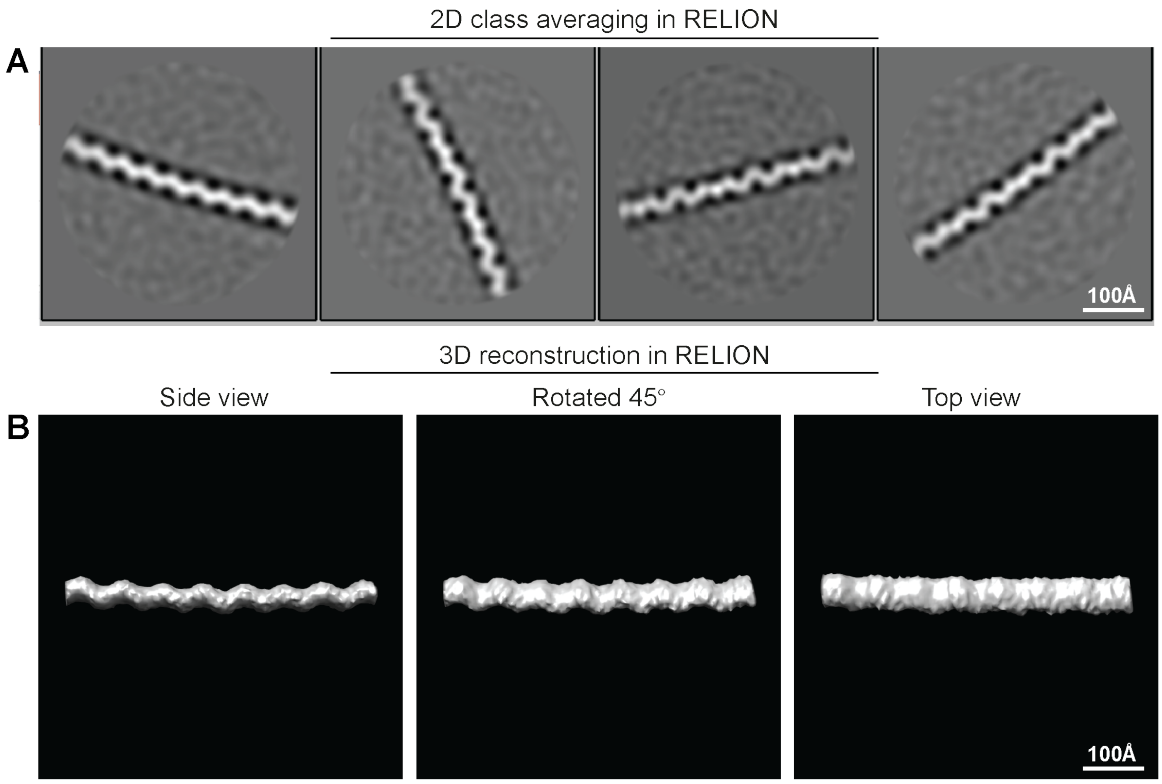


Figure 4.8: Sub-tomogram averaging analysis of CupE filaments using RELION

(A) Two-dimensional class averages of CupE demonstrate filaments are helical in morphology. Class averages were generated from 2D projections of tomographic data in RELION. (B) Sub-tomogram averaging of CupE filaments in RELION reveals severe anisotropy in the final CupE reconstruction (compare side view with rotated 45° and top views of the grey isosurface).

Several software packages have been developed to support particle alignment and averaging in sub-tomogram averaging workflows, each differing in their algorithmic approach (444-448). The AV3 software package (404) was tested to compare sub-tomogram averaging results to those obtained using RELION in this study, and to determine whether the quality of 3D reconstruction could be improved. Sub-tomograms were extracted by randomly sampling filaments with priors perpendicular to the filament axis in 360° (Figure 4.9A). The extracted coordinates were overlaid with original tomograms and visually assessed using USCF chimera (Figure 4.9B) (408). The resulting 3D reconstruction revealed comparable, low-resolution

features along the surface of the helix, implying a solution had not been converged upon (Figure 4.9C). The reconstruction was also not improved by varying initial angular sampling parameters. Collectively, these findings demonstrate the quality of reconstruction may be affected by particle number/data limitation, preferential orientation or the effects of the missing wedge.

As the CupE reconstruction generated in RELION more closely resembled a helix, this volume was selected for initial symmetry estimation using the `relion_helix_toolbox` program (`--search` function). A wide search range was first applied for the helical rise and twist and refined as values stabilised, resulting in an estimated helical rise of 33.23Å and twist of 215°. These helical symmetry parameters, along with the RELION-generated reconstruction, were used as inputs for single particle-based helical reconstruction of CupE (detailed in the following section).

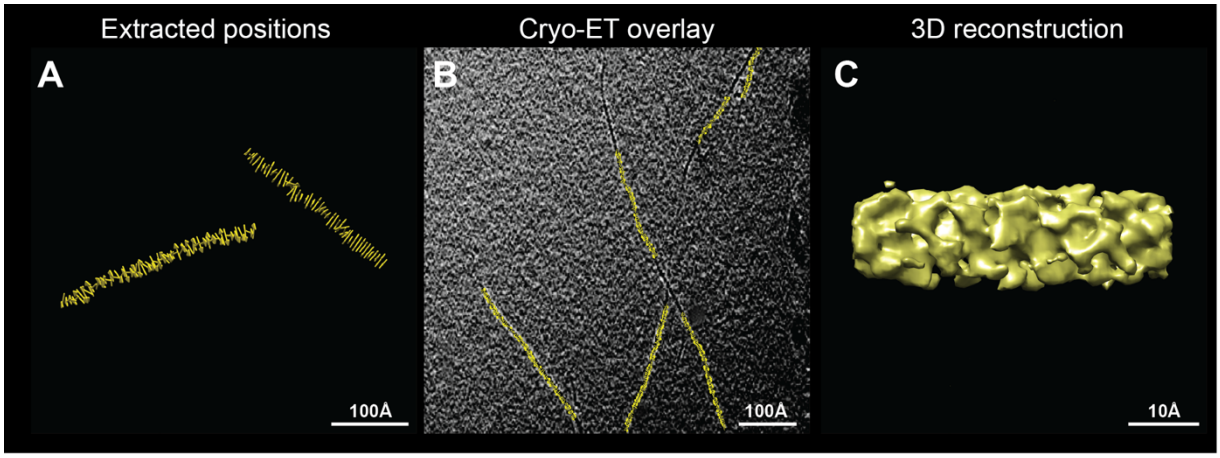


Figure 4.9: Sub-tomogram averaging analysis of CupE filaments using a modified AV3 package.

(A) Examples of sub-tomograms extracted along two CupE filaments, defined randomly in 360° with positions perpendicular to the filament axis. (B) A virtual slice through a tomogram of the Δ*PA2133*‡ sheared fraction illustrates correct positioning of sub-tomograms (yellow, overlaid arrows) along CupE filaments. (C) 3D reconstruction of CupE filaments using the AV3 software package reveals lack of detail or low resolution features from the dataset.

4.6. CupE filaments are helical, consistent with classical chaperone usher assemblies

To gain insight into the structure of CupE filaments at higher resolution, single particle-based helical reconstruction was applied to cryo-EM images of the Δ*PA2133*‡ sheared fraction. Two independent cryo-EM datasets were acquired and combined for image processing in RELION (2,367 micrographs in total) (Materials and Methods). Segments were extracted along the length of CupE filaments at regular intervals (Figure 4.10A). 2D class averaging confirmed the presence of helical filaments, whose morphology was consistent with that witnessed in cryo-ET averages (compare Figure 4.8A and Figure 4.10B). Further, repeating subunits were visible along the helix in the 2D class averages, with one full turn of the helix measuring at ~173Å, encompassing five subunits per turn (Figure 4.10B). This corresponds with the estimated helical rise of 33.23Å (Section 4.5). Fourier-transform of the 2D class averages revealed layer lines, characteristic of helical assemblies, with the outermost layer line measured at approximately 7.5Å (Figure 4.10C, yellow asterisk).

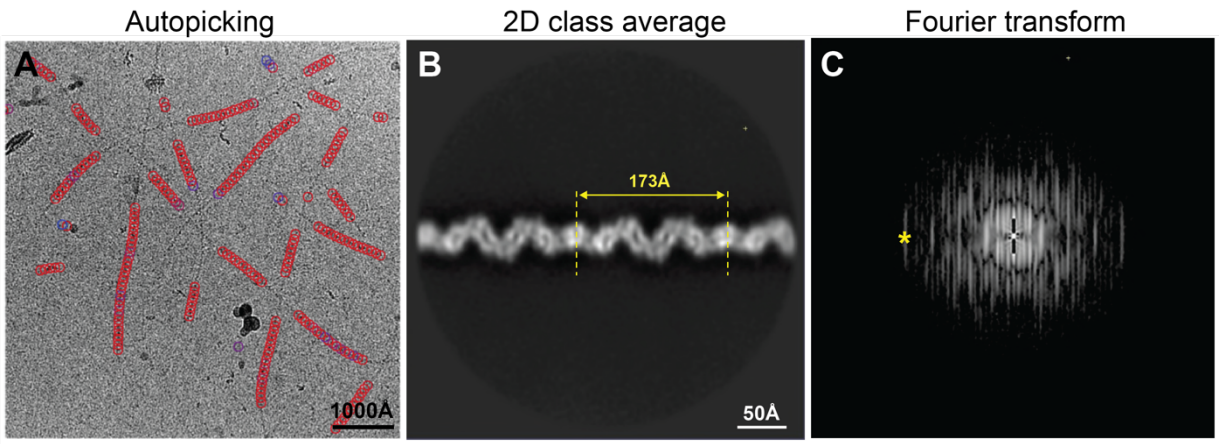


Figure 4.10: 2D classification of CupE filaments confirms a helical assembly

(A) A cryo-EM micrograph overlaid with auto-picked locations (red circles) along CupE filaments generated using the RELION auto-picking algorithm. (B) 2D class averages of CupE illustrates visibly helical filaments, with five subunits per turn and distance of ~173Å per turn. (C) Fourier transform of CupE 2D class averages reveals multiple layer lines in Fourier space, the furthermost layer line at ~7.5Å is highlighted by an asterisk.

2D classes averages containing straight CupE filaments were selected (resulting in 246,558 particles) and proceeded onto 3D refinement. Structural constraints were applied based on previously estimated CupE helical parameters (rise: 33.23Å, twist: 215°), along with the corresponding tomography-generated reconstruction as an initial reference (details in previous section). The final CupE reconstruction was refined to a resolution of 4.54Å (Figure 4.11 and Figure 4.12A). The quality of the data and processing was validated using the gold standard Fourier shell correlation (FSC) criterion by applying a cut-off of 0.143 between two independent half maps (407). A summary of the image processing workflow and FSC curves are illustrated in Figure 4.11.

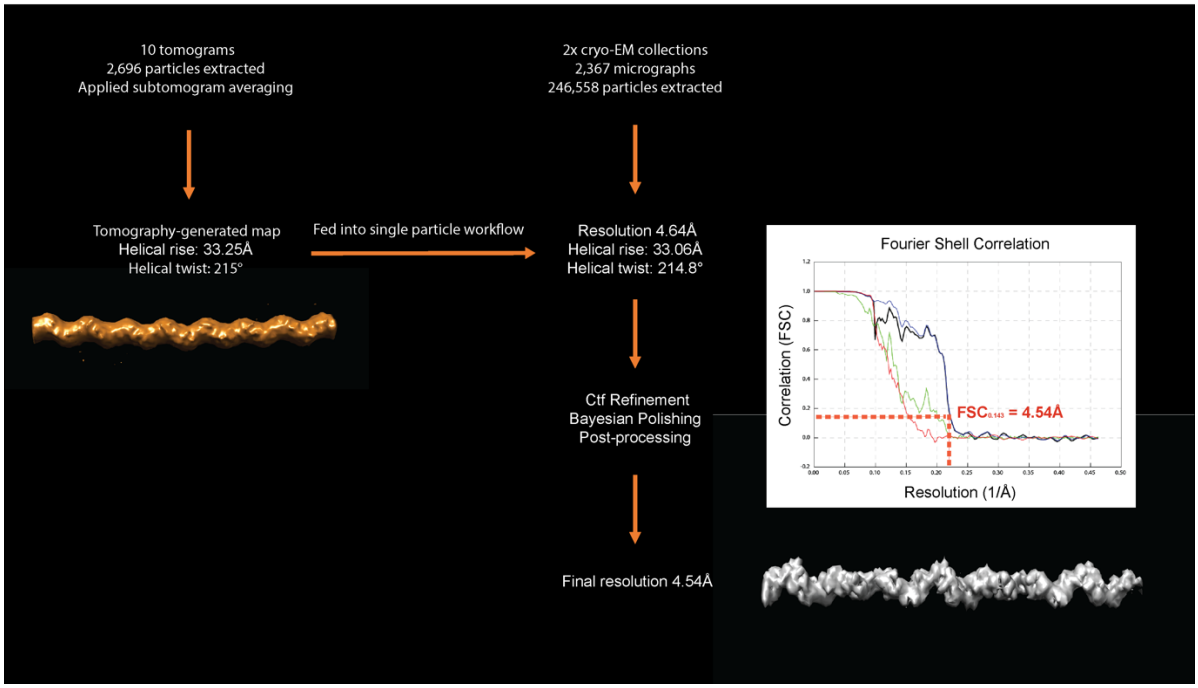


Figure 4.11: Single particle-based helical reconstruction of CupE

Summary of the image processing workflow applied in this work for resolution of CupE filaments to 4.54Å. Micrographs from two independent cryo-EM collections were inputted for processing in RELION. In parallel, electron cryo-tomograms were collected to generate an initial 3D reference (orange volume), from which helical symmetry parameters were estimated, and subsequently inputted into single particle-based workflows. The reconstruction reached a resolution of 4.54Å following several rounds of 3D refinement, with a final resolution of 4.54Å following application of CTF refinement, Bayesian polishing and B-factor sharpening during post-processing. The final CupE reconstruction (grey isosurface) and corresponding Fourier shell correlation (FSC) are illustrated. The density was filtered to a resolution of 4.54Å using the gold standard FSC at a 0.143 cut-off.

The reconstructed CupE filament shows a helical rise of 33.06Å and twist of 214.8°, with five subunits per helix turn, reaffirming 2D class averages. Although Fim and Pap fimbriae are tightly-packed helically-wound rods with a central lumen, CupE filament appear to be a single chain of alternating subunits with a diameter of ~60Å. A predicted model of the CupE1 monomer was generated using the CsuE crystal structure; with which CupE1 shares the highest structural similarity (16.5%, probability 99.46, E-value: $8.2x10^{12}$). Although secondary structural elements are not resolved, the predicted CupE1 monomer fits reasonably into subunit densities, strengthening the accuracy of reconstruction (Figure 4.12B). The orientation/ positioning of CupE1 subunits in the CupE volume is based on the hypothesized donor stand complementation mechanism between archaeal pilin subunits (complementation of the P2-P5 pocket of one CupE1 subunit by the Nte of the neighbouring subunit) (56, 180). The angle between the binding domains of two subunits creates an overall C-shape, which repeats along the length of the CupE chain.

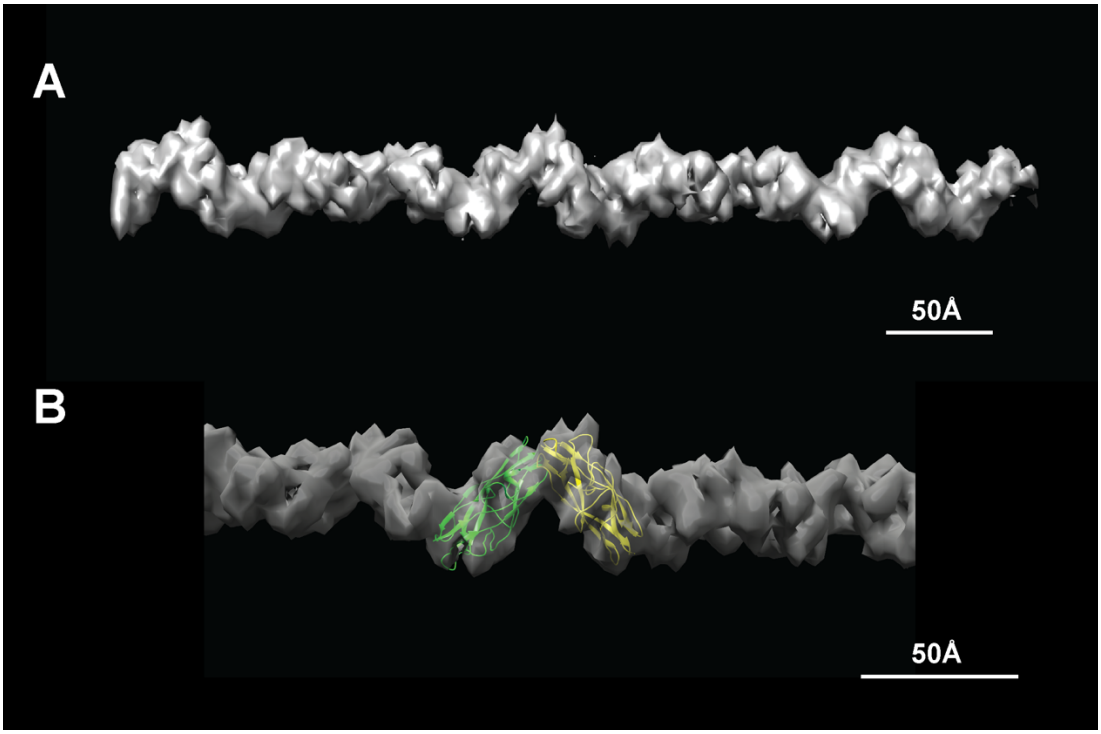


Figure 4.12: Cryo-EM structure of CupE filaments at 4.54Å resolution

(A) Final reconstruction of CupE to 4.54Å resolution (grey isosurface), demonstrating alternating helical subunits along the length of the filament. (B) The predicted CupE1 monomer fitted within subunit densities of the CupE reconstruction (gold and green ribbon structures represent two independent monomers; generated using Modeller packaged in the MPI Toolkit (243)). The two monomers were fitted into the CupE reconstruction using USCF chimera (408). The orientation of CupE1 monomers was chosen based on the hypothetical DSC mechanism between archaeal pilin subunits (56, 180).

To improve the resolution of the CupE reconstruction, conformational heterogeneity and flexibility of the filament were explored. Slight curvature was noted in a proportion of filaments in early 2D classification runs; suspected to affect the quality of alignment during downstream 3D refinement (compare Figure 4.13A,C with B,D). To remove classes containing curved filaments, four additional rounds of 2D classification were performed with increased class number (from an initial value of 10 to between 25-200 per round), iteration number (from an initial value of 15 to 25) and resolution E-step (increased from 7Å to filter for features from

25Å to prevent overfitting during alignment). Further, the `--maxsig` parameter was used (value of 5) to reduce the number of orientations searched per iteration, facilitating the population of additional classes. The applied parameters visibly separated out classes containing curved and straight filaments, with 233,950 'cleaned' particles obtained following the final round of 2D classification (Figure 4.13E). Despite the removal of curved and bad classes, no improvement in resolution was observed in the final CupE reconstruction.

In light of this, conformational heterogeneity was explored by applying 3D classification to the 'cleaned' dataset following refinement. 3D classification returned comparable symmetry parameters and filament distribution per class (2-4 classes trialled), confirmed by visual inspection and overlay of reconstructions using USCF chimera (Figure 4.14) (408). These results support rigidity in the CupE helix and that a single conformational state is likely to be present in the dataset. Lack of improvement in the resolution of the CupE reconstruction suggests further data collection and image processing experiments are required.

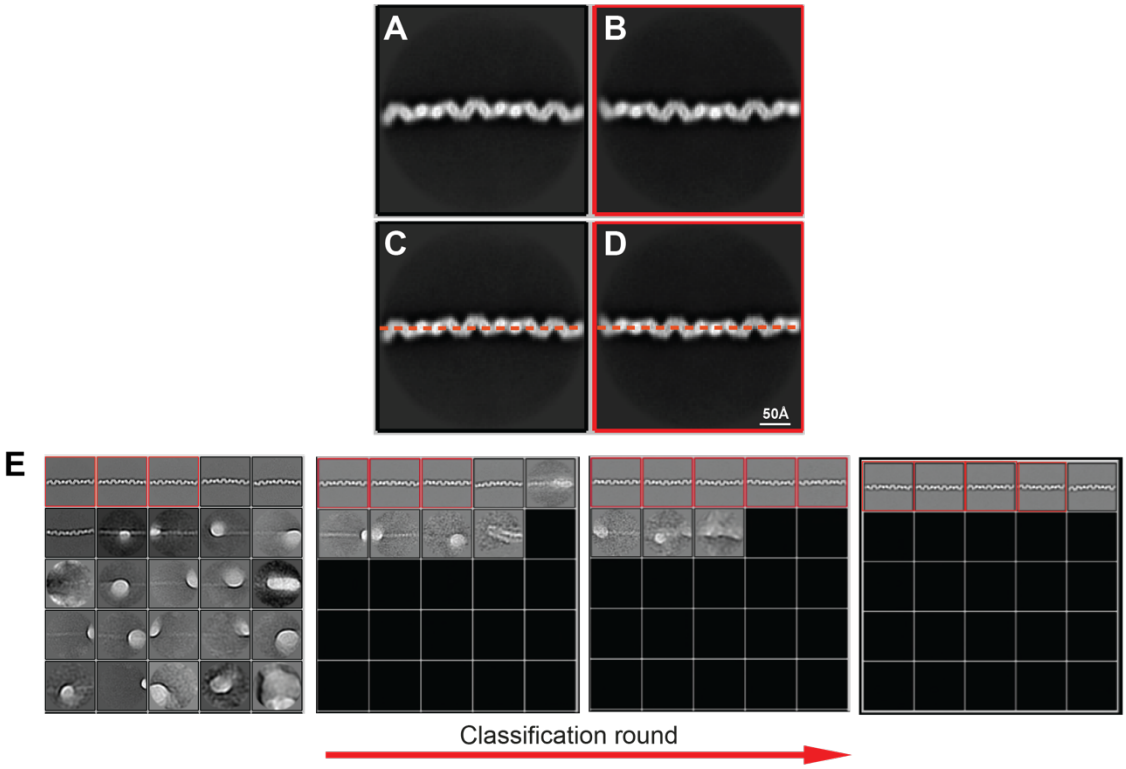


Figure 4.13: Removal of curved CupE filament classes from single particle datasets in RELION

(A) Example of 2D class averages of curved and (B) straight CupE filaments (red box) generated in RELION. (C, D) A dotted line is drawn across the centre of the filaments to further demonstrate the difference between (C) curved classes which visibly taper downward at both ends relative to the central axis, as compared with (D) straight classes which to not deviate from the central axis. (E) Image processing strategy to separate curved and straight CupE filament classes. The 2D class averages outputted after four rounds of sequential 2D classification are illustrated, where curved filaments, straight filaments and junk classes are clearly distinguishable. The selected straight CupE classes which proceeded onto the following round of classification are highlighted by red boxes.

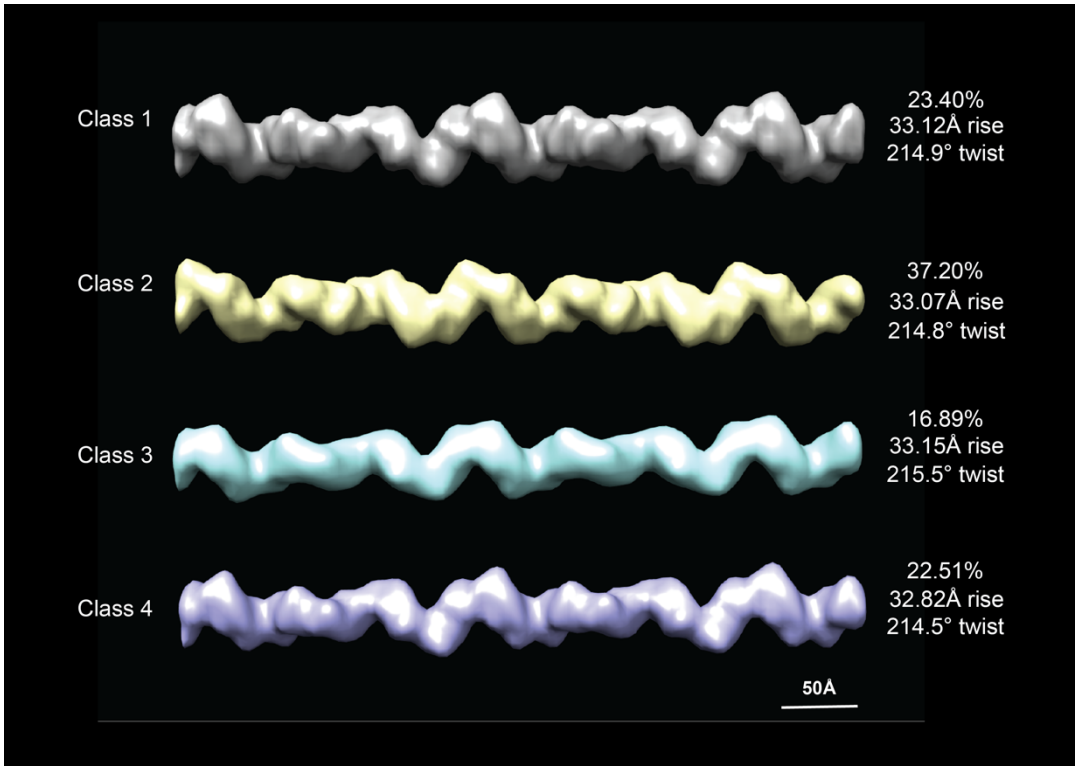


Figure 4.14: 3D classification of CupE filaments in RELION

Results following 3D classification of refined CupE filaments in RELION. The class number, three-dimensional volume and helical symmetry parameters for each 3D class are illustrated. All volumes were filtered to the same threshold and displayed using USCF chimera (408).

CHAPTER 4 DISCUSSION

Proteinaceous adhesins mediate attachment of bacteria to surfaces during biofilm formation, including type IV pili, curli fibres and chaperone usher proteins (CUPs) (73). The pathogen *P. aeruginosa* PAO1 encodes four putative chaperone usher pathways (*cupA*, *cupB*, *cupC* and *cupE*) which contribute to biofilm formation (3, 56, 149). Whilst the regulation and structure of classical CUPs, such as Fim and Pap fimbriae, have been extensively investigated in *E. coli*, the *cup* clusters of *P. aeruginosa* and other bacterial species remain largely unexplored.

In this study, genetic components influencing the assembly of CupE filaments on the PAO1 cell-surface were identified. Although the global transcriptional regulator MvaT represses *cupA*, *cupB*, *cupC* and *cupE* gene expression (4), this work demonstrated Δ*mvaT* deletion is insufficient to achieve filament assembly alone. In line with this, additional regulatory elements are required for assembly of CupB and CupC in Δ*mvaT* deletion strains (50, 56). Further, whilst Δ*mvaT* deletion upregulates *cupA1* gene expression to the greatest extent (15-fold), CupA has not been shown to be expressed on the cell surface in this genetic background previously (4).

PA2133, an EAL-domain containing phosphodiesterase, is encoded directly following the *cupA5* gene (19). Although PA2133 is widely hypothesized to repress *cupA* expression given its proximity to the *cupA* operon (210), this study demonstrated Δ*PA2133* deletion upregulates CupE filaments in an Δ*mvaT* deletion strain, as oppose to CupA. Whilst *cupA1* is most upregulated 15-fold upon Δ*mvaT* deletion, elements of the *cupE* cluster are collectively upregulated between 2.5-6.5 fold (4). The presence of cell-surface CupE is therefore not unexpected. In addition, these findings suggest *cupA* is repressed by other regulatory elements in the absence of MvaT and PA2133, such as the MvaU transcriptional regulator or PA2110,

MorA and PvrR phosphodiesterases (211, 449). Although CupA filaments are not upregulated in Δ*PA2133* Δ*mvaT* deletion strains, successful purification of soluble recombinant CupA1 was achieved during this project. The insights gained from protein purification and polymerization trials may help inform future biochemical and structural CupA experiments *in vitro*. Finally, these results are the first to implicate c-di-GMP signalling in *cupE* regulation. Elevated intracellular c-di-GMP is associated with the recruitment of chaperone usher fimbriae and transition to a sessile lifestyle. Deletion of PA2133, and subsequent increase in c-di-GMP, may therefore drive CupE-mediated attachment and biofilm formation (investigated in the next chapter).

The PprAB two-component system is implicated in the regulation of CupE cell-surface assembly in wild-type PAO1 under static conditions (56). Similarly, this study demonstrated CupE filaments are upregulated to a greater extent on static cells in a Δ*PA2133* Δ*mvaT* background. The marked increase of CupE on static Δ*PA2133* Δ*mvaT* deletion strains relative to Δ*mvaT* deletion strains suggest the relative contribution of PA2133 is greater than PprAB or that the effects may be cumulative. Indeed, the activity of numerous two-component systems are coordinated with intracellular c-di-GMP signalling (450). The PprA sensor kinase receiver encodes a GAF domain known to bind the secondary messengers cGMP and cAMP (Figure 1.9) (451). Further, the PrpA histidine kinase encodes the canonical H1 and D1 domains which participate in binding and transfer of phosphate, a by-product of secondary messenger hydrolysis (452). PA2133 may therefore influence the PprAB two-component system through its phosphodiesterase activity (453). Although PA2133 is encoded in the *cupA* operon, cross-talk has been demonstrated between two-component systems governing *cupB*, *cupC* and *cupE* expression (18, 50, 52). The presence of several *cup* clusters in the PAO1 genome and overlap in regulatory pathways suggests recruitment of fimbriae during biofilm formation is finely tuned, allowing diversity in substrates and/or environmental stimuli. Further, the upregulation

of CupE filaments under static conditions supports a role in attachment upon surface sensing or in the latter stages of biofilm formation (56).

The major constituent of CupE filaments is the CupE1 fimbrial subunit, consistent with previous cell biology experiments (56). It is unclear if CupE2 and CupE3 contribute to the filament, however CupE1 is still present on the cell surface upon their deletion (56), suggesting assembly is able to proceed. Future deletion and structural experiments will help elucidate whether CupE2 and CupE3 contribute to the CupE filament and the relative stoichiometry between subunits.

The structure of CupE filaments reveals a helical morphology that more closely resembles that of archaic chaperone usher assemblies. Classical chaperone usher assembles are thick and rigid rods (7-10 nm in diameter), whilst archaic chaperone usher fimbriae are typically flexible and thin (2-5 nm) (454). The macroscopic diameter of CupE filaments is ~4 nm, consistent for archaic fimbriae of the σ-clade (172). Further, whilst classical Fim and Pap fimbriae are large, helically wound rods with a central lumen (126, 152), CupE is a single-start filament similar to actin - in that it is not tubular. The angle between the binding domains of two CupE subunits creates an overall C-shape (Figure 4.12), resembling that between the adhesin and pilin domains of CsuE (56). This study hence provides the first high resolution insights into CupE structure and architecture of a completely assembled archaic filament. Whilst the achieved resolution is insufficient for model building, this study provides the initial data, helical symmetry parameters, conformational investigations and 3D reconstructions for input into future CupE structural investigations. Further, a library of recombinant CupE1 constructs were cloned and characterised; providing the foundation for future monomer crystallization and model-fitting experiments. Although evidence supports the 3C protease cleavage site is occluded in the soluble CupE1-MBP construct, alternate tag positioning or protease cleavage sites may be trialled.

Chaperone usher proteins play a crucial role in adhesion and biofilm maturation, though their regulation, structure and function remain relatively unexplored beyond classical assemblies of the *E. coli* spp. This study identifies an additional axis within the complex regulatory network governing *cup* expression in *P. aeruginosa* PAO1 and sets the framework for future structural investigations of archaic CupE fimbriae, ultimately improving our understanding of proteinaceous adhesion in bacteria.

Acknowledgements

I gratefully acknowledge Dr Tanmay Bharat for his assistance across cryo-EM and cryo-ET data collections at the Sir William Dunn School of Pathology. Image processing and sub-tomogram averaging of CupE filaments, including symmetry determination, was supported by Andriko von Kügelgen and Jan Böhning (DPhil students, Bharat Lab). Further, I thank Andriko von Kügelgen for plunging cryo-EM grids in support of the second CupE micrograph collection during the COVID-19 lockdown. A proportion of recombinant CupA1 and CupE1 cloning was assisted by Dr Abul Tarafder (Bharat Lab). A proportion of recombinant CupE1 cloning and expression tests were also conducted by Cara Press (DPhil rotation student, Wellcome Trust). Finally, I sincerely thank Professor Alain Filloux, Eleni Manoli and Kira Glatzel (Imperial College of London) for genetic manipulation and provision of *P. aeruginosa* strains.

CHAPTER 5 AIMS

CupE are archaic chaperone usher fimbriae expressed on the surface of *P. aeruginosa* PAO1. CupE filaments are upregulated in Δ*PA2133* mutants[†] under static conditions; suggesting c-di-GMP signalling influences *cupE* expression. The relative contribution of CupE on adhesion and biofilm formation in a Δ*PA2133*‡ background have not yet been explored. Further, the arrangement of filaments on the cell surface has not been examined for CupE or indeed any other chaperone usher fimbriae to date. The aims of this chapter were hence as follows:

(i) Study the localisation of CupE filaments along the PAO1 cell surface by imaging strains expressing GFP-tagged CupE5 usher and immunofluorescence of CupE filaments using anti-CupE1 antibodies raised previously in this work.

(ii) Compare and quantify the CupE-mediated adhesion phenotype in a Δ*PA2133*‡ genetic background against a library of PAO1 strains, using the crystal violet biofilm assay (409).

(iii) Observe the contribution of CupE filaments to surface attachment and biofilm development in the Δ*PA2133*‡ genetic background using light microscopy.

[†] As in Chapter 4, for simplicity, the Δ*PA2133* Δ*mvaT* Δ*fliC* Δ*pilA* mutant will be referred to as the Δ*PA2133*‡ mutant here-forth.

CHAPTER 5. RESULTS

5.1. Fluorescent labelling and imaging of the CupE5-usher

To study the distribution of CupE filaments along the PAO1 cell surface, the CupE5 usher was tagged with super-folder green fluorescent protein (sfGFP) (455) and imaged using fluorescence microscopy (Table 2.1, Materials and Methods). Tagging was performed in a Δ*PA2133*‡ genetic background given cell-surface CupE is over-expressed in this strain, theoretically increasing the number of CupE5 sites for labelling. Based on HHPred homology predictions (243), CupE5 shares 85% structural homology with the FimD usher (probability 100%, E-value 4.9×10^{-67}) and 52% with the PapC usher (probability 100%, E-value 3.3×10^{-57}). The genomic sfGFP tag was hence cloned at the C-terminus of CupE5 as this site is most frequently modified in affinity and fluorescently-tagged PapC and FimD constructs. Importantly, the function of C-terminally tagged PapC and FimD is unaffected, allowing for pilus assembly (161, 163, 456, 457). Examination of cells using fluorescence microscopy revealed lack of sGFP signal in the CupE5-tagged fusion strain (Figure 5.1A-D) and in the Δ*PA2133*‡ control (Figure 5.1E-H). Autofluorescence was observed in both strains (Figure 5.1C,G), which was removed upon background subtraction (Figure 5.1D,H). These results suggest improper assembly of the sfGFP tag or CupE5-sfGFP complex at the outer membrane, or that the signal was below the limit of detection. As a control for the limit of detection, previously acquired images of an in-house *C. crescentus* strain, which expresses a genomic mCherry tag on the C-terminus of the HfaB cell surface anchor protein, were inspected. The mCherry signal is clearly visible at the centre of clustered cell/rosettes (Figure 5.2D), but absent at the tips of single cells (Figure 5.2A-C), suggesting multiple fluorophores are needed for detection under the imaging conditions tested. The lack of CupE5-sfGFP signal may therefore suggest the usher is either diffusely or evenly localised along the cell membrane rather than clustered at specific foci, possibly requiring an alternative approach for visualisation.

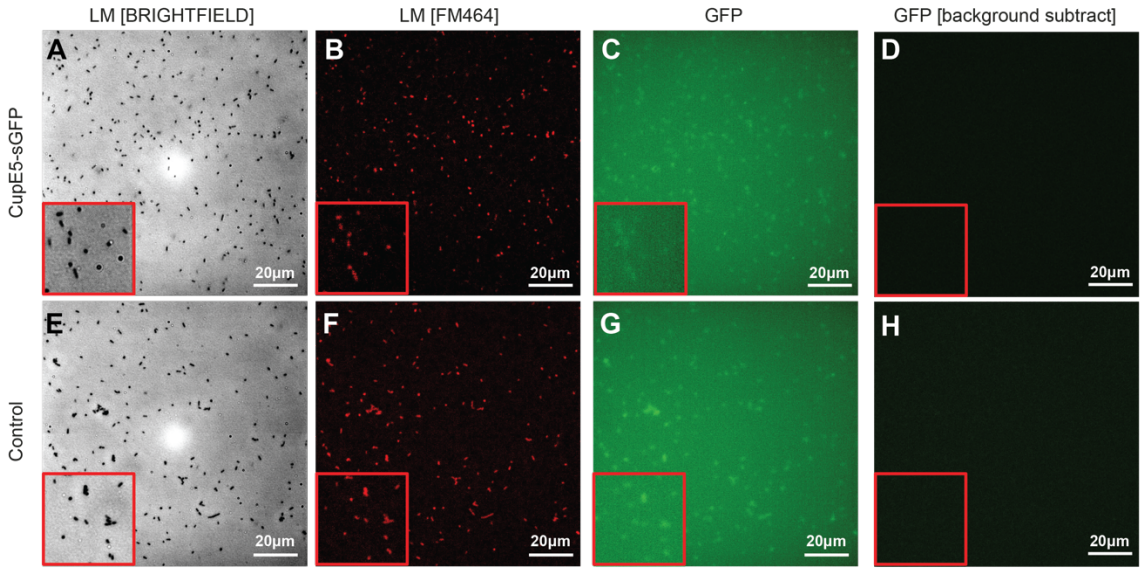


Figure 5.1: Fluorescence imaging of a PAO1 Δ*PA2133*‡ CupE5-sfGFP fusion strain

Light microscopy imaging of PAO1 Δ*PA2133*‡ CupE5-sGFP fusion and Δ*PA2133*‡ control strains using (A, E) brightfield and (B, F) following straining with the FM464 membrane dye. Cells are further illustrated by zoomed panels in left hand corner. (C, G) Raw images demonstrate autofluorescence in PAO1 cells in the green fluorescence channel. (D,H) Subtraction of background fluorescence demonstrates lack of sfGFP signal in CupE5-sGFP fusion and control strains. All images were processed using Fiji/ImageJ image analysis software (421).

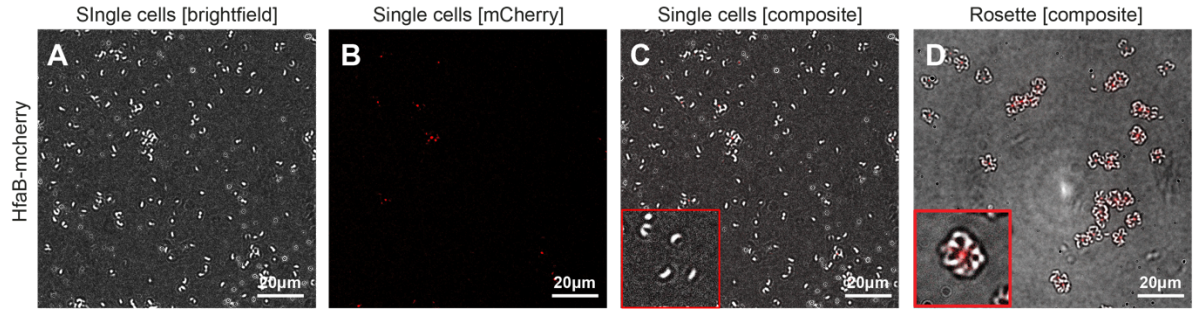


Figure 5.2: Comparison of fluorescent signal in single *C. crescentus* cells and rosettes, illustrates the limit of detection

(A) Light microscopy imaging of *C. crescentus* HfaB-mCherry fusion strain illustrating primarily single cells in liquid culture, as well as rosetted cells. (B, C) HfaB-mCherry signal is not resolved at the cell pole of single cells, as further shown by the zoomed panel in left hand corner. (D) HfaB-mCherry localises at the centre of rosettes as evident by the mCherry:brightfield composite shown. A magnified rosette in bottom left hand corner is shown for clarity. Panel D is the same as in Figure 3.8C. All images were contrasted using Fiji/ImageJ image analysis software (421).

5.2. Immunofluorescent labelling of cell surface CupE filaments

As an additional strategy to examine CupE localisation along the cell surface of PAO1, immunofluorescent-labelling was trialled using polyclonal antibodies re-generated against two synthetic CupE1 peptides (amino acids NQWGTLDFGSHSDLTN and HASGGQRYMQNTTTTSE) (Materials and Methods) (56). These antibodies successfully bind CupE1 in the sheared Δ*PA2133*‡ fraction by western blot, with a prominent band at ~16 kDa (Figure 5.3A), as also demonstrated previously (Figure 4.2B). The ~16 kDa species absent in the sheared fraction of Δ*cupE1-E2* mutants and rescued in the sheared fraction upon complementation (Figure 5.3A), further supporting detection of CupE1. Both anti-CupE1 antibodies were tested as the primary labelling reagent, followed by the application of an Alexa-Fluor 488-labelled anti-rabbit secondary antibody for visualisation (Materials and Methods). A range of primary antibody concentrations (0, 1, 5, 10, 50 μg/mL), as well as blocking and wash conditions were trialled to optimise labelling. Microscopy revealed lack of Alexa-Fluor 488 signal in Δ*PA2133*‡ cells labelled with either antibody (Figure 5.3B-D and E-G), with images resembling that of the unlabelled control (Figure 5.3H-J). These findings suggest that although the antibodies bind CupE1 under denaturing conditions, binding sites may be occluded in the assembled, native CupE filament. Alternatively, further optimisation of the immunofluorescence protocol may be required.

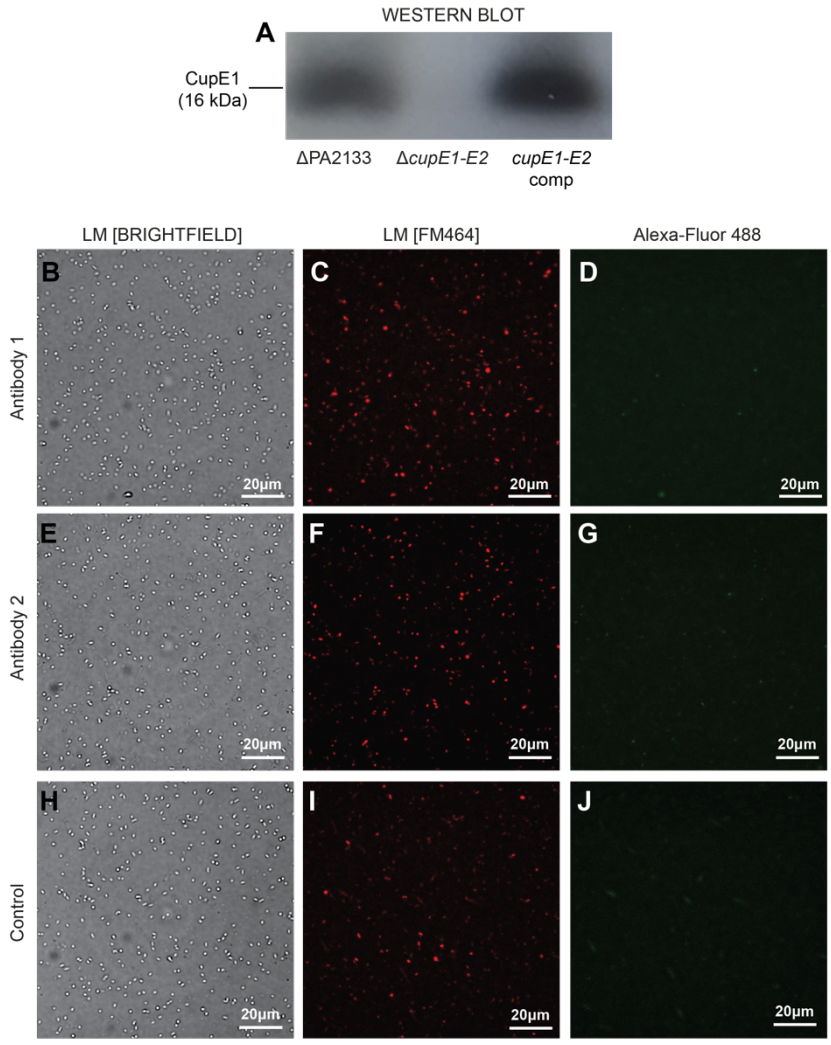


Figure 5.3: Immunofluorescent labelling of native CupE filaments using generated anti-CupE1 antibodies

(A) Western blot illustrating binding of anti-CupE1 antibody 1 (raised against synthetic peptide NQWGTLDFGSHSDLTN) to CupE1 (16 kDa band) in the Δ*PA2133*‡ sheared fraction. The 16 kDa species is lost in the sheared fraction of Δ*cupE1-E2* mutants and rescued upon complementation. (B-D) Immunofluorescence microscopy of Δ*PA2133*‡ cells labelled with anti-CupE1 antibody 1 (anti-NQWGTLDFGSHSDLTN, 50 μg/mL concentration) illustrates lack of Alexa-Fluor 488 signal. (E-G) Immunofluorescence microscopy of Δ*PA2133*‡ cells labelled with anti-CupE1 antibody 2 (anti-HASGGQRYMQNTTTTSE, 50 μg/mL concentration) similarly illustrates lack of Alexa-Fluor 488 signal. (E-G) Immunofluorescence microscopy of the unlabelled (no primary antibody) Δ*PA2133*‡ control. All images were contrasted using Fiji/ImageJ image analysis software (421).

5.3. CupE contributes to biofilm formation in a Δ*PA2133*‡ genetic background

To observe the contribution of CupE filaments to adhesion during biofilm formation, a series of *P. aeruginosa* PAO1 mutants were engineered (Table 2.1) and examined using crystal violet staining (409) (Methods and Materials). Strains were initially screened following overnight growth in plastic (polystyrene) tubes under static conditions. As controls, strains harbouring single deletion in flagella (Δ*fliC*) and type IV pili (Δ*pilA*), as well as a Δ*fliC* Δ*pilA* double deletion were compared to wild-type PAO1 (WT). A visible reduction of staining was observed macroscopically in single mutants, as well as complete loss of staining in the double mutant (Figure 5.4A), in line with previous reports (77). Further, biofilm formation was rescued by deletion of the MvaT repressor in a Δ*fliC* Δ*pilA* background (Figure 5.4A), as established in previous screens (4). Finally, a strain harbouring deletion in the Δ*wspF* regulator of the *wsp* chemosensory system was tested as a positive control (19). Deletion of Δ*wspF* results in pronounced aggregative phenotype and increased biofilm formation through elevated c-di-GMP (20). Consistent with this, a thick, prominent biofilm band was observed in Δ*wspF* mutants (Figure 5.4A). From here, a collection of mutants were examined to study the influence of CupE filaments on biofilm formation. All strains harboured deletion in Δ*mvaT*, Δ*fliC* and Δ*pilA* to promote adhesin expression and eliminate contribution by flagella and type IV pili. Deletion of the Δ*PA2133* phosphodiesterase resulted in a thick biofilm band, which was reversed upon chromosomal complementation (Figure 5.4A). Further, deletion of *cupE1-E2* in the Δ*PA2133*‡ mutant led to loss of the biofilm phenotype, which was restored upon chromosomal complementation (Figure 5.4A).

To quantify the macroscopically observed phenotype, the PAO1 mutant panel was subjected to a micro-titre crystal violet assay in triplicate as previously described (409) (Methods and Materials). Absorbance readings were consistent with macroscopic results. Notably, an increase in absorbance was observed upon Δ*PA2133* deletion, which was reduced

upon mutation of Δ*cupE1-E2* fimbrial subunits (Figure 5.4B). The observed phenotypes were independent of any effects on cell viability, as evident by similar cell counts between mutant strains (Figure 5.4C). The comparatively lower cell counts in the Δ*wspF* mutant is likely attributable to increased cell aggregation in culture, highly characteristic of this strain (19). Collectively, these results support the observation that CupE filaments are expressed in Δ*PA2133*‡ mutants, where they contribute to adhesion and biofilm formation

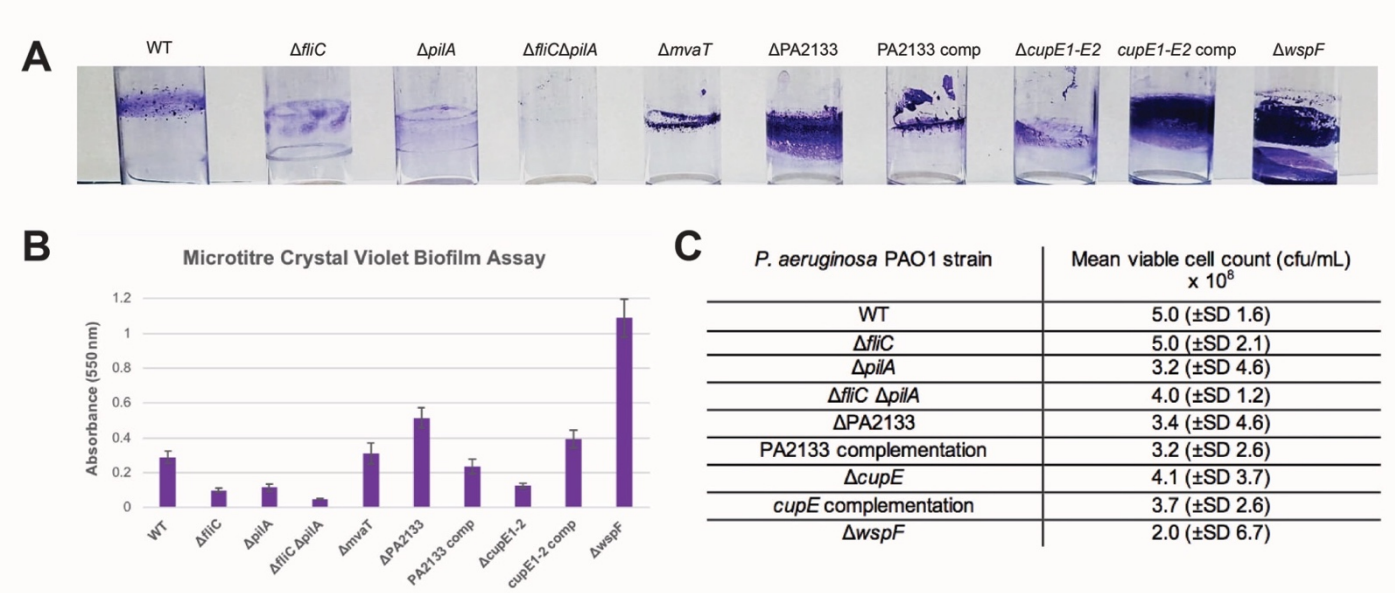


Figure 5.4: Assessment of CupE-mediated adhesion using the crystal violet biofilm assay

(A) Crystal violet staining of biofilms produced by PAO1 mutants grown upon polystyrene tubes. Single deletion of flagella (Δ*fliC*) and type IV pili (Δ*pilA*) results in reduced biofilm, whilst double deletion (Δ*fli*C Δ*pilA*) abolishes adherence. Deletion of Δ*mvaT* repressor restores biofilm formation in a Δ*fli*C Δ*pilA* background. Deletion of Δ*PA2133*‡ visibly promotes biofilm formation, which is reversed upon complementation (*PA2133* comp). Deletion of the major fimbrial subunits Δ*cupE1-E2* results in loss of biofilm formation in Δ*PA2133*‡ mutants and is restored upon complementation (*cupE1-E2* comp). The Δ*wspF* positive control demonstrates pronounced crystal violet staining. (B) Quantitative assessment of biofilm formation by a *P. aeruginosa* mutant panel using the microtitre crystal violet assay (409). $Absorbance_{550nm}$ values are consistent with macroscopic observations of mutants in panel A, further demonstrating CupE promotes adhesion in Δ*PA2133*‡ mutants. (C) Cell viability assay revealing similar cell counts between PAO1 strains examined (means and standard deviations [SD] are reported).

5.4. Upregulation of CupE in a Δ*PA2133*‡ background influences cell clustering and biofilm architecture

To study the effect of CupE on biofilm architecture in Δ*PA2133*‡ mutants, a set of *P. aeruginosa* PAO1 strains were grown upon glass coverslips for three days and examined using light microscopy (Methods and Materials) (410). Briefly, glass coverslips were mounted upon plastic slides and submerged in growth medium so as to establish an air-liquid interface for study (Figure 5.5A,B). Following inoculation and growth, coverslips were removed and a macroscopic biofilm band visualised at the air-liquid interface (Figure 5.5C).

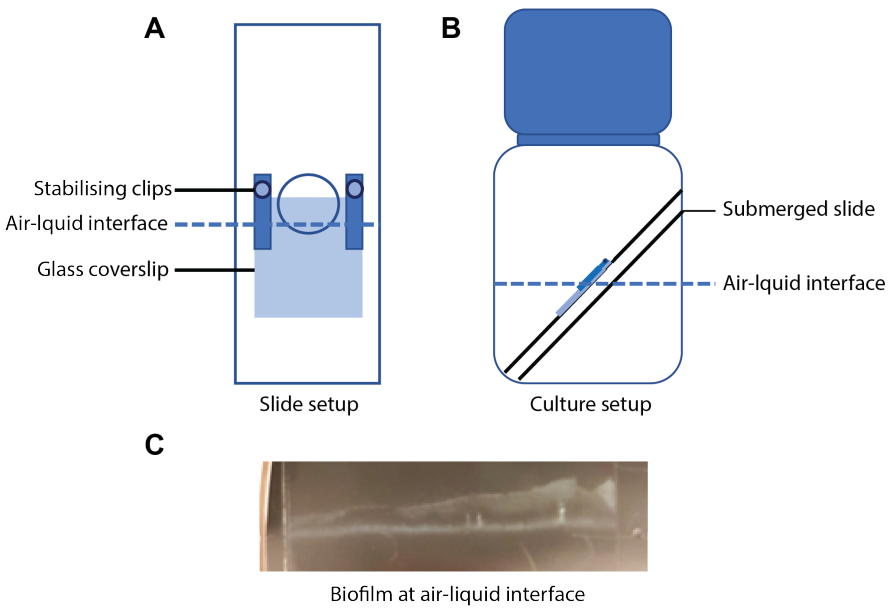


Figure 5.5: Experimental setup for examination of biofilm formation at the air-liquid interface

(A) Schematic illustrating slide setup for adhesion studies. Glass coverslips were mounted on plastic slides, stabilised by two metal clips in-built within the plastic slide. The position of the air liquid interface is indicated. (B) Plastic coverslips were placed in sterile glass Schott DURAN® bottles and submerged under liquid medium. The air-liquid interface is similarly indicated. (C) Image illustrating an example of biofilm band formed at the air-liquid interface after three days of growth.

Observation of the resulting biofilms using brightfield light microscopy revealed distinct morphological features characterised by varying degrees of cell clustering and organisation. These ranged from single cells to the formation of cell mats, elevated cell clusters and ordered channels. Examples of each feature are summarised in Figure 5.6 for reference purposes.

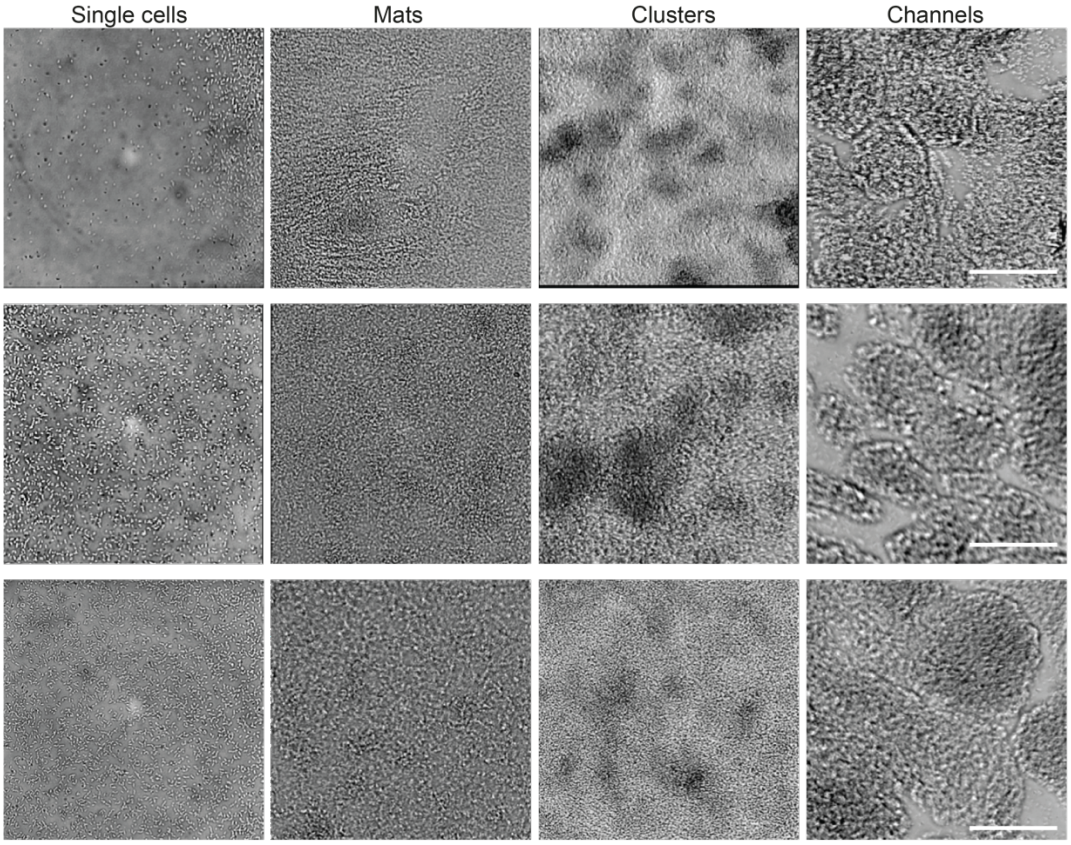


Figure 5.6: Morphological features of PAO1 biofilms at the air-liquid interface.

Brightfield microscopy images illustrating morphological features witnessed in PAO1 biofilms at the air-liquid interface; including single cells, cell mats, raised cell clusters and channels. Three examples for each feature are provided in each column. Scale bar represents 100 μm.

Coverslips containing biofilms (Figure 5.7A) of each strain were imaged at low magnification (5x) and periodic sites selected for imaging at high magnification (20x); scanning from the air-liquid interface to the distal end of the biofilm (sites indicated by blue boxes, Figure 5.7B). The control strain, harbouring deletion in Δ*mvaT* Δ*fliC* Δ*pilA*, exhibited reduced cell density toward the air-liquid interface. Single cells were visualized toward the air-liquid interface, followed by cell mats toward the distal end of the biofilm (Figure 5.7C). Deletion of Δ*PA2133* induced a notable change in biofilm morphology; with the formation of raised, channel-like structures toward the air-liquid interface. Further, raised cell clusters were visualised at the mid- and distal sections of the biofilm biofilm (Figure 5.7C). To determine whether this phenotype was influenced by CupE filaments, a Δ*cupE1-E2* deletion strain was imaged. Channel formation was visibly lost in the Δ*cupE1-E2* mutant; with single cells visualised at the air-liquid interface. Cell clusters were present at the mid- and distal ends of the biofilm, as seen in the Δ*PA2133*‡ mutant (Figure 5.7C). Chromosomal complementation of the Δ*cupE1-E2* genes rescued channel formation toward the air-liquid interface (Figure 5.7C). Together, these results indicate that CupE influences cell clustering and biofilm architecture in Δ*PA2133*‡ mutants; in turn strengthening its role as an adhesin.

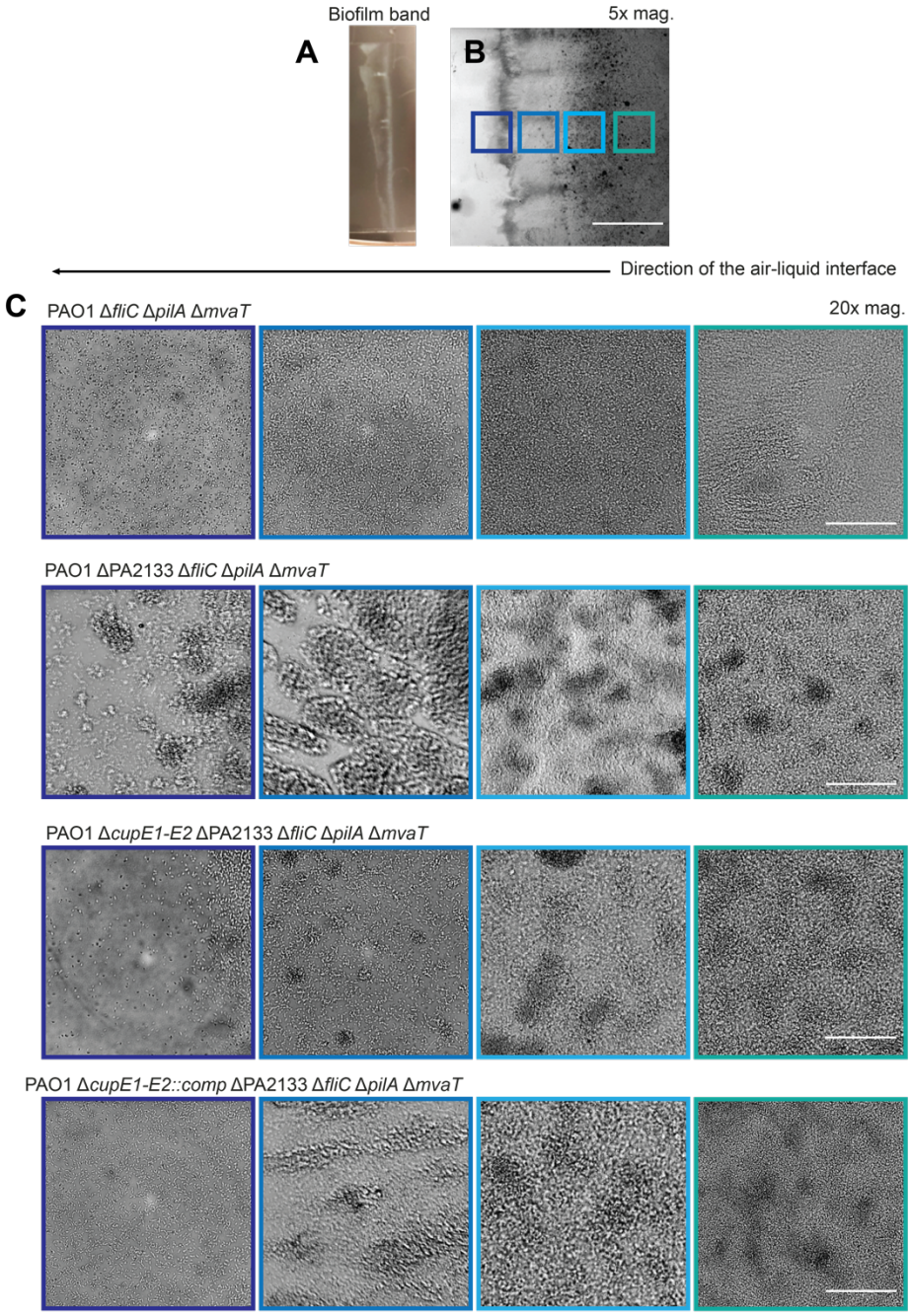


Figure 5.7: CupE upregulation results in increased cell clustering and organisation at the microscopic level

(A) Macroscopic appearance of a PAO1 biofilm formed on glass coverslips at the air-liquid interface. (B) Image of a biofilm at 5x magnification illustrating the location of periodic sites (blue boxes) selected for imaging at higher magnification. Scale bar represents 1000 µm. The direction of the air-liquid interface is indicated by the arrow below panel A and B, and similarly applies to panel C. (C) Biofilms formed by a PAO1 mutant panel at the air-liquid interface, imaged at 20x magnification. Locations along the biofilm correspond to those shown in panel B for each strain. Scale bar represents 100 µm.

CHAPTER 5 DISCUSSION

P. aeruginosa PAO1 harbours four chaperone usher fimbriae; CupA, CupB, CupC and CupE (3, 50, 56). In this work, archaic CupE fimbriae were identified as upregulated on the PAO1 cell surface upon deletion of the PA2133 phosphodiesterase. However, the contribution of CupE to adhesion, biofilm development and architecture in a Δ*PA2133*‡ background has not been investigated. Further, the molecular details with respect to how CupE filaments mediate attachment, as well as the arrangement of filaments at the PAO1 cell surface remain unknown.

In this study, the contribution of CupE fimbriae and PA2133 on adhesion and biofilm formation were demonstrated. Deletion of *PA2133* results in a significant increase in biofilm formation at the air liquid interface, as well as changes in cell clustering at the microscopic level. Consistent with these observations, *PA2133* deletion in *P. aeruginosa* PA14 results in increased crystal violet staining (239). In addition, PAO1 and PAK strains over-expressing *PA2133* exhibit defects in biofilm formation (19, 240). CupE fimbriae are assembled and contribute to biofilm formation at the air-liquid interface in Δ*PA2133*‡ mutants. These results indicate that CupE filaments influence biofilm architecture, with increased cell clustering and organisation at the microscopic level. In line with this, upregulation of CupE through PprAB over-expression promotes initial attachment and development of the characteristic mushroom-shaped architecture of mature biofilms (56). As PA2133 downregulates expression of other cellular components e.g. T3SS, flagella and chemotaxis proteins (240), the relative contribution of these factors versus CupE in Δ*PA2133*‡ cells should be further investigated. Additionally, Δ*PA2133*‡ cells expressing the MvaT repressor could also be examined to deduce whether Δ*mvaT* deletion is additionally necessary for CupE assembly and to observe the resulting biofilm phenotype.

Although the localisation of CupE filaments along the cell surface was not revealed in the timeframe of this work, the foundations for future molecular studies were established, including a Δ*PA2133*‡ strain encoding a C-terminal sfGFP tag on the CupE5 usher. To differentiate whether lack of sfGFP signal in this strain is attributable to diffuse CupE5 localisation along the cell surface or improper tag assembly, alternative imaging techniques may be trialled at higher resolution (e.g. super-resolution confocal microscopy). In the case of improper tag assembly, alternative sites along the CupE5 usher may be labelled, such as the N-terminus or extracellular loops along the central β-barrel pore.

Labelling with anti-CupE1 peptide antibodies regenerated in this work did not reveal positive binding to assembled, native CupE filament on the Δ*PA2133*‡ cell surface in immunofluorescence experiments. Previous reports illustrate weak binding to CupE using these antibodies in immuno-gold/TEM experiments (56). The authors similarly speculate poor labelling may be due to decreased reactivity of anti-CupE1 antibodies against native versus denatured CupE filaments (56). Indeed, this study illustrated strong binding of antibodies under denaturing conditions (western blotting), where the corresponding CupE1 amino acid residues are presumably more available. Atomic resolution structural insights into the assembled CupE filament will help determine whether the CupE1 peptide residues (NQWGTLDFGSHSDLTN and HASGGQRYMQNTTTTSE) interface the external environment and are readily available for antibody binding. This information will help to improve the design of anti-CupE1 antibodies for future labelling experiments.

Collectively, this work supports a link between PA2133 and CupE upregulation, as well as the function of CupE as an adhesin in PAO1 which promotes biofilm formation. Additionally, these studies set the framework for future molecular investigations into the localisation of CupE filaments on the cell-surface; ultimately improving our understanding of CupE-mediated adhesion.

Acknowledgements

I sincerely thank Professor Alain Filloux and Kira Glatzel (Imperial College of London) for genetic manipulation and provision of *P. aeruginosa* strains. Further, I thank Dr Charlotte Melia (Bharat Lab) for providing materials and instructions relevant to slide setups for biofilm studies.

CHAPTER 6. CONCLUDING REMARKS

By studying both proteinaceous and polysaccharide adhesins, this project provides structural insights into two fundamental arms during biofilm formation and sets the framework for future studies of the holdfast anchor complex of *C. crescentus* and CupE fimbriae of *P. aeruginosa* PAO1.

Importantly, this thesis provides understanding of a previously uncharacterized mechanism of polysaccharide anchoring (Figure 6.1). The holdfast of *C. crescentus* is anchored to cells by a defined complex made up of the HfaABD proteins. The HfsDAB secretion proteins are required for assembly and localization of the HfaABD anchor, which spans the outer membrane of the stalk tip. The anchor protein HfaB is the major component of the anchor complex located on the periplasmic side of the outer membrane, while HfaA and HfaD are located on the cell surface. HfaB is the critical component of the complex, without which no HfaABD complex is observed in cells. An atomic structure of HfaB will help provide insights into its potential role in holdfast translocation and anchoring, and may be attempted by in vitro reconstitution of the nonameric HfaB pore *in vitro,* which will in turn assist template matching experiments *in situ*. The HfaA, HfaD and HfaE holdfast anchor proteins localise at the extracellular side of the outer membrane, though their structure and function remain unclear. Purification of these proteins will help to examine these questions and interaction with HfaB. Finally, anchor densities are present along the cell envelope of other alphaproteobacteria including *Asticcacaulis* and *Hirschia* spp., supporting a conserved mechanism in holdfast anchoring across these bacterial species.

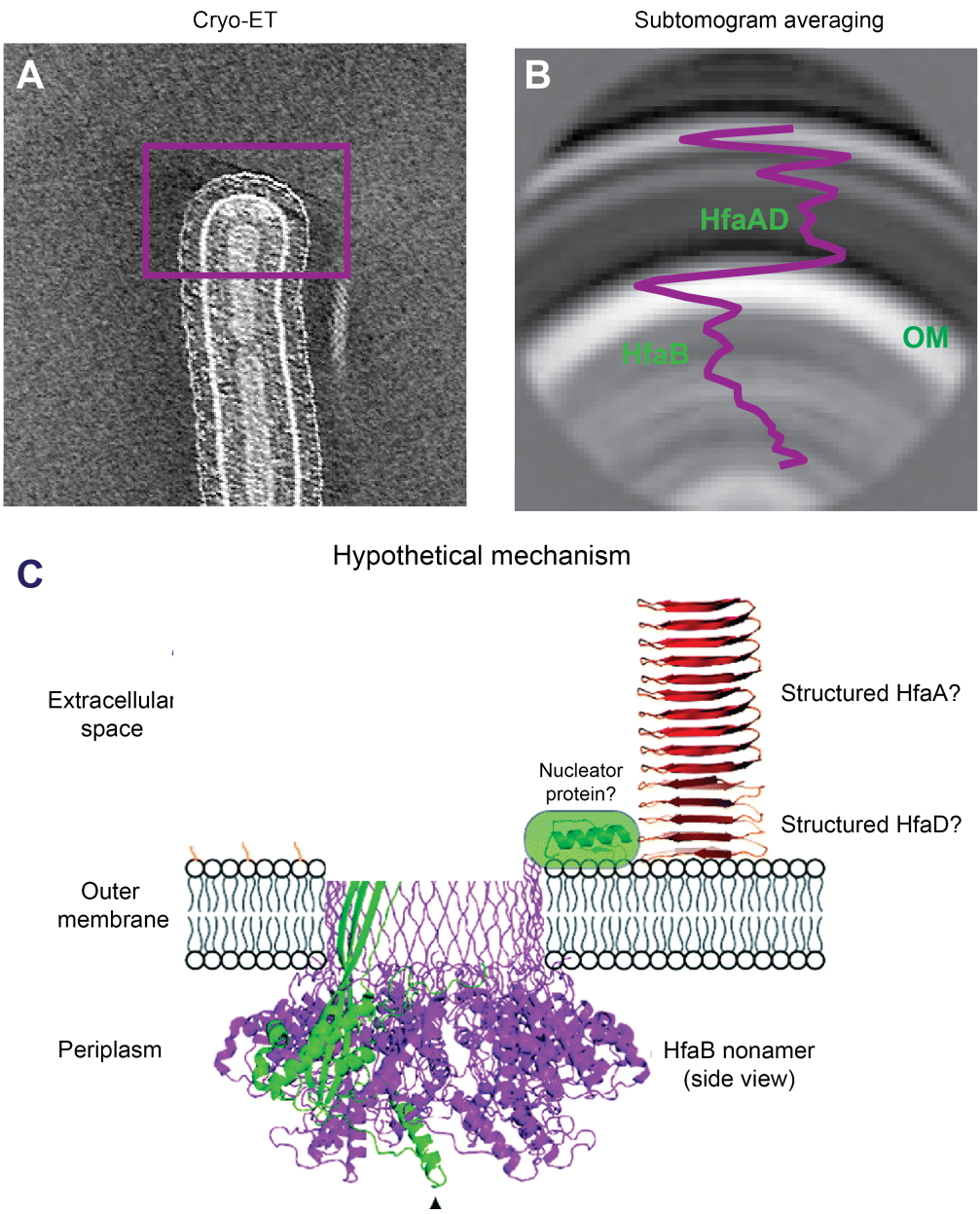


Figure 6.1: Schematic of investigations into the holdfast anchor at the cell surface of *C. crescentus*.

Summary of key project findings relating to the localisation and function of the holdfast anchor complex. Cryo-ET imaging (A) and sub-tomogram averaging (B) of *C. crescentus* stalk tips assisted in the localisation of HfaB, HfaA and HfaD along the cell envelope. Linear intensity plot (purple line) is overlaid with the 2D class average of the *C. crescentus* stalk tip. (C) Bottom panel illustrates the hypothetical mechanism for holdfast anchoring. The HfaB density is localised toward the periplasmic side of the outer membrane, where it functions as a putative translocation pore based on homology predictions. The HfaA and HfaD are amyloid-like proteins, which localise at the extracellular side of the outer membrane. These amyloid structures may act as a structural mesh or platform to which the holdfast is tethered.

Additionally, this thesis provides insight into the regulation, structure and physiological role of archaic CupE fimbriae in *P. aeruginosa* (Figure 6.2). Deletion of the PA2133 phosphodiesterase upregulates CupE filaments under static conditions, supporting filament assembly is promoted upon c-di-GMP elevation and surface sensing. Though it remains to be investigated, PA2133 may influence the PprAB two component system through its phosphodiesterase activity, in turn upregulating *cupE* gene expression. The diameter of CupE filaments is ~4 nm, consistent with fimbriae of the archaic σ-clade. The cryo-EM structure of native CupE at 4.5 Å reveals a single-start, helical morphology that does not resemble the tubular structure of classical chaperone usher assemblies. Future investigations of *PA2133*‡ CupE5-sfGFP constructs, designed in this work, will aid in mapping the localisation of CupE filaments along the cell surface. Further, the atomic structure of CupE will aid in design of antibodies for future immunofluorescent-labelling of surface filaments. CupE fimbriae are a major contributor to biofilm formation in Δ*PA2133*‡ mutants, with increased biofilm formation at the air-liquid interface as well as cell clustering and organisation at the microscopic level. These results support CupE filaments function as an adhesin in *P. aeruginosa* PAO1 which contribute to biofilm formation and provide the first structural insights into a fully assembled, archaic chaperone usher filament in bacteria.

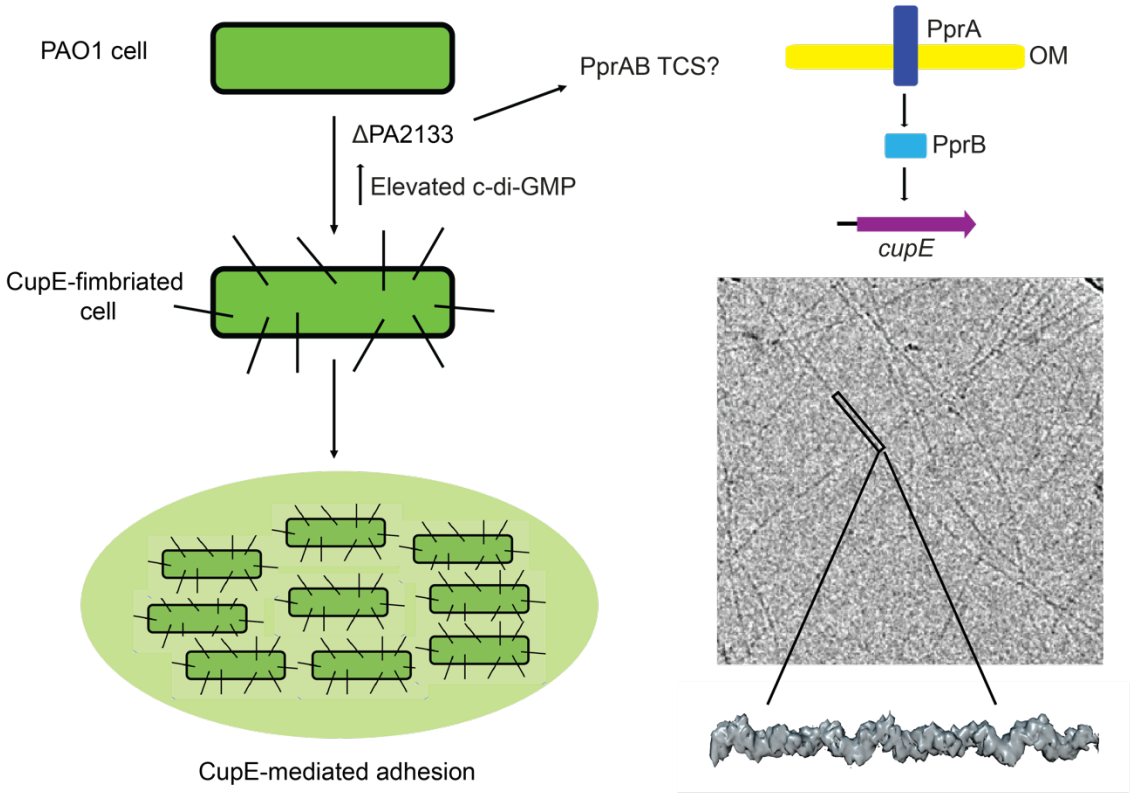


Figure 6.2: Schematic of investigations into the regulation and structure of CupE of *P. aeruginosa*

Summary of key project findings relating to the regulation, structure and function of archaic CupE fimbriae. Deletion of the PA2133 phosphodiesterase upregulates CupE fimbriae on the PAO1 cell surface. This is presumably through elevated c-di-GMP levels which may act upon the PprAB two component system, ultimately influencing *cupE* expression. Cryo-EM investigations of native CupE filaments, isolated from the cell surface, reveal CupE possesses a single-start, helical morphology. CupE promotes increase in cell density and clustering during biofilm formation, supporting its role as an adhesin.

REFERENCES

1. O'Toole G, Kaplan HB, Kolter R. Biofilm formation as microbial development. Annu Rev Microbiol. 2000;54:49-79.
2. Tolker-Nielsen T. Pseudomonas aeruginosa biofilm infections: from molecular biofilm biology to new treatment possibilities. APMIS Suppl. 2014(138):1-51.
3. Vallet I, Olson JW, Lory S, Lazdunski A, Filloux A. The chaperone/usher pathways of Pseudomonas aeruginosa: identification of fimbrial gene clusters (cup) and their involvement in biofilm formation. Proc Natl Acad Sci U S A. 2001;98(12):6911-6.
4. Vallet I, Diggle SP, Stacey RE, Camara M, Ventre I, Lory S, et al. Biofilm formation in Pseudomonas aeruginosa: fimbrial cup gene clusters are controlled by the transcriptional regulator MvaT. J Bacteriol. 2004;186(9):2880-90.
5. Schurr MJ. Which bacterial biofilm exopolysaccharide is preferred, Psl or alginate? J Bacteriol. 2013;195(8):1623-6.
6. Kostakioti M, Hadjifrangiskou M, Hultgren SJ. Bacterial biofilms: development, dispersal, and therapeutic strategies in the dawn of the postantibiotic era. Cold Spring Harb Perspect Med. 2013;3(4):a010306.
7. Muhl D. Molecular characteristics of the CupB chaperone-usher pathway and the Tps4-two partner secretion system in P. aeruginosa. 2014;PhD Thesis.
8. Karatan E, Watnick P. Signals, regulatory networks, and materials that build and break bacterial biofilms. Microbiol Mol Biol Rev. 2009;73(2):310-47.
9. McDonough KA, Rodriguez A. The myriad roles of cyclic AMP in microbial pathogens: from signal to sword. Nat Rev Microbiol. 2011;10(1):27-38.
10. Gundlach J, Herzberg C, Kaever V, Gunka K, Hoffmann T, Weiss M, et al. Control of potassium homeostasis is an essential function of the second messenger cyclic di-AMP in Bacillus subtilis. Sci Signal. 2017;10(475).
11. Jenal U, Reinders A, Lori C. Cyclic di-GMP: second messenger extraordinaire. Nat Rev Microbiol. 2017;15(5):271-84.
12. Davies BW, Bogard RW, Young TS, Mekalanos JJ. Coordinated regulation of accessory genetic elements produces cyclic di-nucleotides for V. cholerae virulence. Cell. 2012;149(2):358-70.
13. Hall-Stoodley L, Costerton JW, Stoodley P. Bacterial biofilms: from the natural environment to infectious diseases. Nat Rev Microbiol. 2004;2(2):95-108.
14. Ha DG, O'Toole GA. c-di-GMP and its Effects on Biofilm Formation and Dispersion: a Pseudomonas Aeruginosa Review. Microbiol Spectr. 2015;3(2):MB-0003-2014.
15. Navarro MV, De N, Bae N, Wang Q, Sondermann H. Structural analysis of the GGDEF-EAL domain-containing c-di-GMP receptor FimX. Structure. 2009;17(8):1104-16.
16. Chen MW, Kotaka M, Vonrhein C, Bricogne G, Rao F, Chuah ML, et al. Structural insights into the regulatory mechanism of the response regulator RocR from Pseudomonas aeruginosa in cyclic Di-GMP signaling. J Bacteriol. 2012;194(18):4837-46.
17. Pesavento C, Hengge R. Bacterial nucleotide-based second messengers. Curr Opin Microbiol. 2009;12(2):170-6.
18. Kulasakara H, Lee V, Brencic A, Liberati N, Urbach J, Miyata S, et al. Analysis of Pseudomonas aeruginosa diguanylate cyclases and phosphodiesterases reveals a role for bis-(3'-5')-cyclic-GMP in virulence. Proc Natl Acad Sci U S A. 2006;103(8):2839-44.
19. Hickman JW, Tifrea DF, Harwood CS. A chemosensory system that regulates biofilm formation through modulation of cyclic diguanylate levels. Proc Natl Acad Sci U S A. 2005;102(40):14422-7.

20. Huangyutitham V, Guvener ZT, Harwood CS. Subcellular clustering of the phosphorylated WspR response regulator protein stimulates its diguanylate cyclase activity. mBio. 2013;4(3):e00242-13.
21. O'Connor JR, Kuwada NJ, Huangyutitham V, Wiggins PA, Harwood CS. Surface sensing and lateral subcellular localization of WspA, the receptor in a chemosensory-like system leading to c-di-GMP production. Mol Microbiol. 2012;86(3):720-9.
22. Guvener ZT, Harwood CS. Subcellular location characteristics of the Pseudomonas aeruginosa GGDEF protein, WspR, indicate that it produces cyclic-di-GMP in response to growth on surfaces. Mol Microbiol. 2007;66(6):1459-73.
23. Moradali MF, Ghods S, Rehm BH. Pseudomonas aeruginosa Lifestyle: A Paradigm for Adaptation, Survival, and Persistence. Front Cell Infect Microbiol. 2017;7:39.
24. Caiazza NC, O'Toole GA. SadB is required for the transition from reversible to irreversible attachment during biofilm formation by Pseudomonas aeruginosa PA14. J Bacteriol. 2004;186(14):4476-85.
25. Kuchma SL, Brothers KM, Merritt JH, Liberati NT, Ausubel FM, O'Toole GA. BifA, a cyclic-Di-GMP phosphodiesterase, inversely regulates biofilm formation and swarming motility by Pseudomonas aeruginosa PA14. J Bacteriol. 2007;189(22):8165-78.
26. Ryan RP. Cyclic di-GMP signalling and the regulation of bacterial virulence. Microbiology (Reading). 2013;159(Pt 7):1286-97.
27. Newell PD, Boyd CD, Sondermann H, O'Toole GA. A c-di-GMP effector system controls cell adhesion by inside-out signaling and surface protein cleavage. PLoS Biol. 2011;9(2):e1000587.
28. Borlee BR, Goldman AD, Murakami K, Samudrala R, Wozniak DJ, Parsek MR. Pseudomonas aeruginosa uses a cyclic-di-GMP-regulated adhesin to reinforce the biofilm extracellular matrix. Mol Microbiol. 2010;75(4):827-42.
29. Cooley RB, Smith TJ, Leung W, Tierney V, Borlee BR, O'Toole GA, et al. Cyclic Di-GMP-Regulated Periplasmic Proteolysis of a Pseudomonas aeruginosa Type Vb Secretion System Substrate. J Bacteriol. 2016;198(1):66-76.
30. Navarro MV, Newell PD, Krasteva PV, Chatterjee D, Madden DR, O'Toole GA, et al. Structural basis for c-di-GMP-mediated inside-out signaling controlling periplasmic proteolysis. PLoS Biol. 2011;9(2):e1000588.
31. Newell PD, Monds RD, O'Toole GA. LapD is a bis-(3',5')-cyclic dimeric GMP-binding protein that regulates surface attachment by Pseudomonas fluorescens Pf0-1. Proc Natl Acad Sci U S A. 2009;106(9):3461-6.
32. Gooderham WJ, Hancock RE. Regulation of virulence and antibiotic resistance by two-component regulatory systems in Pseudomonas aeruginosa. FEMS Microbiol Rev. 2009;33(2):279-94.
33. Brencic A, McFarland KA, McManus HR, Castang S, Mogno I, Dove SL, et al. The GacS/GacA signal transduction system of Pseudomonas aeruginosa acts exclusively through its control over the transcription of the RsmY and RsmZ regulatory small RNAs. Mol Microbiol. 2009;73(3):434-45.
34. Morris ER, Hall G, Li C, Heeb S, Kulkarni RV, Lovelock L, et al. Structural rearrangement in an RsmA/CsrA ortholog of Pseudomonas aeruginosa creates a dimeric RNA-binding protein, RsmN. Structure. 2013;21(9):1659-71.
35. Reimmann C, Beyeler M, Latifi A, Winteler H, Foglino M, Lazdunski A, et al. The global activator GacA of Pseudomonas aeruginosa PAO positively controls the production of the autoinducer N-butyryl-homoserine lactone and the formation of the virulence factors pyocyanin, cyanide, and lipase. Mol Microbiol. 1997;24(2):309-19.
36. Parkins MD, Ceri H, Storey DG. Pseudomonas aeruginosa GacA, a factor in multihost virulence, is also essential for biofilm formation. Mol Microbiol. 2001;40(5):1215-26.

37. Pessi G, Williams F, Hindle Z, Heurlier K, Holden MT, Camara M, et al. The global posttranscriptional regulator RsmA modulates production of virulence determinants and N-acylhomoserine lactones in Pseudomonas aeruginosa. J Bacteriol. 2001;183(22):6676-83.
38. Heurlier K, Williams F, Heeb S, Dormond C, Pessi G, Singer D, et al. Positive control of swarming, rhamnolipid synthesis, and lipase production by the posttranscriptional RsmA/RsmZ system in Pseudomonas aeruginosa PAO1. J Bacteriol. 2004;186(10):2936-45.
39. Burrowes E, Baysse C, Adams C, O'Gara F. Influence of the regulatory protein RsmA on cellular functions in Pseudomonas aeruginosa PAO1, as revealed by transcriptome analysis. Microbiology (Reading). 2006;152(Pt 2):405-18.
40. Allsopp LP, Wood TE, Howard SA, Maggiorelli F, Nolan LM, Wettstadt S, et al. RsmA and AmrZ orchestrate the assembly of all three type VI secretion systems in Pseudomonas aeruginosa. Proc Natl Acad Sci U S A. 2017;114(29):7707-12.
41. Ventre I, Goodman AL, Vallet-Gely I, Vasseur P, Soscia C, Molin S, et al. Multiple sensors control reciprocal expression of Pseudomonas aeruginosa regulatory RNA and virulence genes. Proc Natl Acad Sci U S A. 2006;103(1):171-6.
42. Chambonnier G, Roux L, Redelberger D, Fadel F, Filloux A, Sivaneson M, et al. The Hybrid Histidine Kinase LadS Forms a Multicomponent Signal Transduction System with the GacS/GacA Two-Component System in Pseudomonas aeruginosa. PLoS Genet. 2016;12(5):e1006032.
43. Broder UN, Jaeger T, Jenal U. LadS is a calcium-responsive kinase that induces acute-to-chronic virulence switch in Pseudomonas aeruginosa. Nat Microbiol. 2016;2:16184.
44. Goodman AL, Merighi M, Hyodo M, Ventre I, Filloux A, Lory S. Direct interaction between sensor kinase proteins mediates acute and chronic disease phenotypes in a bacterial pathogen. Genes Dev. 2009;23(2):249-59.
45. Kong W, Chen L, Zhao J, Shen T, Surette MG, Shen L, et al. Hybrid sensor kinase PA1611 in Pseudomonas aeruginosa regulates transitions between acute and chronic infection through direct interaction with RetS. Mol Microbiol. 2013;88(4):784-97.
46. Francis VI, Stevenson EC, Porter SL. Two-component systems required for virulence in Pseudomonas aeruginosa. FEMS Microbiol Lett. 2017;364(11).
47. Heeb S, Blumer C, Haas D. Regulatory RNA as mediator in GacA/RsmA-dependent global control of exoproduct formation in Pseudomonas fluorescens CHA0. J Bacteriol. 2002;184(4):1046-56.
48. Soscia C, Hachani A, Bernadac A, Filloux A, Bleves S. Cross talk between type III secretion and flagellar assembly systems in Pseudomonas aeruginosa. J Bacteriol. 2007;189(8):3124-32.
49. Rahme LG, Ausubel FM, Cao H, Drenkard E, Goumnerov BC, Lau GW, et al. Plants and animals share functionally common bacterial virulence factors. Proc Natl Acad Sci U S A. 2000;97(16):8815-21.
50. Kulasekara HD, Ventre I, Kulasekara BR, Lazdunski A, Filloux A, Lory S. A novel two-component system controls the expression of Pseudomonas aeruginosa fimbrial cup genes. Mol Microbiol. 2005;55(2):368-80.
51. Kuchma SL, Connolly JP, O'Toole GA. A three-component regulatory system regulates biofilm maturation and type III secretion in Pseudomonas aeruginosa. J Bacteriol. 2005;187(4):1441-54.
52. Sivaneson M, Mikkelsen H, Ventre I, Bordi C, Filloux A. Two-component regulatory systems in Pseudomonas aeruginosa: an intricate network mediating fimbrial and efflux pump gene expression. Mol Microbiol. 2011;79(5):1353-66.
53. Mikkelsen H, Ball G, Giraud C, Filloux A. Expression of Pseudomonas aeruginosa CupD fimbrial genes is antagonistically controlled by RcsB and the EAL-containing PvrR response regulators. PLoS One. 2009;4(6):e6018.

54. Drenkard E, Ausubel FM. Pseudomonas biofilm formation and antibiotic resistance are linked to phenotypic variation. Nature. 2002;416(6882):740-3.
55. Wang Y, Ha U, Zeng L, Jin S. Regulation of membrane permeability by a two-component regulatory system in Pseudomonas aeruginosa. Antimicrob Agents Chemother. 2003;47(1):95-101.
56. Giraud C, Bernard CS, Calderon V, Yang L, Filloux A, Molin S, et al. The PprA-PprB two-component system activates CupE, the first non-archetypal Pseudomonas aeruginosa chaperone-usher pathway system assembling fimbriae. Environ Microbiol. 2011;13(3):666-83.
57. de Bentzmann S, Giraud C, Bernard CS, Calderon V, Ewald F, Plesiat P, et al. Unique biofilm signature, drug susceptibility and decreased virulence in Drosophila through the Pseudomonas aeruginosa two-component system PprAB. PLoS Pathog. 2012;8(11):e1003052.
58. Intile PJ, Diaz MR, Urbanowski ML, Wolfgang MC, Yahr TL. The AlgZR two-component system recalibrates the RsmAYZ posttranscriptional regulatory system to inhibit expression of the Pseudomonas aeruginosa type III secretion system. J Bacteriol. 2014;196(2):357-66.
59. Okkotsu Y, Little AS, Schurr MJ. The Pseudomonas aeruginosa AlgZR two-component system coordinates multiple phenotypes. Front Cell Infect Microbiol. 2014;4:82.
60. Ishimoto KS, Lory S. Identification of pilR, which encodes a transcriptional activator of the Pseudomonas aeruginosa pilin gene. J Bacteriol. 1992;174(11):3514-21.
61. Hobbs M, Collie ES, Free PD, Livingston SP, Mattick JS. PilS and PilR, a two-component transcriptional regulatory system controlling expression of type 4 fimbriae in Pseudomonas aeruginosa. Mol Microbiol. 1993;7(5):669-82.
62. Kilmury SL, Burrows LL. Type IV pilins regulate their own expression via direct intramembrane interactions with the sensor kinase PilS. Proc Natl Acad Sci U S A. 2016;113(21):6017-22.
63. Morici LA, Carterson AJ, Wagner VE, Frisk A, Schurr JR, Honer zu Bentrup K, et al. Pseudomonas aeruginosa AlgR represses the Rhl quorum-sensing system in a biofilm-specific manner. J Bacteriol. 2007;189(21):7752-64.
64. Blus-Kadosh I, Zilka A, Yerushalmi G, Banin E. The effect of pstS and phoB on quorum sensing and swarming motility in Pseudomonas aeruginosa. PLoS One. 2013;8(9):e74444.
65. Faure LM, Llamas MA, Bastiaansen KC, de Bentzmann S, Bigot S. Phosphate starvation relayed by PhoB activates the expression of the Pseudomonas aeruginosa sigmavreI ECF factor and its target genes. Microbiology (Reading). 2013;159(Pt 7):1315-27.
66. Bielecki P, Jensen V, Schulze W, Godeke J, Strehmel J, Eckweiler D, et al. Cross talk between the response regulators PhoB and TctD allows for the integration of diverse environmental signals in Pseudomonas aeruginosa. Nucleic Acids Res. 2015;43(13):6413-25.
67. Papenfort K, Bassler BL. Quorum sensing signal-response systems in Gram-negative bacteria. Nat Rev Microbiol. 2016;14(9):576-88.
68. Jones S, Yu B, Bainton NJ, Birdsall M, Bycroft BW, Chhabra SR, et al. The lux autoinducer regulates the production of exoenzyme virulence determinants in Erwinia carotovora and Pseudomonas aeruginosa. EMBO J. 1993;12(6):2477-82.
69. Jimenez PN, Koch G, Thompson JA, Xavier KB, Cool RH, Quax WJ. The multiple signaling systems regulating virulence in Pseudomonas aeruginosa. Microbiol Mol Biol Rev. 2012;76(1):46-65.
70. Pearson JP, Gray KM, Passador L, Tucker KD, Eberhard A, Iglewski BH, et al. Structure of the autoinducer required for expression of Pseudomonas aeruginosa virulence genes. Proc Natl Acad Sci U S A. 1994;91(1):197-201.

71. Pearson JP, Passador L, Iglewski BH, Greenberg EP. A second N-acylhomoserine lactone signal produced by Pseudomonas aeruginosa. Proc Natl Acad Sci U S A. 1995;92(5):1490-4.
72. Pesci EC, Milbank JB, Pearson JP, McKnight S, Kende AS, Greenberg EP, et al. Quinolone signaling in the cell-to-cell communication system of Pseudomonas aeruginosa. Proc Natl Acad Sci U S A. 1999;96(20):11229-34.
73. Berne C, Ducret A, Hardy GG, Brun YV. Adhesins Involved in Attachment to Abiotic Surfaces by Gram-Negative Bacteria. Microbiol Spectr. 2015;3(4).
74. Mattick JS. Type IV pili and twitching motility. Annu Rev Microbiol. 2002;56:289-314.
75. Aas FE, Wolfgang M, Frye S, Dunham S, Lovold C, Koomey M. Competence for natural transformation in Neisseria gonorrhoeae: components of DNA binding and uptake linked to type IV pilus expression. Mol Microbiol. 2002;46(3):749-60.
76. Saiman L, Ishimoto K, Lory S, Prince A. The effect of piliation and exoproduct expression on the adherence of Pseudomonas aeruginosa to respiratory epithelial monolayers. J Infect Dis. 1990;161(3):541-8.
77. O'Toole GA, Kolter R. Flagellar and twitching motility are necessary for Pseudomonas aeruginosa biofilm development. Mol Microbiol. 1998;30(2):295-304.
78. Bradley DE, Pitt TL. Pilus-dependence of four Pseudomonas aeruginosa bacteriophages with non-contractile tails. J Gen Virol. 1974;24(1):1-15.
79. Maier B, Potter L, So M, Long CD, Seifert HS, Sheetz MP. Single pilus motor forces exceed 100 pN. Proc Natl Acad Sci U S A. 2002;99(25):16012-7.
80. Pelicic V. Type IV pili: e pluribus unum? Mol Microbiol. 2008;68(4):827-37.
81. Ayers M, Howell PL, Burrows LL. Architecture of the type II secretion and type IV pilus machineries. Future Microbiol. 2010;5(8):1203-18.
82. Bernard CS, Bordi C, Termine E, Filloux A, de Bentzmann S. Organization and PprB-dependent control of the Pseudomonas aeruginosa tad Locus, involved in Flp pilus biology. J Bacteriol. 2009;191(6):1961-73.
83. Carter MQ, Chen J, Lory S. The Pseudomonas aeruginosa pathogenicity island PAPI-1 is transferred via a novel type IV pilus. J Bacteriol. 2010;192(13):3249-58.
84. Imam S, Chen Z, Roos DS, Pohlschroder M. Identification of surprisingly diverse type IV pili, across a broad range of gram-positive bacteria. PLoS One. 2011;6(12):e28919.
85. Ellison CK, Kan J, Dillard RS, Kysela DT, Ducret A, Berne C, et al. Obstruction of pilus retraction stimulates bacterial surface sensing. Science. 2017;358(6362):535-8.
86. de Bentzmann S, Aurouze M, Ball G, Filloux A. FppA, a novel Pseudomonas aeruginosa prepilin peptidase involved in assembly of type IVb pili. J Bacteriol. 2006;188(13):4851-60.
87. Lory S, Strom MS. Structure-function relationship of type-IV prepilin peptidase of Pseudomonas aeruginosa--a review. Gene. 1997;192(1):117-21.
88. Craig L, Forest KT, Maier B. Type IV pili: dynamics, biophysics and functional consequences. Nat Rev Microbiol. 2019;17(7):429-40.
89. Collins RF, Frye SA, Kitmitto A, Ford RC, Tonjum T, Derrick JP. Structure of the Neisseria meningitidis outer membrane PilQ secretin complex at 12 A resolution. J Biol Chem. 2004;279(38):39750-6.
90. Koo J, Tammam S, Ku SY, Sampaleanu LM, Burrows LL, Howell PL. PilF is an outer membrane lipoprotein required for multimerization and localization of the Pseudomonas aeruginosa Type IV pilus secretin. J Bacteriol. 2008;190(21):6961-9.
91. Chang YW, Rettberg L, Treuner-Lange A, Iwasa J, Sogaard-Andersen L, Jensen G. Architecture of the Type IVA Pilus Machine. Biophys J. 2016;110(3):468A-9A.

92. Takhar HK, Kemp K, Kim M, Howell PL, Burrows LL. The platform protein is essential for type IV pilus biogenesis. J Biol Chem. 2013;288(14):9721-8.
93. Ayers M, Sampaleanu LM, Tammam S, Koo J, Harvey H, Howell PL, et al. PilM/N/O/P proteins form an inner membrane complex that affects the stability of the Pseudomonas aeruginosa type IV pilus secretin. J Mol Biol. 2009;394(1):128-42.
94. Nguyen Y, Sugiman-Marangos S, Harvey H, Bell SD, Charlton CL, Junop MS, et al. Pseudomonas aeruginosa minor pilins prime type IVa pilus assembly and promote surface display of the PilY1 adhesin. J Biol Chem. 2015;290(1):601-11.
95. Craig L, Taylor RK, Pique ME, Adair BD, Arvai AS, Singh M, et al. Type IV pilin structure and assembly: X-ray and EM analyses of Vibrio cholerae toxin-coregulated pilus and Pseudomonas aeruginosa PAK pilin. Mol Cell. 2003;11(5):1139-50.
96. Parge HE, Forest KT, Hickey MJ, Christensen DA, Getzoff ED, Tainer JA. Structure of the fibre-forming protein pilin at 2.6 A resolution. Nature. 1995;378(6552):32-8.
97. Craig L, Volkmann N, Arvai AS, Pique ME, Yeager M, Egelman EH, et al. Type IV pilus structure by cryo-electron microscopy and crystallography: implications for pilus assembly and functions. Mol Cell. 2006;23(5):651-62.
98. Kolappan S, Coureuil M, Yu X, Nassif X, Egelman EH, Craig L. Structure of the Neisseria meningitidis Type IV pilus. Nat Commun. 2016;7:13015.
99. Merz AJ, So M, Sheetz MP. Pilus retraction powers bacterial twitching motility. Nature. 2000;407(6800):98-102.
100. Hospenthal MK, Costa TRD, Waksman G. A comprehensive guide to pilus biogenesis in Gram-negative bacteria. Nat Rev Microbiol. 2017;15(6):365-79.
101. Van Gerven N, Van der Verren SE, Reiter DM, Remaut H. The Role of Functional Amyloids in Bacterial Virulence. J Mol Biol. 2018;430(20):3657-84.
102. Olsen A, Jonsson A, Normark S. Fibronectin binding mediated by a novel class of surface organelles on Escherichia coli. Nature. 1989;338(6217):652-5.
103. Dueholm MS, Petersen SV, Sonderkaer M, Larsen P, Christiansen G, Hein KL, et al. Functional amyloid in Pseudomonas. Mol Microbiol. 2010;77(4):1009-20.
104. Romero D, Aguilar C, Losick R, Kolter R. Amyloid fibers provide structural integrity to Bacillus subtilis biofilms. Proc Natl Acad Sci U S A. 2010;107(5):2230-4.
105. Taglialegna A, Navarro S, Ventura S, Garnett JA, Matthews S, Penades JR, et al. Staphylococcal Bap Proteins Build Amyloid Scaffold Biofilm Matrices in Response to Environmental Signals. PLoS Pathog. 2016;12(6):e1005711.
106. Alteri CJ, Xicohtencatl-Cortes J, Hess S, Caballero-Olin G, Giron JA, Friedman RL. Mycobacterium tuberculosis produces pili during human infection. Proc Natl Acad Sci U S A. 2007;104(12):5145-50.
107. Chapman MR, Robinson LS, Pinkner JS, Roth R, Heuser J, Hammar M, et al. Role of Escherichia coli curli operons in directing amyloid fiber formation. Science. 2002;295(5556):851-5.
108. Collinson SK, Emody L, Muller KH, Trust TJ, Kay WW. Purification and characterization of thin, aggregative fimbriae from Salmonella enteritidis. J Bacteriol. 1991;173(15):4773-81.
109. Hammar M, Arnqvist A, Bian Z, Olsen A, Normark S. Expression of two csg operons is required for production of fibronectin- and congo red-binding curli polymers in Escherichia coli K-12. Mol Microbiol. 1995;18(4):661-70.
110. Hammar M, Bian Z, Normark S. Nucleator-dependent intercellular assembly of adhesive curli organelles in Escherichia coli. Proc Natl Acad Sci U S A. 1996;93(13):6562-6.
111. Wang X, Smith DR, Jones JW, Chapman MR. In vitro polymerization of a functional Escherichia coli amyloid protein. J Biol Chem. 2007;282(6):3713-9.

112. Nenninger AA, Robinson LS, Hammer ND, Epstein EA, Badtke MP, Hultgren SJ, et al. CsgE is a curli secretion specificity factor that prevents amyloid fibre aggregation. Mol Microbiol. 2011;81(2):486-99.
113. Nenninger AA, Robinson LS, Hultgren SJ. Localized and efficient curli nucleation requires the chaperone-like amyloid assembly protein CsgF. Proc Natl Acad Sci U S A. 2009;106(3):900-5.
114. Taylor JD, Hawthorne WJ, Lo J, Dear A, Jain N, Meisl G, et al. Electrostatically-guided inhibition of Curli amyloid nucleation by the CsgC-like family of chaperones. Sci Rep. 2016;6:24656.
115. Brombacher E, Dorel C, Zehnder AJB, Landini P. The curli biosynthesis regulator CsgD co-ordinates the expression of both positive and negative determinants for biofilm formation in Escherichia coli. Microbiology (Reading). 2003;149(Pt 10):2847-57.
116. Robinson LS, Ashman EM, Hultgren SJ, Chapman MR. Secretion of curli fibre subunits is mediated by the outer membrane-localized CsgG protein. Mol Microbiol. 2006;59(3):870-81.
117. Cao B, Zhao Y, Kou Y, Ni D, Zhang XC, Huang Y. Structure of the nonameric bacterial amyloid secretion channel. Proc Natl Acad Sci U S A. 2014;111(50):E5439-44.
118. Dueholm MS, Sondergaard MT, Nilsson M, Christiansen G, Stensballe A, Overgaard MT, et al. Expression of Fap amyloids in Pseudomonas aeruginosa, P. fluorescens, and P. putida results in aggregation and increased biofilm formation. Microbiologyopen. 2013;2(3):365-82.
119. Aubrey L.D BBJF, Lutter L., Serpell C.J., Tuite M.F., Serpell L.C., Xue W-F. . Quantification of amyloid fibril polymorphism by nano-morphometry reveals the individuality of filament assembly. Communications Chemistry. 2020.
120. Klein RD, Shu Q, Cusumano ZT, Nagamatsu K, Gualberto NC, Lynch AJL, et al. Structure-Function Analysis of the Curli Accessory Protein CsgE Defines Surfaces Essential for Coordinating Amyloid Fiber Formation. mBio. 2018;9(4).
121. Wurpel DJ, Beatson SA, Totsika M, Petty NK, Schembri MA. Chaperone-usher fimbriae of Escherichia coli. PLoS One. 2013;8(1):e52835.
122. Geibel S, Waksman G. The molecular dissection of the chaperone-usher pathway. Biochim Biophys Acta. 2014;1843(8):1559-67.
123. Choudhury D, Thompson A, Stojanoff V, Langermann S, Pinkner J, Hultgren SJ, et al. X-ray structure of the FimC-FimH chaperone-adhesin complex from uropathogenic Escherichia coli. Science. 1999;285(5430):1061-6.
124. Hultgren SJ, Lindberg F, Magnusson G, Kihlberg J, Tennent JM, Normark S. The PapG adhesin of uropathogenic Escherichia coli contains separate regions for receptor binding and for the incorporation into the pilus. Proc Natl Acad Sci U S A. 1989;86(12):4357-61.
125. Werneburg GT, Thanassi DG. Pili Assembled by the Chaperone/Usher Pathway in Escherichia coli and Salmonella. EcoSal Plus. 2018;8(1).
126. Hospenthal MK, Redzej A, Dodson K, Ukleja M, Frenz B, Rodrigues C, et al. Structure of a Chaperone-Usher Pilus Reveals the Molecular Basis of Rod Uncoiling. Cell. 2016;164(1-2):269-78.
127. Kline KA, Falker S, Dahlberg S, Normark S, Henriques-Normark B. Bacterial adhesins in host-microbe interactions. Cell Host Microbe. 2009;5(6):580-92.
128. Marklund BI, Tennent JM, Garcia E, Hamers A, Baga M, Lindberg F, et al. Horizontal gene transfer of the Escherichia coli pap and prs pili operons as a mechanism for the development of tissue-specific adhesive properties. Mol Microbiol. 1992;6(16):2225-42.
129. Hagberg L, Hull R, Hull S, Falkow S, Freter R, Svanborg Eden C. Contribution of adhesion to bacterial persistence in the mouse urinary tract. Infect Immun. 1983;40(1):265-72.

130. O'Hanley P, Lark D, Falkow S, Schoolnik G. Molecular basis of Escherichia coli colonization of the upper urinary tract in BALB/c mice. Gal-Gal pili immunization prevents Escherichia coli pyelonephritis in the BALB/c mouse model of human pyelonephritis. J Clin Invest. 1985;75(2):347-60.
131. Salminen A, Loimaranta V, Joosten JA, Khan AS, Hacker J, Pieters RJ, et al. Inhibition of P-fimbriated Escherichia coli adhesion by multivalent galabiose derivatives studied by a live-bacteria application of surface plasmon resonance. J Antimicrob Chemother. 2007;60(3):495-501.
132. Kuehn MJ, Heuser J, Normark S, Hultgren SJ. P pili in uropathogenic E. coli are composite fibres with distinct fibrillar adhesive tips. Nature. 1992;356(6366):252-5.
133. Roberts JA, Marklund BI, Ilver D, Haslam D, Kaack MB, Baskin G, et al. The Gal(alpha 1-4)Gal-specific tip adhesin of Escherichia coli P-fimbriae is needed for pyelonephritis to occur in the normal urinary tract. Proc Natl Acad Sci U S A. 1994;91(25):11889-93.
134. Abraham SN, Sun D, Dale JB, Beachey EH. Conservation of the D-mannose-adhesion protein among type 1 fimbriated members of the family Enterobacteriaceae. Nature. 1988;336(6200):682-4.
135. Langermann S, Palaszynski S, Barnhart M, Auguste G, Pinkner JS, Burlein J, et al. Prevention of mucosal Escherichia coli infection by FimH-adhesin-based systemic vaccination. Science. 1997;276(5312):607-11.
136. Wellens A, Garofalo C, Nguyen H, Van Gerven N, Slattegard R, Hernalsteens JP, et al. Intervening with urinary tract infections using anti-adhesives based on the crystal structure of the FimH-oligomannose-3 complex. PLoS One. 2008;3(4):e2040.
137. Lintermans P, Pohl P, Deboeck F, Bertels A, Schlicker C, Vandekerckhove J, et al. Isolation and nucleotide sequence of the F17-A gene encoding the structural protein of the F17 fimbriae in bovine enterotoxigenic Escherichia coli. Infect Immun. 1988;56(6):1475-84.
138. Merckel MC, Tanskanen J, Edelman S, Westerlund-Wikstrom B, Korhonen TK, Goldman A. The structural basis of receptor-binding by Escherichia coli associated with diarrhea and septicemia. J Mol Biol. 2003;331(4):897-905.
139. Marron MB, Smyth CJ. Molecular analysis of the cso operon of enterotoxigenic Escherichia coli reveals that CsoA is the adhesin of CS1 fimbriae and that the accessory genes are interchangeable with those of the cfa operon. Microbiology (Reading). 1995;141 (Pt 11):2849-59.
140. Baker KK, Levine MM, Morison J, Phillips A, Barry EM. CfaE tip mutations in enterotoxigenic Escherichia coli CFA/I fimbriae define critical human intestinal binding sites. Cell Microbiol. 2009;11(5):742-54.
141. Li YF, Poole S, Rasulova F, McVeigh AL, Savarino SJ, Xia D. A receptor-binding site as revealed by the crystal structure of CfaE, the colonization factor antigen I fimbrial adhesin of enterotoxigenic Escherichia coli. J Biol Chem. 2007;282(33):23970-80.
142. Sakellaris H, Munson GP, Scott JR. A conserved residue in the tip proteins of CS1 and CFA/I pili of enterotoxigenic Escherichia coli that is essential for adherence. Proc Natl Acad Sci U S A. 1999;96(22):12828-32.
143. Dobrindt U, Blum-Oehler G, Hartsch T, Gottschalk G, Ron EZ, Funfstuck R, et al. S-Fimbria-encoding determinant sfa(I) is located on pathogenicity island III(536) of uropathogenic Escherichia coli strain 536. Infect Immun. 2001;69(7):4248-56.
144. Prasadarao NV, Wass CA, Hacker J, Jann K, Kim KS. Adhesion of S-fimbriated Escherichia coli to brain glycolipids mediated by sfaA gene-encoded protein of S-fimbriae. J Biol Chem. 1993;268(14):10356-63.

145. Khan AS, Kniep B, Oelschlaeger TA, Van Die I, Korhonen T, Hacker J. Receptor structure for F1C fimbriae of uropathogenic Escherichia coli. Infect Immun. 2000;68(6):3541-7.
146. Zav'yalov VP, Chernovskaya TV, Navolotskaya EV, Karlyshev AV, MacIntyre S, Vasiliev AM, et al. Specific high affinity binding of human interleukin 1 beta by Caf1A usher protein of Yersinia pestis. FEBS Lett. 1995;371(1):65-8.
147. Sebbane F, Jarrett C, Gardner D, Long D, Hinnebusch BJ. The Yersinia pestis caf1M1A1 fimbrial capsule operon promotes transmission by flea bite in a mouse model of bubonic plague. Infect Immun. 2009;77(3):1222-9.
148. Pakharukova N, Tuittila M, Paavilainen S, Malmi H, Parilova O, Teneberg S, et al. Structural basis for Acinetobacter baumannii biofilm formation. Proc Natl Acad Sci U S A. 2018;115(21):5558-63.
149. Ruer S, Stender S, Filloux A, de Bentzmann S. Assembly of fimbrial structures in Pseudomonas aeruginosa: functionality and specificity of chaperone-usher machineries. J Bacteriol. 2007;189(9):3547-55.
150. Waksman G, Hultgren SJ. Structural biology of the chaperone-usher pathway of pilus biogenesis. Nat Rev Microbiol. 2009;7(11):765-74.
151. Fronzes R, Remaut H, Waksman G. Architectures and biogenesis of non-flagellar protein appendages in Gram-negative bacteria. EMBO J. 2008;27(17):2271-80.
152. Hospenthal MK, Zyla D, Costa TRD, Redzej A, Giese C, Lillington J, et al. The Cryoelectron Microscopy Structure of the Type 1 Chaperone-Usher Pilus Rod. Structure. 2017;25(12):1829-38 e4.
153. Rose RJ, Verger D, Daviter T, Remaut H, Paci E, Waksman G, et al. Unraveling the molecular basis of subunit specificity in P pilus assembly by mass spectrometry. Proc Natl Acad Sci U S A. 2008;105(35):12873-8.
154. Ford B, Verger D, Dodson K, Volkan E, Kostakioti M, Elam J, et al. The structure of the PapD-PapGII pilin complex reveals an open and flexible P5 pocket. J Bacteriol. 2012;194(23):6390-7.
155. Dodson KW, Jacob-Dubuisson F, Striker RT, Hultgren SJ. Outer-membrane PapC molecular usher discriminately recognizes periplasmic chaperone-pilus subunit complexes. Proc Natl Acad Sci U S A. 1993;90(8):3670-4.
156. Saulino ET, Thanassi DG, Pinkner JS, Hultgren SJ. Ramifications of kinetic partitioning on usher-mediated pilus biogenesis. EMBO J. 1998;17(8):2177-85.
157. Jacob-Dubuisson F, Heuser J, Dodson K, Normark S, Hultgren S. Initiation of assembly and association of the structural elements of a bacterial pilus depend on two specialized tip proteins. EMBO J. 1993;12(3):837-47.
158. Lee YM, Dodson KW, Hultgren SJ. Adaptor function of PapF depends on donor strand exchange in P-pilus biogenesis of Escherichia coli. J Bacteriol. 2007;189(14):5276-83.
159. Striker R, Jacob-Dubuisson F, Freiden C, Hultgren SJ. Stable fiber-forming and nonfiber-forming chaperone-subunit complexes in pilus biogenesis. J Biol Chem. 1994;269(16):12233-9.
160. Thanassi DG, Stathopoulos C, Dodson K, Geiger D, Hultgren SJ. Bacterial outer membrane ushers contain distinct targeting and assembly domains for pilus biogenesis. J Bacteriol. 2002;184(22):6260-9.
161. Remaut H, Tang C, Henderson NS, Pinkner JS, Wang T, Hultgren SJ, et al. Fiber formation across the bacterial outer membrane by the chaperone/usher pathway. Cell. 2008;133(4):640-52.
162. Capitani G, Eidam O, Grutter MG. Evidence for a novel domain of bacterial outer membrane ushers. Proteins. 2006;65(4):816-23.

163. Phan G, Remaut H, Wang T, Allen WJ, Pirker KF, Lebedev A, et al. Crystal structure of the FimD usher bound to its cognate FimC-FimH substrate. Nature. 2011;474(7349):49-53.
164. Eidam O, Dworkowski FS, Glockshuber R, Grutter MG, Capitani G. Crystal structure of the ternary FimC-FimF(t)-FimD(N) complex indicates conserved pilus chaperone-subunit complex recognition by the usher FimD. FEBS Lett. 2008;582(5):651-5.
165. Huang Y, Smith BS, Chen LX, Baxter RH, Deisenhofer J. Insights into pilus assembly and secretion from the structure and functional characterization of usher PapC. Proc Natl Acad Sci U S A. 2009;106(18):7403-7.
166. Nishiyama M, Vetsch M, Puorger C, Jelesarov I, Glockshuber R. Identification and characterization of the chaperone-subunit complex-binding domain from the type 1 pilus assembly platform FimD. J Mol Biol. 2003;330(3):513-25.
167. Nishiyama M, Ishikawa T, Rechsteiner H, Glockshuber R. Reconstitution of pilus assembly reveals a bacterial outer membrane catalyst. Science. 2008;320(5874):376-9.
168. Saulino ET, Bullitt E, Hultgren SJ. Snapshots of usher-mediated protein secretion and ordered pilus assembly. Proc Natl Acad Sci U S A. 2000;97(16):9240-5.
169. Jacob-Dubuisson F, Striker R, Hultgren SJ. Chaperone-assisted self-assembly of pili independent of cellular energy. J Biol Chem. 1994;269(17):12447-55.
170. Geibel S, Procko E, Hultgren SJ, Baker D, Waksman G. Structural and energetic basis of folded-protein transport by the FimD usher. Nature. 2013;496(7444):243-6.
171. Du M, Yuan Z, Yu H, Henderson N, Sarowar S, Zhao G, et al. Handover mechanism of the growing pilus by the bacterial outer-membrane usher FimD. Nature. 2018;562(7727):444-7.
172. Nuccio SP, Baumler AJ. Evolution of the chaperone/usher assembly pathway: fimbrial classification goes Greek. Microbiol Mol Biol Rev. 2007;71(4):551-75.
173. Hung DL, Knight SD, Woods RM, Pinkner JS, Hultgren SJ. Molecular basis of two subfamilies of immunoglobulin-like chaperones. EMBO J. 1996;15(15):3792-805.
174. Pakharukova N, Garnett JA, Tuittila M, Paavilainen S, Diallo M, Xu Y, et al. Structural Insight into Archaic and Alternative Chaperone-Usher Pathways Reveals a Novel Mechanism of Pilus Biogenesis. PLoS Pathog. 2015;11(11):e1005269.
175. Li YF, Poole S, Nishio K, Jang K, Rasulova F, McVeigh A, et al. Structure of CFA/I fimbriae from enterotoxigenic Escherichia coli. Proc Natl Acad Sci U S A. 2009;106(26):10793-8.
176. Tomaras AP, Dorsey CW, Edelmann RE, Actis LA. Attachment to and biofilm formation on abiotic surfaces by Acinetobacter baumannii: involvement of a novel chaperone-usher pili assembly system. Microbiology (Reading). 2003;149(Pt 12):3473-84.
177. Gollop R, Inouye M, Inouye S. Protein U, a late-developmental spore coat protein of Myxococcus xanthus, is a secretory protein. J Bacteriol. 1991;173(11):3597-600.
178. Salih O, Remaut H, Waksman G, Orlova EV. Structural analysis of the Saf pilus by electron microscopy and image processing. J Mol Biol. 2008;379(1):174-87.
179. Gounon P, Jouve M, Le Bouguenec C. Immunocytochemistry of the AfaE adhesin and AfaD invasin produced by pathogenic Escherichia coli strains during interaction of the bacteria with HeLa cells by high-resolution scanning electron microscopy. Microbes Infect. 2000;2(4):359-65.
180. Zavialov AV, Kersley J, Korpela T, Zav'yalov VP, MacIntyre S, Knight SD. Donor strand complementation mechanism in the biogenesis of non-pilus systems. Mol Microbiol. 2002;45(4):983-95.
181. Zavialov AV, Berglund J, Pudney AF, Fooks LJ, Ibrahim TM, MacIntyre S, et al. Structure and biogenesis of the capsular F1 antigen from Yersinia pestis: preserved folding energy drives fiber formation. Cell. 2003;113(5):587-96.

182. Anderson KL, Billington J, Pettigrew D, Cota E, Simpson P, Roversi P, et al. An atomic resolution model for assembly, architecture, and function of the Dr adhesins. Mol Cell. 2004;15(4):647-57.
183. Remaut H, Rose RJ, Hannan TJ, Hultgren SJ, Radford SE, Ashcroft AE, et al. Donor-strand exchange in chaperone-assisted pilus assembly proceeds through a concerted beta strand displacement mechanism. Mol Cell. 2006;22(6):831-42.
184. Clegg S, Wilson J, Johnson J. More than one way to control hair growth: regulatory mechanisms in enterobacteria that affect fimbriae assembled by the chaperone/usher pathway. J Bacteriol. 2011;193(9):2081-8.
185. Abraham JM, Freitag CS, Clements JR, Eisenstein BI. An invertible element of DNA controls phase variation of type 1 fimbriae of Escherichia coli. Proc Natl Acad Sci U S A. 1985;82(17):5724-7.
186. Olsen PB, Klemm P. Localization of promoters in the fim gene cluster and the effect of H-NS on the transcription of fimB and fimE. FEMS Microbiol Lett. 1994;116(1):95-100.
187. Gally DL, Leathart J, Blomfield IC. Interaction of FimB and FimE with the fim switch that controls the phase variation of type 1 fimbriae in Escherichia coli K-12. Mol Microbiol. 1996;21(4):725-38.
188. Corcoran CP, Dorman CJ. DNA relaxation-dependent phase biasing of the fim genetic switch in Escherichia coli depends on the interplay of H-NS, IHF and LRP. Mol Microbiol. 2009;74(5):1071-82.
189. Holden NJ, Totsika M, Mahler E, Roe AJ, Catherwood K, Lindner K, et al. Demonstration of regulatory cross-talk between P fimbriae and type 1 fimbriae in uropathogenic Escherichia coli. Microbiology (Reading). 2006;152(Pt 4):1143-53.
190. Sohanpal BK, El-Labany S, Lahooti M, Plumbridge JA, Blomfield IC. Integrated regulatory responses of fimB to N-acetylneuraminic (sialic) acid and GlcNAc in Escherichia coli K-12. Proc Natl Acad Sci U S A. 2004;101(46):16322-7.
191. Gally DL, Bogan JA, Eisenstein BI, Blomfield IC. Environmental regulation of the fim switch controlling type 1 fimbrial phase variation in Escherichia coli K-12: effects of temperature and media. J Bacteriol. 1993;175(19):6186-93.
192. Gally DL, Rucker TJ, Blomfield IC. The leucine-responsive regulatory protein binds to the fim switch to control phase variation of type 1 fimbrial expression in Escherichia coli K-12. J Bacteriol. 1994;176(18):5665-72.
193. El-Labany S, Sohanpal BK, Lahooti M, Akerman R, Blomfield IC. Distant cis-active sequences and sialic acid control the expression of fimB in Escherichia coli K-12. Mol Microbiol. 2003;49(4):1109-18.
194. Baga M, Goransson M, Normark S, Uhlin BE. Transcriptional activation of a pap pilus virulence operon from uropathogenic Escherichia coli. EMBO J. 1985;4(13B):3887-93.
195. Peterson SN, Reich NO. GATC flanking sequences regulate Dam activity: evidence for how Dam specificity may influence pap expression. J Mol Biol. 2006;355(3):459-72.
196. Goransson M, Forsman P, Nilsson P, Uhlin BE. Upstream activating sequences that are shared by two divergently transcribed operons mediate cAMP-CRP regulation of pilus-adhesin in Escherichia coli. Mol Microbiol. 1989;3(11):1557-65.
197. White-Ziegler CA, Villapakkam A, Ronaszeki K, Young S. H-NS controls pap and daa fimbrial transcription in Escherichia coli in response to multiple environmental cues. J Bacteriol. 2000;182(22):6391-400.
198. Blyn LB, Braaten BA, White-Ziegler CA, Rolfson DH, Low DA. Phase-variation of pyelonephritis-associated pili in Escherichia coli: evidence for transcriptional regulation. EMBO J. 1989;8(2):613-20.
199. Peterson SN, Reich NO. Competitive Lrp and Dam assembly at the pap regulatory region: implications for mechanisms of epigenetic regulation. J Mol Biol. 2008;383(1):92-105.

200. Weyand NJ, Low DA. Regulation of Pap phase variation. Lrp is sufficient for the establishment of the phase off pap DNA methylation pattern and repression of pap transcription in vitro. J Biol Chem. 2000;275(5):3192-200.
201. van der Woude MW, Kaltenbach LS, Low DA. Leucine-responsive regulatory protein plays dual roles as both an activator and a repressor of the Escherichia coli pap fimbrial operon. Mol Microbiol. 1995;17(2):303-12.
202. White-Ziegler CA, Angus Hill ML, Braaten BA, van der Woude MW, Low DA. Thermoregulation of Escherichia coli pap transcription: H-NS is a temperature-dependent DNA methylation blocking factor. Mol Microbiol. 1998;28(6):1121-37.
203. Valentini M, Filloux A. Biofilms and Cyclic di-GMP (c-di-GMP) Signaling: Lessons from Pseudomonas aeruginosa and Other Bacteria. J Biol Chem. 2016;291(24):12547-55.
204. Romling U, Galperin MY, Gomelsky M. Cyclic di-GMP: the first 25 years of a universal bacterial second messenger. Microbiol Mol Biol Rev. 2013;77(1):1-52.
205. Hornick DB, Thommandru J, Smits W, Clegg S. Adherence properties of an mrkD-negative mutant of Klebsiella pneumoniae. Infect Immun. 1995;63(5):2026-32.
206. Duguid JP. Fimbriae and adhesive properties in Klebsiella strains. J Gen Microbiol. 1959;21:271-86.
207. Allen BL, Gerlach GF, Clegg S. Nucleotide sequence and functions of mrk determinants necessary for expression of type 3 fimbriae in Klebsiella pneumoniae. J Bacteriol. 1991;173(2):916-20.
208. Johnson JG, Murphy CN, Sippy J, Johnson TJ, Clegg S. Type 3 fimbriae and biofilm formation are regulated by the transcriptional regulators MrkHI in Klebsiella pneumoniae. J Bacteriol. 2011;193(14):3453-60.
209. Johnson JG, Clegg S. Role of MrkJ, a phosphodiesterase, in type 3 fimbrial expression and biofilm formation in Klebsiella pneumoniae. J Bacteriol. 2010;192(15):3944-50.
210. Giraud C, de Bentzmann S. Inside the complex regulation of Pseudomonas aeruginosa chaperone usher systems. Environ Microbiol. 2012;14(8):1805-16.
211. Meissner A, Wild V, Simm R, Rohde M, Erck C, Bredenbruch F, et al. Pseudomonas aeruginosa cupA-encoded fimbriae expression is regulated by a GGDEF and EAL domain-dependent modulation of the intracellular level of cyclic diguanylate. Environ Microbiol. 2007;9(10):2475-85.
212. D'Argenio DA, Calfee MW, Rainey PB, Pesci EC. Autolysis and autoaggregation in Pseudomonas aeruginosa colony morphology mutants. J Bacteriol. 2002;184(23):6481-9.
213. Klebensberger J, Birkenmaier A, Geffers R, Kjelleberg S, Philipp B. SiaA and SiaD are essential for inducing autoaggregation as a specific response to detergent stress in Pseudomonas aeruginosa. Environ Microbiol. 2009;11(12):3073-86.
214. Vallet-Gely I, Sharp JS, Dove SL. Local and global regulators linking anaerobiosis to cupA fimbrial gene expression in Pseudomonas aeruginosa. J Bacteriol. 2007;189(23):8667-76.
215. Nicastro GG, Boechat AL, Abe CM, Kaihami GH, Baldini RL. Pseudomonas aeruginosa PA14 cupD transcription is activated by the RcsB response regulator, but repressed by its putative cognate sensor RcsC. FEMS Microbiol Lett. 2009;301(1):115-23.
216. Mikkelsen H, Hui K, Barraud N, Filloux A. The pathogenicity island encoded PvrSR/RcsCB regulatory network controls biofilm formation and dispersal in Pseudomonas aeruginosa PA14. Mol Microbiol. 2013;89(3):450-63.
217. Schmidt KD, Tummler B, Romling U. Comparative genome mapping of Pseudomonas aeruginosa PAO with P. aeruginosa C, which belongs to a major clone in cystic fibrosis patients and aquatic habitats. J Bacteriol. 1996;178(1):85-93.
218. Cardo D, Horan, T., Andrus, M., Dembinski, M., Edwards, J., Peavy, G. National nosocomial infections surveillance (NNIS) system report, data

summary from January 1992 through June 2004. Am J Infect Control 2004;32: 470–85.
219. Nathwani D, Raman G, Sulham K, Gavaghan M, Menon V. Clinical and economic consequences of hospital-acquired resistant and multidrug-resistant Pseudomonas aeruginosa infections: a systematic review and meta-analysis. Antimicrob Resist Infect Control. 2014;3(1):32.
220. Abadi ATB, Rizvanov AA, Haertlé T, Blatt NL. World Health Organization Report: Current Crisis of Antibiotic Resistance. BioNanoScience. 2019(9):778–88.
221. Lambert ML, Suetens C, Savey A, Palomar M, Hiesmayr M, Morales I, et al. Clinical outcomes of health-care-associated infections and antimicrobial resistance in patients admitted to European intensive-care units: a cohort study. Lancet Infect Dis. 2011;11(1):30-8.
222. Tabak YP, Merchant S, Ye G, Vankeepuram L, Gupta V, Kurtz SG, et al. Incremental clinical and economic burden of suspected respiratory infections due to multi-drug-resistant Pseudomonas aeruginosa in the United States. J Hosp Infect. 2019;103(2):134-41.
223. Rosenthal VD, Al-Abdely, H. M., El-Kholy, A. A., AlKhawaja, S. A. A., Leblebicioglu, H., Mehta, Y. International nosocomial infection control consortium report, data summary of 50 countries for 2010-2015: device-associated module. Am J Infect Control 2016;44:1495–504.
224. Kiewitz C, Tummler B. Sequence diversity of Pseudomonas aeruginosa: impact on population structure and genome evolution. J Bacteriol. 2000;182(11):3125-35.
225. Stover CK, Pham XQ, Erwin AL, Mizoguchi SD, Warrener P, Hickey MJ, et al. Complete genome sequence of Pseudomonas aeruginosa PAO1, an opportunistic pathogen. Nature. 2000;406(6799):959-64.
226. Mathee K, Narasimhan G, Valdes C, Qiu X, Matewish JM, Koehrsen M, et al. Dynamics of Pseudomonas aeruginosa genome evolution. Proc Natl Acad Sci U S A. 2008;105(8):3100-5.
227. Frimmersdorf E, Horatzek S, Pelnikevich A, Wiehlmann L, Schomburg D. How Pseudomonas aeruginosa adapts to various environments: a metabolomic approach. Environ Microbiol. 2010;12(6):1734-47.
228. Castang S, Dove SL. Basis for the essentiality of H-NS family members in Pseudomonas aeruginosa. J Bacteriol. 2012;194(18):5101-9.
229. Westfall LW, Carty NL, Layland N, Kuan P, Colmer-Hamood JA, Hamood AN. mvaT mutation modifies the expression of the Pseudomonas aeruginosa multidrug efflux operon mexEF-oprN. FEMS Microbiol Lett. 2006;255(2):247-54.
230. Diggle SP, Winzer K, Lazdunski A, Williams P, Camara M. Advancing the quorum in Pseudomonas aeruginosa: MvaT and the regulation of N-acylhomoserine lactone production and virulence gene expression. J Bacteriol. 2002;184(10):2576-86.
231. Vallet-Gely I, Donovan KE, Fang R, Joung JK, Dove SL. Repression of phase-variable cup gene expression by H-NS-like proteins in Pseudomonas aeruginosa. Proc Natl Acad Sci U S A. 2005;102(31):11082-7.
232. Higgins CF, Dorman CJ, Stirling DA, Waddell L, Booth IR, May G, et al. A physiological role for DNA supercoiling in the osmotic regulation of gene expression in S. typhimurium and E. coli. Cell. 1988;52(4):569-84.
233. Kawula TH, Orndorff PE. Rapid site-specific DNA inversion in Escherichia coli mutants lacking the histonelike protein H-NS. J Bacteriol. 1991;173(13):4116-23.
234. Melville SB GR. Mutations in fnr that alter anaerobic regulation of electron transport-associated genes in Escherichia coli. J Biol Chem. 1990 265(31):18733-6.
235. McManus HR, Dove SL. The CgrA and CgrC proteins form a complex that positively regulates cupA fimbrial gene expression in Pseudomonas aeruginosa. J Bacteriol. 2011;193(22):6152-61.

236. Worlitzsch D, Tarran R, Ulrich M, Schwab U, Cekici A, Meyer KC, et al. Effects of reduced mucus oxygen concentration in airway Pseudomonas infections of cystic fibrosis patients. J Clin Invest. 2002;109(3):317-25.
237. Yoon SS, Hennigan RF, Hilliard GM, Ochsner UA, Parvatiyar K, Kamani MC, et al. Pseudomonas aeruginosa anaerobic respiration in biofilms: relationships to cystic fibrosis pathogenesis. Dev Cell. 2002;3(4):593-603.
238. Andersen JB, Kragh KN, Hultqvist LD, Rybtke M, Nilsson M, Jakobsen TH, et al. Induction of Native c-di-GMP Phosphodiesterases Leads to Dispersal of Pseudomonas aeruginosa Biofilms. Antimicrob Agents Chemother. 2021;65(4).
239. Zhang Y, Xia B, Li M, Shi J, Long Y, Jin Y, et al. HigB Reciprocally Controls Biofilm Formation and the Expression of Type III Secretion System Genes through Influencing the Intracellular c-di-GMP Level in Pseudomonas aeruginosa. Toxins (Basel). 2018;10(11).
240. Rossello J, Lima A, Gil M, Rodriguez Duarte J, Correa A, Carvalho PC, et al. The EAL-domain protein FcsR regulates flagella, chemotaxis and type III secretion system in Pseudomonas aeruginosa by a phosphodiesterase independent mechanism. Sci Rep. 2017;7(1):10281.
241. Ueda A, Wood TK. Tyrosine Phosphatase TpbA of Pseudomonas aeruginosa Controls Extracellular DNA via Cyclic Diguanylic Acid Concentrations. Environ Microbiol. 2010;2(3):449-55.
242. Petrova OE, Cherny KE, Sauer K. The diguanylate cyclase GcbA facilitates Pseudomonas aeruginosa biofilm dispersion by activating BdlA. J Bacteriol. 2015;197(1):174-87.
243. Alva V, Nam SZ, Soding J, Lupas AN. The MPI bioinformatics Toolkit as an integrative platform for advanced protein sequence and structure analysis. Nucleic Acids Res. 2016;44(W1):W410-5.
244. Locht C, Geoffroy MC, Renauld G. Common accessory genes for the Bordetella pertussis filamentous hemagglutinin and fimbriae share sequence similarities with the papC and papD gene families. EMBO J. 1992;11(9):3175-83.
245. Gentle IE, Burri L, Lithgow T. Molecular architecture and function of the Omp85 family of proteins. Mol Microbiol. 2005;58(5):1216-25.
246. Jacob-Dubuisson F, Fernandez R, Coutte L. Protein secretion through autotransporter and two-partner pathways. Biochim Biophys Acta. 2004;1694(1-3):235-57.
247. Jacob-Dubuisson F, Locht C, Antoine R. Two-partner secretion in Gram-negative bacteria: a thrifty, specific pathway for large virulence proteins. Mol Microbiol. 2001;40(2):306-13.
248. Ruer S, Ball G, Filloux A, de Bentzmann S. The 'P-usher', a novel protein transporter involved in fimbrial assembly and TpsA secretion. EMBO J. 2008;27(20):2669-80.
249. Cai X, Wang R, Filloux A, Waksman G, Meng G. Structural and functional characterization of Pseudomonas aeruginosa CupB chaperones. PLoS One. 2011;6(1):e16583.
250. Rasheed M, Garnett J, Perez-Dorado I, Muhl D, Filloux A, Matthews S. Crystal structure of the CupB6 adhesive tip from the chaperone-usher family of pili from Pseudomonas aeruginosa. Biochim Biophys Acta. 2016;1864(11):1500-5.
251. Coppens F, Iyyathurai J, Ruer S, Fioravanti A, Taganna J, Vereecke L, et al. Structural and adhesive properties of the long polar fimbriae protein LpfD from adherent-invasive Escherichia coli. Acta Crystallogr D Biol Crystallogr. 2015;71(Pt 8):1615-26.
252. Bock A, Gross R. The BvgAS two-component system of Bordetella spp.: a versatile modulator of virulence gene expression. Int J Med Microbiol. 2001;291(2):119-30.
253. Rao F, Yang Y, Qi Y, Liang ZX. Catalytic mechanism of cyclic di-GMP-specific phosphodiesterase: a study of the EAL domain-containing RocR from Pseudomonas aeruginosa. J Bacteriol. 2008;190(10):3622-31.

254. Stintzi A, Johnson Z, Stonehouse M, Ochsner U, Meyer JM, Vasil ML, et al. The pvc gene cluster of Pseudomonas aeruginosa: role in synthesis of the pyoverdine chromophore and regulation by PtxR and PvdS. J Bacteriol. 1999;181(13):4118-24.
255. Clarke-Pearson MF, Brady SF. Paerucumarin, a new metabolite produced by the pvc gene cluster from Pseudomonas aeruginosa. J Bacteriol. 2008;190(20):6927-30.
256. Qaisar U, Luo L, Haley CL, Brady SF, Carty NL, Colmer-Hamood JA, et al. The pvc operon regulates the expression of the Pseudomonas aeruginosa fimbrial chaperone/usher pathway (cup) genes. PLoS One. 2013;8(4):e62735.
257. Rahme LG, Stevens EJ, Wolfort SF, Shao J, Tompkins RG, Ausubel FM. Common virulence factors for bacterial pathogenicity in plants and animals. Science. 1995;268(5219):1899-902.
258. Pakharukova N, Tuittila M, Paavilainen S, Zavialov A. Methylation, crystallization and SAD phasing of the Csu pilus CsuC-CsuE chaperone-adhesin subunit pre-assembly complex from Acinetobacter baumannii. Acta Crystallogr F Struct Biol Commun. 2017;73(Pt 8):450-4.
259. Ma L, Conover M, Lu H, Parsek MR, Bayles K, Wozniak DJ. Assembly and development of the Pseudomonas aeruginosa biofilm matrix. PLoS Pathog. 2009;5(3):e1000354.
260. Friedman L, Kolter R. Two genetic loci produce distinct carbohydrate-rich structural components of the Pseudomonas aeruginosa biofilm matrix. J Bacteriol. 2004;186(14):4457-65.
261. Cramton SE, Gerke C, Schnell NF, Nichols WW, Gotz F. The intercellular adhesion (ica) locus is present in Staphylococcus aureus and is required for biofilm formation. Infect Immun. 1999;67(10):5427-33.
262. Wang X, Preston JF, 3rd, Romeo T. The pgaABCD locus of Escherichia coli promotes the synthesis of a polysaccharide adhesin required for biofilm formation. J Bacteriol. 2004;186(9):2724-34.
263. Jackson KD, Starkey M, Kremer S, Parsek MR, Wozniak DJ. Identification of psl, a locus encoding a potential exopolysaccharide that is essential for Pseudomonas aeruginosa PAO1 biofilm formation. J Bacteriol. 2004;186(14):4466-75.
264. Roberts IS. The biochemistry and genetics of capsular polysaccharide production in bacteria. Annu Rev Microbiol. 1996;50:285-315.
265. Merker RI, Smit J. Characterization of the adhesive holdfast of marine and freshwater caulobacters. Appl Environ Microbiol. 1988;54(8):2078-85.
266. Whitney JC, Howell PL. Synthase-dependent exopolysaccharide secretion in Gram-negative bacteria. Trends Microbiol. 2013;21(2):63-72.
267. Schmid J, Sieber V, Rehm B. Bacterial exopolysaccharides: biosynthesis pathways and engineering strategies. Front Microbiol. 2015;6:496.
268. McGrath BC, Osborn MJ. Localization of the terminal steps of O-antigen synthesis in Salmonella typhimurium. J Bacteriol. 1991;173(2):649-54.
269. Liu D, Cole RA, Reeves PR. An O-antigen processing function for Wzx (RfbX): a promising candidate for O-unit flippase. J Bacteriol. 1996;178(7):2102-7.
270. Woodward R, Yi W, Li L, Zhao G, Eguchi H, Sridhar PR, et al. In vitro bacterial polysaccharide biosynthesis: defining the functions of Wzy and Wzz. Nat Chem Biol. 2010;6(6):418-23.
271. Cuthbertson L, Mainprize IL, Naismith JH, Whitfield C. Pivotal roles of the outer membrane polysaccharide export and polysaccharide copolymerase protein families in export of extracellular polysaccharides in gram-negative bacteria. Microbiol Mol Biol Rev. 2009;73(1):155-77.
272. Whitfield C. Biosynthesis and assembly of capsular polysaccharides in Escherichia coli. Annu Rev Biochem. 2006;75:39-68.

273. Cuthbertson L, Kos V, Whitfield C. ABC transporters involved in export of cell surface glycoconjugates. Microbiol Mol Biol Rev. 2010;74(3):341-62.
274. Hashimoto A, Shimono K, Horikawa Y, Ichikawa T, Wada M, Imai T, et al. Extraction of cellulose-synthesizing activity of Gluconacetobacter xylinus by alkylmaltoside. Carbohydr Res. 2011;346(17):2760-8.
275. Cartee RT, Forsee WT, Jensen JW, Yother J. Expression of the Streptococcus pneumoniae type 3 synthase in Escherichia coli. Assembly of type 3 polysaccharide on a lipid primer. J Biol Chem. 2001;276(52):48831-9.
276. Hubbard C, McNamara JT, Azumaya C, Patel MS, Zimmer J. The hyaluronan synthase catalyzes the synthesis and membrane translocation of hyaluronan. J Mol Biol. 2012;418(1-2):21-31.
277. Merighi M, Lee VT, Hyodo M, Hayakawa Y, Lory S. The second messenger bis-(3'-5')-cyclic-GMP and its PilZ domain-containing receptor Alg44 are required for alginate biosynthesis in Pseudomonas aeruginosa. Mol Microbiol. 2007;65(4):876-95.
278. Ryjenkov DA, Simm R, Romling U, Gomelsky M. The PilZ domain is a receptor for the second messenger c-di-GMP: the PilZ domain protein YcgR controls motility in enterobacteria. J Biol Chem. 2006;281(41):30310-4.
279. Jain S, Ohman DE. Deletion of algK in mucoid Pseudomonas aeruginosa blocks alginate polymer formation and results in uronic acid secretion. J Bacteriol. 1998;180(3):634-41.
280. Rohde H, Burandt EC, Siemssen N, Frommelt L, Burdelski C, Wurster S, et al. Polysaccharide intercellular adhesin or protein factors in biofilm accumulation of Staphylococcus epidermidis and Staphylococcus aureus isolated from prosthetic hip and knee joint infections. Biomaterials. 2007;28(9):1711-20.
281. Gristina A. Biomaterial-centered infection: microbial adhesion versus tissue integration. 1987. Clin Orthop Relat Res. 2004(427):4-12.
282. Heilmann C, Schweitzer O, Gerke C, Vanittanakom N, Mack D, Gotz F. Molecular basis of intercellular adhesion in the biofilm-forming Staphylococcus epidermidis. Mol Microbiol. 1996;20(5):1083-91.
283. Gerke C, Kraft A, Sussmuth R, Schweitzer O, Gotz F. Characterization of the N-acetylglucosaminyltransferase activity involved in the biosynthesis of the Staphylococcus epidermidis polysaccharide intercellular adhesin. J Biol Chem. 1998;273(29):18586-93.
284. Vuong C, Voyich JM, Fischer ER, Braughton KR, Whitney AR, DeLeo FR, et al. Polysaccharide intercellular adhesin (PIA) protects Staphylococcus epidermidis against major components of the human innate immune system. Cell Microbiol. 2004;6(3):269-75.
285. Vuong C, Kocianova S, Voyich JM, Yao Y, Fischer ER, DeLeo FR, et al. A crucial role for exopolysaccharide modification in bacterial biofilm formation, immune evasion, and virulence. J Biol Chem. 2004;279(52):54881-6.
286. Conlon KM, Humphreys H, O'Gara JP. icaR encodes a transcriptional repressor involved in environmental regulation of ica operon expression and biofilm formation in Staphylococcus epidermidis. J Bacteriol. 2002;184(16):4400-8.
287. Valle J, Toledo-Arana A, Berasain C, Ghigo JM, Amorena B, Penades JR, et al. SarA and not sigmaB is essential for biofilm development by Staphylococcus aureus. Mol Microbiol. 2003;48(4):1075-87.
288. Xu L, Li H, Vuong C, Vadyvaloo V, Wang J, Yao Y, et al. Role of the luxS quorum-sensing system in biofilm formation and virulence of Staphylococcus epidermidis. Infect Immun. 2006;74(1):488-96.
289. Knobloch JK, Bartscht K, Sabottke A, Rohde H, Feucht HH, Mack D. Biofilm formation by Staphylococcus epidermidis depends on functional RsbU, an activator of the sigB

operon: differential activation mechanisms due to ethanol and salt stress. J Bacteriol. 2001;183(8):2624-33.
290. Jefferson KK, Pier DB, Goldmann DA, Pier GB. The teicoplanin-associated locus regulator (TcaR) and the intercellular adhesin locus regulator (IcaR) are transcriptional inhibitors of the ica locus in Staphylococcus aureus. J Bacteriol. 2004;186(8):2449-56.
291. O'Neill E, Pozzi C, Houston P, Smyth D, Humphreys H, Robinson DA, et al. Association between methicillin susceptibility and biofilm regulation in Staphylococcus aureus isolates from device-related infections. J Clin Microbiol. 2007;45(5):1379-88.
292. Lauderdale KJ, Malone CL, Boles BR, Morcuende J, Horswill AR. Biofilm dispersal of community-associated methicillin-resistant Staphylococcus aureus on orthopedic implant material. J Orthop Res. 2010;28(1):55-61.
293. Hennig S, Nyunt Wai S, Ziebuhr W. Spontaneous switch to PIA-independent biofilm formation in an ica-positive Staphylococcus epidermidis isolate. Int J Med Microbiol. 2007;297(2):117-22.
294. Bobrov AG, Kirillina O, Forman S, Mack D, Perry RD. Insights into Yersinia pestis biofilm development: topology and co-interaction of Hms inner membrane proteins involved in exopolysaccharide production. Environ Microbiol. 2008;10(6):1419-32.
295. Choi AH, Slamti L, Avci FY, Pier GB, Maira-Litran T. The pgaABCD locus of Acinetobacter baumannii encodes the production of poly-beta-1-6-N-acetylglucosamine, which is critical for biofilm formation. J Bacteriol. 2009;191(19):5953-63.
296. Limoli DH, Jones CJ, Wozniak DJ. Bacterial Extracellular Polysaccharides in Biofilm Formation and Function. Microbiol Spectr. 2015;3(3).
297. Wozniak DJ, Wyckoff TJ, Starkey M, Keyser R, Azadi P, O'Toole GA, et al. Alginate is not a significant component of the extracellular polysaccharide matrix of PA14 and PAO1 Pseudomonas aeruginosa biofilms. Proc Natl Acad Sci U S A. 2003;100(13):7907-12.
298. Ma L, Jackson KD, Landry RM, Parsek MR, Wozniak DJ. Analysis of Pseudomonas aeruginosa conditional psl variants reveals roles for the psl polysaccharide in adhesion and maintaining biofilm structure postattachment. J Bacteriol. 2006;188(23):8213-21.
299. Colvin KM, Gordon VD, Murakami K, Borlee BR, Wozniak DJ, Wong GC, et al. The pel polysaccharide can serve a structural and protective role in the biofilm matrix of Pseudomonas aeruginosa. PLoS Pathog. 2011;7(1):e1001264.
300. Vasseur P, Vallet-Gely I, Soscia C, Genin S, Filloux A. The pel genes of the Pseudomonas aeruginosa PAK strain are involved at early and late stages of biofilm formation. Microbiology (Reading). 2005;151(Pt 3):985-97.
301. Ma L, Lu H, Sprinkle A, Parsek MR, Wozniak DJ. Pseudomonas aeruginosa Psl is a galactose- and mannose-rich exopolysaccharide. J Bacteriol. 2007;189(22):8353-6.
302. Tielker D, Hacker S, Loris R, Strathmann M, Wingender J, Wilhelm S, et al. Pseudomonas aeruginosa lectin LecB is located in the outer membrane and is involved in biofilm formation. Microbiology (Reading). 2005;151(Pt 5):1313-23.
303. Passos da Silva D, Matwichuk ML, Townsend DO, Reichhardt C, Lamba D, Wozniak DJ, et al. The Pseudomonas aeruginosa lectin LecB binds to the exopolysaccharide Psl and stabilizes the biofilm matrix. Nat Commun. 2019;10(1):2183.
304. Byrd MS, Sadovskaya I, Vinogradov E, Lu H, Sprinkle AB, Richardson SH, et al. Genetic and biochemical analyses of the Pseudomonas aeruginosa Psl exopolysaccharide reveal overlapping roles for polysaccharide synthesis enzymes in Psl and LPS production. Mol Microbiol. 2009;73(4):622-38.
305. Franklin MJ, Nivens DE, Weadge JT, Howell PL. Biosynthesis of the Pseudomonas aeruginosa Extracellular Polysaccharides, Alginate, Pel, and Psl. Front Microbiol. 2011;2:167.

306. Collins RF, Beis K, Dong C, Botting CH, McDonnell C, Ford RC, et al. The 3D structure of a periplasm-spanning platform required for assembly of group 1 capsular polysaccharides in Escherichia coli. Proc Natl Acad Sci U S A. 2007;104(7):2390-5.
307. Campisano A, Schroeder C, Schemionek M, Overhage J, Rehm BH. PslD is a secreted protein required for biofilm formation by Pseudomonas aeruginosa. Appl Environ Microbiol. 2006;72(4):3066-8.
308. Yu S, Su T, Wu H, Liu S, Wang D, Zhao T, et al. PslG, a self-produced glycosyl hydrolase, triggers biofilm disassembly by disrupting exopolysaccharide matrix. Cell Res. 2015;25(12):1352-67.
309. Wu H, Wang D, Tang M, Ma LZ. The advance of assembly of exopolysaccharide Psl biosynthesis machinery in Pseudomonas aeruginosa. Microbiologyopen. 2019;8(10):e857.
310. Friedman L, Kolter R. Genes involved in matrix formation in Pseudomonas aeruginosa PA14 biofilms. Mol Microbiol. 2004;51(3):675-90.
311. Jennings LK, Storek KM, Ledvina HE, Coulon C, Marmont LS, Sadovskaya I, et al. Pel is a cationic exopolysaccharide that cross-links extracellular DNA in the Pseudomonas aeruginosa biofilm matrix. Proc Natl Acad Sci U S A. 2015;112(36):11353-8.
312. Ghafoor A, Jordens Z, Rehm BH. Role of PelF in pel polysaccharide biosynthesis in Pseudomonas aeruginosa. Appl Environ Microbiol. 2013;79(9):2968-78.
313. Colvin KM, Alnabelseya N, Baker P, Whitney JC, Howell PL, Parsek MR. PelA deacetylase activity is required for Pel polysaccharide synthesis in Pseudomonas aeruginosa. J Bacteriol. 2013;195(10):2329-39.
314. Marmont LS, Whitfield GB, Rich JD, Yip P, Giesbrecht LB, Stremick CA, et al. PelA and PelB proteins form a modification and secretion complex essential for Pel polysaccharide-dependent biofilm formation in Pseudomonas aeruginosa. J Biol Chem. 2017;292(47):19411-22.
315. Whitfield GB, Marmont LS, Ostaszewski A, Rich JD, Whitney JC, Parsek MR, et al. Pel Polysaccharide Biosynthesis Requires an Inner Membrane Complex Comprised of PelD, PelE, PelF, and PelG. J Bacteriol. 2020;202(8).
316. Vasseur P, Soscia C, Voulhoux R, Filloux A. PelC is a Pseudomonas aeruginosa outer membrane lipoprotein of the OMA family of proteins involved in exopolysaccharide transport. Biochimie. 2007;89(8):903-15.
317. Marmont LS, Rich JD, Whitney JC, Whitfield GB, Almblad H, Robinson H, et al. Oligomeric lipoprotein PelC guides Pel polysaccharide export across the outer membrane of Pseudomonas aeruginosa. Proc Natl Acad Sci U S A. 2017;114(11):2892-7.
318. Smith EE, Buckley DG, Wu Z, Saenphimmachak C, Hoffman LR, D'Argenio DA, et al. Genetic adaptation by Pseudomonas aeruginosa to the airways of cystic fibrosis patients. Proc Natl Acad Sci U S A. 2006;103(22):8487-92.
319. Starkey M, Hickman JH, Ma L, Zhang N, De Long S, Hinz A, et al. Pseudomonas aeruginosa rugose small-colony variants have adaptations that likely promote persistence in the cystic fibrosis lung. J Bacteriol. 2009;191(11):3492-503.
320. Lee VT, Matewish JM, Kessler JL, Hyodo M, Hayakawa Y, Lory S. A cyclic-di-GMP receptor required for bacterial exopolysaccharide production. Mol Microbiol. 2007;65(6):1474-84.
321. Irie Y, Starkey M, Edwards AN, Wozniak DJ, Romeo T, Parsek MR. Pseudomonas aeruginosa biofilm matrix polysaccharide Psl is regulated transcriptionally by RpoS and post-transcriptionally by RsmA. Mol Microbiol. 2010;78(1):158-72.
322. Sakuragi Y, Kolter R. Quorum-sensing regulation of the biofilm matrix genes (pel) of Pseudomonas aeruginosa. J Bacteriol. 2007;189(14):5383-6.

323. Colvin KM, Irie Y, Tart CS, Urbano R, Whitney JC, Ryder C, et al. The Pel and Psl polysaccharides provide Pseudomonas aeruginosa structural redundancy within the biofilm matrix. Environ Microbiol. 2012;14(8):1913-28.
324. Yang L, Hu Y, Liu Y, Zhang J, Ulstrup J, Molin S. Distinct roles of extracellular polymeric substances in Pseudomonas aeruginosa biofilm development. Environ Microbiol. 2011;13(7):1705-17.
325. Hentzer M, Teitzel GM, Balzer GJ, Heydorn A, Molin S, Givskov M, et al. Alginate overproduction affects Pseudomonas aeruginosa biofilm structure and function. J Bacteriol. 2001;183(18):5395-401.
326. Yu H, Hanes M, Chrisp CE, Boucher JC, Deretic V. Microbial pathogenesis in cystic fibrosis: pulmonary clearance of mucoid Pseudomonas aeruginosa and inflammation in a mouse model of repeated respiratory challenge. Infect Immun. 1998;66(1):280-8.
327. Nivens DE, Ohman DE, Williams J, Franklin MJ. Role of alginate and its O acetylation in formation of Pseudomonas aeruginosa microcolonies and biofilms. J Bacteriol. 2001;183(3):1047-57.
328. Hay ID, Gatland K, Campisano A, Jordens JZ, Rehm BH. Impact of alginate overproduction on attachment and biofilm architecture of a supermucoid Pseudomonas aeruginosa strain. Appl Environ Microbiol. 2009;75(18):6022-5.
329. Pier GB, Coleman F, Grout M, Franklin M, Ohman DE. Role of alginate O acetylation in resistance of mucoid Pseudomonas aeruginosa to opsonic phagocytosis. Infect Immun. 2001;69(3):1895-901.
330. Slack MP, Nichols WW. The penetration of antibiotics through sodium alginate and through the exopolysaccharide of a mucoid strain of Pseudomonas aeruginosa. Lancet. 1981;2(8245):502-3.
331. Simpson JA, Smith SE, Dean RT. Alginate inhibition of the uptake of Pseudomonas aeruginosa by macrophages. J Gen Microbiol. 1988;134(1):29-36.
332. Evans LR, Linker A. Production and characterization of the slime polysaccharide of Pseudomonas aeruginosa. J Bacteriol. 1973;116(2):915-24.
333. Osman SF, Fett WF, Fishman ML. Exopolysaccharides of the phytopathogen Pseudomonas syringae pv. glycinea. J Bacteriol. 1986;166(1):66-71.
334. Braccini I, Grasso RP, Perez S. Conformational and configurational features of acidic polysaccharides and their interactions with calcium ions: a molecular modeling investigation. Carbohydr Res. 1999;317(1-4):119-30.
335. Hay I.D. RZU, Ghafoor A., Rehm B.H.A. Bacterial biosynthesis of alginates. J Chem Technol Biotechnol 2010;85:752–9.
336. Chitnis CE, Ohman DE. Genetic analysis of the alginate biosynthetic gene cluster of Pseudomonas aeruginosa shows evidence of an operonic structure. Mol Microbiol. 1993;8(3):583-93.
337. Zielinski NA, Chakrabarty AM, Berry A. Characterization and regulation of the Pseudomonas aeruginosa algC gene encoding phosphomannomutase. J Biol Chem. 1991;266(15):9754-63.
338. Shinabarger D, Berry A, May TB, Rothmel R, Fialho A, Chakrabarty AM. Purification and characterization of phosphomannose isomerase-guanosine diphospho-D-mannose pyrophosphorylase. A bifunctional enzyme in the alginate biosynthetic pathway of Pseudomonas aeruginosa. J Biol Chem. 1991;266(4):2080-8.
339. Roychoudhury S, May TB, Gill JF, Singh SK, Feingold DS, Chakrabarty AM. Purification and characterization of guanosine diphospho-D-mannose dehydrogenase. A key enzyme in the biosynthesis of alginate by Pseudomonas aeruginosa. J Biol Chem. 1989;264(16):9380-5.

340. Remminghorst U, Rehm BH. Alg44, a unique protein required for alginate biosynthesis in Pseudomonas aeruginosa. FEBS Lett. 2006;580(16):3883-8.
341. Remminghorst U, Rehm BH. In vitro alginate polymerization and the functional role of Alg8 in alginate production by Pseudomonas aeruginosa. Appl Environ Microbiol. 2006;72(1):298-305.
342. Jain S, Franklin MJ, Ertesvag H, Valla S, Ohman DE. The dual roles of AlgG in C-5-epimerization and secretion of alginate polymers in Pseudomonas aeruginosa. Mol Microbiol. 2003;47(4):1123-33.
343. Franklin MJ, Ohman DE. Mutant analysis and cellular localization of the AlgI, AlgJ, and AlgF proteins required for O acetylation of alginate in Pseudomonas aeruginosa. J Bacteriol. 2002;184(11):3000-7.
344. Bakkevig K, Sletta H, Gimmestad M, Aune R, Ertesvag H, Degnes K, et al. Role of the Pseudomonas fluorescens alginate lyase (AlgL) in clearing the periplasm of alginates not exported to the extracellular environment. J Bacteriol. 2005;187(24):8375-84.
345. Hay ID, Rehman ZU, Rehm BH. Membrane topology of outer membrane protein AlgE, which is required for alginate production in Pseudomonas aeruginosa. Appl Environ Microbiol. 2010;76(6):1806-12.
346. Deretic V, Schurr MJ, Boucher JC, Martin DW. Conversion of Pseudomonas aeruginosa to mucoidy in cystic fibrosis: environmental stress and regulation of bacterial virulence by alternative sigma factors. J Bacteriol. 1994;176(10):2773-80.
347. Yu H, Mudd M, Boucher JC, Schurr MJ, Deretic V. Identification of the algZ gene upstream of the response regulator algR and its participation in control of alginate production in Pseudomonas aeruginosa. J Bacteriol. 1997;179(1):187-93.
348. Leech AJ, Sprinkle A, Wood L, Wozniak DJ, Ohman DE. The NtrC family regulator AlgB, which controls alginate biosynthesis in mucoid Pseudomonas aeruginosa, binds directly to the algD promoter. J Bacteriol. 2008;190(2):581-9.
349. Castaneda M, Sanchez J, Moreno S, Nunez C, Espin G. The global regulators GacA and sigma(S) form part of a cascade that controls alginate production in Azotobacter vinelandii. J Bacteriol. 2001;183(23):6787-93.
350. Hay ID, Remminghorst U, Rehm BH. MucR, a novel membrane-associated regulator of alginate biosynthesis in Pseudomonas aeruginosa. Appl Environ Microbiol. 2009;75(4):1110-20.
351. Roberts I, Mountford R, High N, Bitter-Suermann D, Jann K, Timmis K, et al. Molecular cloning and analysis of genes for production of K5, K7, K12, and K92 capsular polysaccharides in Escherichia coli. J Bacteriol. 1986;168(3):1228-33.
352. Kroll JS, Zamze S, Loynds B, Moxon ER. Common organization of chromosomal loci for production of different capsular polysaccharides in Haemophilus influenzae. J Bacteriol. 1989;171(6):3343-7.
353. Frosch M, Weisgerber C, Meyer TF. Molecular characterization and expression in Escherichia coli of the gene complex encoding the polysaccharide capsule of Neisseria meningitidis group B. Proc Natl Acad Sci U S A. 1989;86(5):1669-73.
354. Hashimoto Y, Li N, Yokoyama H, Ezaki T. Complete nucleotide sequence and molecular characterization of ViaB region encoding Vi antigen in Salmonella typhi. J Bacteriol. 1993;175(14):4456-65.
355. Arakawa Y, Wacharotayankun R, Nagatsuka T, Ito H, Kato N, Ohta M. Genomic organization of the Klebsiella pneumoniae cps region responsible for serotype K2 capsular polysaccharide synthesis in the virulent strain Chedid. J Bacteriol. 1995;177(7):1788-96.
356. Qin L, Kida Y, Imamura Y, Kuwano K, Watanabe H. Impaired capsular polysaccharide is relevant to enhanced biofilm formation and lower virulence in Streptococcus pneumoniae. J Infect Chemother. 2013;19(2):261-71.

357. Joseph LA, Wright AC. Expression of Vibrio vulnificus capsular polysaccharide inhibits biofilm formation. J Bacteriol. 2004;186(3):889-93.
358. Ophir T, Gutnick DL. A role for exopolysaccharides in the protection of microorganisms from desiccation. Appl Environ Microbiol. 1994;60(2):740-5.
359. Roberts IS, Saunders FK, Boulnois GJ. Bacterial capsules and interactions with complement and phagocytes. Biochem Soc Trans. 1989;17(3):462-4.
360. Burns SM, Hull SI. Loss of resistance to ingestion and phagocytic killing by O(-) and K(-) mutants of a uropathogenic Escherichia coli O75:K5 strain. Infect Immun. 1999;67(8):3757-62.
361. Noel GJ, Hoiseth SK, Edelson PJ. Type b capsule inhibits ingestion of Haemophilus influenzae by murine macrophages: studies with isogenic encapsulated and unencapsulated strains. J Infect Dis. 1992;166(1):178-82.
362. Vimr ER, Steenbergen SM. Early molecular-recognition events in the synthesis and export of group 2 capsular polysaccharides. Microbiology. 2009;155(Pt 1):9-15.
363. Willis LM, Whitfield C. KpsC and KpsS are retaining 3-deoxy-D-manno-oct-2-ulosonic acid (Kdo) transferases involved in synthesis of bacterial capsules. Proc Natl Acad Sci U S A. 2013;110(51):20753-8.
364. Liston SD, Ovchinnikova OG, Whitfield C. Unique lipid anchor attaches Vi antigen capsule to the surface of Salmonella enterica serovar Typhi. Proc Natl Acad Sci U S A. 2016;113(24):6719-24.
365. Bushell SR, Mainprize IL, Wear MA, Lou H, Whitfield C, Naismith JH. Wzi is an outer membrane lectin that underpins group 1 capsule assembly in Escherichia coli. Structure. 2013;21(5):844-53.
366. Flemming HC. EPS-Then and Now. Microorganisms. 2016;4(4).
367. Poindexter JS. Biological Properties and Classification of the Caulobacter Group. Bacteriol Rev. 1964;28:231-95.
368. Tomlinson AD, Fuqua C. Mechanisms and regulation of polar surface attachment in Agrobacterium tumefaciens. Curr Opin Microbiol. 2009;12(6):708-14.
369. Van der Henst C, de Barsy M, Zorreguieta A, Letesson JJ, De Bolle X. The Brucella pathogens are polarized bacteria. Microbes Infect. 2013;15(14-15):998-1004.
370. Fritts RK, LaSarre B, Stoner AM, Posto AL, McKinlay JB. A Rhizobiales-Specific Unipolar Polysaccharide Adhesin Contributes to Rhodopseudomonas palustris Biofilm Formation across Diverse Photoheterotrophic Conditions. Appl Environ Microbiol. 2017;83(4).
371. Poindexter JS. The caulobacters: ubiquitous unusual bacteria. Microbiol Rev. 1981;45(1):123-79.
372. Hernando-Perez M, Setayeshgar S, Hou Y, Temam R, Brun YV, Dragnea B, et al. Layered Structure and Complex Mechanochemistry Underlie Strength and Versatility in a Bacterial Adhesive. MBio. 2018;9(1).
373. Fang G, Passalacqua KD, Hocking J, Llopis PM, Gerstein M, Bergman NH, et al. Transcriptomic and phylogenetic analysis of a bacterial cell cycle reveals strong associations between gene co-expression and evolution. BMC Genomics. 2013;14:450.
374. Smith CS, Hinz A, Bodenmiller D, Larson DE, Brun YV. Identification of genes required for synthesis of the adhesive holdfast in Caulobacter crescentus. J Bacteriol. 2003;185(4):1432-42.
375. Mitchell D, Smit J. Identification of genes affecting production of the adhesion organelle of Caulobacter crescentus CB2. J Bacteriol. 1990;172(9):5425-31.
376. Toh E, Kurtz HD, Brun YV. Characterization of the Caulobacter crescentus Holdfast Polysaccharide Biosynthesis Pathway Reveals Significant Redundancy in the Initiating Glycosyltransferase and Polymerase Steps. Journal of Bacteriology. 2008;190(21):7219-31.

377. Hardy GG, Allen RC, Toh E, Long M, Brown PJ, Cole-Tobian JL, et al. A localized multimeric anchor attaches the Caulobacter holdfast to the cell pole. Mol Microbiol. 2010;76(2):409-27.
378. Kurtz HD, Jr., Smit J. The Caulobacter crescentus holdfast: identification of holdfast attachment complex genes. FEMS Microbiol Lett. 1994;116(2):175-82.
379. Cole JL, Hardy GG, Bodenmiller D, Toh E, Hinz A, Brun YV. The HfaB and HfaD adhesion proteins of Caulobacter crescentus are localized in the stalk. Mol Microbiol. 2003;49(6):1671-83.
380. Hardy GG, Toh E, Berne C, Brun YV. Mutations in Sugar-Nucleotide Synthesis Genes Restore Holdfast Polysaccharide Anchoring to Caulobacter crescentus Holdfast Anchor Mutants. J Bacteriol. 2018;200(3).
381. Lepault J, Booy FP, Dubochet J. Electron microscopy of frozen biological suspensions. J Microsc. 1983;129(Pt 1):89-102.
382. Williams DBC, C.B. The Transmission Electron Microscope. Springer. 1996(Transmission Electron Microscopy):3-17.
383. Sartori Blanc N, Studer D, Ruhl K, Dubochet J. Electron beam-induced changes in vitreous sections of biological samples. J Microsc. 1998;192(Pt 2):194-201.
384. Nogales E, Scheres SH. Cryo-EM: A Unique Tool for the Visualization of Macromolecular Complexity. Mol Cell. 2015;58(4):677-89.
385. Midgley PA, Weyland M. 3D electron microscopy in the physical sciences: the development of Z-contrast and EFTEM tomography. Ultramicroscopy. 2003;96(3-4):413-31.
386. Baumeister W. Electron tomography: towards visualizing the molecular organization of the cytoplasm. Curr Opin Struct Biol. 2002;12(5):679-84.
387. Sigworth FJ. Principles of single-particle processing Microscopy. 2016;65(1):57-67.
388. Brilot AF, Chen JZ, Cheng A, Pan J, Harrison SC, Potter CS, et al. Beam-induced motion of vitrified specimen on holey carbon film. J Struct Biol. 2012;177(3):630-7.
389. Scheres SH. RELION: implementation of a Bayesian approach to cryo-EM structure determination. J Struct Biol. 2012;180(3):519-30.
390. Bharat TA, Scheres SH. Resolving macromolecular structures from electron cryo-tomography data using subtomogram averaging in RELION. Nat Protoc. 2016;11(11):2054-65.
391. Erickson HP, Klug A. The Fourier transform of an electron micrograph: effects of defocussing and aberrations, and implications for the use of underfocus contrast enhancement. Berichte
der Bunsengesellschaft für physikalische Chemie. 1970;74(11):1129-37.
392. Singer A, Shkolnisky Y. Three-Dimensional Structure Determination from Common Lines in Cryo-EM by Eigenvectors and Semidefinite Programming(). SIAM J Imaging Sci. 2011;4(2):543-72.
393. Frangakis AS, Bohm J, Forster F, Nickell S, Nicastro D, Typke D, et al. Identification of macromolecular complexes in cryoelectron tomograms of phantom cells. Proc Natl Acad Sci U S A. 2002;99(22):14153-8.
394. Egelman EH. Reconstruction of helical filaments and tubes. Methods Enzymol. 2010;482:167-83.
395. Gibson D.G YL, Chuang R-Y., Venter C.J , Hutchison C.A, Smith H.O. Enzymatic assembly of DNA molecules up to several hundred kilobases. Nature Methods. 2009;6:343-5.
396. Paradis E, Schliep K. ape 5.0: an environment for modern phylogenetics and evolutionary analyses in R. Bioinformatics. 2019;35(3):526-8.
397. Poindexter JS, Hagenzieker JG. Novel peptidoglycans in Caulobacter and Asticcacaulis spp. J Bacteriol. 1982;150(1):332-47.

398. Mastronarde DN. Automated electron microscope tomography using robust prediction of specimen movements. J Struct Biol. 2005;152(1):36-51.
399. Mindell JA, Grigorieff N. Accurate determination of local defocus and specimen tilt in electron microscopy. J Struct Biol. 2003;142(3):334-47.
400. Kremer JR, Mastronarde DN, McIntosh JR. Computer visualization of three-dimensional image data using IMOD. J Struct Biol. 1996;116(1):71-6.
401. Bharat TAM, Hoffmann PC, Kukulski W. Correlative Microscopy of Vitreous Sections Provides Insights into BAR-Domain Organization In Situ. Structure. 2018;26(6):879-86 e3.
402. Bharat TAM, Scheres SHW. Resolving macromolecular structures from electron cryo-tomography data using subtomogram averaging in RELION. Nature Protocols. 2016;11(11):9-20.
403. Bharat TA, Russo CJ, Lowe J, Passmore LA, Scheres SH. Advances in Single-Particle Electron Cryomicroscopy Structure Determination applied to Sub-tomogram Averaging. Structure. 2015;23(9):1743-53.
404. Wan W, Kolesnikova L, Clarke M, Koehler A, Noda T, Becker S, et al. Structure and assembly of the Ebola virus nucleocapsid. Nature. 2017;551(7680):394-7.
405. Zheng SQ, Palovcak E, Armache JP, Verba KA, Cheng Y, Agard DA. MotionCor2: anisotropic correction of beam-induced motion for improved cryo-electron microscopy. Nat Methods. 2017;14(4):331-2.
406. Rohou A, Grigorieff N. CTFFIND4: Fast and accurate defocus estimation from electron micrographs. J Struct Biol. 2015;192(2):216-21.
407. Scheres SH, Chen S. Prevention of overfitting in cryo-EM structure determination. Nat Methods. 2012;9(9):853-4.
408. Pettersen EF, Goddard TD, Huang CC, Couch GS, Greenblatt DM, Meng EC, et al. UCSF Chimera--a visualization system for exploratory research and analysis. J Comput Chem. 2004;25(13):1605-12.
409. O'Toole GA. Microtiter dish biofilm formation assay. J Vis Exp. 2011(47).
410. Xavier JB, Martinez-Garcia E, Foster KR. Social evolution of spatial patterns in bacterial biofilms: when conflict drives disorder. Am Nat. 2009;174(1):1-12.
411. Poindexter JS. Selection for nonbuoyant morphological mutants of Caulobacter crescentus. J Bacteriol. 1978;135(3):1141-5.
412. Ireland MM, Karty JA, Quardokus EM, Reilly JP, Brun YV. Proteomic analysis of the Caulobacter crescentus stalk indicates competence for nutrient uptake. Mol Microbiol. 2002;45(4):1029-41.
413. Gonin M, Quardokus EM, O'Donnol D, Maddock J, Brun YV. Regulation of stalk elongation by phosphate in Caulobacter crescentus. J Bacteriol. 2000;182(2):337-47.
414. Schlesner H, Bartels C, Sittig M, Dorsch M, Stackebrandt E. Taxonomic and phylogenetic studies on a new taxon of budding, hyphal Proteobacteria, Hirschia baltica gen. nov., sp. nov. Int J Syst Bacteriol. 1990;40(4):443-51.
415. Melia CE, Bharat TAM. Locating macromolecules and determining structures inside bacterial cells using electron cryotomography. Biochim Biophys Acta Proteins Proteom. 2018;1866(9):973-81.
416. Ong CJ, Wong MLY, Smit J. Attachment of the Adhesive Holdfast Organelle to the Cellular Stalk of Caulobacter-Crescentus. Journal of Bacteriology. 1990;172(3):1448-56.
417. Javens J, Wan Z, Hardy GG, Brun YV. Bypassing the need for subcellular localization of a polysaccharide export-anchor complex by overexpressing its protein subunits. Mol Microbiol. 2013;89(2):350-71.
418. Bharat TAM, Kureisaite-Ciziene D, Hardy GG, Yu EW, Devant JM, Hagen WJH, et al. Structure of the hexagonal surface layer on Caulobacter crescentus cells. Nat Microbiol. 2017;2:17059.

419. Goyal P, Krasteva PV, Van Gerven N, Gubellini F, Van den Broeck I, Troupiotis-Tsailaki A, et al. Structural and mechanistic insights into the bacterial amyloid secretion channel CsgG. Nature. 2014;516(7530):250-3.
420. Hershey DM, Fiebig A, Crosson S. A Genome-Wide Analysis of Adhesion in Caulobacter crescentus Identifies New Regulatory and Biosynthetic Components for Holdfast Assembly. mBio. 2019;10(1).
421. Schindelin J, Arganda-Carreras I, Frise E, Kaynig V, Longair M, Pietzsch T, et al. Fiji: an open-source platform for biological-image analysis. Nat Methods. 2012;9(7):676-82.
422. Goyal P, Van Gerven N, Jonckheere W, Remaut H. Crystallization and preliminary X-ray crystallographic analysis of the curli transporter CsgG. Acta Crystallogr Sect F Struct Biol Cryst Commun. 2013;69(Pt 12):1349-53.
423. Zhang M, Shi H, Zhang X, Zhang X, Huang Y. Cryo-EM structure of the nonameric CsgG-CsgF complex and its implications for controlling curli biogenesis in Enterobacteriaceae. PLoS Biol. 2020;18(6):e3000748.
424. Narita S, Tokuda H. Sorting of bacterial lipoproteins to the outer membrane by the Lol system. Methods Mol Biol. 2010;619:117-29.
425. Okuda S, Tokuda H. Lipoprotein sorting in bacteria. Annu Rev Microbiol. 2011;65:239-59.
426. Calabrese AN, Watkinson TG, Henderson PJ, Radford SE, Ashcroft AE. Amphipols outperform dodecylmaltoside micelles in stabilizing membrane protein structure in the gas phase. Anal Chem. 2015;87(2):1118-26.
427. Vinothkumar KR, Henderson R. Single particle electron cryomicroscopy: trends, issues and future perspective. Q Rev Biophys. 2016;49:e13.
428. Chertkov O, Brown PJ, Kysela DT, de Pedro MA, Lucas S, Copeland A, et al. Complete genome sequence of Hirschia baltica type strain (IFAM 1418(T)). Stand Genomic Sci. 2011;5(3):287-97.
429. Chepkwony NK, Berne C, Brun YV. Comparative Analysis of Ionic Strength Tolerance between Freshwater and Marine Caulobacterales Adhesins. J Bacteriol. 2019;201(18).
430. Wan Z, Brown PJ, Elliott EN, Brun YV. The adhesive and cohesive properties of a bacterial polysaccharide adhesin are modulated by a deacetylase. Mol Microbiol. 2013;88(3):486-500.
431. Levi A, Jenal U. Holdfast formation in motile swarmer cells optimizes surface attachment during Caulobacter crescentus development. Journal of Bacteriology. 2006;188(14):5315-8.
432. Bodenmiller D, Toh E, Brun YV. Development of surface adhesion in Caulobacter crescentus. J Bacteriol. 2004;186(5):1438-47.
433. Nickell S, Kofler C, Leis AP, Baumeister W. A visual approach to proteomics. Nat Rev Mol Cell Biol. 2006;7(3):225-30.
434. Koning RI, Koster AJ, Sharp TH. Advances in cryo-electron tomography for biology and medicine. Ann Anat. 2018;217:82-96.
435. Diebolder CA, Koster AJ, Koning RI. Pushing the resolution limits in cryo electron tomography of biological structures. J Microsc. 2012;248(1):1-5.
436. Chambers JR, Cherny KE, Sauer K. Susceptibility of Pseudomonas aeruginosa Dispersed Cells to Antimicrobial Agents Is Dependent on the Dispersion Cue and Class of the Antimicrobial Agent Used. Antimicrob Agents Chemother. 2017;61(12).
437. Lee YM, DiGiuseppe PA, Silhavy TJ, Hultgren SJ. P pilus assembly motif necessary for activation of the CpxRA pathway by PapE in Escherichia coli. J Bacteriol. 2004;186(13):4326-37.
438. Verger D, Bullitt E, Hultgren SJ, Waksman G. Crystal structure of the P pilus rod subunit PapA. PLoS Pathog. 2007;3(5):e73.

439. Capelli R, Peri C, Villa R, Nithichanon A, Conchillo-Sole O, Yero D, et al. BPSL1626: Reverse and Structural Vaccinology Reveal a Novel Candidate for Vaccine Design against Burkholderia pseudomallei. Antibodies (Basel). 2018;7(3).
440. He S, Scheres SHW. Helical reconstruction in RELION. J Struct Biol. 2017;198(3):163-76.
441. Klug A CF, Wyckoff HW. . Diffraction by helical structures. . Acta Cryst 1958;11:199–213.
442. Bharat TA, Riches JD, Kolesnikova L, Welsch S, Krahling V, Davey N, et al. Cryo-electron tomography of Marburg virus particles and their morphogenesis within infected cells. PLoS Biol. 2011;9(11):e1001196.
443. Baumeister W, Grimm R, Walz J. Electron tomography of molecules and cells. Trends Cell Biol. 1999;9(2):81-5.
444. Forster F, Hegerl R. Structure determination in situ by averaging of tomograms. Methods Cell Biol. 2007;79:741-67.
445. Winkler H. 3D reconstruction and processing of volumetric data in cryo-electron tomography. J Struct Biol. 2007;157(1):126-37.
446. Tang G, Peng L, Baldwin PR, Mann DS, Jiang W, Rees I, et al. EMAN2: an extensible image processing suite for electron microscopy. J Struct Biol. 2007;157(1):38-46.
447. Castano-Diez D, Kudryashev M, Arheit M, Stahlberg H. Dynamo: a flexible, user-friendly development tool for subtomogram averaging of cryo-EM data in high-performance computing environments. J Struct Biol. 2012;178(2):139-51.
448. Hrabe T, Chen Y, Pfeffer S, Cuellar LK, Mangold AV, Forster F. PyTom: a python-based toolbox for localization of macromolecules in cryo-electron tomograms and subtomogram analysis. J Struct Biol. 2012;178(2):177-88.
449. Castang S, Dove SL. High-order oligomerization is required for the function of the H-NS family member MvaT in Pseudomonas aeruginosa. Mol Microbiol. 2010;78(4):916-31.
450. Valentini M, Filloux A. Biofilms and Cyclic di-GMP (c-di-GMP) Signaling: Lessons from Pseudomonas aeruginosa and Other Bacteria. J Biol Chem. 2016;291(24):12547-55.
451. Ho YS, Burden LM, Hurley JH. Structure of the GAF domain, a ubiquitous signaling motif and a new class of cyclic GMP receptor. EMBO J. 2000;19(20):5288-99.
452. Brown JM, Firtel RA. Phosphorelay signalling: new tricks for an ancient pathway. Curr Biol. 1998;8(18):R662-5.
453. Gao R, Stock AM. Biological insights from structures of two-component proteins. Annu Rev Microbiol. 2009;63:133-54.
454. Busch A, Waksman G. Chaperone-usher pathways: diversity and pilus assembly mechanism. Philos Trans R Soc Lond B Biol Sci. 2012;367(1592):1112-22.
455. Pedelacq JD, Cabantous S, Tran T, Terwilliger TC, Waldo GS. Engineering and characterization of a superfolder green fluorescent protein. Nat Biotechnol. 2006;24(1):79-88.
456. Werneburg GT, Henderson NS, Portnoy EB, Sarowar S, Hultgren SJ, Li H, et al. The pilus usher controls protein interactions via domain masking and is functional as an oligomer. Nat Struct Mol Biol. 2015;22(7):540-6.
457. Thanassi DG, Saulino ET, Lombardo MJ, Roth R, Heuser J, Hultgren SJ. The PapC usher forms an oligomeric channel: implications for pilus biogenesis across the outer membrane. Proc Natl Acad Sci U S A. 1998;95(6):3146-51.